Mapping Chemical, Ionic and Electronic Properties of High Capacity Cathode Materials for Lithium-ion Batteries

Michael W. Fraser

Corpus Christi College

University of Oxford

A thesis submitted for the degree of

Doctor of Philosophy

Supervised by Prof. Robert Weatherup

Trinity 2024

Declaration

I, Michael W. Fraser, confirm that the content of my thesis is solely my own work. Where information has been sourced from external references, appropriate acknowledgements have been made within the thesis.

17/04/2024

Acknowledgements

First and foremost, I sincerely thank my supervisor, Professor Rob Weatherup, for entrusting me with the opportunity to embark on this project. His unwavering guidance and support throughout the experimental phase, beamtimes, and the culmination of this Thesis have been invaluable.

I express my special appreciation to the dedicated team of postdoctoral researchers who have played pivotal roles in shaping the trajectory of my Thesis. To Dr Peixi Cong, I extend my sincere gratitude for your invaluable assistance, particularly in harnessing your expertise in XANES, which has proven indispensable to the success of this project. Dr Erik Björklund, your extensive knowledge of batteries and unwavering support during numerous beamtimes have been instrumental in advancing our research. Dr Leanne Jones, Dr Joshua Gibson, and Dr Pravin Diwal, I appreciate your guidance and insights into synchrotron sources and your help during beamtimes. Lastly, I extend my heartfelt thanks to Dr Jack Swallow for our long discussions and collaborative efforts on the operando paper, and for the invaluable moral support provided throughout my DPhil journey.

I want to extend my gratitude to all current and former DPhil students in the Weatherup Group, whose contributions have been invaluable to the progress of this Thesis. Special thanks to Jodie Charlton, Conor Phelan, Jasper Singh, and Lizzie Jones for their unwavering support during numerous beamtimes and pub quizzes.

On a personal note, I extend heartfelt gratitude to my parents, whose unwavering support kept me motivated through the challenges of COVID-19 lockdowns and throughout my DPhil

journey. I am also grateful to all my siblings for their steadfast support and my growing number of nieces and nephews, whose presence brings joy to my life.

To my DPhil friends from Kingston Road – Dom, Axel, and Marco – your support during my time in Oxford has been invaluable. Thank you for the friendship, guidance, and positive energy that have enriched my experience. From late-night poker sessions to long conversations into the wee hours, our shared moments are treasured, and I eagerly anticipate many more to come.

Last but certainly not least, I want to extend my deepest appreciation to my future wife, Angela. Angela, your unwavering support and encouragement have been the bedrock of my journey through this DPhil. Your selflessness and limitless good humour have been instrumental in seeing me through the challenges and triumphs of completing this Thesis. I am profoundly grateful for your unwavering presence in my life and excited to share the rest with you.

Abstract

Nickel-rich layered cathode materials, such as $Li(Ni_{0.8}Mn_{0.1}Co_{0.1})O_2$ (NMC811), are integral to commercial Li-ion batteries for portable electronics and electric vehicles. However, the elevated nickel content in NMC811 induces accelerated degradation, limiting battery cycle life and performance. Increasing the upper cut-off potential enhances energy density. However, it exacerbates irreversible degradation at the cathode electrolyte interface (CEI), resulting in oxygen release and transition metal dissolution that impacts long-term battery cycling.

This study initially employed spatially resolved synchrotron source X-ray photoemission electron microscopy (XPEEM) to resolve the distribution of degradation products in the CEI and transition metal oxidation states at cycled polycrystalline NMC811 surfaces. Characterisation revealed particle-to-particle variation in degradation mechanisms, offering insights into transition metal dissolution.

Secondly, the role of transition metal dissolution from the cathode and subsequent deposition at graphitic anode interfaces is examined using X-ray Absorption Near Edge Structure (XANES) and Near Edge X-ray Absorption Fine Structure (NEXAFS) techniques. XANES measurements revealed ion exchange pathways for dissolved cations (Ni and Mn) and probed the redox activity of Ni and Mn on graphite electrodes. This investigation sheds light on the mechanisms of transition metal incorporation onto the graphite solid-electrolyte interphase (SEI) and the redox activity of Ni and Mn on the electrode surface.

In the final results chapter, an environmental cell was developed to track the evolution of solid-electrolyte interphase (SEI) formation on Ni and MnO using operando NEXAFS techniques. This novel ultra-high vacuum-compatible electrochemical cell design,

incorporating SiN_x membranes, enabled monitoring of electronic structure changes during potential dependent SEI evolution.

This thesis thus presents advancements in material characterisation and offers crucial insights into the role of transition metals at battery interfaces. High-resolution XPEEM enables precise spatial resolution of surface electrode changes. XAS was utilised as a powerful tool for elucidating cation exchange and redox processes of transition metal cations at the anode interface. Moreover, the development of environmental cells facilitates the acquisition of valuable potential-dependent data under realistic battery operating conditions.

Statement of Authorship

1. In Chapter 3, soft NEXAFS measurements of NMC811 were published by Bjorklund et al. and the raw data was replotted in Chapter 3 Figure 3.5.
2. EXAFS refinement detailed in Chapter 4 Figure 4.12, Table 4.1 and 4.2 was performed by Dr Peixi Cong.

Table of Contents

Abbreviations

LiB	Lithium-ion battery
BEVs	Battery Electric Vehicles
NMC	Lithium Nickel Manganese Cobalt Oxide
SEI	Solid Electrolyte Interphase
SHE	Standard Hydrogen Electrode
EC	Ethylene Carbonate
DMC	Dimethyl Carbonate
EMC	Ethyl Methyl Carbonate
PC	Propyl Carbonate
DEC	Diethyl Carbonate
LTMO	Lithium Transition Metal Oxide
LMO	Lithium Manganese Oxide
LFP	Lithium Iron Phosphate
NCA	Lithium Nickel Cobalt Aluminium Oxide
NMC811	$Li(Ni_{0.8}Mn_{0.1}Co_{0.1})O_2$
NMC622	$Li(Ni_{0.6}Mn_{0.2}Co_{0.2})O_2$
NMC111	$Li(Ni_{0.33}Mn_{0.33}Co_{0.33})O_2$
CEI	Cathode Electrolyte Interphase
E_g	Energy Separation
OCV	Open Circuit Voltage
LLI	Loss of Lithium Inventory
LAM_{CE}	Loss of Active Material on the Cathode Electrode
LAM_{AE}	Loss of Active Material on the Anode Electrode
UCV	Upper Cut-off Voltage
LCV	Lower Cutoff Voltage

HF	Hydrofluoric Acid
XANES	X-ray Absorption Near Edge Structure
EPR	Electron Paramagnetic Resonance
EXAFS	Extended X-ray Absorption Fine Structure
XPEEM	X-ray Photoemission Electron Microscopy
NEXAFS	Near Edge X-ray Absorption Fine Structure
XAFS	X-ray Absorption Fine Structure
XPS	X-ray photoelectron Spectroscopy
TM	Transition Metal
RF	Radio Frequency
CV	Cyclic Voltammetry
CC	Constant Current
CCCV	Constant Current Constant Voltage
NA	Numerical Aperture
SEM	Scanning Electron Microscopy
DLS	Diamond Light Source
PC	Polycrystalline
NMP	N-methyl-2-pyrolidone
CA	Conductive Additive
CAM	Cathode Active Material
TEY	Total Electron Yield
FY	Fluorescence Yield

List of Figures

List of Tables

List of Publications

1. Swallow, J.E.N., Fraser, M.W., Kneusels, NJ.H. *et al.* Revealing solid electrolyte interphase formation through interface-sensitive *Operando* X-ray absorption spectroscopy. *Nat Commun* **13**, 6070 (2022). https://doi.org/10.1038/s41467-022-33691-1
2. Jack E. N. Swallow, Elizabeth S. Jones, Ashley R. Head, Joshua S. Gibson, Roey Ben David, Michael W. Fraser, Matthijs A. van Spronsen, Shaojun Xu, Georg Held, Baran Eren, and Robert S. Weatherup. *Journal of the American Chemical Society* **2023** *145* (12), 6730-6740. DOI: 10.1021/jacs.2c12728
3. Conor M. E. Phelan, Erik Björklund, Jasper Singh, Michael Fraser, Pravin N. Didwal, Gregory J. Rees, Zachary Ruff, Pilar Ferrer, David C. Grinter, Clare P. Grey, and Robert S. Weatherup. *Chemistry of Materials* **2024** *36* (7), 3334-3344. DOI:10.1021/acs.chemmater.4c00004

Scope of the Thesis

This DPhil research aims to enhance characterisation techniques to understand interfacial degradation, focusing on high-capacity cathode materials relevant to advanced battery applications like BEVs. The study investigates degradation mechanisms associated with aged NMC811 and graphite using a comprehensive approach involving electrochemical methods, X-ray spectroscopy, and electron microscopy techniques.

Chapter I introduces the lithium-ion battery landscape, highlighting the critical areas requiring further research. Chapter II focuses on describing the characterisation techniques carried out for this research. Chapter III showcases a novel electrode preparation method tailored for X-ray photoemission electron microscopy (XPEEM) analysis, revealing degradation at NMC811 interfaces with high spatiochemical resolution. Chapter IV investigates the consequences of TM migration from NMC-class cathode materials to the SEI, examining TM incorporation into the anode SEI and TM redox activity during electrochemical cycling. Chapter V presents the development of an environmental cell for near-edge X-ray absorption fine structure (NEXAFS) measurements, shedding light on the potential-dependent evolution of the SEI on nickel (Ni) and manganese oxide (MnO) electrodes during electrochemical cycling. Finally, the concluding chapter combines the key findings and outlines potential future research projects.

Chapter 1 - Introduction

In 2019, John B. Goodenough, Stanley Whittingham, and Akira Yoshino were awarded the Nobel Prize in Chemistry for their groundbreaking work on lithium-ion batteries (LIBs). Sony's commercialisation of LIBs in 1991 revolutionised portable energy storage, transforming the landscape of handheld electronic devices such as mobile phones, laptops, tablets, and cameras.[1–4]

The urgency for energy storage solutions has intensified due to the intermittent nature of renewable energy sources like wind and solar power amidst a global dependency on fossil fuels. Fossil fuels account for approximately 83% of primary energy sources, contributing to anthropogenic climate change and emissions of harmful pollutants such as NO_x, SO_x, and CO_x. Transportation alone consumes about 20% of global primary energy.[5]

In response, many nations plan to phase out internal combustion engines by the 2030s, with a shift towards battery electric vehicles (BEVs) by automotive manufacturers. Recognising the crucial role of advanced battery technologies in this transition, the UK government announced a significant investment of £541 million between 2017 and 2025 to advance battery technology and promote the widespread adoption of BEVs. This initiative aims to accelerate the shift towards sustainable transportation and mitigate the adverse impacts of fossil fuel dependence on local and global scales.[6]

LIBs are stable and high-capacity electrochemical storage systems. They boast attributes such as high efficiency, low self-discharge rates, elevated nominal voltage (compared to other battery storage systems), and an extensive operating temperature range.[7–10] With projected battery prices declining to approximately $73 per kilowatt-hour by 2030, LIBs have emerged

as the frontrunner for energy storage within the automotive industry.[11] However, the evolving landscape demands enhanced energy densities, stringent safety standards, reduced costs, and prolonged cycle lives for future batteries. Despite the promise of next-generation battery materials such as solid electrolytes and sulfur-based cathodes, stability concerns have hindered their widespread adoption. Immediate attention is warranted toward enhancing our fundamental understanding of existing and forthcoming battery anode and cathode materials. Such efforts are pivotal in facilitating the mass adoption of BEVs in the near term. Since the early 1990s, the energy density of lithium-ion batteries (LIBs) has demonstrated an average annual increase of 8-9%, attributable to the discovery of novel materials, advanced pack-level designs, and a deeper comprehension of fundamental physio-electrochemistry.[12]

Nickel-rich cathode materials are promising for enhancing LIB performance by increasing energy density and reducing reliance on cobalt, which raises environmental, ethical, and supply chain concerns. The substitution of cobalt with higher nickel content, as seen in lithium nickel manganese cobalt oxide (NMC) class cathodes, offers advantages such as high theoretical capacity, lower cost, and abundance.[13,14] However, challenges arise from voltage-induced phase transitions and structural degradation during cycling, leading to rapid capacity loss and low cycle life. Elevated nickel content can also induce material instability, causing electrolyte decomposition and transition metal dissolution compromising long-term performance.[15] Addressing these issues necessitates a comprehensive approach involving novel material design, synthesis, and advanced characterisation techniques.

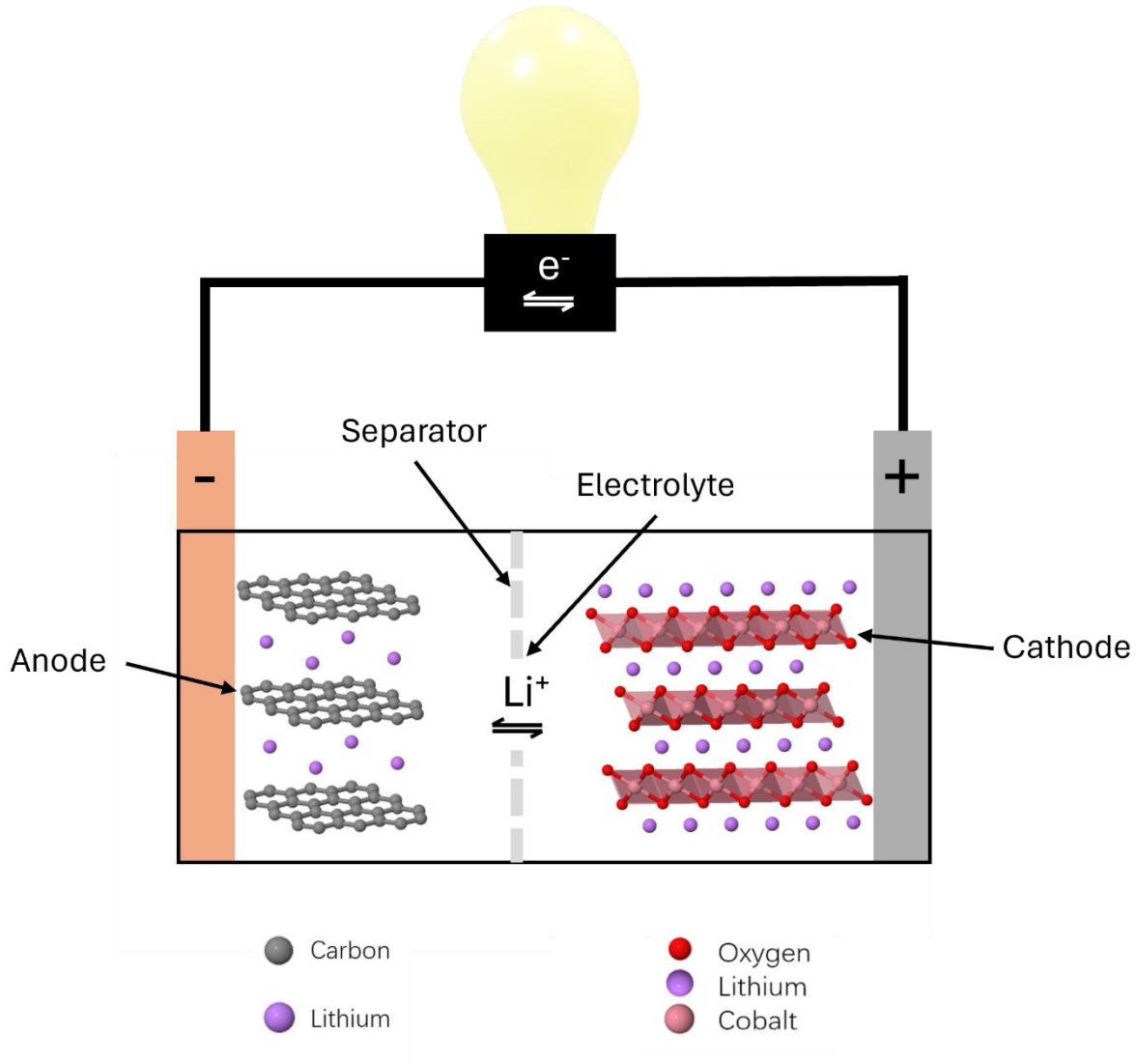

Figure 1.1. Schematic diagram showing the components of a lithium-ion battery.

In a lithium-ion cell as depicted in Figure 1.1, the positive and negative electrodes are stacked with an electrolyte and separator in between, preventing direct contact. This setup enables the flow of Li^+ ions while blocking electrons. Electrons flow from the active material to the current collector and through the external circuit, releasing or consuming electrical energy. These electrons are charge compensated by Li^+ ions flowing in the opposite direction.

The primary active materials in lithium-ion cells, such as $LiCoO_2$ for the positive electrode (cathode) and graphite for the negative electrode (anode), constitute the bulk of electrode

mass and volume (about 95%). Since they are powders, they require binding with a polymer to secure them to the current collector. Positive electrode materials often have poor electronic conductivities and are supplemented with finely dispersed carbon powder to form a conductive network between active particles. The electrolyte, usually $LiPF_6$ dissolved in a non-aqueous solvent, percolates the pores of each electrode, ensuring particle wetting and facilitating Li^+ ion diffusion between the active material and the electrolyte. The other main non-active component separators are essential components in batteries, preventing direct contact between electrodes and facilitating the movement of lithium ions. Typically made of porous materials like polyethylene or polypropylene, they allow electrolyte flow between electrodes during charging and discharging, preventing short circuits and ensuring safe battery operation.[16,17]

How batteries store energy

Electrochemistry involves converting electrical energy to chemical energy and vice versa in energy storage systems. Two active electrodes drive chemical energy storage through oxidation and reduction reactions facilitated by electron transfer in an external circuit. In batteries, positive ion migration between electrodes occurs via an electronically non-conductive electrolyte. The change in Gibbs free energy quantifies the stored or released chemical energy during these electron and ion redistributions:

$$\Delta G = -nFE_{cell} \qquad [1.1]$$

Where the Gibbs free energy ΔG represents the equilibrium state of the cell, it shows the relationship between chemical changes and electrical potentials. The number of electrons involved in this process is denoted by n, while F represents the Faraday constant, which serves

as a conversion factor between electrical charge and moles of electrons. The full cell potential E_{cell} measures the driving force behind energy conversion in a battery system.

According to the Nernst equation, the equilibrium voltage of a cell correlates with the disparity in chemical potentials at each electrode displayed below:

$$E_{cell} = \mu_{pos} - \mu_{neg} \quad [1.2]$$

Here, E_{cell} represents the equilibrium cell voltage, while μ_{pos} and μ_{neg} represent the chemical potentials of the positive and negative electrodes, respectively. As lithium ions undergo insertion or extraction within an electrode and are compensated by electrons via an external circuit, their chemical potential changes are indicative of the changing oxidation or reduction state. At full states of charge, a large difference emerges in the chemical potentials between the electrodes, driving electrode reactions until the cell reaches a discharged state or the external circuit is broken.[18]

The cell's specific capacity is linked to the electrode's ability to accommodate both Li-ions and electrons during charge-discharge cycles. This capacity is determined by the chemical compositions and redox states of the elements within the host material, which are accessible within the voltage window of the electrolyte while avoiding irreversible structural changes expressed as:

$$Specific\ Capacity = \frac{nF}{3600M_w} \quad [1.3]$$

Here, n represents the number of electrons (and Li^+) transferred, F stands for the Faraday constant, and M_w denotes the molecular weight of the electrode active material. A factor of 3600 is applied to give the units mAh g^{-1}.[18,19]

The theoretical energy of a battery can be calculated as E_{cell} (V) multiplied by capacity (Ah), to give watthour (Wh), representing the maximum energy deliverable by the electrochemical system as shown in equation:[19]

$$Energy\ (Wh) = E_{cell}(V) \times Specific\ Capacity\ (Ah) \quad [1.4]$$

Lithium-ion battery redox

Two half-cell reactions occur at each electrode: oxidation occurring at the anode and reduction occurring at the cathode during discharge cycles:

$$Li_x\ C_6 \leftrightharpoons xLi^+ + xe^- + C_6 \quad [1.5]$$

$$Li_{1-x}CoO_2 + xLi^+ + xe^- \leftrightharpoons LiCoO_2 \quad [1.6]$$

The LIB is sometimes referred to as the “rocking chair” battery due to the intercalating nature of Li^+ ions with electrode materials. The half-cell reaction of equation [1.5] occurs at the anode electrode, lithium-ions are intercalated/de-intercalated into/from the layered structure of the graphite. The half-cell reaction of equation [1.6] occurs at the cathode electrode, lithium-ions are intercalated/de-intercalated to/from the crystal structure of the cathode electrode. Both redox reactions occurring during charge and discharge cycles are represented by equation [1.7]:

$$Li_{1-x}CoO_2 + Li_xC_6 \leftrightharpoons LiCoO_2 + C_6 \quad [1.7]$$

The overall cell equation [7] represents a simple overview of the electrochemical process for a LIB. In reality there are several other reactions occurring during this process, including the formation of the solid electrolyte interphase (SEI) layer which is integral to the thermodynamic stability of the cell. Other parasitic side reactions also occur (oxidation/reduction of

electrolyte, gas evolution etc…) contributing to degradation mechanisms that affect cycle life and capacity fade.[8,9]

Materials

Anode

Lithium, the third-lightest element in the periodic table, possesses a relatively small radius for a singly charged ion and exhibits the lowest reduction potential among all elements. These distinctive characteristics confer upon lithium metal remarkably high energy density, rendering it a desirable candidate for anode electrode applications within energy storage systems. However, challenges persist due to stability issues arising from an unstable interface during cycling and the propensity for lithium dendrite growth, ultimately contributing to diminished cycle lives and short circuits.[20,21]

Carbonaceous anode materials, such as graphite, have been used widely in commercial cells since SONY's commercialisation in 1991. Graphite possesses a similar reduction potential as lithium metal (~0.3 V - 0.05 V vs Li^+/Li) and can store one Li^+ per six carbon atoms. Graphite also has a relatively high specific capacity (~370 mAh g^{-1}), which is much less than lithium metal but still significantly greater than the practical, specific capacities of conventional lithium transition metal oxides.[22] Silicon ($Li_{22}Si_5$) anodes also exhibit low reduction potentials (<0.5 V vs Li^+/Li) while offering more than ten times the theoretical specific capacity (~4.2 Ah g-1) compared to graphite. However, pure silicon anodes suffer from a volume expansion of ~300% during lithium intercalation, leading to pulverisation of the silicon particles, causing rapid capacity loss and poor cycle life as further SEI forms on the newly exposed active material.[23] Furthermore, the slow lithium diffusion (10^{-14} - 10^{-13} $cm^2\ s^{-1}$) and low electronic

conductivity of silicon (10^{-5} - 10^{-3} S cm^{-1}) can limit high-rate applications using purely silicon-based anodes.[24,25]

Graphite-silicon composite electrodes offer a promising alternative approach, balancing increased capacity and extended cycle life by addressing silicon volume expansion. Various innovations, including novel silicon nanostructures, silicon fibres, and silicon-nanolayer-modified graphite electrodes, achieve practical capacities ranging from 820 to 1503 mAh g^{-1}. However, challenges associated with volume expansion, including particle cracking, loss of electrical contact, and subsequent SEI formation on newly exposed surfaces, remain significant obstacles. [26,27] Additionally, the operational voltage is contingent on the silicon-to-graphite capacity ratio due to differing delithiation potentials, with higher silicon content typically resulting in reduced operational voltage in full-cell configurations. [28] To address these issues structural.

In summary, significant progress has been made in improving the electrochemical properties of silicon-based anodes for commercial applications. Various strategies have been employed, with structural design emerging as a promising solution. This approach includes developing silicon nanostructures by reducing silicon to nanoscale dimensions with diverse morphologies and porous architectures, such as yolk-shell and double-wall structures.[29,30]

Early investigations have shown that nanoscale silicon can mitigate volume expansion and pulverisation issues. However, the increased specific surface area of nanosised silicon consumes active lithium from the electrolyte through continued SEI formation and lithium-ion consumption, leading to low coulombic efficiency. Electrolyte additives such as Fluorethylene carbonate (FEC) have increased capacity retention by forming stable interfaces.[31,32]

Integrating silicon with carbon has demonstrated significant promise in enhancing the electrical conductivity of silicon-based materials and improving their rate performance. Carbon materials serve as a buffer to accommodate silicon's volume changes and prevent increased contact between silicon and the electrolyte. The silicon content of the composite electrodes is limited as the volume expansion of silicon can decrease the volumetric energy density of a full cell.[33]

Electrolyte

A commercial LIB features a liquid electrolyte containing a dissolved lithium salt in non-aqueous polar organic solvents. It is vital in facilitating ionic transport to support redox reactions at the electrodes. The salt is typically 1M $LiPF_6$ to balance high ionic mobility and low electrolyte viscosity, producing a conductivity of about ~10^{-2} S cm^{-1}.[34] Non-aqueous solvents are preferred over aqueous ones due to their stability and the potential window exceeding approximately 1.23 V vs SHE (Standard hydrogen electrode), leading to the oxygen evolution reaction.[35]

Commonly used electrolyte solvent additives, such as ethylene carbonate (EC), dimethyl carbonate (DMC), and ethyl methyl carbonate (EMC), expand the electrolyte's potential window to <4.5 V vs Li^+/Li.[36] EC and propyl carbonate (PC) have high dielectric constants (95.3 and 65.5 at 25˚C, respectively) and effectively solvate Li^+ ions but exhibit high viscosities (1.9 mPa s), impeding electrode wettability and ionic conductivity.[37]

Therefore, a blend of cyclic carbonates (with high dielectric constants and viscosity) and linear carbonates (with low dielectric constants and viscosity) is used to balance lithium solvation and electrolyte viscosity. Adding linear carbonates like ethyl methyl carbonate (EMC), with

lower viscosity (0.544 mPa s), reduces overall viscosity to around 2.8 mPa s, facilitating Li^+ ion transport. Additionally, solvents such as DMC or diethyl carbonate (DEC), are commonly used in electrolytes.[38]

Cathodes

The cathode active material is typically a lithium transition metal oxide (LTMO) due to attractive properties such as high operating potentials and raw material availability.[39] Cell potential (governed by the thermodynamic stability of the electrolyte) and capacity of LTMO are limiting factors in terms of energy density, as a result intensive research has been undertaken to improve this shortfall. Lots of attention is focused on improving layered cathode electrodes which are solid host matrices consisting of a close packed array allowing foreign cationic insertion into octahedral sites, this Li^+ charge is balanced by electrons. The structures consist of divalent oxides (O^{2-}) with ionic radii of 1.4 Å tightly packed creating octahedral holes (0.58Å). The ionic radii of the transition metal ion Me^{3+} and Me^{4+} vary in the region of 0.5-0.7 Å and are packed into octahedral sites of the packed anionic structure. The monovalent lithium cations with an ionic radius of 0.74 Å can be inserted or extracted from the matrix.[40] Three structures (spinel, layered and olivine) are the most prominent intercalating cathodes. Spinel $LiMn_2O_4$ (LMO) and olivine $LiFePO_4$ (LFP) compounds have had some commercial success, however layered LTMO compounds (LCO, NMC and NCA) are favoured due to their increased energy density and high stability.

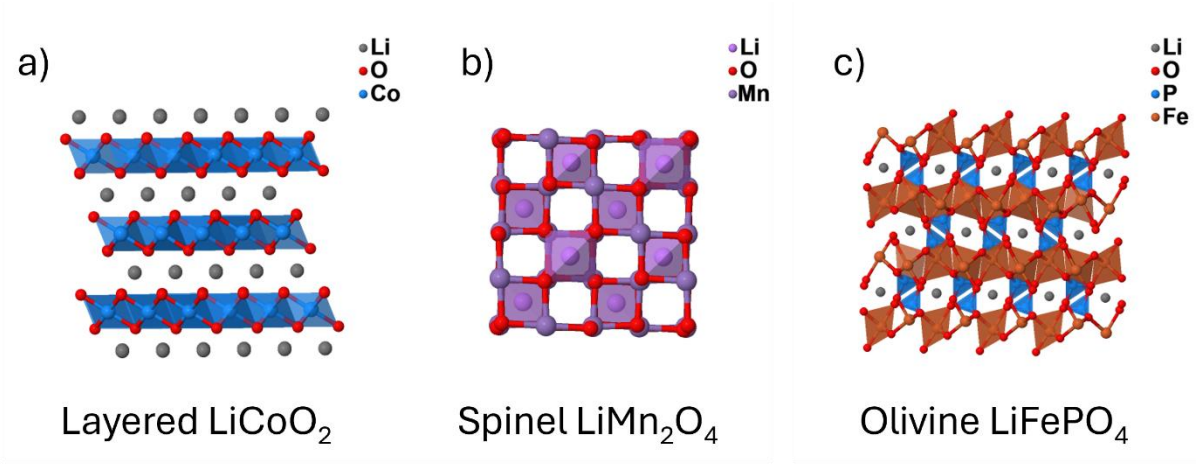

Figure 1.2. Lithium transition metal oxide structures a) layered structure b) spinel structure and c) olivine structure.

LMO is a low cost and non-toxic material making it an attractive cathode material for LIBs. LMO has a relatively low energy density even though it has a high average operating voltage (4.1 V), a low theoretical specific capacity of ~140 mAh g^{-1} of which ~120 mAh g^{-1} is a practically available as the spinel structure remains relatively intact when de-lithiated. LMO also suffers from poor cycle life due to parasitic side reactions stemming from electrochemically active Mn^{2+} ions dissolving in the electrolyte and oxidising or reducing forming Mn^{4+} and Mn^{2+} ions respectively which are involved in parasitic side reactions. This causes structural instability due to oxygen loss causing conditions for thermal runaway. These factors have limited adoption for high energy density applications.[8,41,42]

LFP is a low cost and environmentally friendly material known for its thermal stability due to strong covalent P-O bonds in the polyanion $(PO_4)^{3-}$ giving LFP cells a long cycle life.[43] LFPs poly-oxyanioic olivine structure as described in Figure 1.2 consists of LiO_6 and FeO_6 occupying octahedra sites and phosphates occupying tetrahedra sites in a distorted hexagonal close packed array. LFP has a theoretical capacity of 170mAh g^{-1} but, suffers from a number of drawbacks including poor energy density due to a low reduction potential 3.45 V vs Li^+/Li and

sluggish kinetics; low ionic (10^{-14} – 10^{-16} cm^2 S^{-1}) and electrical conductivity (<10^{-9} S cm^{-1}) result from impurities blocking 1D channels facilitating Li^+ diffusion.[44–47] This severely limits rate capabilities however, manufacturers are overcoming these limitations by using a number of methods: reducing particle size, cationic doping and highly amorphous carbon coatings to name a few.[48]

Prior to the BEV revolution Lithium cobalt oxide was by far the most commercially successful layered LTMO cathode material being used in modern LIBs. LCO has a high theoretical capacity (274 mAh g^{-1}) although practical capacity is limited to ~50% as a phase transition from hexagonal to monoclinic occurs during deep cycling (>4.2 V) and this negatively impacts cycle life and capacity fade. The high cost, toxicity of cobalt and high profile safety incidents have driven research to find alternative layered cathode materials.[49] Nickel rich layered oxide materials such as lithium nickel manganese cobalt oxide (NMC) and lithium nickel cobalt aluminium oxide (NCA) offer much higher practical energy densities at a much lower cost by replacing cobalt with nickel, commonly utilised in battery packs for the Nissan Leaf and in Tesla automobiles respectively.[50]

Both NCA and NMC were born from partial cation substitution of $LiNO_2$, doped with Al^{3+} and Mn^{4+} respectively to provide stability of the layered structure. NMC and NCA both offer benefits over LCO due to their lower cost and toxicity (lower cobalt content) and higher capacities ranging from 150-200 mAh g^{-1} (which is dependant stoichiometric ratio of transition metals and assuming cut-off potentials <4.2 V vs Li^+/Li). Nickel rich $LiNi_{0.8}Mn_{0.1}Co_{0.1}O_2$ (NMC811) is an attractive cathode material for its ability to provide high specific capacity at ~200 mAh g^{-1} at ~3.8 V vs. Li^+/Li with fast ionic diffusion coefficients (10^{-8} – 10^{-9} cm^2S^{-1}).[51] Accessing higher capacity requires higher upper cut-off voltages (>4.3 V), this can lead to

significant degradation and gas (O_2, CO and CO_2) evolution.[52] Parasitic oxidation reactions of the electrolyte forming a cathode electrolyte interphase (CEI) layer have also been detected when cycling to higher cut-off voltages leading to capacity fade and impedance rise.[53] Surface reconstruction via electrode/electrolyte interaction and electrochemical cycling can lead to formation of a reduced surface layer of the crystal lattice, with the electrode electrolyte interface having a rock-salt like structure containing Ni^{2+}, Mn^{2+} and Co^{2+} ions as determined with soft XAS.[54,55] Cationic mixing (Ni^{2+}/Li^{+}) is partially responsible for the formation of a Ni-O rock salt layer on the cathode surface due to similar ionic radii of Ni^{2+}/Li^{+} (0.69Å and 0.76 Å respectively) reducing Li^{+} ion diffusion and capacity. [56]

Charging to elevated voltages (e.g., 4.8 V) can induce the formation of a disordered spinel structure within the Fd3m space group, attributed to non-ideal cation mixing.[57–59] This structure encompasses both LiM_2O_4 and M_3O_4 spinel phases, contingent upon the migration of Co into tetrahedral sites.[60] The formation of these spinel phases is not confined to electrochemical cycling. Thermal decomposition significantly influences spinel phase formation. Charged cathodes exposed to prolonged elevated temperatures undergo a phase transition from a layered to a spinel structure.[61]

In the $LiMe_2O_4$ spinel, the transition metal (Me) typically exists in a mixed-valence state, such as Co^{3+}/Co^{4+}, to balance the lithium ions in the lattice. Conversely, in the Me_3O_4 spinel structure, the transition metal adopts different oxidation states, such as Co^{2+}/Co^{3+}, to stabilize the structure.[62]

Mn cations also play a critical role, exhibiting oxidation states of Mn^{3+} and Mn^{4+}, thereby contributing to charge balance and structural integrity. Mn^{3+}, with its d^4 electronic configuration, is prone to Jahn-Teller distortion, resulting in the elongation or contraction of

Mn-O bonds in the octahedral coordination environment. This distortion can cause local lattice deformations, impacting stability.[63] Additionally, Mn^{3+} can undergo disproportionation reactions, wherein two Mn^{3+} ions transform into Mn^{2+} and Mn^{4+}, with the Mn^{2+} cations dissolving out of the cathode. [64,65]

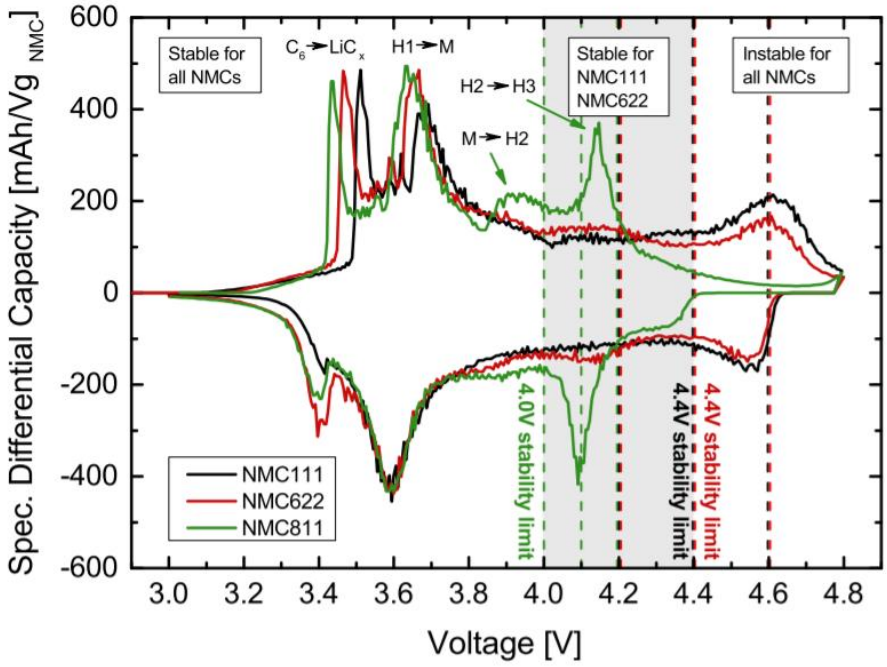

Figure 1.3. Differential capacity versus cell voltage plots of NMC-graphite cells. Vertical dotted lines indicate the upper cutoff voltage stability limits with peaks corresponding to phase transitions: H1, H2, and H3 represent the three hexagonal phases, while M represents the monoclinic phase. "$C_6 \rightarrow LiC_x$" represents the lithiation of graphite. Adapted from ref. [66]

NMC exhibits complex valence of different transition metal ions (Ni^{2+}, Ni^{3+}, Ni^{4+}, Co^{3+} and Co^{4+}) caused by variations in charge and electronegativity contributing to the larger capacities at the cost of instability of the layered structure. The weak bonding between Ni^{3+} (Jahn-Teller active ion)/Ni^{4+} ions and oxygen are thought to lead to instabilities in the layered structure whereas Mn^{4+} which does not partake in redox reactions provide stability.[67] X-ray absorption spectroscopy and X-ray absorption near edge structure has been used to determine Ni^{2+}/Ni^{4+} and Co^{3+}/Co^{4+} redox couples, which are believed to have the greatest contribution to charge

compensation.[68,69] *Figure 1.3.* Shows that nickel rich NMC811 exhibits a hexagonal-to-hexagonal phase transition (H2 → H3) at much lower potentials compared to NMC111 and NMC622, this has been attributed primarily to O_2 evolution on the surface layers eluding to the possibility that anionic redox may also contribute to charge compensation through surface reconstruction and CEI layer growth.[53,70]

Interfaces

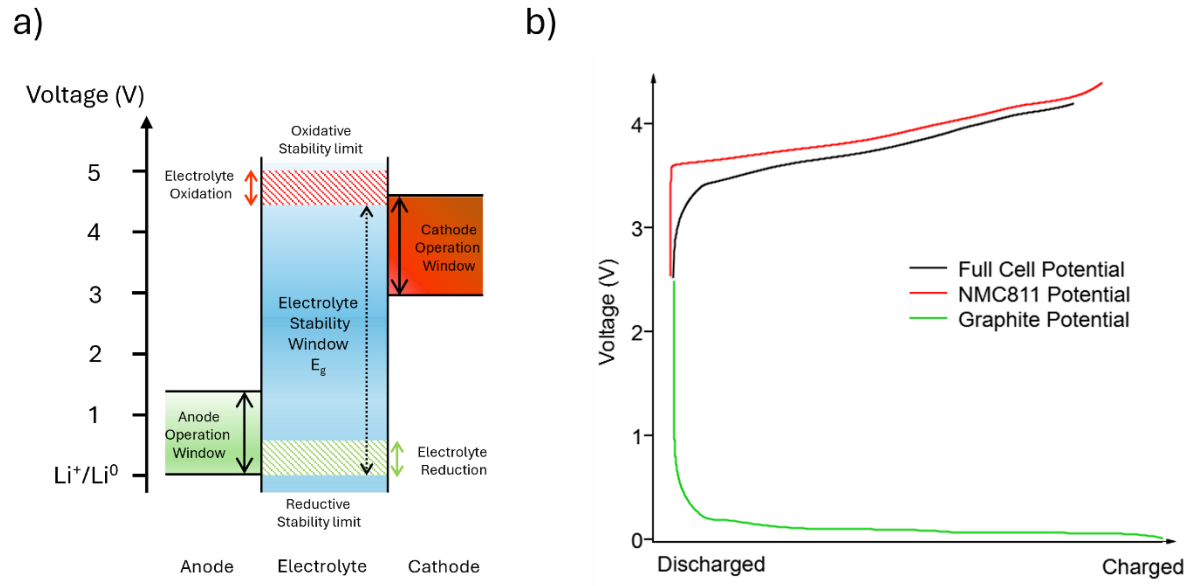

Figure 1.4. a) Schematic illustrating the operational windows of each electrode relative to the stability limits of the electrolyte and b) Representation demonstrating the potential variation of each electrode during cell charging.

The electrolyte stability window, which lies within the energy separation (E_g) of the electrolyte as depicted in Figure 1.4a. The open circuit voltage (OCV) of the cell is dictated by the electrochemical potentials between the anode and the cathode. During discharge, the anode undergoes electrolyte reduction, leading to the formation of a SEI layer. This process elevates the thermodynamic stability window towards the lowest unoccupied molecular orbital. Simultaneously, electrolyte oxidation occurs at the cathode electrode, resulting in the formation of the CEI layer, which obstructs electron transfer to the cathode, lowering the thermodynamic stability window towards the highest occupied molecular orbital. Figure 1.4b

illustrates the potentials of each electrode relative to Li^+/Li, showcasing how the potential of the cathode electrode increases during charge whilst the potential of the anode decreases and vice versa during discharge. [49,71,72]

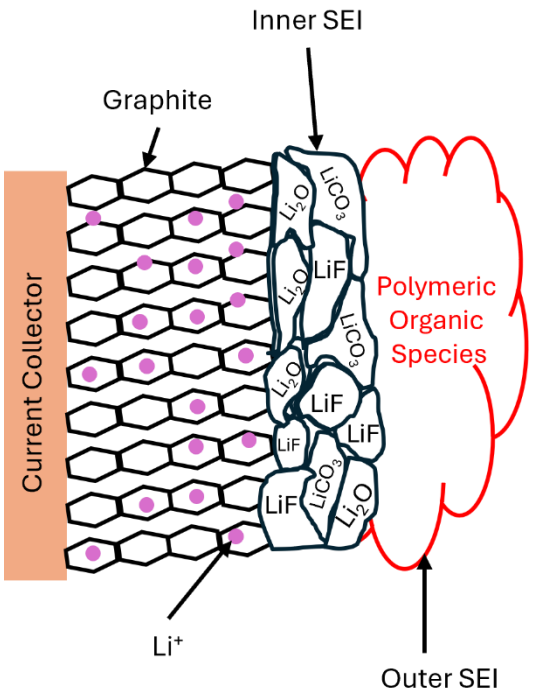

Figure 1.5. Schematic Diagram showcasing the inner and outer SEI on graphite electrodes from a lithium-ion battery.

The SEI layer formed on the anode electrode during the initial charging cycles consumes 10-20% of the initial capacity.[73] The SEI comprises of an inner layer of inorganic and an outer layer organic compounds demonstrated by *Figure 1.5.*[74] The inner layer (SEI/electrode boundary) comprises of inorganic compounds (e.g. Li_2CO_3, LiF and Li_2O) and the outer layer (SEI) comprises of organic compounds (e.g. $CH_2OCO_2Li_2$ and ROLi Where R denotes an organic group from additive present in the solvent).[73,75] Properties that make an ideal SEI layer include high electronic resistance, high Li^+ ion conductivity, tens of angstroms in thickness (to prevent electron tunnelling), stability over wide operating potential and temperature ranges. In reality, the SEI layer continues to evolve succumbing to various degradation mechanisms occurring at

various interfaces in the cell known as ageing. Cell ageing results from depletion of active lithium from both the $LiPF_6$ electrolyte salt and lithium inventory from the cathode resulting in capacity fade and reduced cycle life.[76]

SEI layer growth can be considered as an irreversible loss of lithium. Reversible capacity loss also presents itself at high charge/discharge rates due to the diffusion of Li^+ ions becoming limiting whilst inserting/extracting to/from an electrode, but this recovers when cycling at lower rates. Capacity fade is gauged by the coulombic efficiency of each cycle and often references the state of health of the battery governed by equation [1.8]. The cycle life is determined by the number of cycles a cell will perform before the capacity fades to 80% of its initial discharge capacity.[72]

$$Coulombic\ efficiency\ (\%) = \frac{Q_{discharge}}{Q_{charge}} \times 100 \qquad [1.8]$$

Degradation

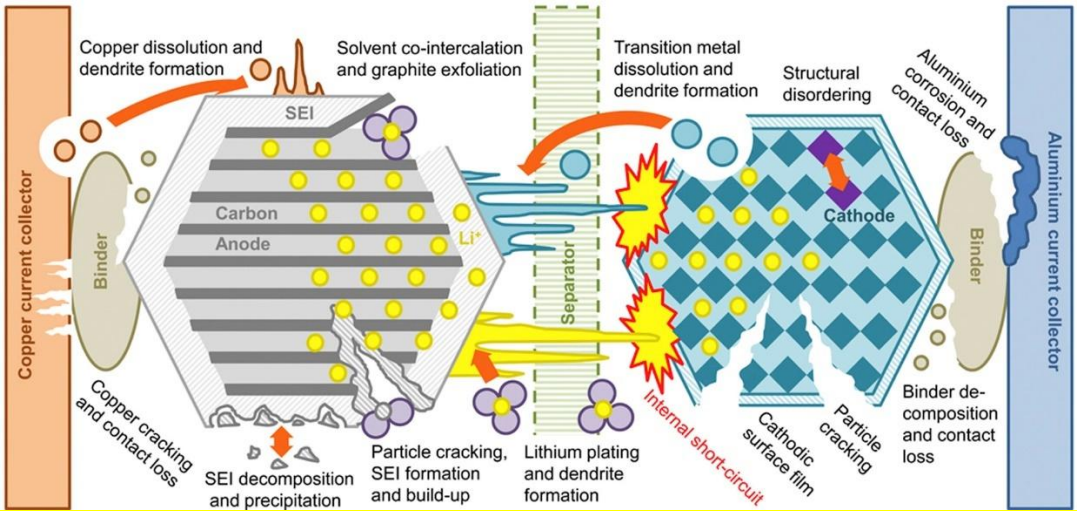

Figure 1.6. provides a comprehensive overview of degradation mechanisms that detrimentally impact battery performance. Adapted from ref.[77]

Degradation in LiBs can be categorised into three main modes: loss of lithium inventory (LLI), loss of active material on the cathode (LAM_{CE}), and loss of active material on the anode

(LAM_{AE}). LLI arises from parasitic side reactions, SEI formation, lithium plating, and decomposition reactions, depleting active Li^+ ions. LAM_{AE} and LAM_{CE} signify the unavailability of active material on electrodes for Li^+ ion insertion due to electrical contact loss, blocked active sites, and particle cracking. These physio-chemical degradation mechanisms are interconnected and are influenced by external factors like charge heterogeneity, temperature, and charge/discharge rate, leading to capacity fade, power fade, and reduced cycle life.[77] Cut-off potentials and temperature play a crucial role in ensuring cell longevity and stability, mitigating severe structural changes and undesired effects such as transition metal dissolution and lithium plating.[78,79]

Slippage

Electrode slippage in lithium-ion batteries describes the gradual deviation in capacity utilisation between the anode and cathode during battery cycling. While the capacity of individual electrode materials is used to balance cells, it may not correspond to the actual capacity of the full cell due to potential window "slippage" between electrodes caused by side reactions. An electron is consumed during electrolyte reduction at the negative electrode, requiring either a lithium-ion to move out of the electrode or an electron from the other electrode to maintain charge neutrality of the circuit. Conversely, during electrolyte oxidation, the electrode receives an electron, leading to a lithium-ion moving into the positive electrode or an electron transfer to the negative electrode, followed by lithium insertion. These side reactions cause LLI as Li^+ are consumed at the anode SEI during cycling, causing potential changes at the anode and resulting in a shift of the potential profile relative to the cathode

i.e. the capacities of the electrodes have become misaligned and therefore not be fully utilised.[54,80]

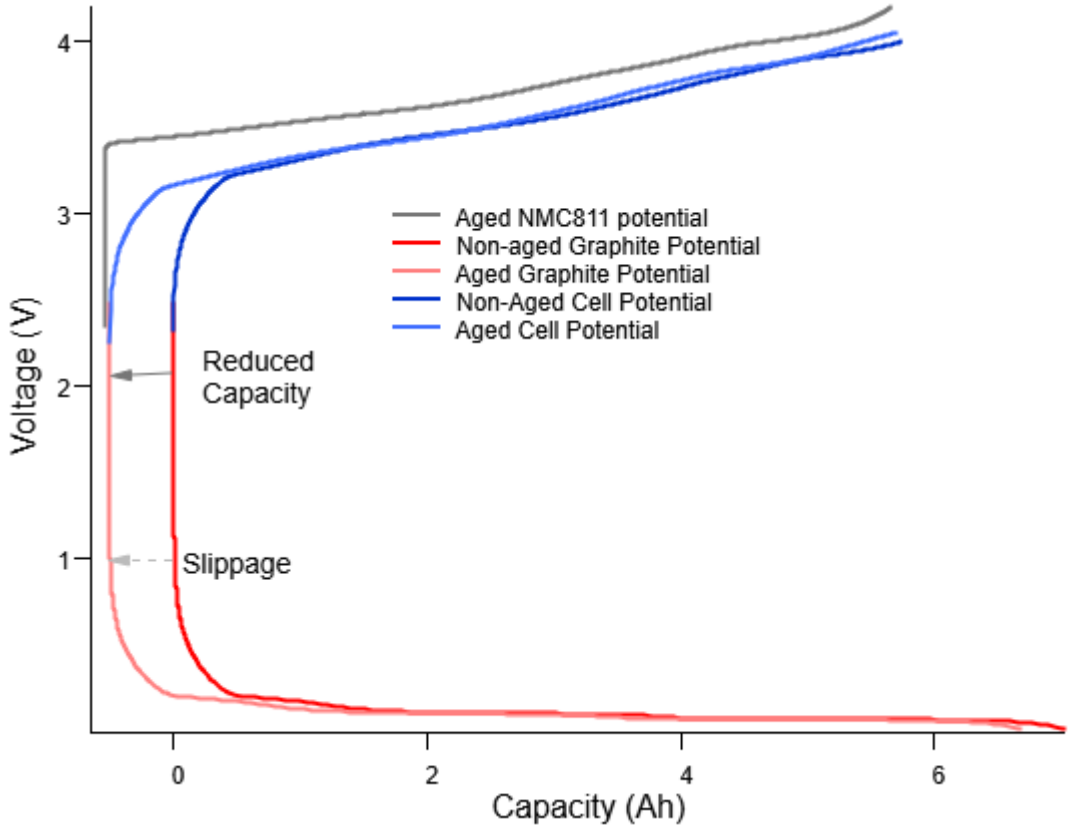

Figure 1.7. Schematic representation of electrode slippage during electrode reduction and the associated capacity loss for a non-aged cell (first cycle) and aged cell (300 cycles).

Electrode slippage significantly affects lithium-ion battery performance and longevity. For instance, in a full cell of NMC811 vs graphite, cycling between fixed upper cutoff voltage (UCV) of 4.2 V and lower cutoff voltage (LCV) of 3.0 V. In the initial cycles the graphite electrode reaches its end of charge at a low potential vs Li^+/Li. However, after hundreds of cycles, the impedance increase at the cathode increases the overpotential, pushing the potential of the cathode to a much higher UCV, causing an increase in the number of side reactions. The increased side reactions at the cathode interface, promote oxygen release and transition

metal dissolution. Consequently, this can cause a significant rise in impedance, affecting the battery's performance in later stages of its life.[54,81]

Electrolyte oxidation

In high-voltage applications, the carbonate solvents in lithium-ion battery electrolytes undergo parasitic oxidation, presenting a significant challenge to battery performance and longevity. Notably, cyclic carbonates such as EC exhibit susceptibility to oxidation at approximately 4.2 V vs Li^+/Li, followed by linear counterparts like DMC at around 4.5 V vs Li^+/Li when using $LiNiO_2$ electrodes.[82] This underscores the vulnerability of carbonate-based solvents to parasitic oxidation in lithium-ion batteries producing gaseous products such as O_2, CO_2, and CO.[83–86] The ramifications of parasitic oxidation of the electrolyte are multifaceted and include:

1. Potentially inducing cell casing swelling and rupture under excessive gas evolution.[87,88]
2. The liberated gases can engage in further reactions at the electrode surface, leading to the consumption of electrolyte components or species comprising the SEI/ CEI, ultimately contributing to the LLI.[86]
3. Oxidation byproducts can precipitate on the positive electrode surface, causing a resistive CEI that hinders kinetics and increases overall cell impedance.[54,86]

Jung et al. identified two potential electrolyte oxidation pathways: chemical and electrochemical. A specific threshold voltage initiates the chemical pathway, whereas the electrochemical route correlates with the applied potential. Chemical oxidation starts with releasing gaseous oxygen during positive electrode material undergoing surface reconstruction, reacting with carbonate solvent and leading to lattice oxygen oxidation involving various intermediates. This process is closely linked to positive electrode material

degradation, with onset potential decreasing with higher Ni content, e.g., around 4.6 V vs Li^+/Li for NMC111 and 4.2 V vs Li^+/Li for NMC811. In contrast, electrochemical oxidation involves electron exchange between the electrode and solvent molecules. Despite contributing less to anodic decomposition, electrochemical reactions start before 4.2 V, preceding chemical oxidation. [89] Overall, electrolyte oxidation drives numerous degradation mechanisms, evolving gas and forming CEI products at the cathode electrolyte interface.

Electrolyte Reduction

To utilise high-capacity electrodes effectively, their chemical potentials (μ_A and μ_C) must align with the LUMO and HOMO of the electrolyte. Although graphite is a useful anode with a reduction potential close to Li^0, its Fermi level (ε_F) lies above the LUMO of practical nonaqueous electrolytes, requiring the formation of a passivating SEI layer. This SEI layer enables graphite as an anode by preventing continuous electrolyte reduction.[4] However, repeated cycling can break the SEI, leading to dendrite formation and potential short-circuiting. The LUMO of most electrolyte components is higher than the voltage of lithiated graphite (~0.1 eV) and lithium metal (0 eV), leading to the expected reduction of the electrolyte on the anode. Compared to the cathode CEI, the SEI on the anode is more unstable due to these reduction reactions and the more significant volume expansion of the anode materials. Consequently, it is important to design either an anode with a chemical potential (μ_A) matched to the electrolyte's LUMO or a stable, self-healing SEI layer that supports rapid Li^+ ion transfer while preventing electron reducing the electrolyte.[90]

During the initial formation cycles of commercial lithium-ion batteries, the SEI forms from electrolyte decomposition products, predominantly containing lithium, carbon, fluorine, oxygen, and trace phosphorus.[91–98] Analysis indicates that lithium ethylene dicarbonate

(LEDC) is the leading organic component, while lithium fluoride (LiF) is the primary fluorine-containing species, with minor amounts of lithium fluorophosphate.[99]

LEDC decomposes into a complex mixture of insoluble, soluble, and gaseous components. Insoluble products include lithium alkoxides, lithium fluorophosphates, polyethylene oxides, lithium carboxylates, Li_2CO_3, Li_2O, and LiF.[100,101] Soluble components are ethers, oligoethylene oxides, and fluorophosphates, whereas gaseous species include CO_2 and ethylene.[86,102] Acidic impurities (HF, PF_5) play a significant role in catalysing these decomposition reactions, contributing to the SEI composition's complexity and variability.[86]

LEDC decomposition increases porosity as the SEI evolves, allowing further electrolyte access and continuous reduction, leading to new SEI layer formation. Over time, the SEI thickens, with an inner layer rich in stable inorganic compounds (LiF, Li_2CO_3, Li_2O) and an outer layer of newer reduction products.[99]

Crosstalk

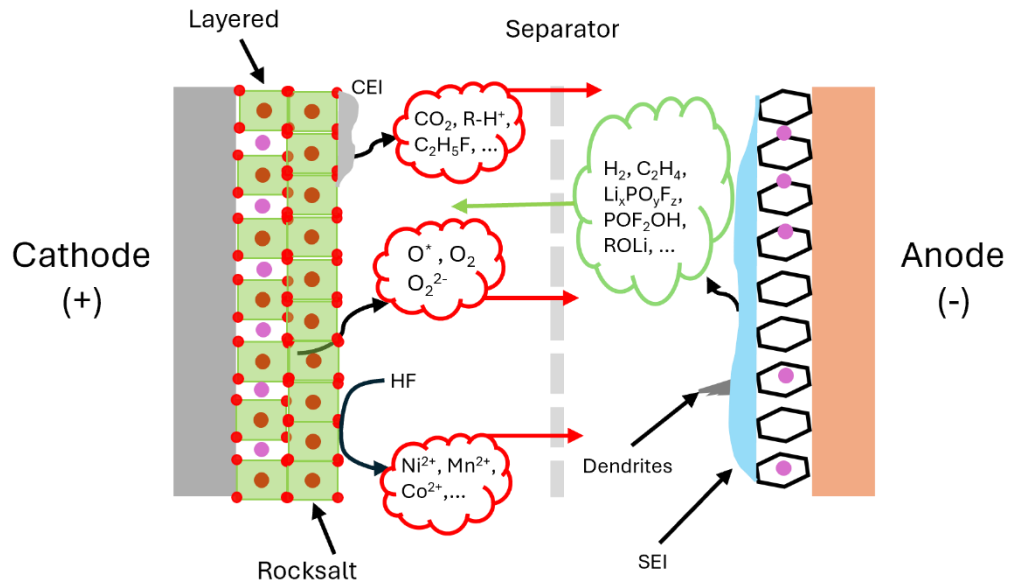

Figure 1.8. Schematic of crosstalk degradation pathways in lithium-ion batteries.

The effects of operating voltage and temperature on electrolyte composition can lead to the release of certain species into the electrolyte, resulting in a phenomenon termed "crosstalk", as depicted in Figure 1.8. These crosstalk species migrate from one electrode to another and are involved in further decomposition reactions at the opposite electrode. For instance, hydrofluoric (HF) acid, generated from the hydrolysis of $LiPF_6$, can etch transition metals from the LiTMO and facilitate their dissolution into the electrolyte. These transition metals solvate compounds in the electrolyte, migrate across the electrolyte and are incorporated into the anode SEI.

Transition metal (TM) dissolution from the cathode (Ni^{2+}, Mn^{2+}, Co^{2+},…) has been correlated with capacity loss, impedance growth, and ultimate cell failure.[103] These TMs migrate through the electrolyte/separator and deposit onto the anode surface, the reactions are particularly aggravated under elevated temperatures and voltages.[54,104,105] Despite extensive study, the comprehensive understanding of all stages of TM dissolution, migration, and subsequent

incorporation is still poorly understood. Nickel-rich cathode materials undergo surface reconstruction at elevated potentials, culminating in the formation of a reduced surface layer primarily comprising NiO.[85,106,107] However, investigations have unveiled the reduction of Mn and Co at the surface of NMC811, with Mn being particularly detrimental to cell performance, correlating with increased capacity loss and impedance rise.[108] The reduced surface layer on NMC811 may undergo chemical etching by protic species in the electrolyte, stemming from the degradation of $LiPF_6$ and potentially from crosstalk species generated at the anode electrode.[109,110] However there are other possible etching agents including carboxylic acids,[86] ketones[111] and acetates[112] have been identified as possible compounds in highly oxidising environments in lithium-ion batteries. Tarascon's group revealed the dissolution of Mn and its effects on spinel LMO electrodes via a disproportion reaction pathway ($Mn^{3+} \rightarrow Mn^{2+} + Mn^{4+}$).[113] However, Mn^{3+} dissolution from the cathode in carbonate-based electrolytes cannot be ruled out, adding complexity to the dissolution process.[114]

TMs migrating towards the anode are incorporated into the SEI. Various pathways could exist for transition metals to incorporate into the SEI. One such pathway involves chemisorption, which directly binds transition metal ions to the SEI surface and alters its composition and stability.[115] Another pathway, ion exchange, occurs when lithium ions within the SEI structure are replaced by transition metal ions from the electrolyte, which are incorporated into the SEI matrix.[91,116]

The precise reaction mechanisms underlying TM behaviour at the anode interface remain a topic of ongoing debate yet are paramount due to their impact on LLI. Generally, it is posited that TMs are incorporated into the SEI in a +2 oxidation state, supported in literature indicating such states on delithiated graphite electrodes.[54,104,109,116] However, observations on lithiated

graphite electrodes present a more nuanced picture, with conflicting reports regarding TM oxidation states in the literature. Wandt et al., employing operando X-ray absorption near-edge structure (XANES) measurements, identified Mn^{2+} and Ni^{2+} on lithiated graphite resulting from cross-talk with NMC111.[117] Conversely, Shkrob et al. using a combination of electron paramagnetic resonance (EPR), XANES, and extended X-ray absorption fine structure (EXAFS) analyses, showed that the reduced Mn exists as isolated non-metallic species rather than metallic clusters.[115] Furthermore, Gowda et al. used ex-situ XANES measurements lithiated graphite electrodes and found evidence of metallic Mn.[118] The implications of TM oxidation states will be explored in greater detail in Chapter 4.

Ellis et al. investigated how CO_2, H_2, C_2H_4, and CO gases can impact degradation by being reduced at the anode. CO_2 reduction produces lithium oxalate as the major product and carbonates as minor products, which $LiPF_6$ then consumes to form fluorophosphates and reform CO_2. However, H_2 was primarily consumed at the positive electrode in smaller amounts than at the negative electrode, suggesting that the H^+/H_2 shuttle reaction has minimal impact on reversible self-discharge at high voltage. C_2H_4 consumption was also observed at the positive electrode, leading to increased impedance. Higher temperatures accelerated H_2 and C_2H_4 consumption at both electrodes. However, the overall impact on degradation was believed to contribute a 2% capacity loss without the presence of additives in the electrolytes.[119]

References

1. Mauger, A., Julien, C. M., Armand, M. & Zaghib, K. Tribute to John B. Goodenough: From Magnetism to Rechargeable Batteries. *Advanced Energy Materials* vol. 11 Preprint at https://doi.org/10.1002/aenm.202000773 (2021).

2. Goodenough, J. B. & Park, K. S. The Li-ion rechargeable battery: A perspective. *J Am Chem Soc* **135**, 1167–1176 (2013).

3. Goodenough, J. B. Electrochemical energy storage in a sustainable modern society. *Energy Environ Sci* **7**, 14–18 (2014).

4. Goodenough, J. B. & Kim, Y. Challenges for rechargeable Li batteries. *Chemistry of Materials* **22**, 587–603 (2010).

5. Ritchie, H. & Roser, M. Energy mix - Our World in Data. *Our World in Data* Preprint at (2020).

6. Faraday battery challenge – UKRI. https://www.ukri.org/what-we-do/browse-our-areas-of-investment-and-support/faraday-battery-challenge/.

7. Goodenough, J. B. & Kim, Y. Challenges for rechargeable Li batteries. *Chemistry of Materials* **22**, 587–603 (2010).

8. Nitta, N., Wu, F., Lee, J. T. & Yushin, G. Li-ion battery materials: Present and future. *Materials Today* **18**, 252–264 (2015).

9. Nishi, Y. Lithium ion secondary batteries; Past 10 years and the future. *J Power Sources* **100**, 101–106 (2001).

10. Barré, A. *et al.* A review on lithium-ion battery ageing mechanisms and estimations for automotive applications. *J Power Sources* **241**, 680–689 (2013).

11. Zeng, X. *et al.* Commercialization of Lithium Battery Technologies for Electric Vehicles. *Adv Energy Mater* **9**, 1–25 (2019).

12. Chiang, Y.-M. Building a Better Battery. *Science (1979)* **330**, 1486–1487 (2010).

13. Xia, Y., Zheng, J., Wang, C. & Gu, M. Designing principle for Ni-rich cathode materials with high energy density for practical applications. *Nano Energy* vol. 49 434–452 Preprint at https://doi.org/10.1016/j.nanoen.2018.04.062 (2018).

14. Liu, J. *et al.* Recent breakthroughs and perspectives of high-energy layered oxide cathode materials for lithium ion batteries. *Materials Today* vol. 43 132–165 Preprint at https://doi.org/10.1016/j.mattod.2020.10.028 (2021).

15. Xiang, J. *et al.* Building Practical High-Voltage Cathode Materials for Lithium-Ion Batteries. *Advanced Materials* vol. 34 Preprint at https://doi.org/10.1002/adma.202200912 (2022).

16. Wang, Q. *et al.* Thermal runaway caused fire and explosion of lithium ion battery. *J Power Sources* **208**, 210–224 (2012).

17. Scrosati, B. & Garche, J. Lithium batteries: Status, prospects and future. *J Power Sources* **195**, 2419–2430 (2010).

18. Bard, A. J. & Faulkner, L. R. *Electrochemical Methods, Fundamentals and Applications*. (John Wiley & Sons, Inc., New York, 2001).

19. Reddy, T. B. *LINDEN'S HANDBOOK OF BATTERIES*. (McGraw Hill, 2011).

20. Dai, H. *et al.* Stabilizing lithium metal anode by octaphenyl polyoxyethylene-lithium complexation. *Nat Commun* **11**, (2020).

21. Liang, X. *et al.* A facile surface chemistry route to a stabilized lithium metal anode. *Nat Energy* **2**, 1–7 (2017).

22. Zhou, D., Kim, C. & Yun, S. Effective modulus of graphite electrode in Li-ion battery by considering ion concentration, porosity, and binding energy during lithium intercalation. *Mater Lett* **224**, 46–49 (2018).

23. Fuchsbichler, B., Stangl, C., Kren, H., Uhlig, F. & Koller, S. High capacity graphite-silicon composite anode material for lithium-ion batteries. *J Power Sources* **196**, 2889–2892 (2011).

24. Liu, X., Zhu, X. & Pan, D. Solutions for the problems of silicon–carbon anode materials for lithium-ion batteries. *R Soc Open Sci* **5**, (2018).

25. Son, S. B. *et al.* Interfacially Induced Cascading Failure in Graphite-Silicon Composite Anodes. *Advanced Science* **6**, 1–8 (2019).

26. Dou, F., Shi, L., Chen, G. & Zhang, D. Silicon/Carbon Composite Anode Materials for Lithium-Ion Batteries. *Electrochemical Energy Reviews* vol. 2 149–198 Preprint at https://doi.org/10.1007/s41918-018-00028-w (2019).

27. Li, P., Hwang, J. & Sun, Y. Nano/Microstructured Silicon − Graphite Composite Anode for High-Energy-Density Li- Ion Battery. (2019) doi:10.1021/acsnano.9b00169.

28. Asenbauer, J. *et al.* The success story of graphite as a lithium-ion anode material-fundamentals, remaining challenges, and recent developments including silicon (oxide) composites. *Sustainable Energy and Fuels* vol. 4 5387–5416 Preprint at https://doi.org/10.1039/d0se00175a (2020).

29. Wu, H. *et al.* Stable cycling of double-walled silicon nanotube battery anodes through solid-electrolyte interphase control. *Nat Nanotechnol* **7**, 310–315 (2012).

30. Liu, N. *et al.* A yolk-shell design for stabilized and scalable Li-ion battery alloy anodes. *Nano Lett* **12**, 3315–3321 (2012).

31. Etacheri, V. *et al.* Effect of fluoroethylene carbonate (FEC) on the performance and surface chemistry of Si-nanowire li-ion battery anodes. *Langmuir* **28**, 965–976 (2012).

32. Schroder, K. *et al.* The Effect of Fluoroethylene Carbonate as an Additive on the Solid Electrolyte Interphase on Silicon Lithium-Ion Electrodes. *Chemistry of Materials* **27**, 5531–5542 (2015).

33. Chae, S., Choi, S., Kim, N., Sung, J. & Cho, J. Integration of Graphite and Silicon Anodes for the Commercialization of High-Energy Lithium-Ion Batteries. *Angewandte Chemie* **132**, 112–138 (2020).

34. Meunier, V. *Unraveling Degradation Patterns in Li-Ion Batteries through Electrochemical Analysis Procedures*. https://theses.hal.science/tel-04347681.

35. Wang, Y., Yi, J. & Xia, Y. Recent progress in aqueous lithium-ion batteries. *Adv Energy Mater* **2**, 830–840 (2012).

36. Zhang, S. S. A review on electrolyte additives for lithium-ion batteries. *J Power Sources* **162**, 1379–1394 (2006).

37. Hall, D. S., Self, J. & Dahn, J. R. Dielectric Constants for Quantum Chemistry and Li-Ion Batteries: Solvent Blends of Ethylene Carbonate and Ethyl Methyl Carbonate. *Journal of Physical Chemistry C* **119**, 22322–22330 (2015).

38. Ding, M. S. Liquid Phase Boundaries, Dielectric Constant, and Viscosity of PC-DEC and PC-EC Binary Carbonates. *J Electrochem Soc* **150**, A455 (2003).

39. Blomgren, G. E. The Development and Future of Lithium Ion Batteries. *J Electrochem Soc* **164**, A5019–A5025 (2017).

40. Ohzuku, T. & Ueda, A. Why transition metal (di) oxides are the most attractive materials for batteries. *Solid State Ion* **69**, 201–211 (1994).

41. Deng, B., Nakamura, H. & Yoshio, M. Capacity fading with oxygen loss for manganese spinels upon cycling at elevated temperatures. *J Power Sources* **180**, 864–868 (2008).

42. Lee, M. J., Lee, S., Oh, P., Kim, Y. & Cho, J. High performance LiMn2O4 cathode materials grown with epitaxial layered nanostructure for Li-Ion batteries. *Nano Lett* **14**, 993–999 (2014).

43. Muruganantham, R., Sivakumar, M. & Subadevi, R. Synthesis and electrochemical characterization of olivine-type lithium iron phosphate cathode materials via different techniques. *Ionics (Kiel)* **22**, 1557–1565 (2016).

44. Orikasa, Y. *et al.* Direct observation of a metastable crystal phase of LixFePO 4 under electrochemical phase transition. *J Am Chem Soc* **135**, 5497–5500 (2013).

45. Chen, W. M. *et al.* Insight into the improvement of rate capability and cyclability in LiFePO4/polyaniline composite cathode. *Electrochim Acta* **56**, 2689–2695 (2011).

46. Etacheri, V., Marom, R., Elazari, R., Salitra, G. & Aurbach, D. Challenges in the development of advanced Li-ion batteries: A review. *Energy Environ Sci* **4**, 3243–3262 (2011).

47. Kang, B. & Ceder, G. Battery materials for ultrafast charging and discharging. *Nature* **458**, 190–193 (2009).

48. Wang, J. & Sun, X. Understanding and recent development of carbon coating on LiFePO 4 cathode materials for lithium-ion batteries. *Energy Environ Sci* **5**, 5163–5185 (2012).

49. Goodenough, J. B. Cathode materials: A personal perspective. *J Power Sources* **174**, 996–1000 (2007).

50. Mats, Z. Life cycle assessment of long life lithium electrode for electric vehicle batteries-cells for Leaf, Tesla and Volvo bus. 56 (2017).

51. Märker, K., Reeves, P. J., Xu, C., Griffith, K. J. & Grey, C. P. Evolution of Structure and Lithium Dynamics in LiNi0.8Mn0.1Co0.1O2 (NMC811) Cathodes during Electrochemical Cycling. *Chemistry of Materials* **31**, 2545–2554 (2019).

52. Jung, R., Metzger, M., Maglia, F., Stinner, C. & Gasteiger, H. A. Chemical versus electrochemical electrolyte oxidation on NMC111, NMC622, NMC811, LNMO, and conductive carbon. *Journal of Physical Chemistry Letters* **8**, 4820–4825 (2017).

53. Tian, C. *et al.* Depth-Dependent Redox Behavior of LiNi 0.6 Mn 0.2 Co 0.2 O 2 . *J Electrochem Soc* **165**, A696–A704 (2018).

54. Björklund, E. *et al.* Cycle-Induced Interfacial Degradation and Transition-Metal Cross-Over in LiNi0.8Mn0.1Co0.1O2-Graphite Cells. *Chemistry of Materials* **34**, 2034–2048 (2022).

55. Phelan, C. M. E. *et al.* Role of Salt Concentration in Stabilizing Charged Ni-Rich Cathode Interfaces in Li-Ion Batteries. doi:10.1021/acs.chemmater.4c00004.

56. Zhang, S. S. Problems and their origins of Ni-rich layered oxide cathode materials. *Energy Storage Mater* **24**, 247–254 (2020).

57. Jung, S. K. *et al.* Understanding the degradation mechanisms of LiNi0.5Co 0.2Mn0.3O2 cathode material in lithium ion batteries. *Adv Energy Mater* **4**, (2014).

58. Konishi, H., Yoshikawa, M. & Hirano, T. The effect of thermal stability for high-Ni-content layer-structured cathode materials, LiNi0.8Mn0.1-xCo0.1Mo xO2 (x = 0, 0.02, 0.04). *J Power Sources* **244**, 23–28 (2013).

59. Gabrisch, H., Yi, T. & Yazami, R. Transmission electron microscope studies of LiNi1/3Mn 1/3Co1/3O2 before and after long-term aging at 70°C. *Electrochemical and Solid-State Letters* **11**, (2008).

60. Bak, S. M. *et al.* Structural changes and thermal stability of charged LiNixMnyCozO2 cathode materials studied by combined in situ time-resolved XRD and mass spectroscopy. *ACS Appl Mater Interfaces* **6**, 22594–22601 (2014).

61. Eom, J., Kim, M. G. & Cho, J. Storage Characteristics of LiNi[sub 0.8]Co[sub 0.1+x]Mn[sub 0.1−x]O[sub 2] (x=0, 0.03, and 0.06) Cathode Materials for Lithium Batteries. *J Electrochem Soc* **155**, A239 (2008).

62. Li, T. *et al.* Degradation Mechanisms and Mitigation Strategies of Nickel-Rich NMC-Based Lithium-Ion Batteries. *Electrochemical Energy Reviews* vol. 3 43–80 Preprint at https://doi.org/10.1007/s41918-019-00053-3 (2020).

63. Yamada, A., Tanaka, M., Tanaka, K. & Sekai, K. *Jahn-Teller Instability in Spinel Li-Mn-O*. *Journal of Power Sources* vol. 81 www.elsevier.comrlocaterjpowsour.

64. Benedek, R. & Thackeray, M. M. Reaction energy for LiMn 2O 4 spinel dissolution in acid. *Electrochemical and Solid-State Letters* **9**, (2006).

65. Morin, H. R. *et al.* Transition-Metal Dissolution from NMC-Family Oxides: A Case Study. *ACS Appl Energy Mater* **3**, 2565–2575 (2020).

66. Jung, R., Metzger, M., Maglia, F., Stinner, C. & Gasteiger, H. A. Oxygen Release and Its Effect on the Cycling Stability of LiNi x Mn y Co z O 2 (NMC) Cathode Materials for Li-Ion Batteries . *J Electrochem Soc* **164**, A1361–A1377 (2017).

67. Liang, C. *et al.* Unraveling the Origin of Instability in Ni-Rich LiNi1-2xCoxMnxO2 (NCM) Cathode Materials. *Journal of Physical Chemistry C* **120**, 6383–6393 (2016).

68. Dolotko, O., Senyshyn, A., Mühlbauer, M. J., Nikolowski, K. & Ehrenberg, H. Understanding structural changes in NMC Li-ion cells by in situ neutron diffraction. *J Power Sources* **255**, 197–203 (2014).

69. Cherkashinin, G., Motzko, M., Schulz, N., Späth, T. & Jaegermann, W. Electron spectroscopy study of Li[Ni,Co,Mn]O2/electrolyte interface: Electronic structure, interface composition, and device implications. *Chemistry of Materials* **27**, 2875–2887 (2015).

70. Jung, R., Metzger, M., Maglia, F., Stinner, C. & Gasteiger, H. A. Oxygen Release and Its Effect on the Cycling Stability of LiNi x Mn y Co z O 2 (NMC) Cathode Materials for Li-Ion Batteries . *J Electrochem Soc* **164**, A1361–A1377 (2017).

71. Peljo, P. & Girault, H. H. Electrochemical potential window of battery electrolytes: The HOMO-LUMO misconception. *Energy Environ Sci* **11**, 2306–2309 (2018).

72. Goodenough, J. B. & Park, K. S. The Li-ion rechargeable battery: A perspective. *J Am Chem Soc* **135**, 1167–1176 (2013).

73. Lin, Y. X. *et al.* Connecting the irreversible capacity loss in Li-ion batteries with the electronic insulating properties of solid electrolyte interphase (SEI) components. *J Power Sources* **309**, 221–230 (2016).

74. Joshi, T., Eom, K., Yushin, G. & Fuller, T. F. Effects of Dissolved Transition Metals on the Electrochemical Performance and SEI Growth in Lithium-Ion Batteries. *J Electrochem Soc* **161**, A1915–A1921 (2014).

75. Shi, S. *et al.* Direct calculation of Li-ion transport in the solid electrolyte interphase. *J Am Chem Soc* **134**, 15476–15487 (2012).

76. An, S. J. *et al.* The state of understanding of the lithium-ion-battery graphite solid electrolyte interphase (SEI) and its relationship to formation cycling. *Carbon N Y* **105**, 52–76 (2016).

77. Birkl, C. R., Roberts, M. R., McTurk, E., Bruce, P. G. & Howey, D. A. Degradation diagnostics for lithium ion cells. *J Power Sources* **341**, 373–386 (2017).

78. Nelson, K. J., Harlow, J. E. & Dahn, J. R. A Comparison of NMC/Graphite Pouch Cells and Commercially Available LiCoO 2 /Graphite Pouch Cells Tested to High Potential . *J Electrochem Soc* **165**, A456–A462 (2018).

79. Krueger, S. *et al.* How Do Reactions at the Anode/Electrolyte Interface Determine the Cathode Performance in Lithium-Ion Batteries? *J Electrochem Soc* **160**, A542–A548 (2013).

80. Gauthier, R. *et al.* How do Depth of Discharge, C-rate and Calendar Age Affect Capacity Retention, Impedance Growth, the Electrodes, and the Electrolyte in Li-Ion Cells? *J Electrochem Soc* (2022) doi:10.1149/1945-7111/ac4b82.

81. Dose, W. M., Xu, C., Grey, C. P. & De Volder, M. F. L. Effect of Anode Slippage on Cathode Cutoff Potential and Degradation Mechanisms in Ni-Rich Li-Ion Batteries. *Cell Rep Phys Sci* **1**, (2020).

82. Azcarate, I. *et al.* Assessing the Oxidation Behavior of EC:DMC Based Electrolyte on Non-Catalytically Active Surface. *J Electrochem Soc* **2020**, (2020).

83. Guéguen, A. *et al.* Decomposition of LiPF 6 in High Energy Lithium-Ion Batteries Studied with Online Electrochemical Mass Spectrometry . *J Electrochem Soc* **163**, A1095–A1100 (2016).

84. Kajiyama, A. *et al.* Principal Factors of Carbon Conductive Agents that Contribute to the Gas Formation in High-Voltage Cathode Systems. *J Electrochem Soc* **162**, A1516–A1522 (2015).

85. Shi, C. G. *et al.* Investigation and Suppression of Oxygen Release by LiNi0.8Co0.1Mn0.1O2 Cathode under Overcharge Conditions. *Adv Energy Mater* **12**, (2022).

86. Rinkel, B. L. D., Hall, D. S., Temprano, I. & Grey, C. P. Electrolyte oxidation pathways in lithium-ion batteries. *J Am Chem Soc* **142**, 15058–15074 (2020).

87. Salomez, B., Grugeon, S., Armand, M., Tran-Van, P. & Laruelle, S. Review—Gassing Mechanisms in Lithium-ion Battery. *J Electrochem Soc* **170**, 050537 (2023).

88. Dose, W. M. *et al.* Electrolyte Reactivity at the Charged Ni-Rich Cathode Interface and Degradation in Li-Ion Batteries. *ACS Appl Mater Interfaces* **14**, 13206–13222 (2022).

89. Jung, R., Metzger, M., Maglia, F., Stinner, C. & Gasteiger, H. A. Oxygen Release and Its Effect on the Cycling Stability of LiNi x Mn y Co z O 2 (NMC) Cathode Materials for Li-Ion Batteries . *J Electrochem Soc* **164**, A1361–A1377 (2017).

90. Vetter, J. *et al.* Ageing mechanisms in lithium-ion batteries. *J Power Sources* **147**, 269–281 (2005).

91. Solchenbach, S., Hong, G., Freiberg, A. T. S., Jung, R. & Gasteiger, H. A. Electrolyte and SEI Decomposition Reactions of Transition Metal Ions Investigated by On-Line Electrochemical Mass Spectrometry. *J Electrochem Soc* **165**, A3304–A3312 (2018).

92. Bryngelsson, H., Stjerndahl, M., Gustafsson, T. & Edström, K. How dynamic is the SEI? *J Power Sources* **174**, 970–975 (2007).

93. Andersson, A. M. & Edström, K. Chemical Composition and Morphology of the Elevated Temperature SEI on Graphite. *J Electrochem Soc* **148**, A1100 (2001).

94. Wood, K. N. & Teeter, G. XPS on Li-Battery-Related Compounds: Analysis of Inorganic SEI Phases and a Methodology for Charge Correction. *ACS Appl Energy Mater* **1**, 4493–4504 (2018).

95. Sacci, R. L. *et al.* Direct visualization of initial SEI morphology and growth kinetics during lithium deposition by in situ electrochemical transmission electron microscopy. *Chemical Communications* **50**, 2104–2107 (2014).

96. Leißing, M. *et al.* The Origin of Gaseous Decomposition Products Formed During SEI Formation Analyzed by Isotope Labeling in Lithium-Ion Battery Electrolytes. *Batter Supercaps* **4**, 1731–1738 (2021).

97. Peled, E. *et al.* Composition, depth profiles and lateral distribution of materials in the SEI built on HOPG-TOF SIMS and XPS studies. *J Power Sources* **97–98**, 52–57 (2001).

98. Schellenberger, M., Golnak, R., Quevedo Garzon, W. G., Risse, S. & Seidel, R. Accessing the solid electrolyte interphase on silicon anodes for lithium-ion batteries in-situ through transmission soft X-ray absorption spectroscopy. *Mater Today Adv* **14**, (2022).

99. Heiskanen, S. K., Kim, J. & Lucht, B. L. Generation and Evolution of the Solid Electrolyte Interphase of Lithium-Ion Batteries. *Joule* vol. 3 2322–2333 Preprint at https://doi.org/10.1016/j.joule.2019.08.018 (2019).

100. Zheng, J. *et al.* Lithium ion diffusion mechanism on the inorganic components of the solid-electrolyte interphase. *J Mater Chem A Mater* **9**, 10251–10259 (2021).

101. An, S. J. *et al.* The state of understanding of the lithium-ion-battery graphite solid electrolyte interphase (SEI) and its relationship to formation cycling. *Carbon* vol. 105 52–76 Preprint at https://doi.org/10.1016/j.carbon.2016.04.008 (2016).

102. Wang, A., Kadam, S., Li, H., Shi, S. & Qi, Y. Review on modeling of the anode solid electrolyte interphase (SEI) for lithium-ion batteries. *npj Computational Materials* vol. 4 Preprint at https://doi.org/10.1038/s41524-018-0064-0 (2018).

103. Harris, O. C., Leung, K. & Tang, M. H. How Transition Metals Enable Electron Transfer through the SEI: Part II. Redox-Cycling Mechanism Model and Experiment. *J Electrochem Soc* **167**, 013503 (2020).

104. Ruff, Z., Xu, C. & Grey, C. P. Transition Metal Dissolution and Degradation in NMC811-Graphite Electrochemical Cells. *J Electrochem Soc* **168**, 060518 (2021).

105. Amine, K. *et al.* Improved lithium manganese oxide spinel/graphite Li-ion cells for high-power applications. in *Journal of Power Sources* vol. 129 14–19 (Elsevier, 2004).

106. Björklund, E. *et al.* Cycle-Induced Interfacial Degradation and Transition-Metal Cross-Over in LiNi0.8Mn0.1Co0.1O2-Graphite Cells. *Chemistry of Materials* **34**, 2034–2048 (2022).

107. Gao, H. *et al.* Surface Modification for Suppressing Interfacial Parasitic Reactions of a Nickel-Rich Lithium-Ion Cathode. *Chemistry of Materials* **31**, 2723–2730 (2019).

108. Zhang, J. *et al.* Destructive effects of transitional metal ions on interfacial film of carbon anode for lithium-ion batteries. *Electrochim Acta* **417**, (2022).

109. Zhan, C., Wu, T., Lu, J. & Amine, K. Dissolution, migration, and deposition of transition metal ions in Li-ion batteries exemplified by Mn-based cathodes-A critical review. *Energy and Environmental Science* vol. 11 243–257 Preprint at https://doi.org/10.1039/c7ee03122j (2018).

110. Morin, H. R. *et al.* Transition-Metal Dissolution from NMC-Family Oxides: A Case Study. *ACS Appl Energy Mater* **3**, 2565–2575 (2020).

111. Jarry, A. *et al.* The Formation Mechanism of Fluorescent Metal Complexes at the LixNi0.5Mn1.5O4-δ/Carbonate Ester Electrolyte Interface. *J Am Chem Soc* **137**, 3533–3539 (2015).

112. Gilbert, J. A., Shkrob, I. A. & Abraham, D. P. Transition Metal Dissolution, Ion Migration, Electrocatalytic Reduction and Capacity Loss in Lithium-Ion Full Cells. *J Electrochem Soc* **164**, A389–A399 (2017).

113. Amatucci, G., Pasquier, A. Du, Blyr, A., Zheng, T. & Tarascon, J.-M. *The Elevated Temperature Performance of the LiMn 2 O 4 /C System: Failure and Solutions*. www.elsevier.nl/locate/electacta.

114. Hanf, L., Henschel, J., Diehl, M., Winter, M. & Nowak, S. Mn2+ or Mn3+? Investigating transition metal dissolution of manganese species in lithium ion battery electrolytes by capillary electrophoresis. *Electrophoresis* **41**, 697–704 (2020).

115. Shkrob, I. A. *et al.* Manganese in graphite anode and capacity fade in Li ion batteries. *Journal of Physical Chemistry C* **118**, 24335–24348 (2014).

116. Zhan, C. *et al.* Mn(II) deposition on anodes and its effects on capacity fade in spinel lithium manganate-carbon systems. *Nat Commun* **4**, (2013).

117. Wandt, J. *et al.* Transition metal dissolution and deposition in Li-ion batteries investigated by operando X-ray absorption spectroscopy. *J Mater Chem A Mater* **4**, 18300–18305 (2016).

118. Gowda, S. R. *et al.* Oxidation state of cross-over manganese species on the graphite electrode of lithium-ion cells. *Physical Chemistry Chemical Physics* **16**, 6898–6902 (2014).

119. Ellis, L. D. *et al.* Quantifying, Understanding and Evaluating the Effects of Gas Consumption in Lithium-Ion Cells. *J Electrochem Soc* **164**, A3518–A3528 (2017).

Chapter 2 - Experimental Methods

Introduction

The initial section of this chapter outlines the material preparation methods utilised for fabricating thin film electrodes, composite electrodes, coin cell battery assembly, and conducting electrochemical testing. The latter part of the chapter is dedicated to synchrotron-based spectroscopy and microscopy techniques, alongside various other characterisation techniques employed for surface-sensitive measurements of lithium-ion battery materials.

Physical Vapour Deposition

Sputter Deposition

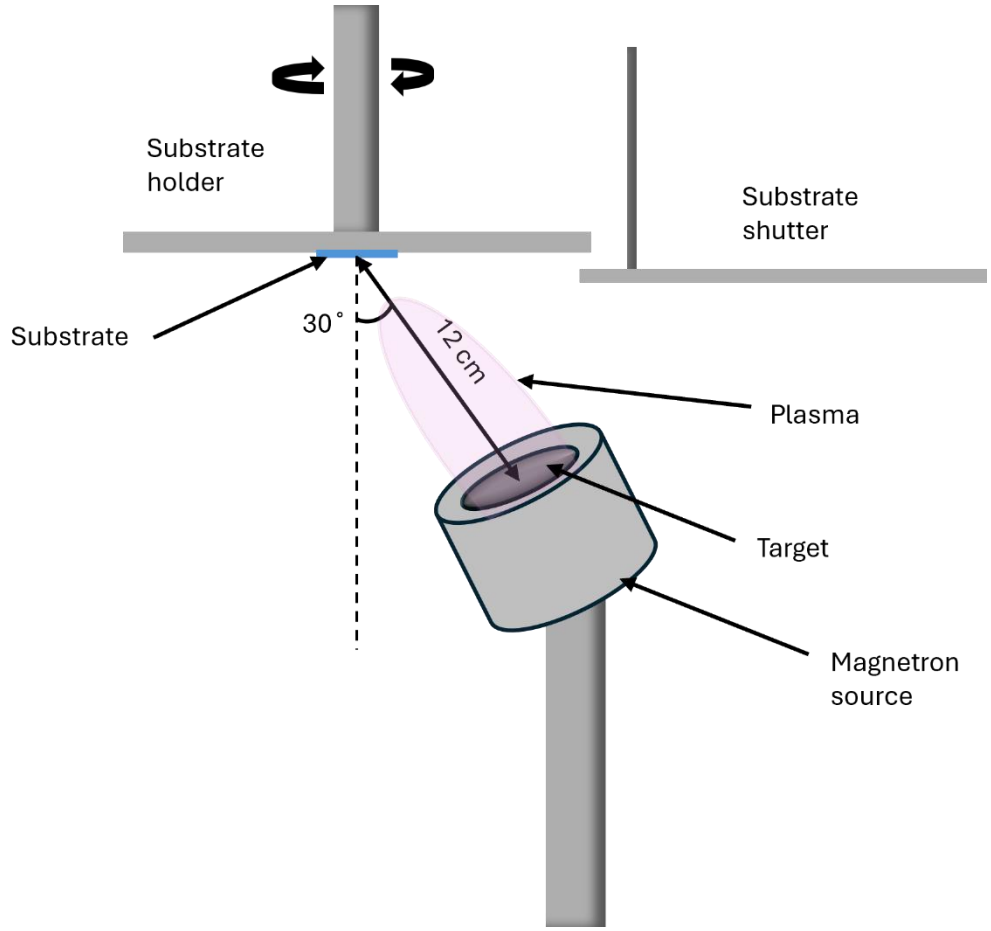

Figure 2.1 Schematic Diagram of the Mbraun MB EVAP PVD chamber used for the deposition of thin films via thermal evaporation and sputtering.

A PVD system integrated into a glovebox (Mbraun) with monitored O_2 and H_2O levels maintained below 0.1 ppm was used for the radio frequency (RF) magnetron sputter deposition of thin film metals for the research in this Thesis. This system featured a circular magnetron source (Gencoa Ltd) positioned at an inclination of approximately 30° towards the substrate holder, as illustrated in Figure 2.1 The target distance to the substrate was fixed at 12 cm. The deposition chamber was evacuated to achieve a base pressure of $<1\times10^{-6}$ mbar prior to deposition.

The primary objective of achieving a low base pressure is to minimise volatile contaminants during the sputtering or thermal evaporation processes. In sputtering, an ionisable gas (argon gas in all deposition cases in this thesis) flowed into the chamber at a rate of 10 standard cubic centimetres per minute (sccm), raising the chamber pressure to approximately 5×10^{-3} bar.

Ionisation of the Ar gas is initiated by applying a RF, typically at 13.56 MHz, establishing an alternating electric field between the target and the chamber.[1] This process produces a negative sheath potential on the target, wherein electrons respond faster than positive ions within the magnetic field. Consequently, the target takes on the role of the cathode, with the remaining chamber acting as the anode, culminating in the formation of a plasma.

Ar^+ ions are accelerated towards the cathode, colliding with atoms of the target material, inducing ionisation and subsequent ejection into the plasma. Simultaneously, electrons are liberated in this process and are directed towards the shield enveloping the target. This event leads to the ionisation of additional argon atoms and the release of more electrons, thereby sustaining the plasma generation process. The magnetic field lines originating from the permanent magnet array within the magnetron source traverse the target from the periphery to the centre, trapping electrons and increase the sputtering rate.[2] The sputtered ions are directed towards the substrate surface, forming a thin film with properties similar to those of the target material.

Resistance-Heated Evaporation Sources

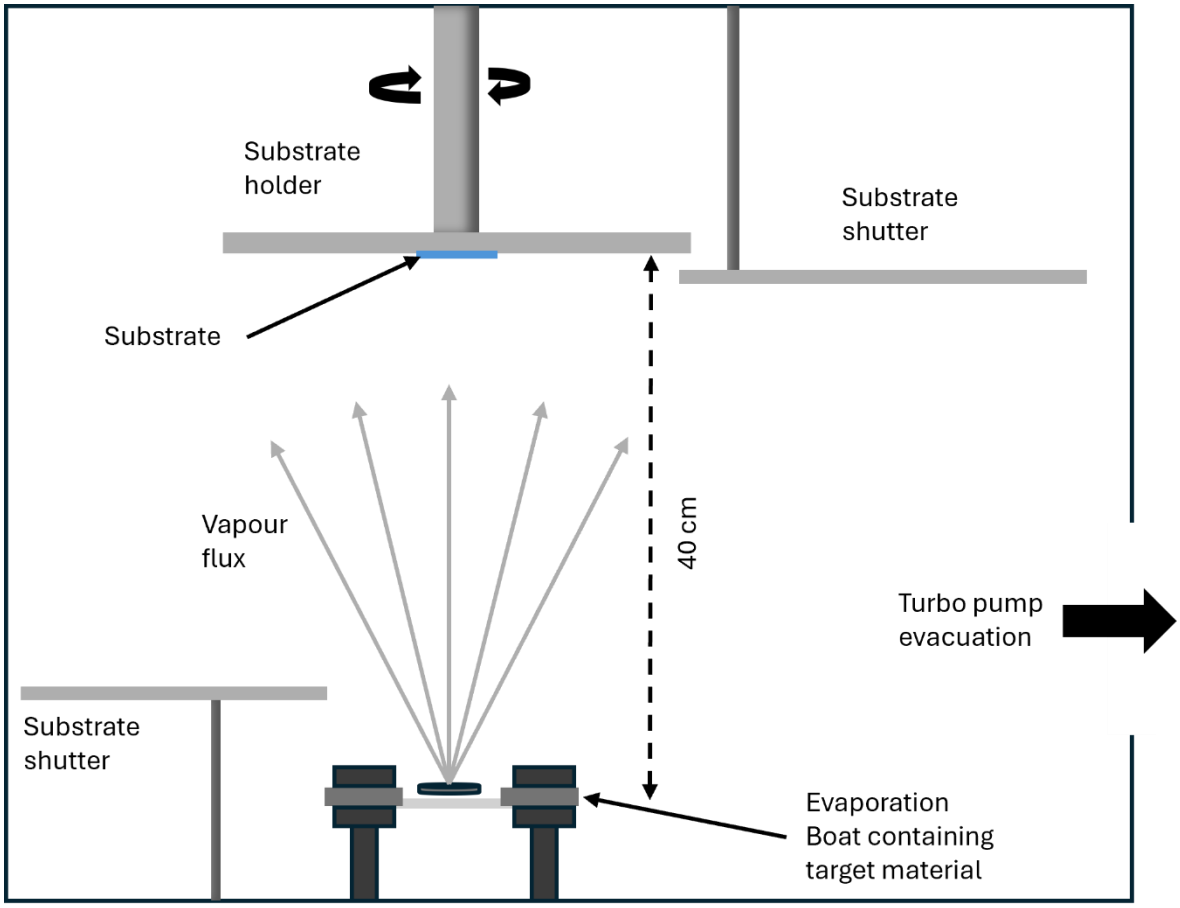

Figure 2.2 Schematic diagram showing the thermal evaporation chamber used for growing metallic thin films.

This section will provide a concise overview of the most commonly employed methods for heating evaporants. Resistant heater sources must achieve the vapourisation temperature whilst maintaining a negligible vapour pressure of the sources material. Ideally, they should not introduce contamination, undergo reactions, alloy with the evaporated element/compound, or release gases such as oxygen, nitrogen, or hydrogen at the evaporation temperature. Resistively heated evaporation sources are diverse and come in various forms, employing refractory metals individually or combined with inert ceramic compound. A current is passed through this crucible until the vapour pressure of the target

material reaches the threshold to generate a vapour flux, which deposits onto the sample substrate as depicted in Figure 2.2 The thermal evaporation setup employed an alumina-coated molybdenum evaporation boat (Kurt Lesker Ltd.) positioned approximately 40 cm from the substrate functioning as a self-resistant heater, was used for research in this thesis. [3]

Electrochemical Techniques

Electrode Preparation

Prior to cell assembly, all cell components active and non-active were dried under vacuum in a Buchi oven overnight at 80˚C to remove any residual water. Electrode Preparation involves mixing the active material with additional components, such as conductive agents and binders, in a slurry before coating it onto a thin metal foil current collector. Lithium transition metal oxides commonly used as the active material for cathode electrodes are poor electrical conductors and require carbon black powder to aid electron transport. Polymer-based binders provide cohesion between the particles and adhesion to the current collector. These components can be dry-mixed but often require a solvent to form a slurry to ensure even dispersion of electrode components. After the electrode components are mixed, they are applied to the current collector and then dried; an additional step, calendering, compresses the electrodes into the current collector foil to improve electrical contact and increase density. However, it is essential to keep the electrode porosity to avoid closing electrode pores, preventing electrolyte percolation. Electrodes are cut to size and then weighed before assembly into a cell.

Coin Cell Assembly

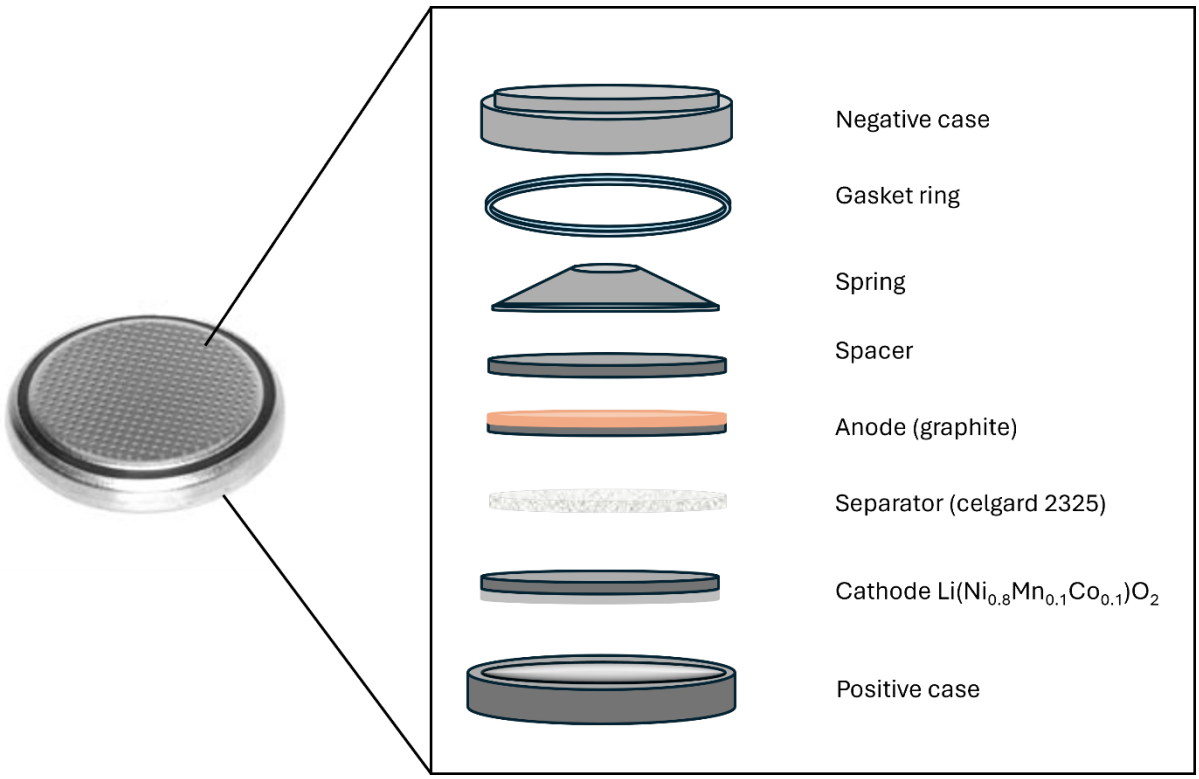

Figure 2.3 Diagram showing the exploded view of stacked components of a coin cell.

The coin cells consist of a stainless-steel base and lid, which also act as current collectors and are electrically isolated from each other by a plastic ring gasket. Inside, the cathode is kept separate from the anode by a disk of Celgard 2325 and or a porous glass fibre soaked with electrolyte, which is typically a Li salt (LiPF6) dissolved in an organic-based solvent mixture (containing a mixture of cyclic and linear carbonates). The anode is usually a thin disk of lithium metal or a graphite-based composite electrode. Detailed cell assembly is discussed in the methods section of Chapters 3, 4 and 5.

Cyclic voltammetry

Cyclic voltammetry (CV) is a fundamental electrochemical technique for investigating electron transfer reactions within electrochemical systems. In analysing lithium-ion cells, this procedure involves applying a linear potential sweep between predefined voltage limits against a lithium reference electrode. CV sweeps serve as a valuable tool for determining the reversibility of redox reactions, and they play a crucial role in assessing the stability and electron transfer kinetics and mass transport limitations of materials. In the case of lithium-ion battery systems (specifically, Li half cells), CV sweeps enable the analysis of redox activity within the working electrode when it interacts with Li^+ ions.[4]

Galvanic cycling

In battery research, the most commonly employed testing method is galvanostatic cycling. CC (constant current) involves applying a stable current, determined by the active material's mass and the desired charging rate until the voltage reaches a predefined upper limit. Upon reaching the potential limit, the current direction switches, and the cell undergoes discharge until it reaches a specified lower cut-off voltage. Current rates are often expressed as current per unit mass of cathode ($mA\ g^{-1}$) or in terms of C-rates, which are more prevalent in industrial applications. A 1C rate signifies that the applied current is adjusted to charge or discharge the cell entirely within one hour.

Alternatively, cells can be charged and discharged potentiostatically by maintaining a constant voltage and observing the current response. Under these conditions, the current typically exhibits an exponential decay as the electrode approaches an equilibrium state at the set potential. This differs from galvanostatic experiments, which, at very low current rates, closely

track reactions near equilibrium conditions. In commercial applications, batteries are charged using CCCV (constant current constant voltage) techniques, which combine these two regimes. Initially, a constant current is employed to reach the upper voltage limit, followed by a "trickle charge" phase where the potential remains constant, allowing the current to drop to a fraction (e.g., C/10 or C/20) of that used in the constant current step. This approach achieves nearly full charge without pushing the cell past its upper voltage limit. In coin cells with limited active cathode material, small currents (typically 0.1 - 1 mA) are sufficient for efficient charging and discharging at various rates (e.g., C/10 to 1C). To achieve precise control over these currents and continuously logging the cell voltage, specialised battery cycling equipment such as a Biologic was commonly employed throughout this research outlined in this thesis.

Synchrotron radiation Techniques

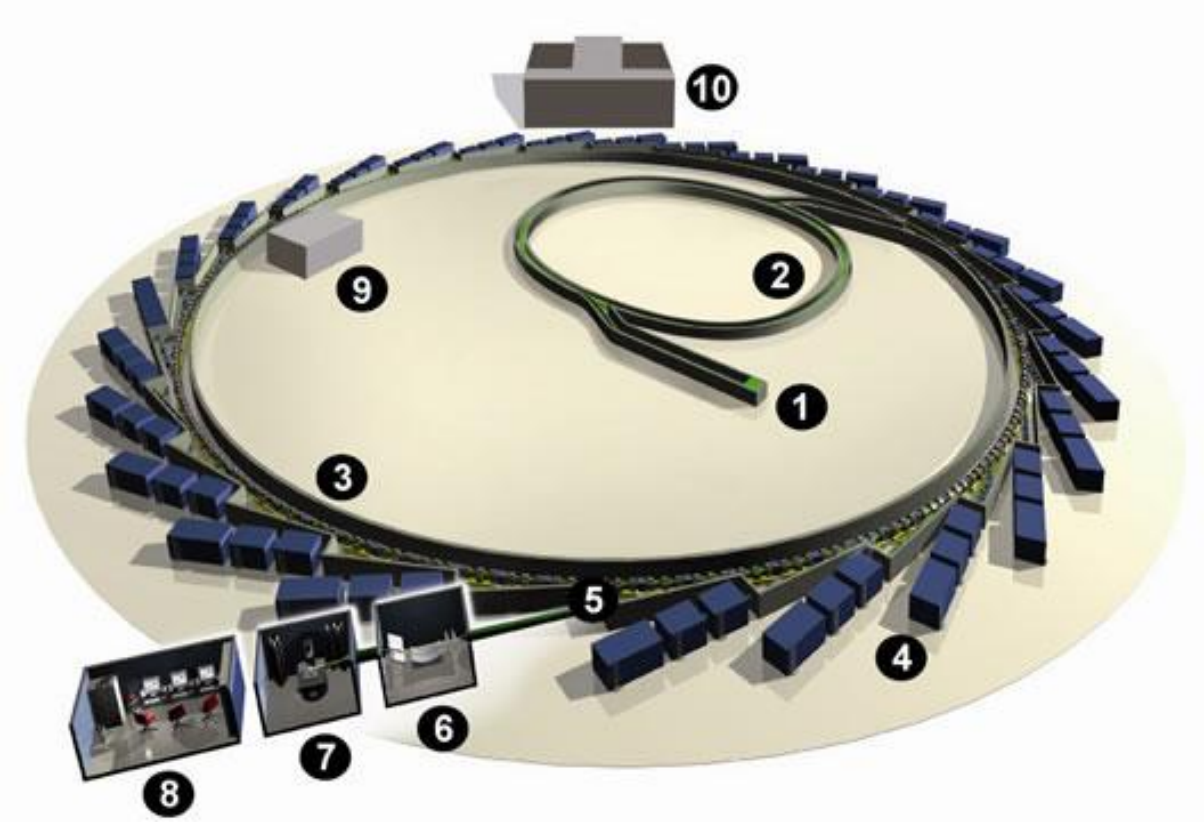

Figure 2.4. Schematic of the synchrotron facility at Diamond Light Source. Image taken from https://www.diamond.ac.uk/Science/Machine/Components/storagering.html. (Accessed 16/02/2024).

Synchrotron x-ray techniques use charged particles accelerated close to the speed of light in a cyclotron under vacuum to generate photons with characteristic wavelengths. Electrons are generated by thermionic emission from an electron gun under vacuum conditions inside the linear accelerator (Linac, labelled 1 in Figure 2.4). The electrons produced are pulsed and propelled to high velocities through an electric field reaching hundreds of MeV. The electrons are then injected into the booster ring, a smaller-scale accelerator that allows the electrons to reach velocities in the GeV region. The electrons are then passed into a storage ring and periodically topped up to ensure a stable operating current (labelled 2 in Figure 2.4). The

electrons are accelerated along a closed path system, typically in a loop or a straight line (labelled 3 in Figure 2.4), and electromagnets control the movement of the electrons.

Dipole bending magnets guide the electron flow, changing the trajectory and releasing bending magnet radiation, causing slight energy losses in the form of synchrotron radiation emission. The energy loss is replenished by radio frequency cavities called klystron to boost the storage ring electrons to maintain acceleration along the circular path of the storage ring. Quadrupole magnets help to refocus and realign the beam amidst its bends, while sextupole magnets rectify chromatic aberration caused by the focusing. The insertion devices (ID), known as wigglers and undulators, house small bending magnets in alternating polarity, forcing the electrons into an oscillating plane parallel to the storage ring. ID offers significant advantages over bending magnets, including higher flux and brilliance.[5–7]

The bending magnets and the insertion devices guide the synchrotron radiation towards the beamline endstations for experimental analysis. Here, the photon beam is focused by a series of mirrors and monochromated before it reaches the experimental hutch (labelled 4-8 in Figure 2.4). The monochromated beam allows scientists to scan across an energy range or hold a known fixed energy when performing analysis.

synchrotron facilities hold several advantages over lab-based systems for sample analysis:

- High brilliance: synchrotron X-rays are at least several orders of magnitude higher than laboratory instruments, enabling more rapid data collection.
- Tuneable energy range: they offer a broad spectrum of X-ray wavelengths.
- High resolution: Synchrotron facilities provide high spatial and energy resolution for capturing dynamic processes.

- Polarisation control: tunes the contrast for imaging in specific techniques, making it a powerful tool for distinguishing different sample environments.

This project utilised many of the advantages listed above to characterise samples enhancing the understanding of lithium-ion battery degradation mechanisms. The ability to perform Near Edge X-ray Absorption Fine Structure (NEXAFS) measurements was crucial for this project and could only be performed at synchrotron facilities.

Spectroscopic techniques

XAS

X-ray absorption Spectroscopy (XAS) operates on the principle of photon absorption by the sample, according to Beer-Lamberts Law. This law correlates the transmitted X-ray intensity (I) to the incident X-ray intensity (I_o), sample thickness (x), and the material's absorption coefficient μ. Consequently, the transmitted X-rays exhibit reduced intensity as they pass through the sample of thickness x, displayed in equation 2.1.

$$I = I_0 e^{-\mu t} \qquad [2.1]$$

XAS involves measuring the absorption coefficient of a material's element as a function of incident photon energy. When the incident X-ray energy matches the binding energy of a core electron within the absorbing atom, absorption increases, producing the absorption edge. This resonance arises from the core electron's excitation to a vacant or partially occupied level. Notably, the element-specific nature of XAS derives from the absorption's energy, uniquely tied to the binding energy of the core electron level distinctive to each element.[8]

The absorption coefficient (μ) depends on the relationship between the density (ρ), atomic number (Z), atomic mass (A) and the incident x-ray energy (E) as described in equation 2.2 below:

$$\mu \approx \frac{\rho Z^4}{AE^3} \qquad [2.2]$$

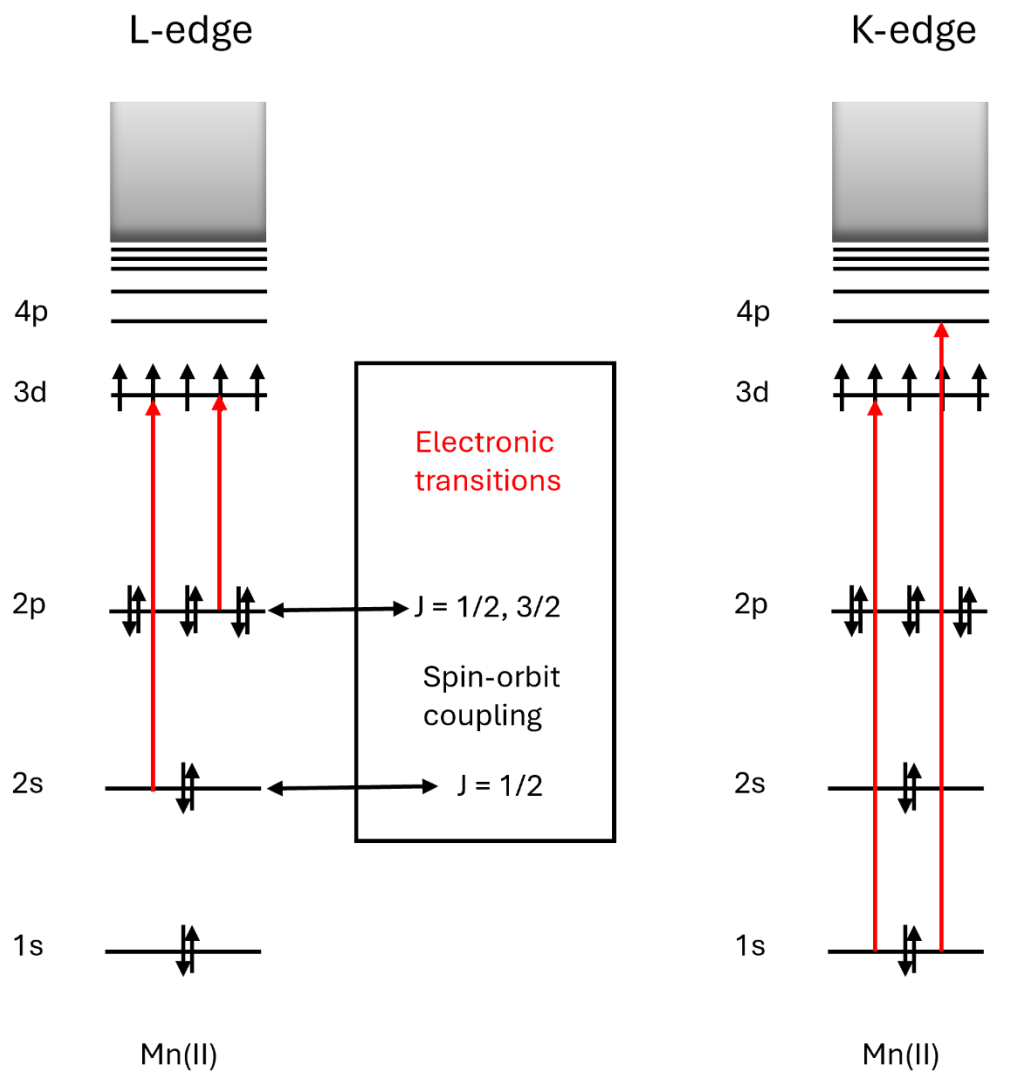

Figure 2.5. Schematic illustrating XAS transitions of the 3d TMs for both "soft" XAS and "tender" XAS incident photon energy regions.

XAS primarily involves the excitation of electrons, typically from the 1s or 2p core shells, facilitating electronic transitions from filled to empty orbitals. This necessitates high-energy X-ray excitation, commonly achieved at synchrotron facilities, to provide a wide energy range to probe each element's core shell. The technique follows selection rules governing electronic transitions between adjacent shells, such as s → p, p → d, d → f, with changes in orbital angular momentum (Δl) restricted to ±1. The absorption edges are designated as K, L, and M, corresponding to the principal quantum number of the lower-level electron, as depicted in Figure 2.5.[9]

Incident X-ray photon energy ranges into three distinct group called "soft x-rays" (<2 KeV), "tender/hard x-rays" (2-8 KeV), and hard x-rays (>8 KeV), with "soft x-rays" corresponding to wavelengths around 1 nanometre. This wavelength scale aligns with the order of magnitude of atom-atom separation in molecular structures, making XAS a valuable tool for probing local atomic structures. XAS is particularly useful in characterising materials based on their unique X-ray absorption "fingerprints," enabling the determination of local atomic environments within a compound. Notably, XAS is a non-destructive method, allowing direct examination of heterogeneous and amorphous samples.[10,11]

Near Edge X-ray Absorption Fine Structure (NEXAFS)

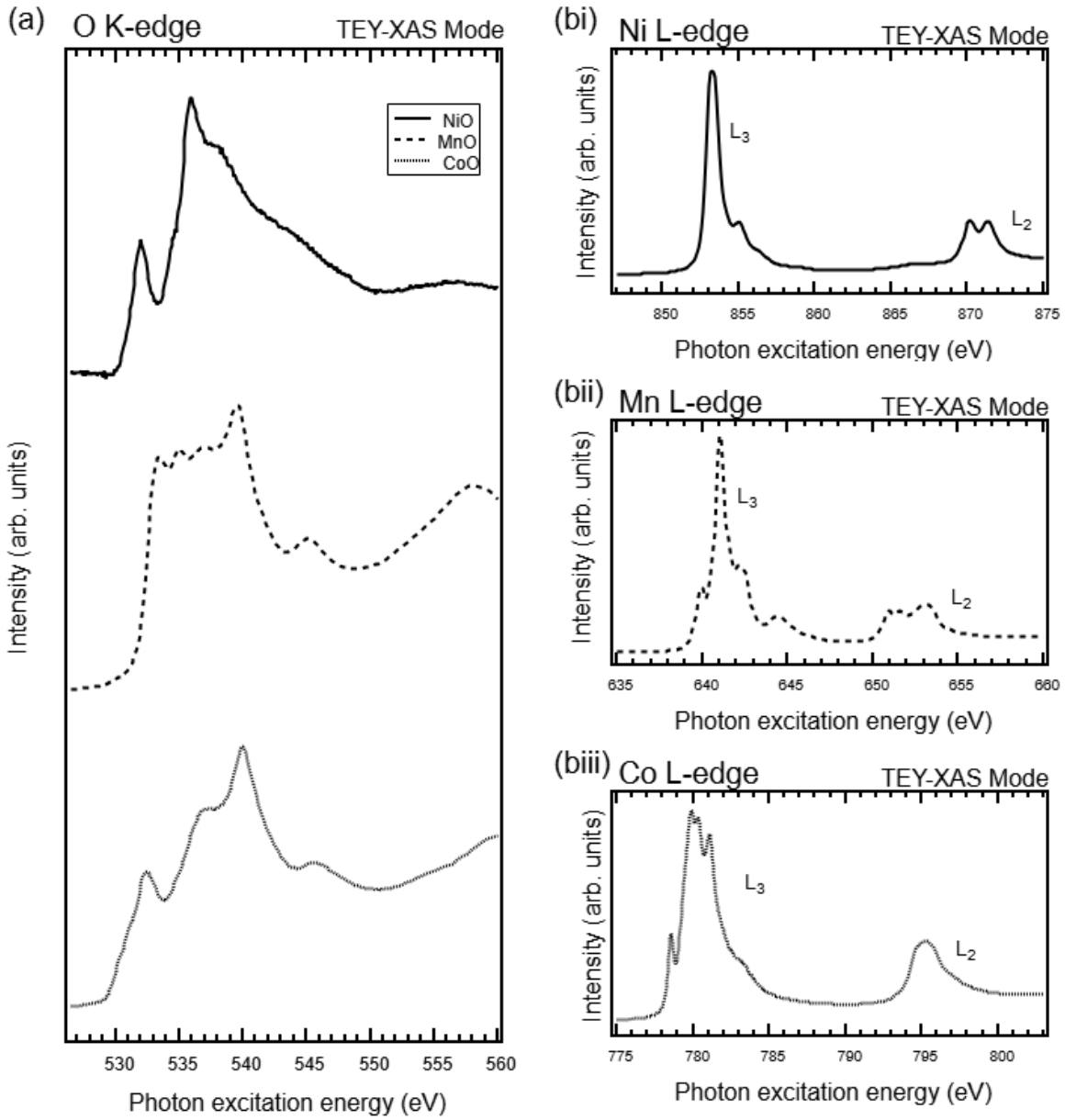

Figure 2.6. Soft XAS of a O K edge of NiO, MnO and CoO. The respective L-edges of NiO (bi), MnO (bii) and CoO (biii) are also plotted.

In order to study the 3d TM L-edges and the O K- and F K-edges, x-ray photon energy must be in the soft x-ray energy range <2 KeV. These measurements often require ultra-high vacuum due to the short attenuation length of x-rays (below 2 KeV). The spectral peak positions and intensities are directly related to the nature of unoccupied electronic states. Decay of core

holes may also occur via the emission of fluorescent photons, which originate from the top 200 nm of the film, compared to Auger electrons, which are also generated at the same depth but loose energy and cannot escape, except from the top 10 nm of the sample. Thus, this technique is surface (TEY detection mode) and bulk-sensitive (FY detection mode) depending on the detection mode used. NEXAFS is capable of simultaneously probing both cathode particle electronic structure and surface functional groups.[9–11]

Due to spin-orbit coupling (between the electron spin s = ±1/2 and the orbital angular momentum l = 1 to give j = 1/2, 3/2), the 2p orbitals are not degenerate in energy giving $2p_{1/2}$ and $2p_{3/2}$ as described in Figure 2.5. Correspondingly, XAS at the metal L-edge tends to exhibit two edge features known as L_{III} and L_{II} as shown in Figure 2.6bi-iii.[12] The O K-edge is strongly influenced by mixing with the TM orbitals, with the main edge feature representing 1s → O 2p/TM 4sp. A pre-edge feature ~ 532 eV arising from 1s → O 2p/TM 3d transitions. The shape of the pre-edge is determined by the electron-hole distribution among the t_{2g} and, e_g orbitals that arise from the crystal-field splitting of the 3d orbitals under octahedral coordination geometry. In the case of MnO, this crystal field splitting is too small to be visible.[13]

X-ray Absorption Fine Structure (XAFS)

XAFS is a powerful tool for investigating the nanoscale's local atomic structure and molecular arrangements. The XAFS phenomenon represents the modulation of the linear absorption coefficient $\mu(E)$ due to the backscattering of photoelectrons from electrons of neighbouring atoms. This scattering induces interference with the outgoing photoelectrons originating from the absorbing atom, ultimately modulating the intensity of the observed absorption coefficient.[14]

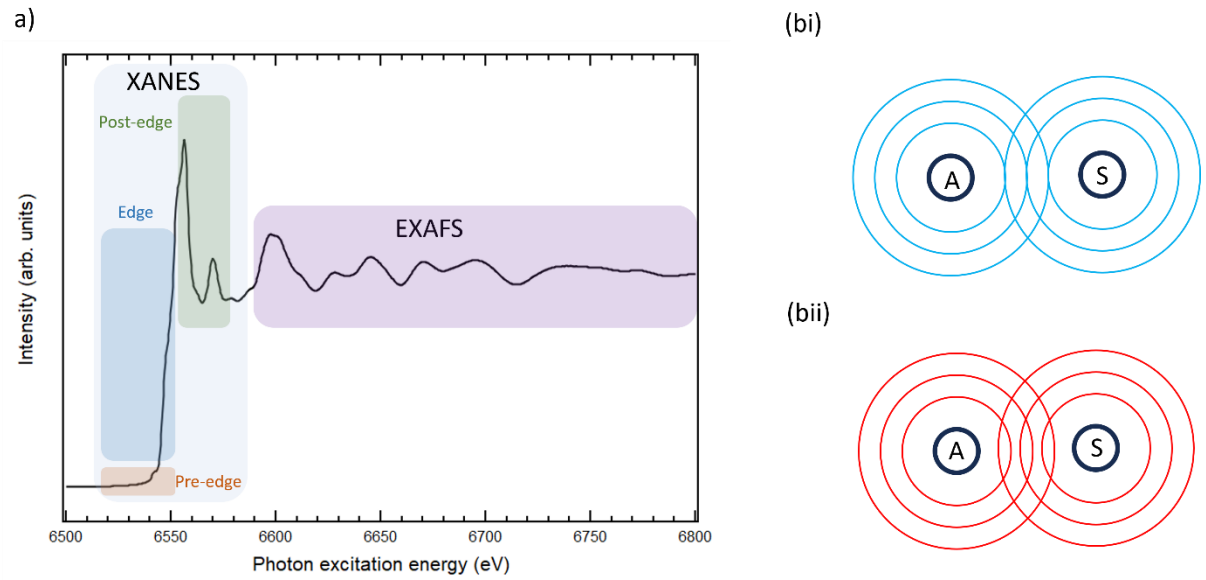

Figure 2.7. A typical XAFS with extended edge measurements for MnO compound. Figure a highlights the XANES (light blue) and EXAFS (purple) regions within the spectra. Figure b illustrates the photoelectron scattering interfering with neighbouring atoms.

The photoelectron excited by X-rays is depicted in figure 2.7bi as concentric circles centred around the absorbing atom (A), where the separation between circles corresponds to the de Broglie wavelength of the photoelectron. Interaction occurs as the photoelectron is scattered by neighbouring atoms, represented by a single atom (S) in the illustration. Figure 2.7bi. represents scattering at a lower incident photon energy, where the outgoing and backscattered waves are in phase, leading to constructive interference and a local maximum in the photoabsorption cross-section. In Figure 2.7bii. represents a slightly higher incident photon energy, which is associated with a shorter photoelectron wavelength, resulting in destructive interference due to the absorber-scatterer distance, causing a local minimum in absorbance.[14–16]

The X-ray Absorption Fine Structure (XAFS) analysis involves a series of systematic steps to extract meaningful information from measured intensities. Initially, the measured intensities are converted to the absorption coefficient μ(E), with potential corrections for systematic

measurement errors like self-absorption effects and detector dead time. Subsequently, a smooth pre-edge function is subtracted from μ(E) to eliminate instrumental background and absorption signals from other edges. The threshold energy E_0 is typically identified as the energy at the maximum derivative of μ(E). To facilitate XANES analysis, the post-edge region of μ(E) is then normalized to 1 between a pre-edge and a fitted spline function E_0, representing the absorption of a single X-ray. Following normalization, a smooth post-edge background function is removed to approximate μ_0(E). The XAFS k is isolated, where k is calculated by equation 2.3 below:

$$k = \sqrt{2m(E - E_0)/h^2} \qquad [2.3]$$

The obtained EXAFS signal is subjected to k-weighting, commonly multiplied by K^2 or K^3 to accentuate the oscillations. Fourier transform can be applied to the dataset, converting it into R-space, where R represents pseudo radial distribution function from the absorbing atom.[17]

X-ray Photoelectron Spectroscopy (XPS)

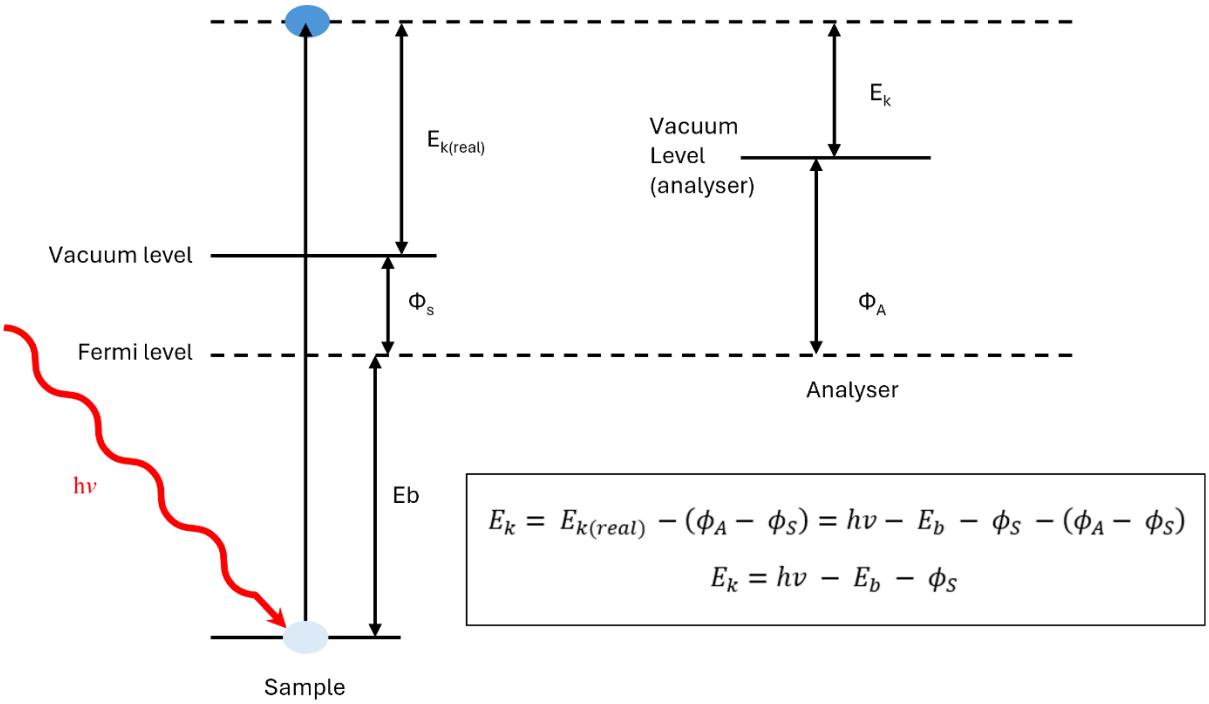

Figure 2.8. Schematic band alignment of the sample and the analyser in electrical contact for XPS measurements. Energies are aligned to the Fermi level. The top dashed line represents the vacuum level.

X-ray photoelectron spectroscopy (XPS) is a surface-sensitive characterisation technique based on the photoelectric effect developed by Kai Siegbahn, for which he won a Nobel prize.[18] XPS has become a powerful materials characterisation tool providing surface-sensitive information on chemical composition, chemical states, and surface interactions of compounds and materials. The photoemission process, in effect, works in three distinct phases demonstrated in Figure 2.8:

1. Photons of a characteristic energy *hv* (e.g. Al Kα generate photons with a characteristic energy of 1486.6 eV) illuminate the surface of a material of interest, interacting with the electrons within the atomic orbitals to generate photoelectrons.

2. The electrons move through the sample surface and are influenced by several scattering processes which form the background counts (secondary electrons), whilst primary electrons not suffering from inelastic collision, give rise to distinct spectral features (matching the sample density of states).
3. Electrons at the material surface, which overcome the work function, are emitted into the vacuum.

If the incident x-ray energy is known (e.g. Al Kα = 1486.6 eV) and the emitted electrons emitted from a specific valence or core level kinetic energies are measured, then the binding energy of each emitted electron can be measured using the photoelectric effect equation below.

$$E_b = hv - E_k - \phi \qquad [2.4]$$

E_b is the binding energy of the electron measured relative to the chemical potential, *hv* is the incident photon energy illuminated on the sample surface, and E_k is the kinetic energy of the electrons depending on how tightly bound the electron was to the orbital and on the incident photon energy generated by the instrument. Φ is the work function specific to the material surface (there is also a work function from the instrument due to contact potentials).[19,20]

The surface sensitivity of XPS is governed by the escape depth of the photoelectrons generated, which are in turn caused by the inelastic scattering of electrons in a solid determined by the Beer-Lambert law given below by equation 2.5:

$$I = I_0 e^{\frac{-d}{\lambda}} \qquad [2.5]$$

The equation above relates the intensity I of photoelectrons emitted at the surface to the intensity I_0 of electrons at a depth d below the surface. λ is the inelastic mean free path (IMFP). The IMFP characterises electron scattering and represents the average distance an electron

with a specific energy travels between successive inelastic collisions. In the context of Al Kα x-rays with an energy of 1486.6 eV, the typical sampling depth for most compounds is around 3-10 nm.[21] Rearranging the equation allows us to determine the probing depth of x-rays, shedding light on the effective depth at which the incident radiation is probing the material:

$$d = -ln\left(\frac{I}{I_0}\right) x\, \lambda \qquad [2.6]$$

Microscopy Techniques

X-ray Photoemission electron Microscopy (XPEEM)

Photoemission electron microscopy (PEEM) operates in various modes, distinguished by the photon energy and the method of collecting photoelectrons for analysis. PEEM was first developed through the use of a UV light source to induce photoemission, primarily serving as a non-spectroscopic imaging technique. The technological simplicity of UV-PEEM makes it advantageous, yet it lacks chemical specificity in the obtained information.[22]

In contrast, XPEEM employs higher-energy soft X-rays for sample illumination. Within this energy range, photons can induce elementally specific core-level photoemission, enabling elemental composition analysis. Unlike UV-PEEM, XPEEM provides binding energy spectra similar to XPS and the ability to scan a wide energy range for XAS more detailed explanation will be provided in Chapter 3 for this thesis.

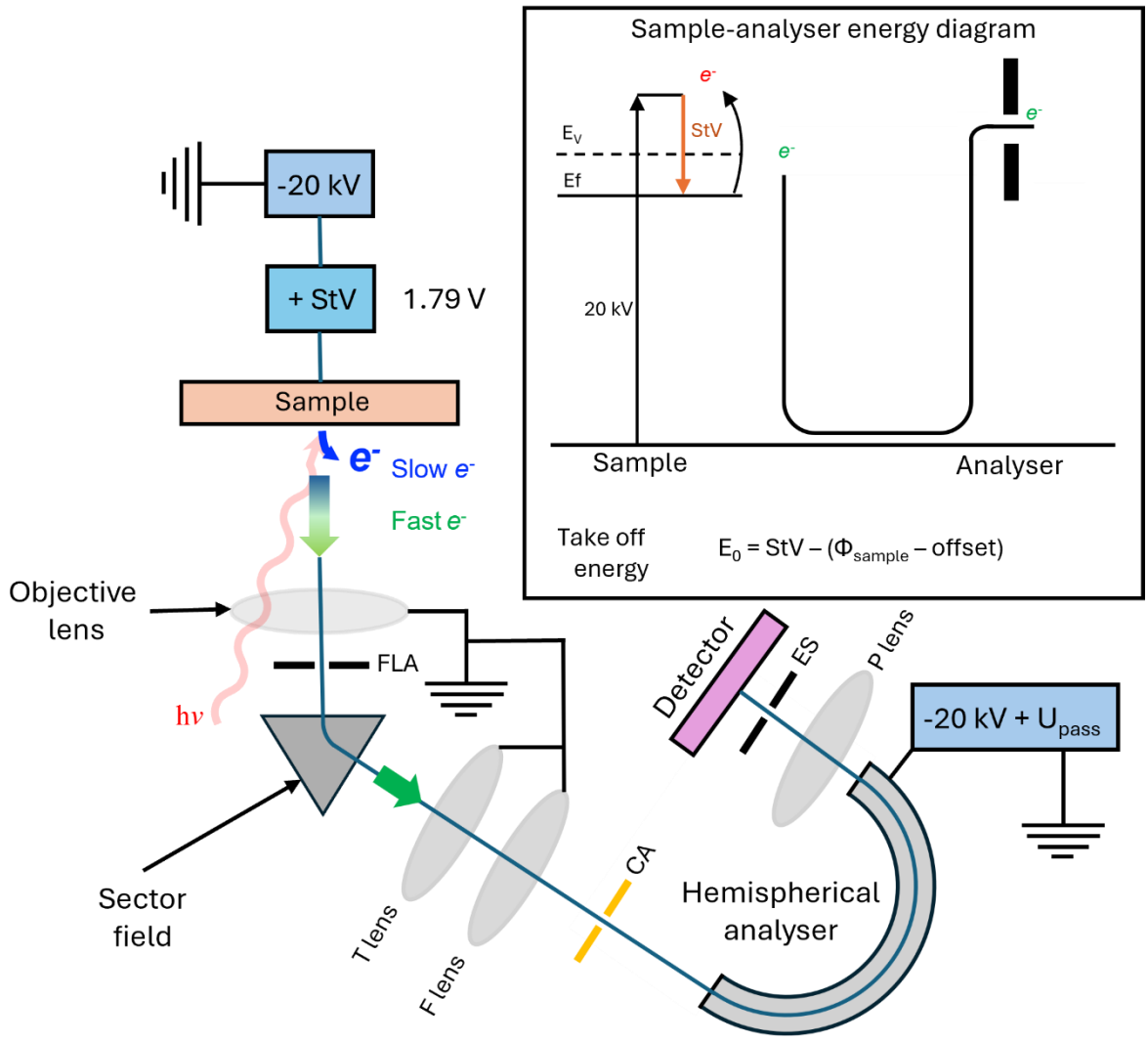

Figure 2.9. A schematic diagram showing the instrumental setup of the Elmitec III PEEM endstation on the IO6 beamline at Diamond Light Source UK. The instrument includes several lenses and apertures the electrons pass through before reaching the detector, including the objective lens, P - projecting lenses, F - field lens, T- transfer lens, CA - contrast aperture, FLA - field limiting aperture and ES- exit slits.

Figure 2.9. illustrates a schematic diagram of the XPEEM instrument. In its basic configuration, the instrument focuses X-rays onto the sample surface. The resulting photoelectrons and secondary electrons generated are passed through a series of lenses and energy-filtered before the image is projected onto a detector. The incident beam's interaction with the surface prompts the emission of electrons from the sample, which is then directed back through the objective lens toward the sector field. The imaging column, comprising a sequence of lenses

(transfer and field), magnifies the image of the beam. The beam then passes through an energy analyser, which filters the beam's energy. The electrons are then accelerated in the hemispherical analyser. Once the electrons leave the analyser, the electrons are further energy filtered by the presence of exit slits before reaching the 2D electron detector to record the PEEM image.[23]

X-ray Absorption Mode

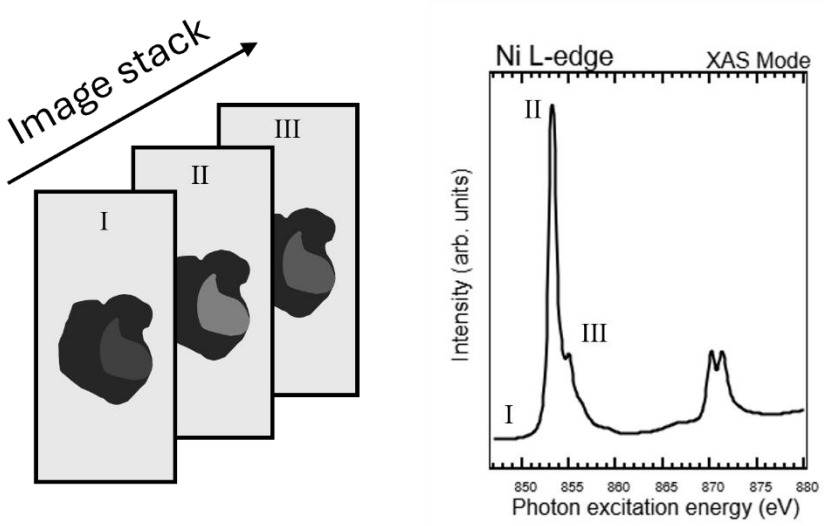

Figure 2.10. Schematic diagram of the image stack generated at point-specific photon energies and the corresponding Ni L edge spectra.

In XAS measurements, the incident photon energy is scanned across a range of photon energies, as detailed in section 2.10. If the incident energy is below the binding energy of a surface core-level electron, it results in a dark region in XAS images (region I, as depicted in figure 2.10), indicating the collection of background information only. Conversely, when the incident energy matches or surpasses the binding energy of a core-level electron, resonance manifests in the emission of electrons excited through secondary processes, creating a bright region in XAS images (regions II and III in Figure 2.10). This resonance arises from the excitation of core-level electrons to previously unoccupied valence states, triggered by the filling of core

holes following the initial excitation. At the resonance maxima, the emission of secondary electrons from the sample intensifies, progressively brightening the corresponding images, as depicted in Figure 10.[24–26] In the XPEEM measurements conducted for this Thesis, total electron yield mode measurements were used to collect information on the TM L-edges of NMC811 particles. The measurements presented in Chapter 3 showcase spatiochemical maps of the surface of high-capacity cathode particles.

Micro-X-ay Photoelectron Spectroscopy

Operating XPEEM in μ-XPS mode shares similarities with conventional XPS, but with spectra gathered from a significantly smaller surface area. μ-XPS utilizes a photon beam with a fixed energy, incorporating a variable band pass filter. Notably, no exit slit is employed for the energy filter, and the last couple of lenses of the microscope are configured to project the dispersive plane of the filter directly onto the detector. The dispersive plane images in μ-XPS manifest as straight lines with varying contrast, where each point on the line corresponds to the binding energy and signal intensity of the dispersed photoemitted electrons, indicated by horizontal position and brightness, respectively. Integrating a line profile from a dispersive plane image enables the generation of a photoemission spectrum for the specified energy window, similar to those acquired in conventional XPS. The spatial resolution of μ-XPS is determined by introducing a field-limiting aperture into the path of the photoemitted electrons, allowing the collection of spectra from an area of less than 2 μm. This technique excels in providing high-energy resolution spectra and is often combined with other PEEM techniques, such as energy filtering microscopy, to enhance its analytical capabilities.[27,28]

Energy Filtering Microscopy

In contrast to XAS, which relies on variable energy photons, energy-filtered imaging microscopy employs a constant energy photon beam to generate photoelectrons. Alongside the standard setup illustrated in Figure 2.9, an energy filter is incorporated into the electron analyser to select electrons of a specific energy. A contrast aperture is inserted into the beam path, allowing the resolution of a surface image from the stream of photoemitted electrons. During the process, images are captured as the energy filter is swept through a range of values. In the resulting images, each pixel appears bright where the photoemission energy of the surface atoms aligns with the band pass energy of the filter. By adjusting the band pass energy of the analyser, certain areas will illuminate based on their chemical identity.[29]

Scanning Electron Microscopy (SEM)

Microscopy is a powerful technique for investigating samples' topography, morphology, and composition. The wavelength of visible light (400nm - 700nm) fundamentally limits the lateral resolution limit of optical microscopes to 200nm based on equation 2.7:

$$Resolution = \frac{0.51 \times \lambda}{NA} \qquad [2.7]$$

The resolution of an optical system, such as a microscope, is defined as the minimum resolvable distance between two points. This is determined by the wavelength of light (λ) and the optical system's numerical aperture (NA). The numerical aperture parameter depends on the medium's refractive index (n) between the lens and the specimen and the half-angle (θ) of the maximum cone of light the lens can gather, typically ranging from 0.1 to 1.4. The

constant 0.61 in the Rayleigh criterion is derived from the analysis of the Airy disk pattern, representing the diffraction pattern produced by a point source of light. This empirical constant establishes a practical criterion for the minimum resolvable separation between two points based on the diffraction patterns observed in optical systems.[30,31]

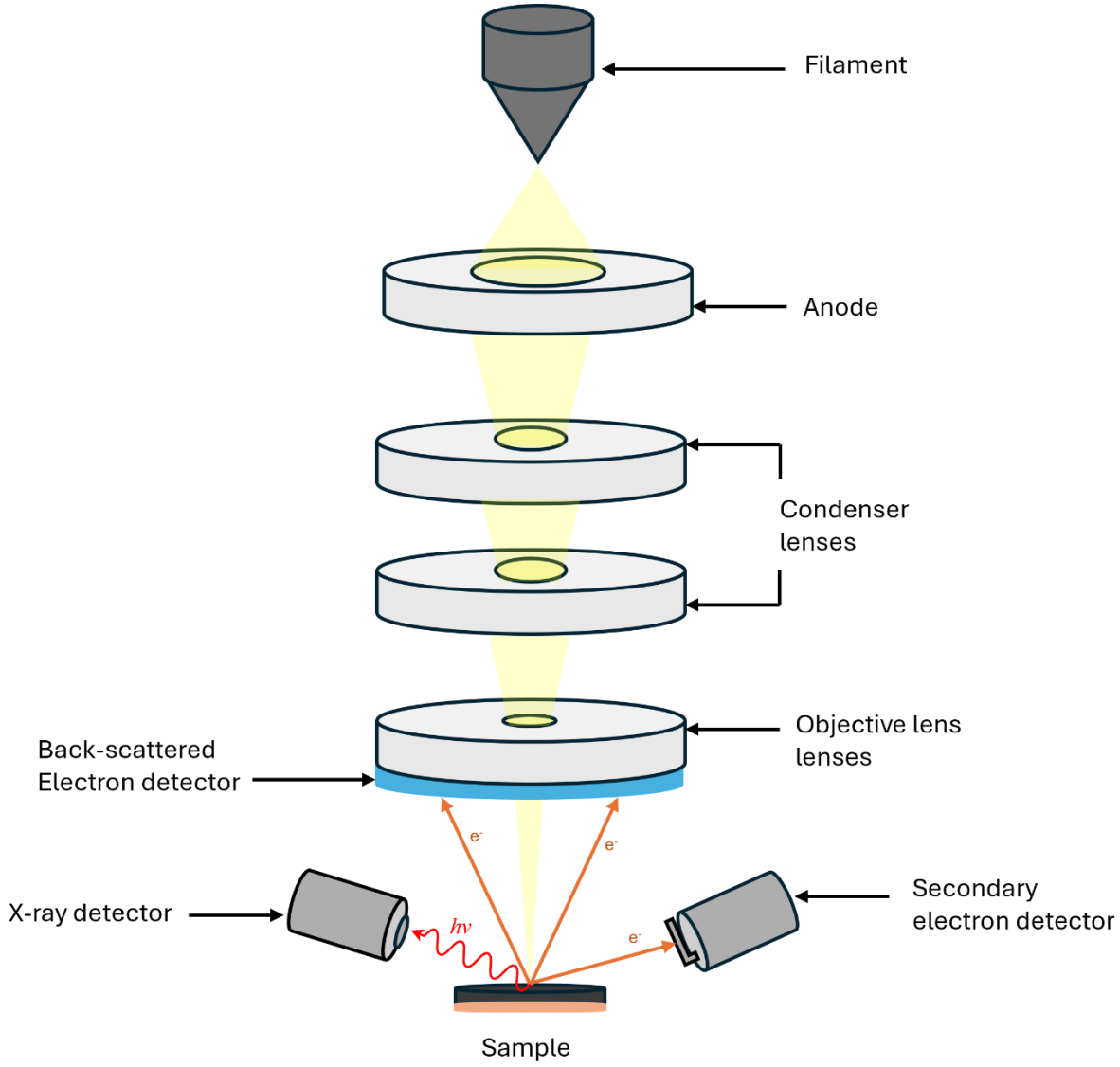

Figure 2.11. Schematic representation of the SEM.

Scanning electron microscopy (SEM) uses electron beams generated by an electron gun, typically by a heated tungsten filament, and offers higher nanometer (nm) resolutions. The accelerating voltage (ranging from 0.2 - 30 kilovolts (kV) determines the energy and

wavelength of the electrons. When the electron beam rasters across the sample's surface in a vacuum, the electrons can interact with the sample, generating signals from both electrons and x-rays, giving details about the sample topography and chemical information.

- **Secondary electrons:** Emitted from inelastic collisions near the surface, these low-energy electrons offer details on the topography and morphology of the surface or nearby regions. Detection commonly employs an Everhart-Thornley detector, converting emitted electrons into photons, then electrical signals for imaging.
- **Backscattered electrons:** Arise from elastic collisions between electrons and atoms, scattering electrons across a more comprehensive depth range in the sample. Intensity relates to atomic number, distinguishing different phases within the sample.

References

1. Swann, S. *Magnetron Sputtering*. (1988).
2. Kindsmüller, A. *OE-Oxide Pt The Role of Interface and Exchange Processes in Forming and Switching of ZrO 2 Based ReRAM Devices The Role of Interface and Exchange Processes in Forming and Switching of ZrO 2 Based ReRAM Devices*.
3. Bashir, A., Awan, T. I., Tehseen, A., Tahir, M. B. & Ijaz, M. Interfaces and surfaces. in *Chemistry of Nanomaterials: Fundamentals and Applications* 51–87 (Elsevier, 2020). doi:10.1016/B978-0-12-818908-5.00003-2.
4. Reddy, T. B. *LINDEN'S HANDBOOK OF BATTERIES*. (McGraw Hill, 2011).
5. Kok, J. G. M. Fixed bending current for Elekta SL25 linear accelerators. *J Med Eng Technol* **25**, 169–172 (2001).
6. Garrett, R. *SRI 2009 : The 10th International Conference on Synchrotron Radiation Instrumentation, Melbourne, Australia, 27 September-2 October 2009*. (American Institute of Physics, 2010).
7. Materlik, G., Rayment, T. & Stuart, D. I. Diamond Light Source: Status and perspectives. *Philosophical Transactions of the Royal Society A: Mathematical, Physical and Engineering Sciences* vol. 373 Preprint at https://doi.org/10.1098/rsta.2013.0161 (2015).
8. Iglesias-Juez, A., Chiarello, G. L., Patience, G. S. & Guerrero-Pérez, M. O. Experimental methods in chemical engineering: X-ray absorption spectroscopy—XAS, XANES, EXAFS. *Canadian Journal of Chemical Engineering* vol. 100 3–22 Preprint at https://doi.org/10.1002/cjce.24291 (2022).
9. Yano, J. & Yachandra, V. K. X-ray absorption spectroscopy. *Photosynthesis Research* vol. 102 241–254 Preprint at https://doi.org/10.1007/s11120-009-9473-8 (2009).
10. Jark, W. An efficient plane-grating monochromator based on conical diffraction for continuous tuning in the entire soft X-ray range including tender X-rays (2-8keV). in *Journal of Synchrotron Radiation* vol. 23 187–195 (International Union of Crystallography, 2016).
11. Favaro, M. *et al.* Spectroscopic analysis with tender X-rays: SpAnTeX, a new AP-HAXPES end-station at BESSY II. *Surf Sci* **713**, (2021).
12. de Groot, F. M. F. *et al.* 2p x-ray absorption spectroscopy of 3d transition metal systems. *Journal of Electron Spectroscopy and Related Phenomena* vol. 249 Preprint at https://doi.org/10.1016/j.elspec.2021.147061 (2021).
13. Frati, F., Hunault, M. O. J. Y. & De Groot, F. M. F. Oxygen K-edge X-ray Absorption Spectra. *Chemical Reviews* vol. 120 4056–4110 Preprint at https://doi.org/10.1021/acs.chemrev.9b00439 (2020).
14. Penner-Hahn, J. E. *X-Ray Absorption Spectroscopy*.
15. Shrivastava, B. D. *X-Ray Absorption Fine Structure (XAFS) Spectroscopy-A Review*. https://www.researchgate.net/publication/261190183.
16. Gaur, A., Shrivastava, B. D. & Nigam, H. L. *X-Ray Absorption Fine Structure (XAFS) Spectroscopy-A Review*. *Proc Indian Natn Sci Acad* vol. 79 (2013).

17. Koningsberger, D. C., Mojet, B. L., Van Dorssen, G. E. & Ramaker, D. E. *XAFS Spectroscopy; Fundamental Principles and Data Analysis*. *Topics in Catalysis* vol. 10 (2000).

18. Fadley, C. S. X-ray photoelectron spectroscopy: Progress and perspectives. *J Electron Spectros Relat Phenomena* **178–179**, 2–32 (2010).

19. Hofmann, S. *Auger-and X-Ray Photoelectron Spectroscopy in Materials Science A User-Oriented Guide*. (2013).

20. Bagus, P. S., Ilton, E. S. & Nelin, C. J. The interpretation of XPS spectra: Insights into materials properties. *Surface Science Reports* vol. 68 273–304 Preprint at https://doi.org/10.1016/j.surfrep.2013.03.001 (2013).

21. Seah, M. P. & Dench, W. A. Quantitative electron spectroscopy of surfaces: A standard data base for electron inelastic mean free paths in solids. *Surface and Interface Analysis* **1**, 2–11 (1979).

22. Johannson, H., Knoll, ; M, Zworykin, F. G. ; V. K., Knoll U, ; M & Lubszynski, . G. *Houtermans u. W. Sehulze, ZS. f. Phys. 78, 340, 1932. 3) Hi. Knoll u. E. Ruska, Ann. d. Phys. 12, 607, 1932. ~)*. *Journ. Frankl. Inst* vol. 20 (1932).

23. Locatelli, A. & Bauer, E. Recent advances in chemical and magnetic imaging of surfaces and interfaces by XPEEM. *Journal of Physics Condensed Matter* **20**, (2008).

24. Qiu, C. *et al.* Resolving the Effect of Oxygen Vacancies on Co Nanostructures Using Soft XAS/X-PEEM. *ACS Catal* **12**, 9125–9134 (2022).

25. Zając, M. *et al.* The first experimental results from the 04BM (PEEM/XAS) beamline at Solaris. *Nucl Instrum Methods Phys Res B* **492**, 43–48 (2021).

26. Frazer, B. H., Gilbert, B., Sonderegger, B. R. & De Stasio, G. The probing depth of total electron yield in the sub-keV range: TEY-XAS and X-PEEM. *Surf Sci* **537**, 161–167 (2003).

27. Locatelli, A., Aballe, L., Mentes, T. O., Kiskinova, M. & Bauer, E. Photoemission electron microscopy with chemical sensitivity: SPELEEM methods and applications. in *Surface and Interface Analysis* vol. 38 1554–1557 (2006).

28. Schmidt, T. *et al.* Speleem: Combining leem and spectroscopic imaging. *Surface Review and Letters* **5**, 1287–1296 (1998).

29. Renault, O. High-resolution XPS spectromicroscopy. in *Surface and Interface Analysis* vol. 42 816–825 (2010).

30. Rayleigh. XXXI. Investigations in optics, with special reference to the spectroscope . *The London, Edinburgh, and Dublin Philosophical Magazine and Journal of Science* **8**, 261–274 (1879).

31. Booth, M. J. *Adaptive Optics for Microscopy*. (2020).

Chapter 3 - Spatiochemical Mapping of Transition Metal Dissolution Pathways on NMC811 using High-Resolution X-ray Photoelectron Microscopy

Abstract

Nickel-rich $LiNi_{0.8}Mn_{0.1}Co_{0.1}O_2$ (NMC811) cathode materials hold promise for high-energy-density and cost-effective battery technologies compared to traditional lithium cobalt oxide counterparts. However, the elevated nickel content in NMC811 is associated with accelerated degradation, limiting the battery's cycle life and performance. Here, we employ spatially resolved synchrotron source X-ray photoemission electron microscopy (XPEEM) to elucidate the spatial distribution of degradation products forming the cathode electrolyte interphase (CEI) and to investigate the evolution of oxidation states of transition metals near the particle surface of polycrystalline (PC)NMC811. This characterisation sheds light on the particle to particle variation in degradation mechanisms within the electrode, providing crucial insights into the origins of transition metal dissolution from cathode particle surfaces.

Introduction

To encourage wider adoption and uptake of electric vehicles significant improvements to battery capacity, cost and cycle life are required. Enhancing the energy density of Lithium-ion batteries (LIBs) involves increasing the cells' specific capacity and average discharge potential. Meanwhile, calendar and cycle life hinges on the structural stability of the active electrode materials and mitigating parasitic reactions within the cell. Lithium-ion cells utilising LCO as the cathode active material can access relatively modest practical capacities (~140mAh g-1) when operating at safe upper cut-off potentials of 4.2 V vs Li/Li^+.[1] However, lithium extraction is limited to $Li_{0.3}CoO_2$ to avoid the detrimental phase transformation O3 – H1-3 – O1 when charged above 4.45 V. This high state of charge can cause oxygen vacancies, generating more parasitic reactions at the cathode electrolyte interface.[2]

Nickel-rich $LiNi_{0.8}Mn_{0.1}Co_{0.1}O_2$ (NMC811) is a promising cathode material providing high energy density and low-cost benefits over conventional cathode materials such as lithium cobalt oxide.[3–5] NMC811 maintains the same layered rhombohedral structure as LCO. However, it delivers a higher specific capacity of 200 mAh g^{-1} at an average discharge potential of ∼3.8 V (vs Li/Li^+) by replacing the Co cations with Ni cations as the primary site of redox activity.[6,7] The substitution of Co for Ni and Mn boosts practical capacity, albeit at the expense of thermal stability, particularly noticeable in Nickel-rich NMC variants. The Co content and favourable kinetics, exhibiting electronic conductivity at approximately 2.8×10^{-5} S cm^{-1} and Li^+ diffusivity ranging from 10^{-8} to 10^{-9} cm^2 s^{-1} position Nickel-rich NMCs as highly desirable cathode materials for advanced lithium-ion batteries.[8] Higher capacities are only accessible for NMC811 if higher cutoff voltages are applied (>4.3 V). However, for NMC811, the surface

reactivity and electrolyte stability at high voltages are crucial because they can cause interfacial degradation, such as oxygen release, formation of a reduced surface layer, and transition metal dissolution.[9–11]

Extended cycling at high voltages (>4.3V) is often linked to increased transition metal (TM) dissolution from the cathode material.[9,10] These TM species migrate through the electrolyte and deposit onto the anode's solid electrolyte interphase (SEI) layer. Out of Ni, Mn and Co metal ions, Mn species are believed to be primarily responsible for ongoing electrolyte solvent reduction at the anode, potentially behaving as an electrocatalyst promoting further SEI growth.[12] The dissolution of manganese (Mn) in cathode materials is widely attributed to the disproportionation reaction of Mn^{3+} ions in acidic environments ($2Mn^{3+} \leftrightarrow Mn^{4+} + Mn^{2+}$), resulting in soluble Mn^{2+} species in the electrolyte.[13,14] However, in high-nickel content NMC811 cathodes, significant deposition of nickel (Ni) species onto the anode SEI layer occurs, yet the impact of Ni dissolution remains poorly understood.[11] Other dissolution mechanisms may involve protic species causing etching,[15] oxygen loss by-products,[16] and transition metal extraction via heterogeneous catalytic chelating ligands.[17] Electrolyte oxidation can reduce transition metals at the surface of the cathode particle forming spinel Me_3O_4 and rocksalt MeO (Me = Ni, Mn or Co). [16] Due to their higher solubility in the common organic solvents used in electrolytes, the dissolved transition metal ions in LIB are likely to be lower valence species, such as Ni^{2+}, Mn^{2+}, and Co^{2+}.[18–21] Historically, significant attention has been devoted to understanding the dissolution process of Mn ions from cathode materials. Tarascons group posited that Mn^{2+} is the predominant dissolved Mn species in LIB electrolytes, a hypothesis grounded in the behaviour of Mn cations in aqueous solutions.[22] However, some findings contradict this viewpoint, suggesting that the dissolved manganese is primarily in the +3

oxidation state, not +2.[23,24] Determining the oxidation states of dissolved transition metal ions is key to revealing likely dissolution mechanisms.

In this chapter, surface regions of individual NMC811 particles were measured using XPEEM, showcasing its efficacy in tracking surface degradation on cycled electrodes and providing spatiochemical measurements at nanoscale resolution. By targeting the metal L- and O K-edges with soft X-rays, we gain insights into the electronic structure of NMC811 particle surfaces. While XPEEM has previously been used to examine electrode surfaces,[25–31] this study focuses on probing individual particles on the same electrode, allowing for comparing different regions on the electrode surface. Additionally, novel XPS imaging of a secondary NMC811 particle was developed as part of this project, providing valuable information on the CEI of the NMC811 particle.

Experimental Methods

Scanning electron microscopy

The particle morphology and structural changes of the NMC811 electrodes before and after compression were analysed by scanning electron microscopy (SEM). SEM imaging was carried out using Zeiss Merlin scanning electron microscope using an airtight transfer device (Gatan). Imaging data were acquired with an electron beam at 2 kV using the in-lens detector to collect the measurements.

Near Edge X-ray Absorption Fine Structure (NEXAFS)

NEXAFS measurements were conducted at the I09 beamline of Diamond Light Source. Spectra were obtained by dividing the sample's drain current by the incident photon flux from the

mirror current, resulting in total electron yield (TEY). Energy calibration of NMC electrode spectra was based on literature-reported transition-metal edges.[32] Straight-line background subtraction was performed before the L_3 edge, and spectra were normalised to a post-edge region after the L_2 edge. Similar processing was applied to the O K-edge, with pre-resonance background subtraction followed by post-edge normalisation at 550 eV.

X-ray Photoemission Electron Microscopy (XPEEM)

XPEEM measurements were conducted on cycled NMC811 electrodes at the I06 beamline, Diamond Light Source, utilising soft X-rays with excitation energies of 0.5-1 keV. This approach provided high lateral resolution (~70 nm) and a probing depth of ~5 nm for spatiochemical information. Electrodes were disassembled in an Ar-filled glovebox (O_2 < 0.1 ppm and H_2O < 0.1 ppm), and then mounted onto the PEEM sample holder. The samples were then transferred to the I06 beamline endstation using a UHV transfer suitcase sealed with a gate valve. The photoemission imaging and near edge x-ray absorption fine structure (NEXAFS) imaging were performed in ultrahigh vacuum (~5 x 10^{-10} mbar) with a 25 µm field of view. Secondary photoelectrons were collected and accelerated by a high voltage (>15 kV) towards the double hemispherical analyser.

The incident photon energy was tuned to probe the Ni L-, Mn L- and Co L- edge and the O K-edge, scanning across the respective resonance whilst recording an image at energy step using linearly polarised light. Valence state contrast maps were generated by pixel-wise subtraction of two images obtained at different energies: one recorded at the resonance of the edge and the other at the pre-edge. These were normalised by an image slice on the post-edge to mitigate concentration effects.

XPEEM is a powerful characterisation technique for investigating material surfaces and interfaces. It offers insights into chemical states, electronic structures, and elemental composition. XPEEM measurements require a flat sample surface to maximise meaningful sample information. This is due to the following reasons:

- Spatial resolution: XPEEM's nanometer-scale spatial resolution requires flat surfaces, as irregularities or roughness can distort electron trajectories causing blurring.
- Depth of field: The depth of field determines the range of distances where objects appear sharp in an image or through a microscope. Higher-energy X-rays can increase the depth of field by penetrating deeper, but this can reduce spatial resolution and surface sensitivity.
- Space Charge Effects: Non-flat surfaces may give rise to space charge effects, manifesting as charge accumulation near irregularities (also known as arcing). These effects can alter electron trajectories, thereby influencing measured photoemission intensities.

These factors represent key considerations and challenges in obtaining meaningful XPEEM measurements, constituting a significant hurdle in characterising battery materials.

Electrode Materials and Preparation

Electrodes containing polycrystalline $LiNi_{0.8}Mn_{0.1}Co_{0.1}O_2$ (LiFun Technology, Hunan, China) were used as the cathode active material (CAM), with carbon black (C45 Sigma Aldrich) and poly(vinylidene fluoride) (PVDF, Kynar) used as the conductive additive (CA) and the binder respectively. A slurry containing a mix ratio of 80:10:10 (CAM:CA:binder) suspended in N-methyl-2-pyrolidone (NMP) with the solids making up 65% of the total mass of the slurry was

cast onto an aluminium foil and dispersed using a doctor blade with a coat weight of ~0.75mg cm^{-2}. The electrodes were dried at 80 ˚C overnight under a vacuum before being cut into 16mm diameter discs using an MTI electrode punch followed by cold pressing to make the electrodes flat.

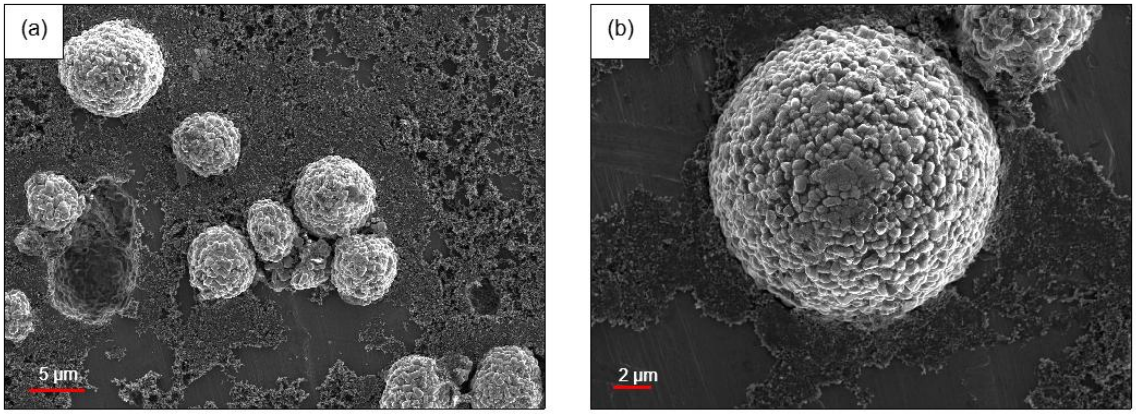

Figure 3.1. Polycrystalline NMC811 particles during different stages of electrode preparation (a) as-cast condition and (b) a representative sample after pressing (12.39 MPa).

Figure 3.1 shows representative examples of the morphology of NMC811 samples and the particle size ranging between 5-15 µm. The XPEEM instrument suffers from a small depth of focus, which can inhibit the spatial resolution in XPEEM. To ensure that the electrodes were compatible with XPEEM analysis, a pressing step was added to the electrode preparation during electrode fabrication. Pressing the electrodes plays a crucial role in commercial electrodes, improving the energy density of the electrode and the electrical contact between the particles and the current collector. An added benefit of XPEEM analysis is that the spatial resolution of the measurement is significantly enhanced when analysing a flat surface, whilst also preventing arcing. To press the electrodes, they were placed between two stainless steel blocks and pressed using a hydraulic press (MTI, America) applied a pressure of 12.39 MPa.

Figure 3.1a shows a pristine NMC811 particle before pressing, and Figure 3.1b shows an NMC811 particle after pressing. The NMC811 particle retains its spherical morphology.

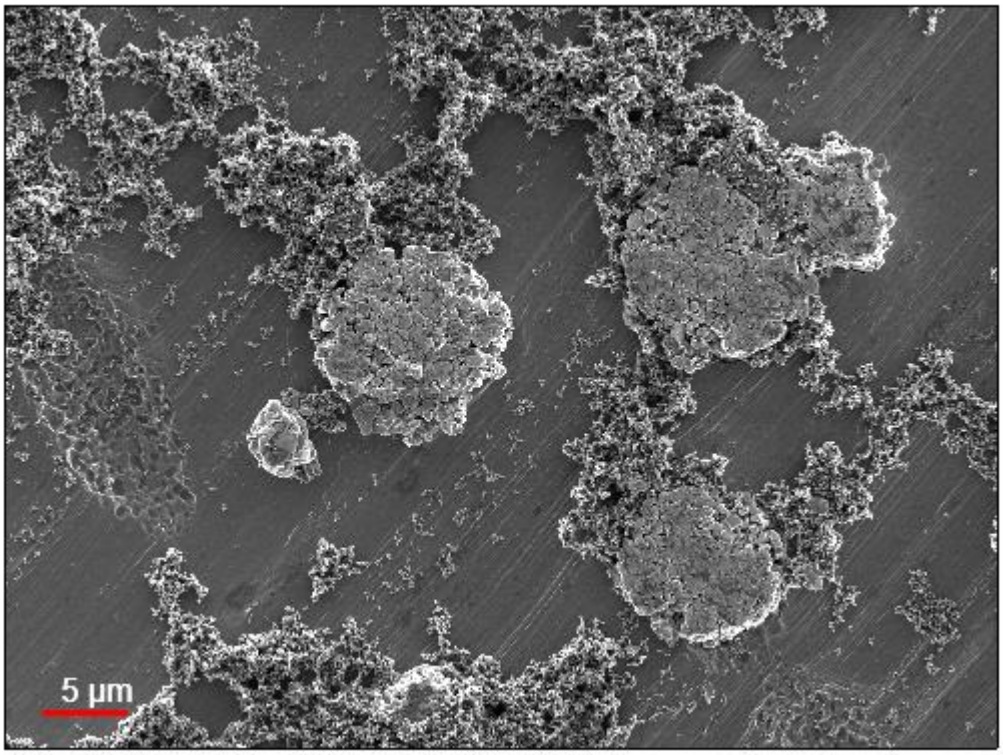

Figure 3.2. A scanning electron microscopy (SEM) image capturing an overpressed electrode (97.58 MPa), revealing mechanical damage to the surface of the NMC811 electrode.

Figure 3.2 displays SEM images of overpressing XPEEM-compatible electrodes, resulting in plastic deformation of cathode particles. In this example, a force of 2 tons (97.58 MPa) was applied to an electrode (2.01 cm^2). The secondary particles retain their spherical morphology with a flat surface conducive to XPEEM measurements. However, microcracks in the NMC811 particles become apparent. These microcracks may introduce degradation artefacts unrelated to electrochemical cycling, signifying potential mechanically induced surface reduction.[25] To avoid unwanted mechanical damage to the NMC811 particle, careful preparation of the electrodes is required, balancing the requirement of flat surfaces for XPEEM compatibility with the integrity of NMC811 particles.

Electrochemical Cycling

Coin cells were assembled in an Ar-filled glove box (O_2 <0.1ppm and H_2O <0.1ppm) using pressed (12.39 MPa) 16 mm diameter NMC811 electrodes as the working electrode and lithium metal discs as the counter electrode. Fibreglass and Celgard 2325 (NMC811 electrode interface) separators were wetted with LP57 electrolyte (1M $LiPF_6$ dissolved in EC:EMC (3:7, v:v)). The cells were rested for 5 hours before being galvanically cycled using a biologic WMP-3 at a 0.05C rate between 4.2 V and 3.0 V to form the CEI layer, followed by cycling between 4.4 V and 3.0 V at a C-rate of 0.2C for 20 cycles. After the cycling the coin cell was disassembled using a decrimper device inside an Ar-filled glovebox, subsequently the NMC811 electrode was then rinsed with dimethyl carbonate to remove any residual lithium salts and ethylene carbonate still present on the electrode surface.

Results

Electrochemical Cycling

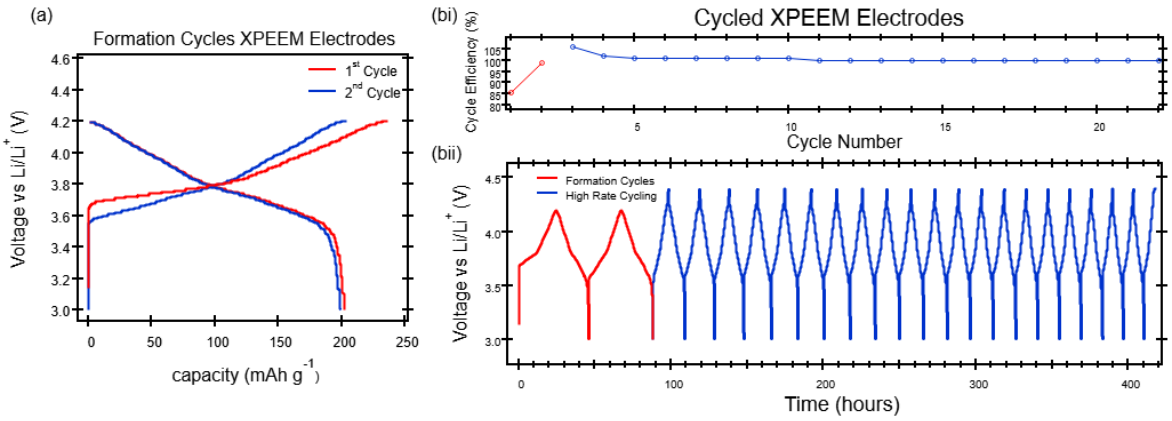

Figure 3.3. Panel a) Voltage capacity profiles for the formation cycles of the XPEEM coin cells containing LP57 electrolytes cycled between 3.0 V and 4.2 V. Panel bi) The electrochemical performance of XPEEM coin cells with lithium metal anode and pressed NMC811 cathode containing LP57 electrolyte and panel bii) displays the cycle efficiency.

Figure 3.3 presents the voltage vs. capacity profile of an NMC811/Li half-cell during the initial two formation cycles. The first charge profile displays a slight overpotential, likely associated with the removal of Li_2CO_3 on the NMC811 surface.[33] The first charge-discharge cycle demonstrates a cycle efficiency of 85.5%, while the subsequent formation cycle achieves a cycle efficiency of 98.9%, resulting in a discharge capacity of approximately ~200 mAh g^{-1}. The electrodes were further cycled for 20 cycles at higher C rates (0.1C) with an upper cutoff potential of 4.4 V to accelerate aging. Notably, a slight increase in cycle efficiency above 100% is observed after transitioning to cycling at higher potentials suggesting potential extra discharge capacity gained in the first high upper cutoff voltage (UCV) cycle, possibly due to surface reconstruction of the NMC811 particle surface[34] or further CEI growth.[35]

SEM

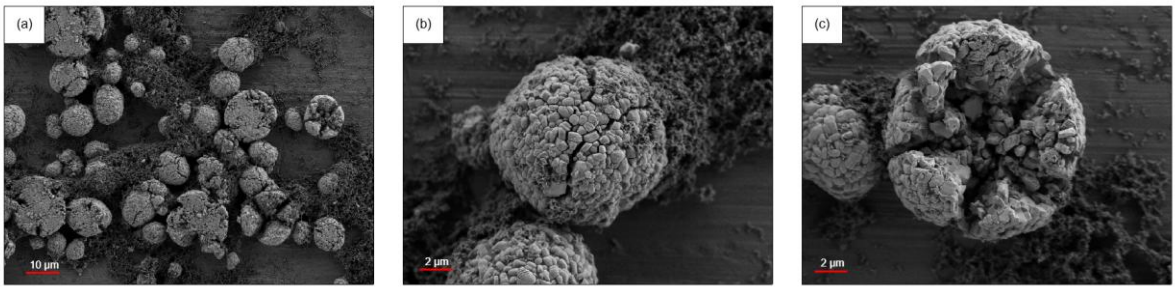

Figure 3.4. Scanning electron microscopy (SEM) of cycled NMC811 particles: (a) Variations in cracked particle morphology on the NMC811 electrode; (b) A higher magnification of a multi-prong crack (c) an enlarged view of a shattered multi-prong fractured particle.

Figure 3.4 depicts the representative morphology of cycled NMC811 XPEEM electrodes after 20 cycles at a high C rate (0.1 C) and high UCV (4.4 V), showcasing particles with sizes ranging from 5 to 15 µm and exhibiting varying degrees of particle cracking. SEM observations in panel b) reveal three-prong cracks on an NMC811 particle, while a neighbouring cathode particle in panel c) displays multifaceted shattering of an NMC811 particle. These distinct variations in

particle degradation underscore the imperative to develop a characterisation technique capable of probing diverse environments within an electrode.

NEXAFS Measurements

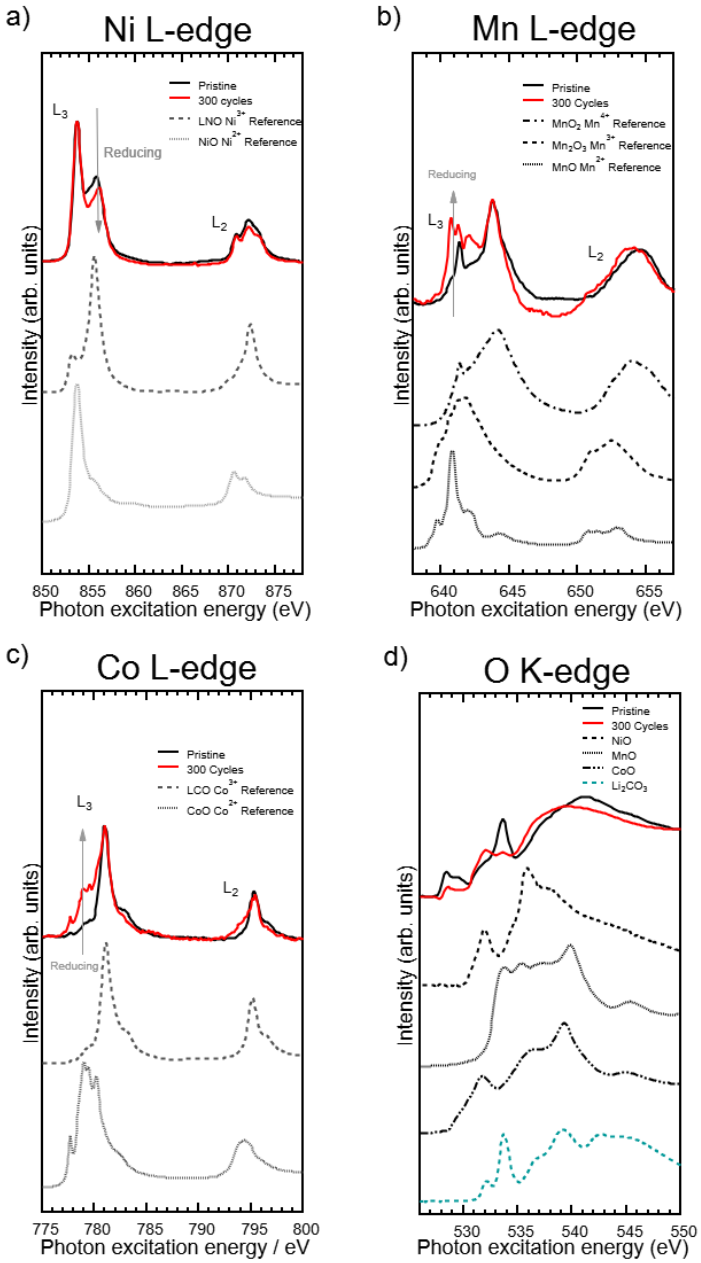

Figure 3.5. presents NEXAFS spectra of (a) Ni, (b) Mn, (c) Co L-edge, and (d) O K-edge for NMC electrodes in their pristine state and post-300 cycles from full cells NMC811 vs Graphite with potential range 3.0 V to 4.2 at a 0.5C rate with two formation cycles at a 0.05C rate in LP57 electrolyte with measured references. Partially replotted data from reference.[36]

Near edge x-ray absorption fine structure (NEXAFS) measurements were conducted in TEY-XAS mode on NMC811 electrodes, as depicted in Figure 3.5. The figure showcases the TM L-edges (Figures 5.5a-c) and the O K-edge (Figure 3.5d) of pristine NMC811 electrodes in black and after undergoing 300 cycles in red. Changes are observed in each spectrum, providing insights into the electrode's structural changes during electrochemically cycling at a fixed potential range 3.0 V to 4.2 at a 0.5C rate with two formation cycles at a 0.05C rate in LP57 electrolyte using LiFun graphite as a counter electrode. Beginning with the Ni L-edge characterised by a distinct doublet feature on the L_3 edge, the higher energy peak diminishes after 300 cycles relative to the pristine electrode. This indicates a reduction of Ni^{3+} to Ni^{2+} near the surface of the electrode.[37,38] Moving to Figures 3.5b and 3.5c, both the Mn L-edge and Co L-edge reveal a +4 oxidation state for Mn and a +3 oxidation state for Co respectively on the surface of pristine electrodes indicating Mn and Co are not reduced. [39,40] Upon cycling, a low-energy peak emerges on both L_3 edges, indicating a surface reduction of Mn and Co in the NMC811 electrode highlighted by the arrow in Figure 3.5b-c.[41] Additionally there is a slight broadening of the L_2 feature to a lower energy corroborating the surface reduction of Mn and Co at the surface. Although Mn and Co exhibit more oxidised states on the surface than Ni, the changes in their oxidation states during cycling are noticeable indicating a trend towards spinel and/or rocksalt phase on the surface. The O K-edge spectra in Figure 3.5d showcase the pristine NMC811 electrode exhibiting distinct features at ~529 eV and ~530 eV, attributed to O 1s core electron excitations into the hybridised TM 3d-O 2p orbitals, herein referred to as lattice oxygen peaks. At higher energies (~534 eV), a peak attributed to surface carbonates is observed, likely Li_2CO_3 formed due to trace moisture and CO_2 reactions during glove box storage.[42,43] After 300 cycles, a reduction in the intensity of lattice oxygen peaks and Li_2CO_3 is observed compared to the pristine NMC811 electrode. A new peak at 532 eV emerges,

attributed to the formation of a reduced surface layer comprising NiO, CoO, and possibly MnO. The weak orbital splitting of MnO, not evident in O K-edge measurements, may contribute some intensity at 534 eV along with some carbonate species.[44] While NEXAFS measurements offer detailed characterisations of the cathode's surface, they represent averaged data across tens or hundreds of particles illuminated by X-rays. In contrast, XPEEM provides equivalent information but with remarkable spatiochemical resolution. This enables the visualisation of chemical heterogeneity on the cathode surface, offering invaluable insights into local chemical environments and reactions.

XAS Contrast Images

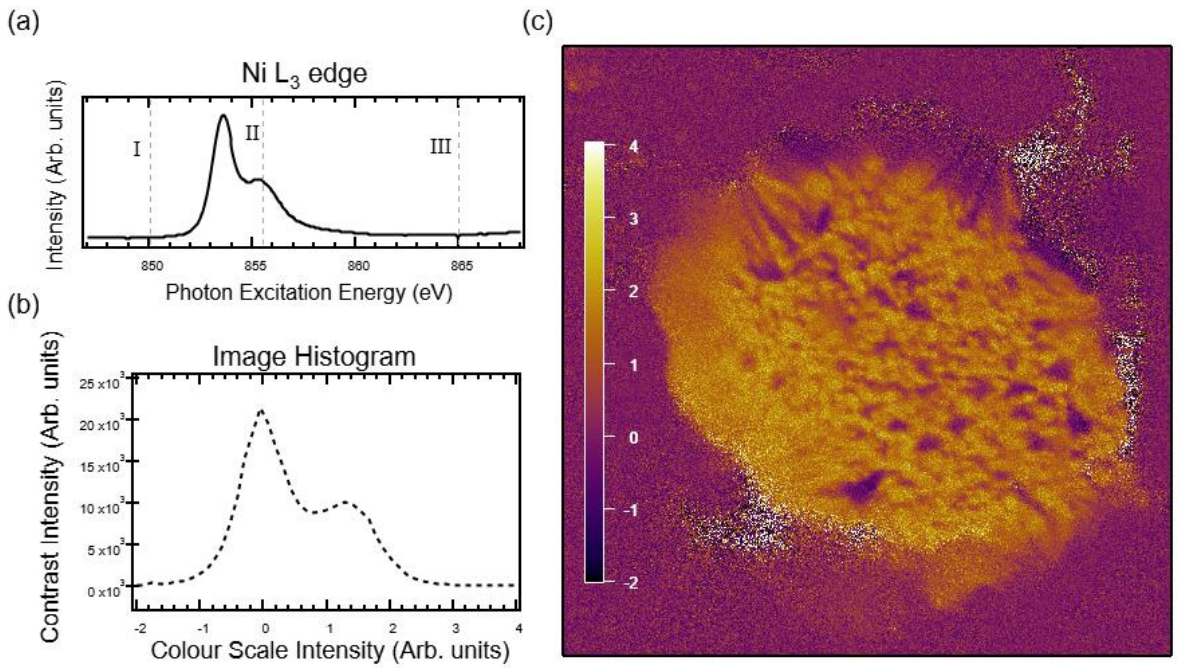

Figure 3.6 The contrast mechanism utilised for generating region-of-interest maps is illustrated with panel (a) showing the Ni L3 edge accompanied by image slices contributing to the formation of the contrast image, explicitly highlighting the background (I), edge resonance (II), and post-edge region (III). Additionally, (b) presents a histogram derived from the contrast map showcased in panel (c).

In order to create contrast images in XPEEM, spectra are generated by integrating a selected region on the particle. The first step is to create a large region of interest for the entire particle

using the XPEEM plotting software developed as part of this project. The integration over all the excitation energies yields a spectra average of all the pixels in the selected region, forming the XAS spectra. It is also possible to create regions on the NMC particles based on the chemical inhomogeneity of the surface. Here an example of the Ni L_3 edge is used to generate regions with different oxidation states of Nickel. In Figure 3.6a, focused on the Ni L_3 edge, notable changes at ~855.6 eV indicate variations in Ni^{3+} and Ni^{2+} oxidation states. An image slice at 855.6 eV, background subtracted to a point below the edge resonance (850 eV), and normalised above the Ni L_3 edge (865 eV) constitute the subtracted spectra, similar to standard XAS normalisation procedures using the formula below to give a contrast image like the one shown in Figure 3.6c:

$$Contrast\ Image\ (CI) = \frac{(II-I)}{(III-I)} \qquad [3.1]$$

The histogram of the contrast image in Figure 3.6b reveals bimodal distribution of the oxidation state of Ni in the NMC811 particle, enabling the creation of region-of-interest maps by constraining the intensity scale. These maps are then integrated through all excitation energies to generate XAS spectra related to the intensity changes based on oxidation state changes in the Ni L-edge. Image slices were selected for Mn L-edge and Co L-edge based on intensity changes observed in Figure 3.5. Specifically, an image slice was chosen at ~642 eV for the Mn L-edge, with a background image slice interpolated at 635 eV and a post-edge image slice at 647 eV. For the Co L-edge, an image slice was selected at ~785 eV, accompanied by a background image slice at 778.5 eV and a post-edge image slice at 787 eV as depicted in Figure 3.7.

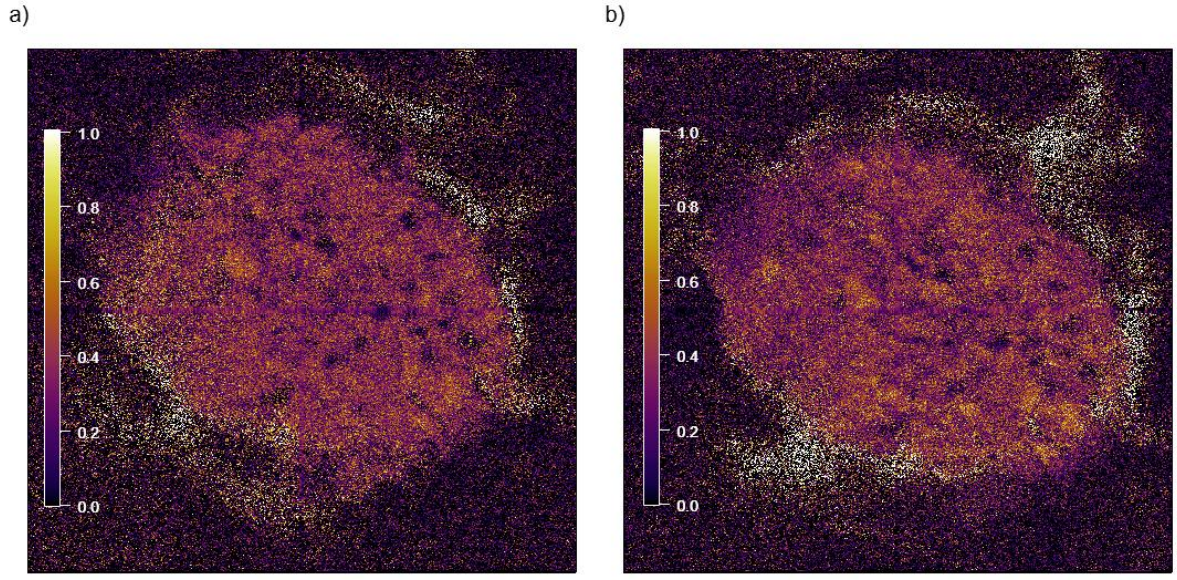

Figure 3.7. The contrast mechanism for (a) Mn, illustrated with image slices at 635 eV, 642 eV, and 647 eV, and (b) Co, depicted with image slices at 778.5 eV, 785 eV, and 787 eV.

In photoelectron microscopy, an energy-dispersive scan of the sample was conducted initially to obtain spectra of the chemical species on the particle. In μ-XPS, a photon beam with fixed energy is used, incorporating a variable bandpass filter. The microscope's last lenses project the filter's dispersive plane directly onto the detector. The resulting dispersive plane images show straight lines with varying contrast, representing different binding energies and signal intensities of dispersed photoemitted electrons. Each point on the line corresponds to a specific binding energy and signal intensity, indicated by horizontal position and brightness, respectively. Integrating a line profile from a dispersive plane image generates a photoemission spectrum for the specified energy window, similar to conventional XPS.

For photoelectron images, peak positions were determined by adjusting the starter voltage to align with peak maxima, and photoelectrons were collected by the Medipix detector. In order to mitigate beam drift during measurements, the sample was scanned three times for ten minutes, and the resulting images were averaged with drift correction applied to ensure pixel alignment across all three scans.

Regions of Interest

XPEEM measurements of the 3d TM (Ni, Mn,Co) L-edges and the O K edge were used to resolve the heterogeneity of degradation behaviour spatially after electrochemical cycling across the NMC811 electrode (4.4 V vs Li/Li^+ after 20 cycles). Three distinct spot positions (referred to as particle one, two and three) were examined with TEY XAS mode XPEEM. The first position was also investigated with novel XPS microscopy measurements, providing high-resolution spatial information about chemical species formed on the CEI.

XAS of Secondary NMC811 Particle One

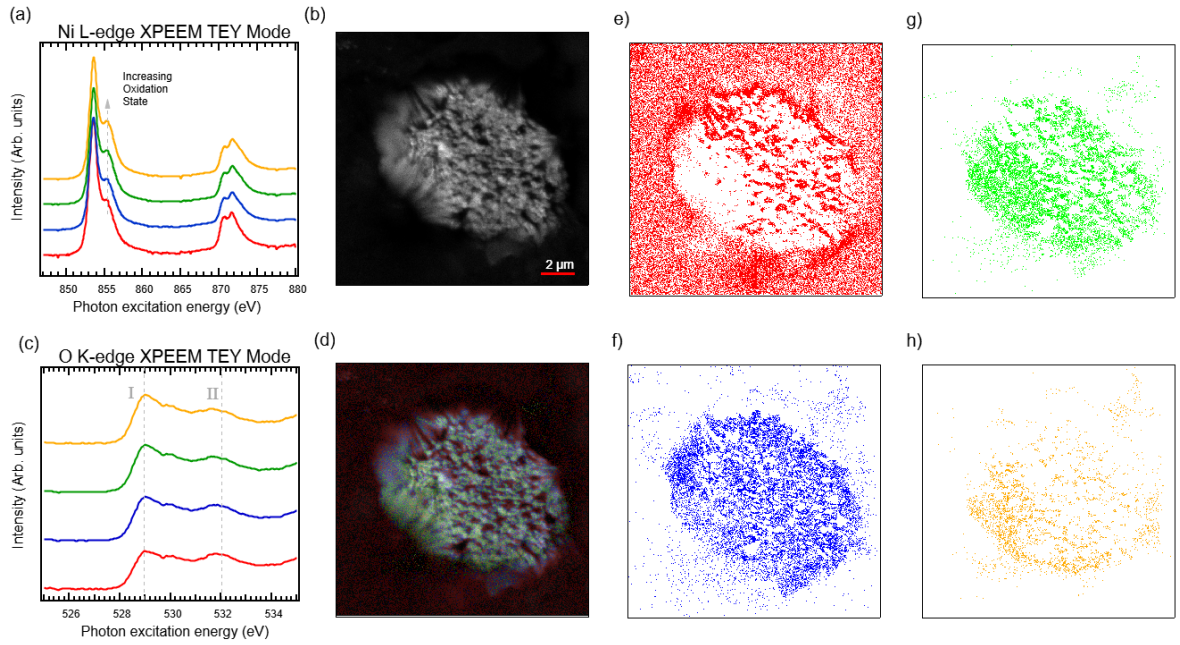

Figure 3.8. X-ray Photoemission Electron Microscopy (XPEEM) analysis of a charged NMC811 particle one. Panel (a) exhibits the Ni L-edge mapped regions on the NMC811 particle, (b) electron map of electron intensity collected at 855.26 eV. (c) Distribution of the O K-edge, (d) A colour map of the Ni L-edge and O K-edge regions integrated throughout the image stack. (e) corresponds to the red spectra, (f) corresponds to the blue spectra, (g) corresponds to the green spectra and (h) corresponds to the orange spectra.

Figure 3.8 presents TEY XPEEM measurements elucidating the structural and chemical characteristics of Ni L-edge and O K-edge spectra extracted from secondary particle one within

NMC811 electrodes, observed in a delithiated state (4.4 V vs Li/Li^+). Panel (a) displays the Ni L edge spectra extracted from and matched to the colour-coded regions, as shown in panel (d). Panel (b) displays an electron yield image interpolated from the image stack at 855.3 eV, providing an image of particle one. Complementing the Ni L-edge analysis, panel (c) presents the O K edge spectra extracted from analogous regions of the Ni L-edge analysis, with corresponding colours matching the highlighted areas depicted in panel (d-h).

The region at low photon energy, referred to as the L_3 edge, corresponds to the transition from $2p_{3/2}$ to unoccupied 3d states, while the other feature located at high photon energy (10–15 eV separation from the L_3 features) is referred to as the L_2 edge, corresponding to the transition from $2p_{1/2}$.[45] The L_3 region can be used to analyse the oxidation state of the Ni throughout the particle. The removal of lithium usually increases the oxidation state of Ni^{2+} to Ni^{3+}/Ni^{4+} to facilitate charge compensation.[32,46,47] Four distinct regions of the NMC811 particle were analysed using the XPEEM analysis software developed in igor Pro 8 (see appendix). The four regions indicate reduced Ni across all regions of the particle surface. Due to XPEEM's ability to visualise the distribution of reduced Ni on the NMC811, we can see that the main sites for Ni reduction on the particle occur around the primary particle equator and clusters close to any voids (dark regions). The reduced surface layer is further confirmed when the O K edge spectra are taken into account with the feature labelled II at 532 eV related to the presence of a reduced surface layer. The 529 eV feature observed in the O K edge spectrum arises from the transition of oxygen core electrons to the 2p oxygen level, which undergoes hybridisation with 3d transition metal bands[48] and will be discussed in more detail in the discussion section of this chapter.

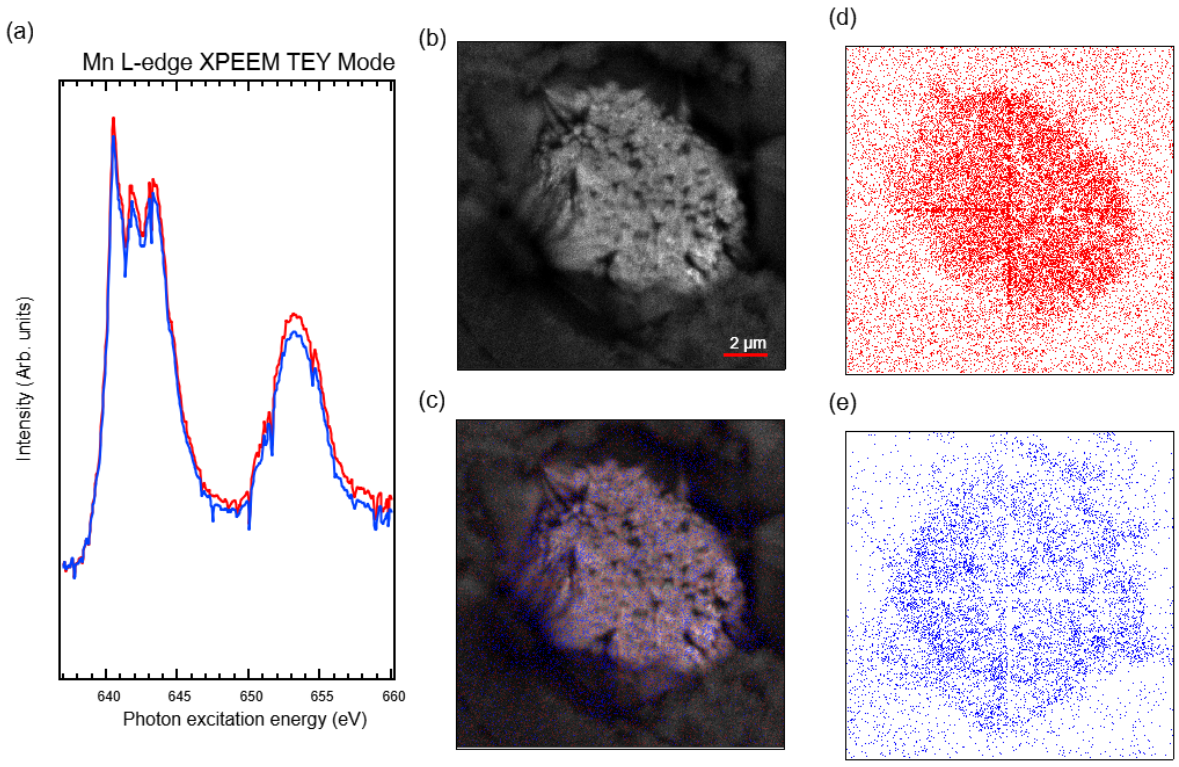

Figure 3.9. X-ray Photoemission Electron Microscopy (XPEEM) analysis of a charged NMC811 particle one. (a) Mn L-edge spectra of the mapped regions on the NMC811 particle. (b) the electron map of electron intensity collected at 642 eV. (c) The distribution of the Mn L-edge regions colour matched to the spectra, (d) corresponds to the red spectra and (e) corresponds to the blue spectra.

TEY XPEEM measurements of the Mn L edge within NMC811 secondary particle one, in a delithiated state (4.4 V vs Li/Li^+), are presented in Figure 3.9. Panel (a) showcases the Mn L edge spectra extracted and correspondingly matched to colour-coded regions shown in panel (c-e), offering insights into the spatial distribution of manganese species within the sample. Complementing this analysis, panel (b) presents an electron yield image interpolated from the image stack at 642 eV. Analysis reveals a distribution of Mn oxidation states within the NMC811 particle, encompassing Mn^{2+}, Mn^{3+}, and Mn^{4+} species.[49,50]

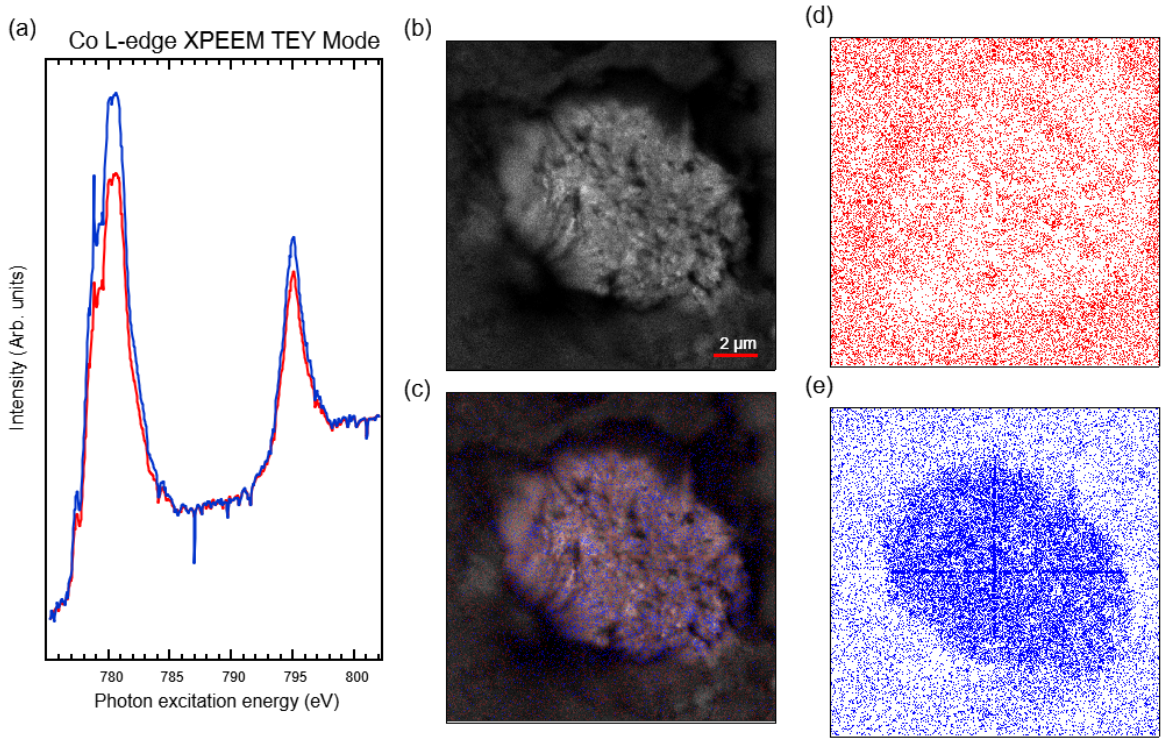

Figure 3.10. X-ray Photoemission Electron Microscopy (XPEEM) analysis of a charged NMC811 particle spot one. (a) the Co L-edge spectra of the mapped regions on the NMC811 particle, (b) the electron map of electron intensity collected at 778.5 eV. (c) The distribution of the Co L-edge regions colour matched to the spectra, (d) corresponds to the red spectra and (e) corresponds to the blue spectra.

Similar to the Mn distribution, there is a weaker signal from the Co compared to the Ni signal. Our observations reveal a relatively homogeneous distribution of cobalt species across the surface of the NMC811 particle. Cobalt's predominant oxidation state is identified as a mix of Co^{2+}/Co^{3+}.[40] The emergence of features at 778 eV and 779 eV, indicate the emergence of more reduced cobalt (Co^{2+}) species on the NMC811 electrode material.

XPS of Secondary NMC811 Particle One

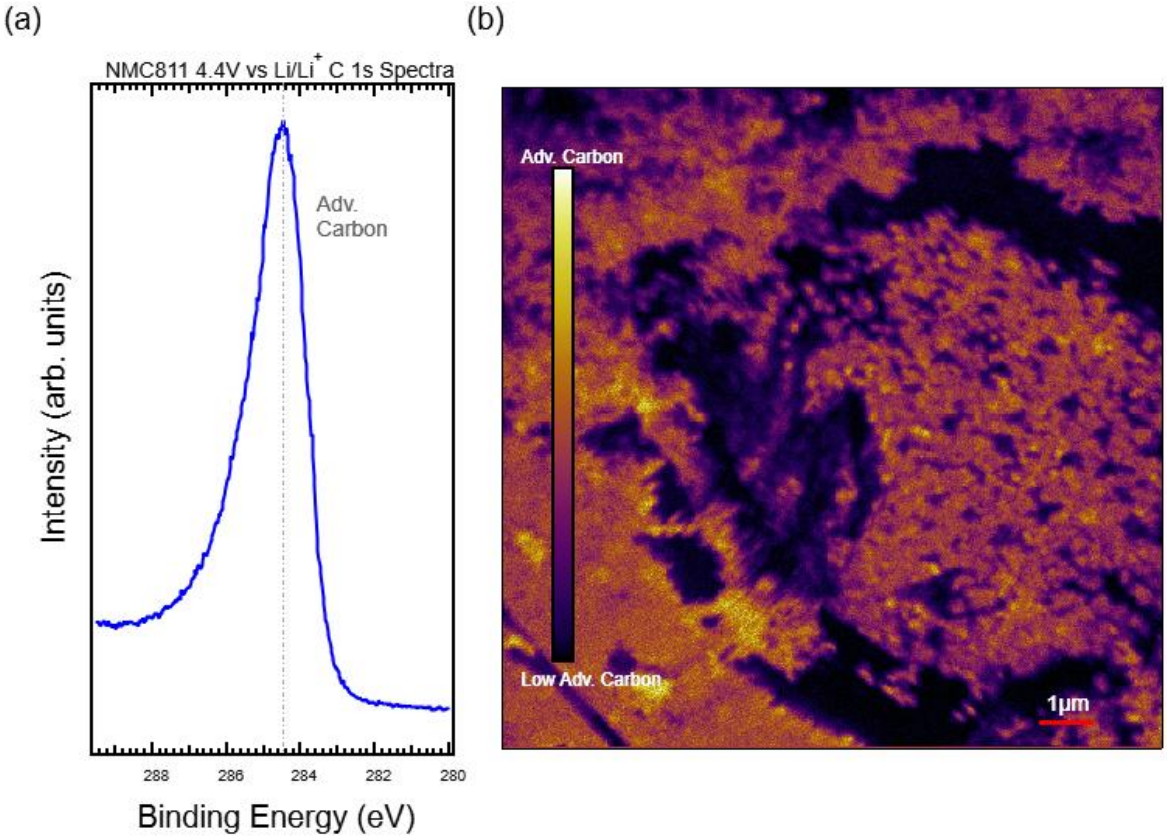

Figure 3.11. (a) Energy dispersion spectrum for the C 1s core level and (b) the XPS image at 285 eV.

Figure 3.11a showcases the energy dispersion spectra of the C 1s core level, collected using the XPEEM instrument. The spectra reveal a prominent peak at 284.5 eV, attributed to adventitious carbon present on the cathode surface.[51] Subsequent core level spectra were energy-calibrated to this reference point. Additionally, Figure 3.11b presents the corresponding XPS image of photoelectrons collected with the XPEEM instrument at a fixed incident energy of 378.5 eV. These measurements were performed with an objective lens current of 1440 mA at 15 kV, and the contrast aperture was set to 70 µm, resulting in a probing depth of 3-4 nm, depending on the core-level energy.

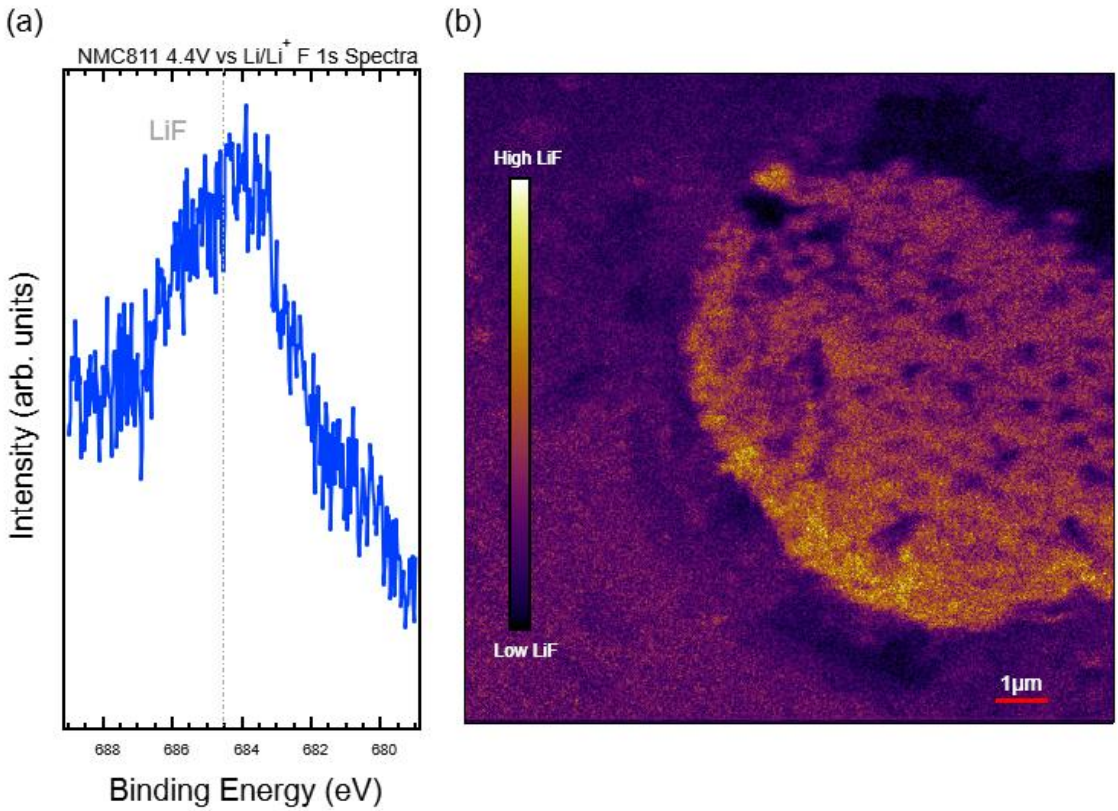

Figure 3.12. (a) Energy dispersion spectrum for the F 1s core level and (b) the XPS image at 685 eV.

Figure 3.12a presents the energy dispersion spectra of the F 1s core level acquired using an excitation energy of 778.98 eV and a starting voltage of 89.58 V. The F 1s spectra exhibit a main feature at 684.5 eV, attributed to LiF.[52,53] The signal intensity is relatively weak, likely due to LiF being buried under the CEI. Figure 3.11b depicts the corresponding XPS image of photoelectrons collected with the XPEEM instrument. Interestingly, the LiF signal intensity is greatest near the bottom region of the particle and particularly intense around the edge of the secondary particles overlapping with the slightly more oxidised regions of the NMC particle as shown in figure 3.8h.

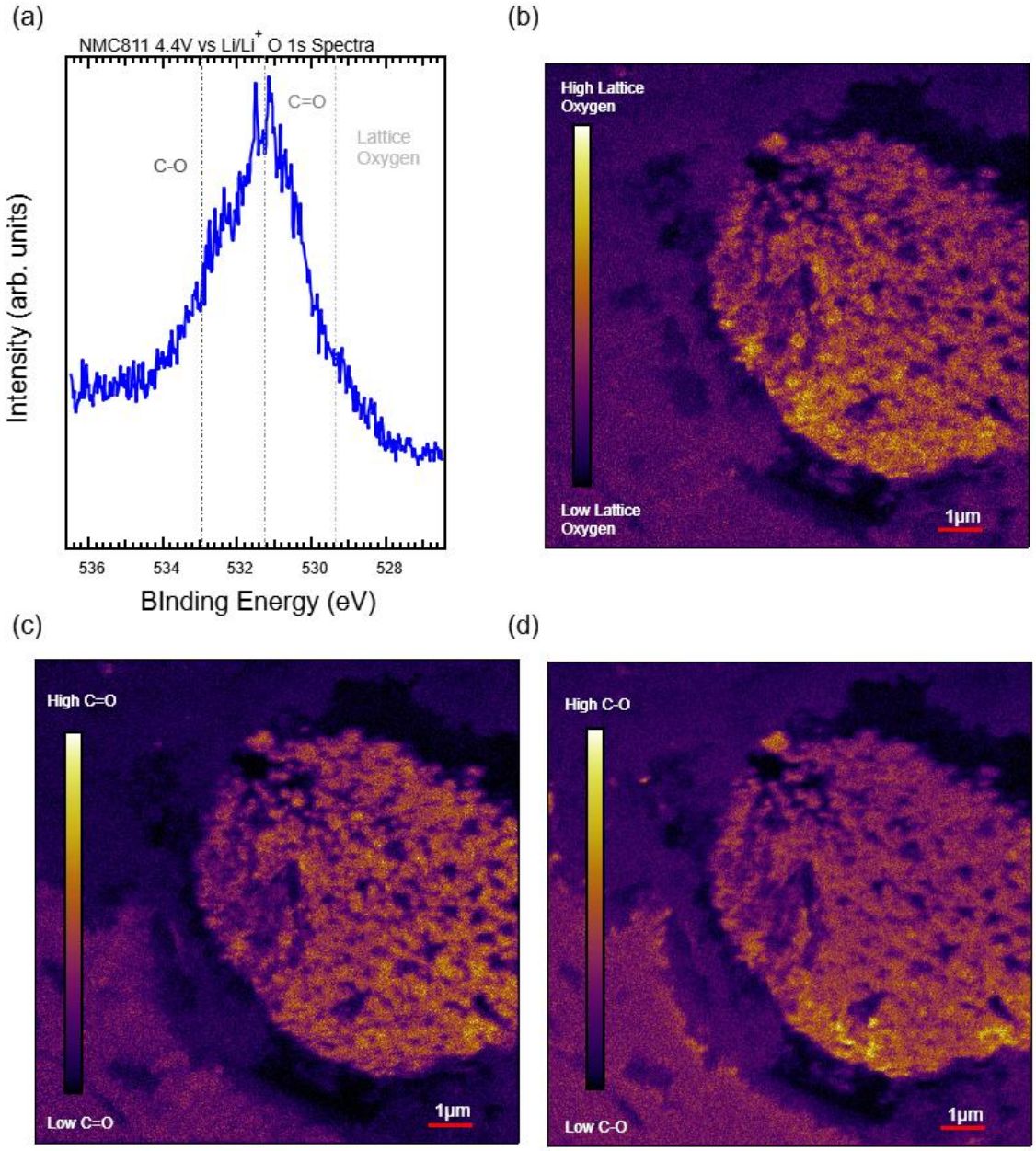

Figure 3.13. (a) the energy dispersion spectrum for the O 1s core level and (b) the XPS image at 529.8 eV, (c) the XPS image at 531.5eV and (d) the XPS image at 533.1 eV.

Figure 3.13a displays the energy dispersion spectra of the O 1s core level, obtained using an excitation energy of 620 eV and varying starting voltages for different peaks: 86.4 V (lattice oxygen peak), 84.6 V (C=O peak), and 83 V (polyether peak). The O 1s spectra reveal a prominent feature at 529.4 eV attributed to lattice oxygen,[54,55] 531.2 eV attributed to C=O[56,57] and a peak at 533 eV attributed to C-O.[56–58]

XAS of Secondary NMC811 Particle Two

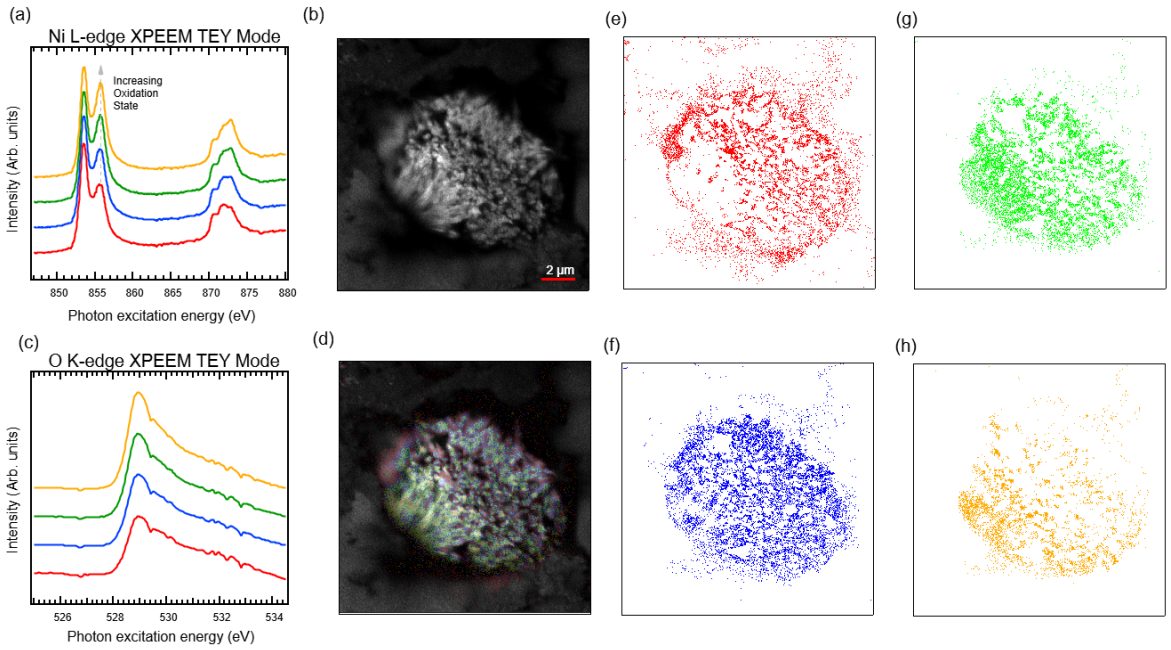

Figure 3. 14. X-ray Photoemission Electron Microscopy (XPEEM) analysis of a charged NMC811 particle spot two. (a) Ni L-edge mapped regions on the NMC811 particle, (b) map of electron intensity collected at 855.3 eV. Panel (c) showcases the distribution of the O K-edge mapped regions (d) colour map of the Ni L-edge and O K-edge regions integrated throughout the image stack, (e) corresponds to the red spectra, (f) corresponds to the blue spectra, (g) corresponds to the green spectra and (h) corresponds to the orange spectra.

Figure 3.14 presents TEY XPEEM measurements elucidating the structural and chemical characteristics of Ni L-edge and O K-edge spectra extracted from secondary particle two within NMC811 electrodes, observed in a delithiated state (4.4 V vs Li/Li^+). Panel (a) displays the Ni L-edge spectra extracted from and matched to the colour-coded regions, as shown in panel (d). Panel (b) displays an electron yield image interpolated from the image stack at 855.3 eV, providing an image of particle two. Complementing the Ni L-edge analysis, panel (c) presents the O K-edge spectra extracted from analogous regions of the Ni L-edge analysis, with corresponding colours matching the highlighted areas depicted in panel (d-h).

The spectral analysis of the Ni L-edge of particle two shows distinct variations in oxidation states across the NMC811 particle, indicative of a heterogeneous charge distribution within the electrode material. Specifically, regions highlighted in orange signify the most extensively delithiated regions of the NMC811 particle, whereas the regions in red highlight the more reduced regions of the particle. The delithiation correlates with a discernible increase in the peak intensity at 529 eV, attributed to the increased covalency of the transition metal-oxygen (TM-O) bonding environment.[59,60] The absence of a reduced surface layer associated with this particle is notable, as evidenced by the lack of a peak at 532 eV.[61,62]

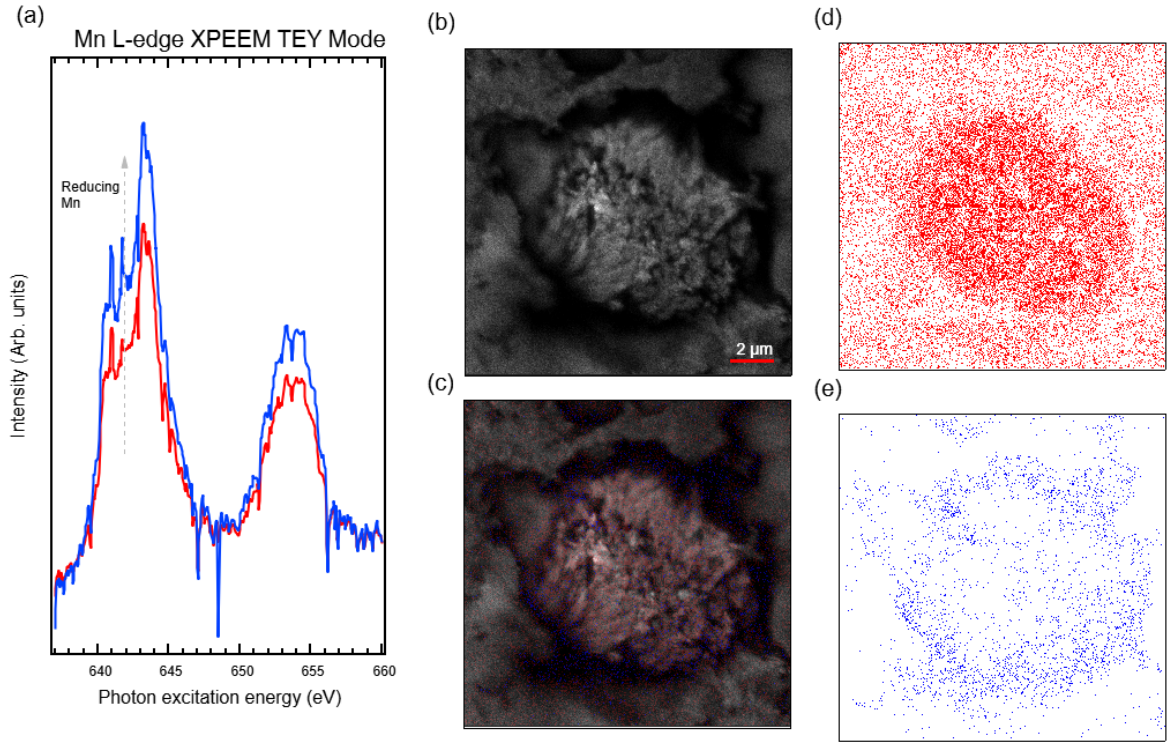

Figure 3.15. X-ray Photoemission Electron Microscopy (XPEEM) analysis of a charged NMC811 particle spot two. (a) Mn L-edge spectra of the mapped regions on the NMC811 particle, (b) electron map of electron intensity collected at 642 eV. (c) Mn L-edge regions colour matched to the spectra, (d) corresponds to the red spectra and (e) corresponds to the blue spectra.

Figure 3.15 presents TEY XPEEM measurements of the Mn L-edge within NMC811 secondary particle two at a delithiated state (4.4 V vs Li/Li^+). Panel (a) displays Mn L-edge spectra aligned

with colour-coded regions from panel (c-e), offering insights into manganese species distribution. Panel (b) provides spatial context with an electron yield image at 642 eV.

We observe a relatively uniform Mn distribution across the particle surface, similar to particle one. However, the Mn in particle two appears more oxidised in +4 oxidation state on the particle surface.[39] A slightly reduced environment, highlighted by the blue regions in panel (c), correlates with discernible spectral features in panel (a), including a subtle emergence of a peak at 642 eV, suggesting the onset of Mn reduction at the particle surface.[39,49,50] Notably, the signal-to-noise ratio for the Mn L-edge in particle two is considerably lower compared to particle one, indicating a lower concentration of Mn species on the surface of particle two.

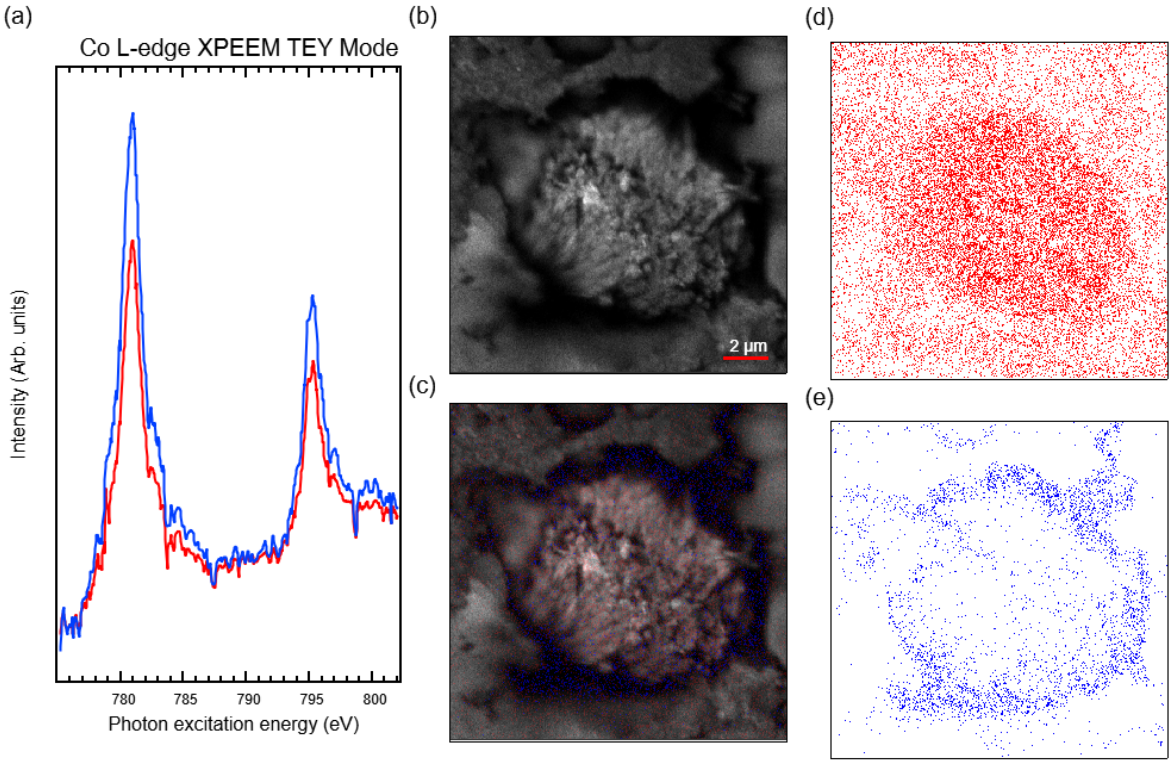

Figure 3.16. X-ray Photoemission Electron Microscopy (XPEEM) analysis of a charged NMC811 particle spot two. (a) Co L-edge spectra of the mapped regions on the NMC811 particle, (b) electron map of electron intensity collected at 778.5 eV. (c) Co L-edge regions colour matched to the spectra, (d) corresponds to the red spectra and (e) corresponds to the blue spectra.

Figure 3.16 depicts TEY XPEEM measurements of the Co L-edge within NMC811 secondary particle two in a delithiated state (4.4 V vs Li/Li^+). Panel (a) displays Co L-edge spectra aligned with colour-coded regions from panel (c-e), revealing spatial distribution insights of Cobalt species. Panel (b) presents an electron yield image at 778.5 eV for spatial context.

Notably, Cobalt distribution in this particle predominantly comprises Co^{3+}, even in regions highlighted in blue.[40] These regions exhibit a more substantial signal-to-noise ratio, suggesting higher concentrations of Co, particularly around the particle's edges.

XAS of Secondary NMC811 Particle Three

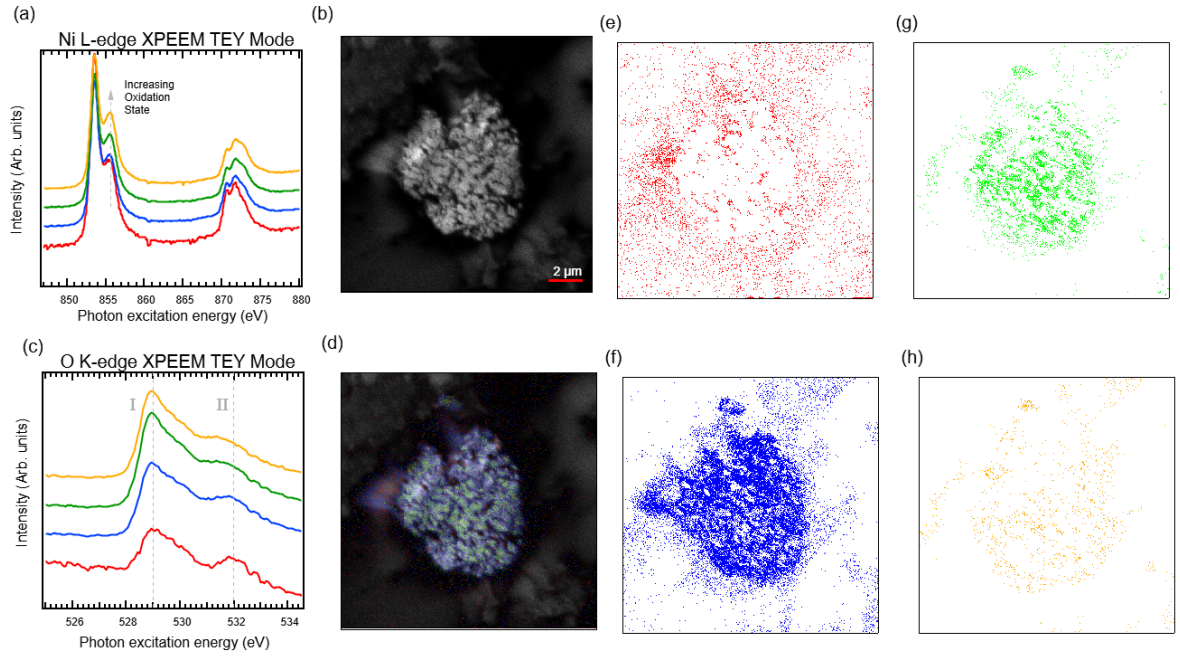

Figure 3.17. X-ray Photoemission Electron Microscopy (XPEEM) analysis of a charged NMC811 particle spot three. (a) Ni L-edge mapped regions on the NMC811 particle, (b)electron map of electron intensity collected at 855.26 eV. (c) O K-edge spectrum of mapped regions, (d) Ni L-edge and O K-edge regions integrated throughout the image stack, (d) A colour map of the Ni L-edge and O K-edge regions integrated throughout the image stack. (e) corresponds to the red spectra, (f) corresponds to the blue spectra, (g) corresponds to the green spectra and (h) corresponds to the orange spectra.

Figure 3.17 presents TEY XPEEM measurements of Ni L-edge and O K-edge spectra extracted from secondary particle three within NMC811 electrodes, observed in a delithiated state (4.4 V vs Li/Li^+). Panel (a) displays Ni L-edge spectra aligned with colour-coded regions from panel (d), while panel (b) offers an electron yield image of particle three at 855.26 eV. Panel (c) presents O K-edge spectra from corresponding regions, matching the highlighted areas in panel (d-h).

The Ni L-edge spectral analysis reveals distinct oxidation state variations across particle three. Red and blue regions indicate more reduced Ni, particularly around cracks. Green and orange regions signify areas with the highest oxidation state, indicating a heterogeneous delithiation pattern across particle threes surface.

The O K-edge spectra mirror the Ni spectra regions, with more oxidised Ni displaying a growth of the peak at 529 eV (peak I), while more reduced Ni regions correlate with a reduced surface layer, as indicated by the emergence of a peak at 532 eV (peak II) in panel (c).[61,62]

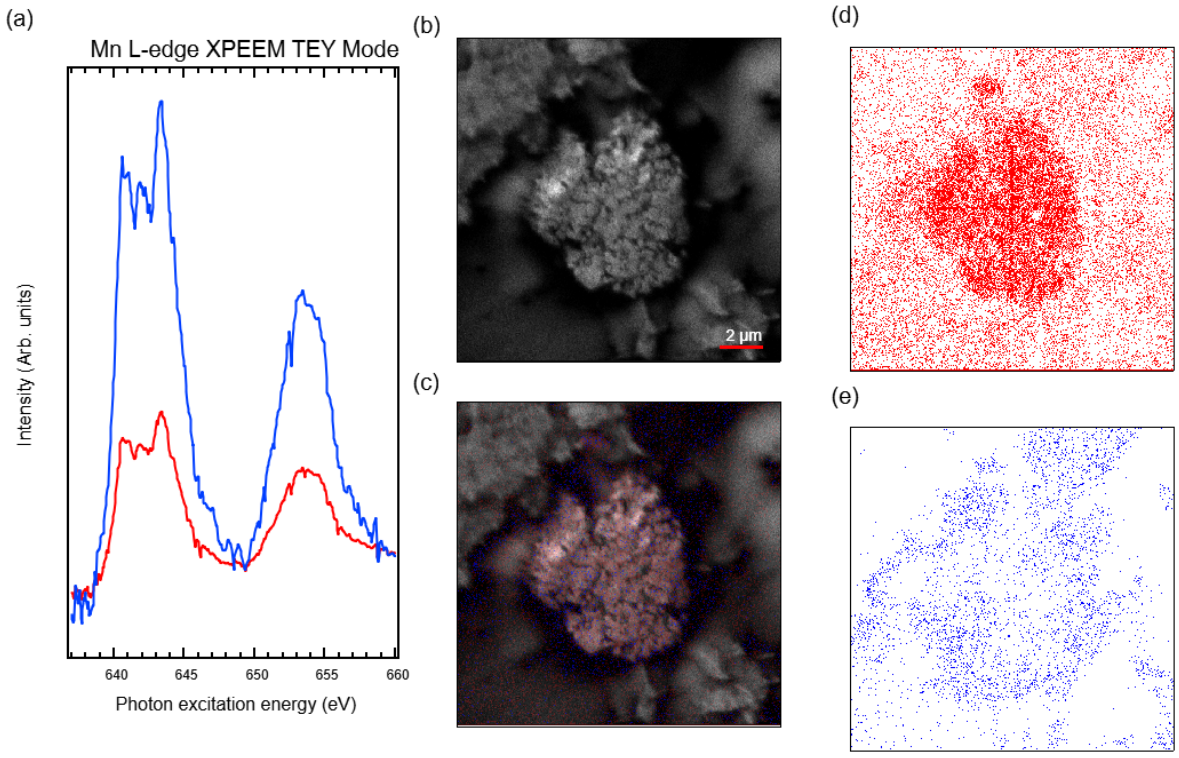

Figure 3.18. X-ray Photoemission Electron Microscopy (XPEEM) analysis of a charged NMC811 particle spot three. (a) Mn L-edge spectra of the mapped regions on the NMC811 particle, (b) electron map of electron intensity collected at 642 eV. (c) Mn L edge regions colour matched to the spectra, (d) corresponds to the red spectra and (e) corresponds to the blue spectra.

Figure 3.18 illustrates TEY XPEEM measurements of the Mn L-edge within NMC811 secondary particle three at a delithiated state (4.4 V vs Li/Li^+). Panel (a) presents Mn L-edge spectra aligned with colour-coded regions from panel (c-e), providing insights into manganese species distribution. Panel (b) offers spatial context with an electron yield image at 642 eV. Similar to the Mn species observed on the surface of particle one, there exists a diverse distribution of Mn oxidation states within the NMC811 particle. This distribution encompasses Mn^{2+}, Mn^{3+}, and Mn^{4+} species,[49,50] with a higher concentrations of Mn found at the edges of the particle highlighted by the blue regions in panel (c and e).

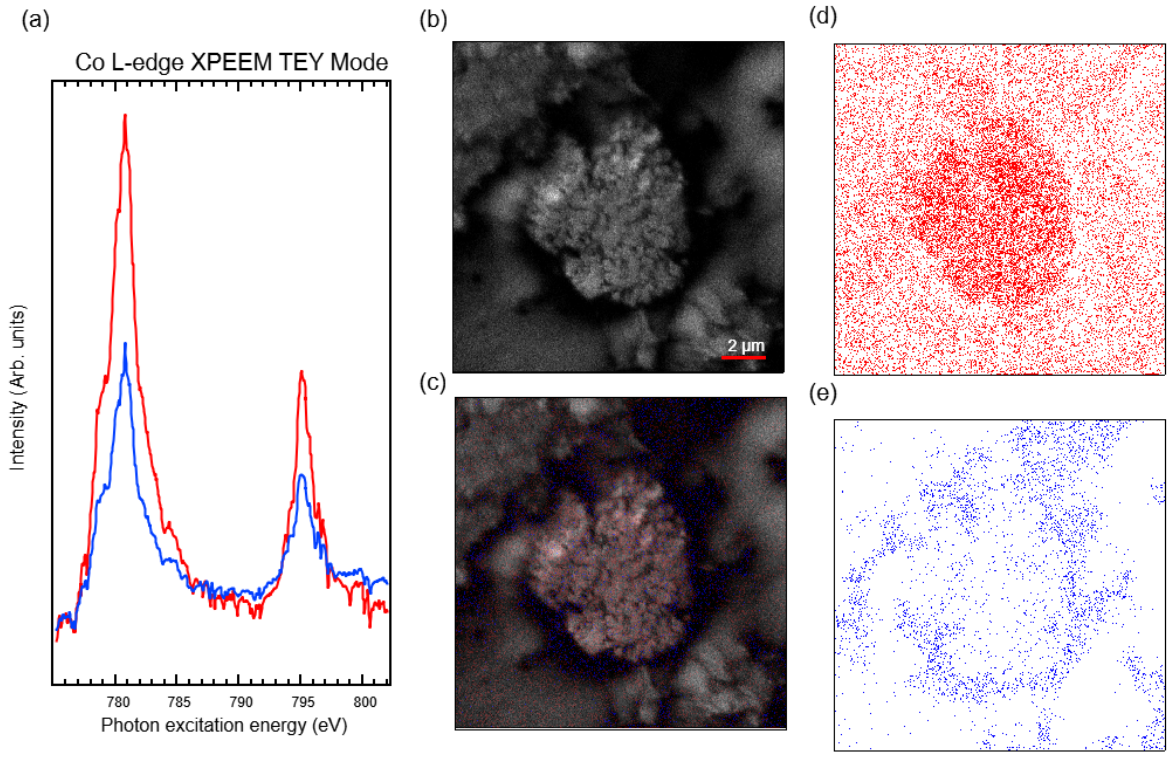

Figure 3.19. X-ray Photoemission Electron Microscopy (XPEEM) analysis of a charged NMC811 particle spot three. (a) Co L-edge spectra of the mapped regions on the NMC811 particle, (b) electron map of electron intensity collected at 778.5 eV. (c) Co L-edge regions colour matched to the spectra, (d) corresponds to the red spectra and (e) corresponds to the blue spectra.

Figure 3.19 presents TEY XPEEM measurements of the Co L-edge within NMC811 secondary particle three at a delithiated state (4.4 V vs Li/Li^+). Panel (a) displays Co L-edge spectra aligned with colour-coded regions from panel (c-e), providing insights into the spatial distribution of Cobalt species. Panel (b) offers spatial context with an electron yield image at 778.5 eV. Cobalt distribution in this particle primarily consists of Co^{3+}, with a small peak emerging at 778 eV indicating of some areas containing reduced Co.[40]

Discussion

Preparation of Electrodes

Sample preparation in XPEEM is crucial for obtaining reliable data. A flat electrode surface is essential to ensure high spatial resolution measurements. Any imperfections in the electrode surface can compromise results. Therefore, careful attention is required to achieve flatness without damaging the electrode during pressing. In this chapter, NMC811 electrodes with mass loading of ~0.7 mg cm^{-2} were cast and pressed with a pressure of ~10 MPa, ensuring a flat surface without compromising the integrity of the particles on the electrode, as over pressing the electrodes has been shown to cause mechanical damage (see Figure 3.2) impacting the chemical and structural properties of the active material reported in literature.[25] The preparation method outlined in this chapter avoids mechanical degradation of the particle whilst providing an adequate flat surface for XPEEM analysis.

TEY-XPEEM

TEY-XPEEM mode measurements conducted on TM (Ni, Mn, and Co) L-edges, in conjunction with the O K edge, unveil diverse degradation patterns across the three different particles within the cycled electrode at a high state of charge (4.4 V vs Li/Li^+). Tracking the Ni L edge XPEEM measurements reveals a progressive increase in Ni oxidation state from Ni^{2+} to Ni^{4+},[27,58,63] typically as the signal originates further from voids or cracks on the secondary particle, offering insights into surface charge compensation mechanisms.

Mapping the same regions for Ni in relation to changes in the O K-edge reveals a notable increase in peak intensity at 529 eV, which correlates with the rising oxidation state of Ni. This phenomenon is intricately linked to oxygen holes characterised by strong O 2p character, as

observed in the electronic structure of LCO electrodes.[59] These oxygen holes are bound to Co^{4+} sites and Li-ion vacancies, facilitating electronic conductivity within the Co^{3+}/Co^{4+} mixed valence CoO_2 layer. This charge compensation mechanism effectively mitigates lattice distortion caused by Li-ion motion, improving both electronic and Li-ion conductivities and enhancing battery performance.[59,60] The same phenomenon is present on the Ni-rich electrodes' surface, with the particle's most oxidised regions exhibiting the highest covalency between the Ni-O bonds. The degree of covalency in these bonds significantly influences cathode material stability, wherein greater covalence implies increased electron sharing between Ni and O atoms, aiding stability to the structure during delithiation. Conversely, reduced covalence suggests diminished electron sharing, potentially compromising material stability due to weaker chemical bonds this is particularly true for areas on the cathode particle which are more delithiated where we see more reduced Ni.[64] The weaker covalency may lead the layered structure to collapse into a rocksalt layer. Studies on the highly delithiated states of lithium nickel oxide have linked a loss of the stabilising influence of Li-O covalency. This loss results in the elongation of Ni-O bonds, coinciding with the collapse of the c-lattice associated with the H2-H3 transition and an amplified charge transfer from oxygen to nickel sites.[65] Fluctuating oxidation states of Ni ions directly impact bond covalency, modulating material stability. Particle two exhibits no NiO at its surface, suggesting limited regions for lithium diffusion not associated with NiO but rather species on the CEI. A Li-deficient layer at the surface during high-voltage cycling leads to forming a metal oxide-type rocksalt phase most likely NiO but there may also be partial be contributions from reduced Co at the surface.[44] This reduced surface layer adversely impacts cell performance due to poor electronic and ionic conductivity increasing impedance. The reduced surface layer also facilitates a pathway for Ni and Co to dissolve into the electrolyte through acid leaching.

TEY-XPEEM measurements on cathode materials indicate a consistent reduction trend of Mn ions from Mn^{4+} to $Mn^{3+/2+}$ across all particles analysed. This reduction occurs amidst cycling-induced structural instability, underscoring the delicate equilibrium governing lithium-ion storage and release within cathode materials. The Jahn-Teller effect causes structural distortions, further driving the disproportionation reaction, wherein Mn^{3+} ions simultaneously oxidise and reduce, forming Mn^{4+} and Mn^{2+} species. [66,67]Consequently, Mn dissolution into the electrolyte initiates adverse effects, including capacity loss, increased impedance, and enhanced formation of solid-electrolyte interphase (SEI) layers at the anode interface.[68]

XPS imaging

XPEEM measurements in this chapter show predominantly TM^{2+} ions and undercoordinated TMs on the cathode surface due to oxygen loss, potentially contributing to TM dissolution. Oxygen release at high potentials aligns with increased EC degradation in the electrolyte, leading to the generation of water and acidic species driven by electrolyte oxidation.[69] XPS images elucidate a thin, organic-rich CEI layer enveloping the electrode surface, seen as the organic components in the O 1s spectra together with inorganic components have too low concentrations to cover the lattice oxygen in the bulk. Analysis of the O 1s spectrum unveils features attributed to C=O and C-O, likely indicative of organic species rather than lithium carbonate due to the absence of features at 534 eV on the O K-edge spectra is consistent with literature documenting carbonate removal at high potentials. [33,58]

The low LiF signal intensity suggests limited concentrations on the particle surface, indicating that the x-rays are attenuated by the coverage of polymeric organic species on the surface of the CEI. This deficiency in CEI thickness may facilitate access for protic species like trace HF

and H_3PO_4 from the electrolyte, triggering acid leaching of transition metals into the electrolyte and crossover into the anode SEI.[29,70]

Conclusion

This chapter focuses on optimising XPEEM imaging for characterising lithium-ion cathode materials, particularly NMC811. Carefully prepared XPEEM-compatible electrodes minimise secondary particle damage and mechanical defects that could interfere with electrochemical degradation. TEY-XAS mode XPEEM measurements were conducted on three different particles within the electrode, revealing heterogeneous transition metal oxidation states and localised degradation at both macro and microscale levels.

Each particle exhibited varying degrees of lithiation and degradation, offering insights into the respective roles of transition metals and oxygen. A correlation was observed between a high Ni oxidation state and the low-energy pre-edge feature of the O K-edge, reflecting the covalency of the Ni-O bonds. The more reduced sites of NMC811 particles with weaker Ni-O covalency displayed more reduced Ni. The O K-edge also identified a reduced surface layer attributed to forming a NiO rocksalt layer, matching areas with significantly reduced Ni.

Microscale degradation regions for Mn and Co within primary particles were challenging to discern, but differences between secondary particles were more pronounced. Mn tended to reduce to Mn^{3+} oxidation state at the surface across all particles leading to disproportionation reactions leaching Mn^{2+} ions into the electrolyte. At the same time, Co exhibited subtle changes, indicating a more stabilising role at the surface of NMC811.

Additionally, high-resolution XPS imaging of the CEI was performed on the particle with the most reduced surface layer, revealing low concentrations of LiF on the particle surface and

pathways to the particle surface, facilitating transition metal dissolution. This chapter emphasises the impactful role of XPEEM characterisation in battery materials. Combining XPEEM measurements with XAS and XPS microscopy will help us spatiochemically resolve surface alterations within electrode particles. This integrated approach offers crucial insights into the CEI. Monitoring local oxidation states is key to optimising the CEI coverage on cathode particlesn and could provide essential spatial data on electrolyte additive impacts. This precision enables targeted engineering strategies to improve battery performance and longevity.

References

1. Liu, Q. *et al.* Approaching the capacity limit of lithium cobalt oxide in lithium ion batteries via lanthanum and aluminium doping. *Nat Energy* **3**, 936–943 (2018).

2. Chen, Z., Lu, Z. & Dahn, J. R. Staging Phase Transitions in Li[sub x]CoO[sub 2]. *J Electrochem Soc* **149**, A1604 (2002).

3. Schipper, F. *et al.* Review—Recent Advances and Remaining Challenges for Lithium Ion Battery Cathodes. *J Electrochem Soc* **164**, A6220–A6228 (2017).

4. Kwade, A. *et al.* Current status and challenges for automotive battery production technologies. *Nat Energy* **3**, 290–300 (2018).

5. Goodenough, J. B. & Kim, Y. Challenges for rechargeable Li batteries. *Chemistry of Materials* **22**, 587–603 (2010).

6. Thapaliya, B. P. *et al.* Enhancing Cycling Stability and Capacity Retention of NMC811 Cathodes by Reengineering Interfaces via Electrochemical Fluorination. *Adv Mater Interfaces* **9**, 1–10 (2022).

7. Märker, K., Reeves, P. J., Xu, C., Griffith, K. J. & Grey, C. P. Evolution of Structure and Lithium Dynamics in LiNi0.8Mn0.1Co0.1O2 (NMC811) Cathodes during Electrochemical Cycling. *Chemistry of Materials* **31**, 2545–2554 (2019).

8. Heenan, T. M. M. *et al.* Identifying the Origins of Microstructural Defects Such as Cracking within Ni-Rich NMC811 Cathode Particles for Lithium-Ion Batteries. *Adv Energy Mater* **10**, (2020).

9. Li, J., Downie, L. E., Ma, L., Qiu, W. & Dahn, J. R. Study of the Failure Mechanisms of LiNi 0.8 Mn 0.1 Co 0.1 O 2 Cathode Material for Lithium Ion Batteries . *J Electrochem Soc* **162**, A1401–A1408 (2015).

10. Jung, R., Metzger, M., Maglia, F., Stinner, C. & Gasteiger, H. A. Chemical versus electrochemical electrolyte oxidation on NMC111, NMC622, NMC811, LNMO, and conductive carbon. *Journal of Physical Chemistry Letters* **8**, 4820–4825 (2017).

11. Björklund, E. *et al.* Cycle-Induced Interfacial Degradation and Transition-Metal Cross-Over in LiNi 0.8 Mn 0.1 Co 0.1 O 2 –Graphite Cells . *Chemistry of Materials* (2022) doi:10.1021/acs.chemmater.1c02722.

12. Shkrob, I. A. *et al.* Manganese in graphite anode and capacity fade in Li ion batteries. *Journal of Physical Chemistry C* **118**, 24335–24348 (2014).

13. Li, T. *et al. Degradation Mechanisms and Mitigation Strategies of Nickel-Rich NMC-Based Lithium-Ion Batteries*. *Electrochemical Energy Reviews* vol. 3 (Springer Singapore, 2020).

14. Gummow, R. J., de Kock, A. & Thackeray, M. M. Improved capacity retention in rechargeable 4 V lithium/lithium-manganese oxide (spinel) cells. *Solid State Ion* **69**, 59–67 (1994).

15. Gao, H. *et al.* Surface Modification for Suppressing Interfacial Parasitic Reactions of a Nickel-Rich Lithium-Ion Cathode. *Chemistry of Materials* **31**, 2723–2730 (2019).

16. Jung, R., Metzger, M., Maglia, F., Stinner, C. & Gasteiger, H. A. Oxygen Release and Its Effect on the Cycling Stability of LiNi x Mn y Co z O 2 (NMC) Cathode Materials for Li-Ion Batteries . *J Electrochem Soc* **164**, A1361–A1377 (2017).

17. Jarry, A. *et al.* The Formation Mechanism of Fluorescent Metal Complexes at the LixNi0.5Mn1.5O4-δ/Carbonate Ester Electrolyte Interface. *J Am Chem Soc* **137**, 3533–3539 (2015).

18. Amine, K. *et al.* Improved lithium manganese oxide spinel/graphite Li-ion cells for high-power applications. in *Journal of Power Sources* vol. 129 14–19 (Elsevier, 2004).

19. Li, W. Review—An Unpredictable Hazard in Lithium-ion Batteries from Transition Metal Ions: Dissolution from Cathodes, Deposition on Anodes and Elimination Strategies. *J Electrochem Soc* **167**, 090514 (2020).

20. Evertz, M. *et al.* Unraveling transition metal dissolution of Li1.04Ni1/3Co1/3Mn1/3O2 (NCM 111) in lithium ion full cells by using the total reflection X-ray fluorescence technique. *J Power Sources* **329**, 364–371 (2016).

21. Zhang, Z. *et al.* The Influence of Cathode Degradation Products on the Anode Interface in Lithium-Ion Batteries. *ACS Nano* **18**, 9389–9402 (2024).

22. Kanamura, K. *et al. Self-Discharge of LiMn2 O 4/C Li-Ion Cells in Their State: Understanding by Means of Three-Electrode Measurements*. *J. Electrochem. Soc* vol. 145 (1998).

23. Hanf, L., Henschel, J., Diehl, M., Winter, M. & Nowak, S. Mn2+ or Mn3+? Investigating transition metal dissolution of manganese species in lithium ion battery electrolytes by capillary electrophoresis. *Electrophoresis* **41**, 697–704 (2020).

24. Banerjee, A. *et al.* On the oxidation state of manganese ions in li-ion battery electrolyte solutions. *J Am Chem Soc* **139**, 1738–1741 (2017).

25. Mirolo, M. *et al.* Post Mortem and Operando XPEEM: A Surface-Sensitive Tool for Studying Single Particles in Li-Ion Battery Composite Electrodes. *Anal Chem* **92**, 3023–3031 (2020).

26. Leanza, D., Mirolo, M., Vaz, C. A. F., Novák, P. & El Kazzi, M. Surface Degradation and Chemical Electrolyte Oxidation Induced by the Oxygen Released from Layered Oxide Cathodes in Li–Ion Batteries. *Batter Supercaps* **2**, 482–492 (2019).

27. Mirolo, M., Vaz, C. A. F., Novák, P. & El Kazzi, M. Multi-length-scale x-ray spectroscopies for determination of surface reactivity at high voltages of LiNi0.8Co0.15Al0.05O2vs Li4Ti5O12. *Journal of Chemical Physics* **152**, (2020).

28. Leanza, D. *et al.* Revealing the Dual Surface Reactions on a HE-NCM Li-Ion Battery Cathode and Their Impact on the Surface Chemistry of the Counter Electrode. *ACS Appl Mater Interfaces* (2019) doi:10.1021/acsami.8b19511.

29. Hestenes, J. C., Sadowski, J. T., May, R. & Marbella, L. E. Transition Metal Dissolution Mechanisms and Impacts on Electronic Conductivity in Composite LiNi0.5Mn1.5O4 Cathode Films. *ACS Materials Au* **3**, 88–101 (2023).

30. Hestenes, J. C., May, R., Sadowski, J. T., Munich, N. & Marbella, L. E. Resolving Chemical and Spatial Heterogeneities at Complex Electrochemical Interfaces in Li-Ion Batteries. *Chemistry of Materials* **34**, 232–243 (2022).

31. Leanza, D., Vaz, C. A. F., Czekaj, I., Novák, P. & El Kazzi, M. Solving the puzzle of Li4Ti5O12 surface reactivity in aprotic electrolytes in Li-ion batteries by nanoscale XPEEM spectromicroscopy. *J Mater Chem A Mater* **6**, 3534–3542 (2018).

32. Tian, C. *et al.* Depth-Dependent Redox Behavior of LiNi 0.6 Mn 0.2 Co 0.2 O 2 . *J Electrochem Soc* **165**, A696–A704 (2018).

33. Märker, K., Reeves, P. J., Xu, C., Griffith, K. J. & Grey, C. P. Evolution of Structure and Lithium Dynamics in LiNi0.8Mn0.1Co0.1O2 (NMC811) Cathodes during Electrochemical Cycling. *Chemistry of Materials* **31**, 2545–2554 (2019).

34. Lin, F. *et al.* Profiling the nanoscale gradient in stoichiometric layered cathode particles for lithium-ion batteries. *Energy Environ Sci* **7**, 3077–3085 (2014).

35. Xue, W. *et al.* Ultra-high-voltage Ni-rich layered cathodes in practical Li metal batteries enabled by a sulfonamide-based electrolyte. *Nat Energy* **6**, 495–505 (2021).

36. Björklund, E. *et al.* Cycle-Induced Interfacial Degradation and Transition-Metal Cross-Over in LiNi0.8Mn0.1Co0.1O2-Graphite Cells. *Chemistry of Materials* **34**, 2034–2048 (2022).

37. Steiner, J. D. *et al.* Accelerated Evolution of Surface Chemistry Determined by Temperature and Cycling History in Nickel-Rich Layered Cathode Materials. *ACS Appl Mater Interfaces* **10**, 23842–23850 (2018).

38. Lin, F. *et al.* Surface reconstruction and chemical evolution of stoichiometric layered cathode materials for lithium-ion batteries. *Nat Commun* **5**, 3529 (2014).

39. Risch, M. *et al.* Redox Processes of Manganese Oxide in Catalyzing Oxygen Evolution and Reduction: An in Situ Soft X-ray Absorption Spectroscopy Study. *Journal of Physical Chemistry C* **121**, 17682–17692 (2017).

40. Zhang, W., Liu, Y. & Wang, C. *Oxygen 1s and Cobalt 2p X-Ray Absorption of Cobalt Oxides You May Also like Role of 1,2,4-Triazole in Co/Cu Removal Rate Selectivity and Galvanic Corrosion during Barrier CMP*. *J. Phys.: Condens. Matter* vol. 5 (1993).

41. Yu, Y. *et al.* Probing Depth-Dependent Transition-Metal Redox of Lithium Nickel, Manganese, and Cobalt Oxides in Li-Ion Batteries. *ACS Appl Mater Interfaces* **12**, 55865–55875 (2020).

42. Tian, C. *et al.* Depth-Dependent Redox Behavior of LiNi 0.6 Mn 0.2 Co 0.2 O 2 . *J Electrochem Soc* **165**, A696–A704 (2018).

43. Jung, R. *et al.* Effect of Ambient Storage on the Degradation of Ni-Rich Positive Electrode Materials (NMC811) for Li-Ion Batteries. *J Electrochem Soc* **165**, A132–A141 (2018).

44. Frati, F., Hunault, M. O. J. Y. & De Groot, F. M. F. Oxygen K-edge X-ray Absorption Spectra. *Chem Rev* **120**, 4056–4110 (2020).

45. Baker, M. L. *et al.* K- and L-edge X-ray absorption spectroscopy (XAS) and resonant inelastic X-ray scattering (RIXS) determination of differential orbital covalency (DOC) of transition metal sites. *Coordination Chemistry Reviews* vol. 345 182–208 Preprint at https://doi.org/10.1016/j.ccr.2017.02.004 (2017).

46. Qiao, R. *et al.* Transition-metal redox evolution in LiNi0.5Mn0.3Co0.2O2 electrodes at high potentials. *J Power Sources* **360**, 294–300 (2017).

47. Li, T. *et al.* Degradation Mechanisms and Mitigation Strategies of Nickel-Rich NMC-Based Lithium-Ion Batteries. *Electrochemical Energy Reviews* vol. 3 43–80 Preprint at https://doi.org/10.1007/s41918-019-00053-3 (2020).

48. Kondrakov, A. O. *et al. Charge-Transfer-Induced Lattice Collapse in Ni-Rich NCM Cathode Materials during Delithiation*.

49. Oishi, M. *et al.* Direct observation of reversible oxygen anion redox reaction in Li-rich manganese oxide, Li2MnO3, studied by soft X-ray absorption spectroscopy. *J Mater Chem A Mater* **4**, 9293–9302 (2016).

50. Shaker, M. N. *et al. Insight into PH-Dependent Formation of Mn Oxide Phases in Electrodeposited Catalytic Films Probed by Soft X-Ray Absorption Spectroscopy*.

51. Greczynski, G. & Hultman, L. Referencing to adventitious carbon in X-ray photoelectron spectroscopy: Can differential charging explain C 1s peak shifts? *Appl Surf Sci* **606**, (2022).

52. Malmgren, S. *et al.* Comparing anode and cathode electrode/electrolyte interface composition and morphology using soft and hard X-ray photoelectron spectroscopy. *Electrochim Acta* **97**, 23–32 (2013).

53. Andersson, A. M. *et al.* Surface Characterization of Electrodes from High Power Lithium-Ion Batteries. *J Electrochem Soc* **149**, A1358 (2002).

54. Hekmatfar, M., Kazzazi, A., Eshetu, G. G., Hasa, I. & Passerini, S. Understanding the Electrode/Electrolyte Interface Layer on the Li-Rich Nickel Manganese Cobalt Layered Oxide Cathode by XPS. *ACS Appl Mater Interfaces* **11**, 43166–43179 (2019).

55. Chen, H. *et al.* Investigating Surface Reactivity of a Ni-Rich Cathode Material toward CO2, H2O, and O2 Using Ambient Pressure X-ray Photoelectron Spectroscopy. *ACS Appl Energy Mater* **6**, 11458–11467 (2023).

56. Malmgren, S. *et al.* Comparing anode and cathode electrode/electrolyte interface composition and morphology using soft and hard X-ray photoelectron spectroscopy. *Electrochim Acta* **97**, 23–32 (2013).

57. Kozlowski~, C. & Sherwood, P. M. A. *X-Ray Photoelectron-Spectroscopic Studies of Carbon-Fibre Surfaces Part 5.-The Effect of PH on Surface Oxidation*. *J. Chem. Soc., Faraday Trans. I* vol. 81 (1985).

58. Björklund, E. *et al.* Cycle-Induced Interfacial Degradation and Transition-Metal Cross-Over in LiNi 0.8 Mn 0.1 Co 0.1 O 2 –Graphite Cells . *Chemistry of Materials* (2022) doi:10.1021/acs.chemmater.1c02722.

59. Mizokawa, T. *et al.* Role of oxygen holes in LixCoO2 revealed by soft X-ray spectroscopy. *Phys Rev Lett* **111**, (2013).

60. De Groot, F. M. F. *et al. Oxygen 1s X-Ray-Absorption Edges of Transition-Metal Oxides*. *PHYSICAL REVIEW B* vol. 40.

61. Liu, H. *et al.* High-Voltage Induced Surface and Intragranular Structural Evolution of Ni-Rich Layered Cathode. *Small* **18**, (2022).

62. Sallis, S. *et al.* Surface degradation of Li1-xNi0.80Co0.15Al0.05O2 cathodes: Correlating charge transfer impedance with surface phase transformations. *Appl Phys Lett* **108**, (2016).

63. Lin, F. *et al.* Surface reconstruction and chemical evolution of stoichiometric layered cathode materials for lithium-ion batteries. *Nat Commun* **5**, 3529 (2014).

64. Kleiner, K. *et al.* On the Origin of Reversible and Irreversible Reactions in LiNi x Co (1−x)/2 Mn (1−x)/2 O 2 . *J Electrochem Soc* **168**, 120533 (2021).

65. Chien, P. H. *et al.* New Insights into Structural Evolution of LiNiO2 Revealed by Operando Neutron Diffraction. *Batter Supercaps* **4**, 1701–1707 (2021).

66. Liu, T. *et al.* Correlation between manganese dissolution and dynamic phase stability in spinel-based lithium-ion battery. *Nat Commun* **10**, (2019).

67. Choi, W. & Manthiram, A. Comparison of Metal Ion Dissolutions from Lithium Ion Battery Cathodes. *J Electrochem Soc* **153**, A1760 (2006).

68. Xiao, X. *et al.* Unraveling manganese dissolution/deposition mechanisms on the negative electrode in lithium ion batteries. *Physical Chemistry Chemical Physics* **16**, 10398–10402 (2014).

69. Dose, W. M. *et al.* Onset Potential for Electrolyte Oxidation and Ni-Rich Cathode Degradation in Lithium-Ion Batteries. *ACS Energy Lett* **7**, 3524–3530 (2022).

70. Phelan, C. M. E. *et al.* Role of Salt Concentration in Stabilizing Charged Ni-Rich Cathode Interfaces in Li-Ion Batteries. doi:10.1021/acs.chemmater.4c00004.

Chapter 4 - Incorporation of Transition Metals and Their Impact on the Anode Solid-Electrolyte Interphase (SEI) in Lithium-Ion Batteries

Abstract

The dissolution and migration of transition metals from the cathode, followed by their incorporation into the anode solid-electrolyte interface (SEI), can contribute significantly to capacity fade in lithium-ion batteries. To thoroughly investigate this mechanism, X-ray Absorption Near Edge Structure (XANES) measurements were performed to explore exchange reactions between Mn(II), Ni(II) ions dissolved in the electrolyte and the lithium salts commonly found in the SEI. Furthermore, the redox behaviour of transition metals within the SEI using a combination of surface sensitive Near edge x-ray absorption fine structure (NEXAFS) and bulk sensitive X-ray Absorption near edge structure (XANES) has provided a comprehensive understanding of the oxidation state of Ni and Mn species on lithiated and delithiated graphite electrodes. Additionally, our use of Extended X-ray Absorption Fine Structure (EXAFS) refinement has allowed us to accurately determine the particle size of Ni and Mn species on both lithiated and delithiated graphite electrodes as <5 nm.

Introduction

Transition metal-based oxides such as layered $LiNi_xMn_yCo_zO_2$ (NMC), spinel $LiNi_{0.5}Mn_{1.5}O_2$ (LNMO), $LiMn_xFe_yPO_4$ (LMFP) and disordered rocksalt $Li_xMn_2\text{-}xO_{2\text{-}y}F_y$ are promising cathode materials that offer high energy densities required for low-cost vehicle electrification.[1–5] However, transition metal crosstalk, especially manganese dissolution, has been identified as detrimental to lithium-ion battery performance.[6–10] Transition metal ions are dissolved into the electrolyte, where they migrate and subsequently incorporate into the anode's solid electrolyte interphase (SEI) driven by the concentration gradient and/or electric field force.[11] The SEI plays a crucial role in graphite-based electrodes preventing runaway solvent reduction whilst facilitating Li^+ ion conduction.[12] The deposition of TM ions onto graphite anodes from the electrolyte, a complex process that is still not fully understood, has been hypothesised to occur via electrochemical reduction,[13] chemisorption[14] and/or ion exchange mechanisms.[15,16] However, the dissolved cathode active material concentration is typically low, insufficient to account for the observed capacity losses based on just the two-electron reduction of $TM^{2+} + 2e^- \rightarrow TM^0$.[17–19] The precise mechanism by which transition metal ions induce degradation and capacity loss remains poorly understood. Notably, the adverse impact of Mn on capacity retention and impedance rise surpasses that of Ni and Co. However, the reasons why Mn is worse than Ni or Co are yet to be determined.

The investigation into the oxidation states and chemical environments of TMs in the SEI is a crucial step towards a comprehensive understanding of their electrochemical behaviour within the SEI. The SEI, a complex structure formed through electrolyte reduction, is often characterised as possessing a bilayer structure. An inner layer consists of lithium salts (for

example, LiF, Li_2CO_3, and Li_2O)[20–24] and a thicker (10 nm - 30 nm) outer organic layer (polymeric species).[25,26] While most of the literature has focused on Mn deposition and its impact on the anode SEI, there have been some reports in the literature on the impact of Ni and Co. Björklund et al. reported Ni, Mn and Co in a +2 oxidation state on the outer surface of the SEI of delithiated graphite electrodes using near edge x-ray absorption fine structure (NEXAFS) measurements.[27] Similar reports of TMs in a +2 oxidation state are also reported in the literature.[10,16] Xiao et al. employed high-resolution transmission electron microscopy to reveal the presence of Mn species within the SEI, highlighting both reduced Mn^0 (20 nm) particles in the inner SEI and Mn^{2+} species in the outer SEI.[28] Ochida et al. reported even larger Mn^0 particles between 100 and 400 nm using a combination of atomic force microscopy and X-ray photoelectron spectroscopy on highly oriented pyrolytic graphite.[29] Additionally, Gowda et al. performed XANES on graphite to identify Mn^0 species on lithiated graphite.[30] Delacourt et al. measured Mn deposition onto the SEI formed on a Cu electrode. They claimed that Mn is initially reduced to Mn^0; however, the Mn L-edge spectra exhibit features consistent with a +2 oxidation state.[31] Shkrob et al., detected evidence of a reduced Mn signature in XANES measurements. Yet, they posited that, based on electron paramagnetic resonance, the Mn may exist as a non-metallic species rather than metallic if the particle sizes exceed 30 nm.[14] These collective studies offer conflicting insights into TM's complex behaviour and chemical states within the SEI.

In this study, XANES measurements coupled with linear combination analysis were employed to investigate ion exchange reactions between TM ions Ni(II) and Mn(II) in the electrolyte and lithium salts (LiF, Li_2CO_3, and Li_2O) commonly found within the anode SEI. To investigate the redox behaviour of TMs on the anode SEI, full cells containing spiked electrolyte were utilised

to simulate the environment of an aged cell with elevated transition metal levels in the electrolyte. The oxidation state was measured through a combination of XANES and NEXAFS techniques on both lithiated and delithiated graphite electrodes. Additionally, EXAFS analysis was conducted on the same electrodes to elucidate the coordination environments and estimate the particle sizes of the TM species on lithiated and delithiated graphite.

Methods

Ion Exchange Reaction

Two spiked LP30 electrolyte (1 M $LiPF_6$ in EC/DMC 1:1 v/v, Sigma Aldrich, ≤15 ppm of H_2O) solutions, one with 60 mM Ni(II)$acac_2$ and the other with 60 mM Mn(II)$acac_2$, The TM$(acac)_2$ salts were dried under vacuum at 100 °C for 24 h in a Büchi oven. The salts were then transferred into an Ar-filled glovebox (H_2O < 0.1 ppm, O_2 < 0.1 ppm, MBraun) and dissolved in LP30 electrolyte. were prepared to simulate transition metal (TM^{2+}) contamination. 100 mg each of three lithium salts commonly found in the anode SEI - lithium fluoride (LiF), lithium oxide (Li_2O), and lithium carbonate (Li_2CO_3) - were each soaked individually in containers filled with 2.5 ml of the doped electrolytes for five days to facilitate ion exchange. After soaking, the doped electrolytes were filtered using Whatman filter paper and Celgard 2325 separator to remove exchanged salts. The remaining salts were rinsed with dimethyl carbonate (DMC) to remove surface contaminants and then dried overnight in a vacuum oven at 30°C. Subsequently, the salts were mixed with 100 mg of cellulose binder, cold pressed into pellets using a 13 mm diameter die, and pressed with a hydraulic press (MTI) at a pressure of 135.5 MPa. The samples were assembled in a vacuum-sealed pouch before the Ni and Mn K-edges of the exchanged salts were measured at the B18 beamline (Diamond Light Source).

Thin film Preparation

Thin film deposition of Ni and Co was performed by radio frequency magnetron sputtering using a PVD system inside an Ar-filled glovebox (H_2O < 0.1 ppm, O_2 < 0.1 ppm, MBraun) using 2” diameter metallic targets (Testbourne Ltd, 99.99%). This system contains a circular magnetron source (Gencoa Ltd), with a target-to-substrate distance of ∼12 cm. The base pressure of the PVD system prior to sputtering was 10^{-6} mbar. Targets were pre-sputtered for at least 30 minutes with the sample shielded from the source to remove oxide layer contamination. Substrates were mounted on a rotating disk (30 rpm) to ensure uniform coating. Argon gas (BOC Pureshield 99.998%) was employed as the process gas for deposition.

Mn thin films were produced in the same PVD system using an evaporation source positioned approximately 20 cm from the Cu foil substrate. Mn chunks (Sigma Aldrich, 98% purity) were evaporated from an Alumina boat at a rate of 5 Å per second. The substrate shield remained in place until the working pressure during deposition reached 5×10^{-3} mbar. Layer thicknesses of both sputtered and evaporated thin films were measured using a quartz crystal microbalance calibrated by profilometry measurements on various Ni, Mn, and Co films deposited as a function of time.

Coin cell Assembly

Coin cell assembly was conducted in an Ar-filled glovebox (H_2O < 0.1 ppm, O_2 < 0.1 ppm, MBraun) using 2032 coin cell components (Cambridge Energy Solutions Ltd.). The cells comprised metal (Ni, Mn, or Co) thin films (200 nm) on deposited on Cu foil (16 mm diameter, 20 µm thick, >99.9%) and Li foil (16.0 mm diameter, 250 µm thick, >99.9%) electrodes. The

counter and working electrodes were separated by a Ø16 mm separator, consisting of glass fibre (borosilicate, grade GF/A, Whatman) on the Li side and Celgard 2325 on the TM electrode side (All separators were dried at 80°C in a vacuum oven before assembly). The separator was saturated with 100 µl of battery-grade liquid LP30 electrolyte. CV measurements were performed on coin cells using a 2-electrode configuration, with a transition metal thin film deposited onto a Cu foil as the working electrode and a lithium counter electrode. CV scans were performed from OCV to 50 mV and then a reverse scan to 1.5 V at a scan rate of 0.1 mVs^{-1}.

Nickel(II) acetyl acetate (Ni(II)$acac_2$), manganese(II) acetyl acetate (Mn(II)$acac_2$) salts and cobalt(II) acetyl acetate (Co(II)$acac_2$) (Sigma Aldrich) were dried under vacuum at 100 °C for 24 h in a Büchi oven. The salts were then transferred into an Ar-filled glovebox (H_2O < 0.1 ppm, O_2 < 0.1 ppm, MBraun) and dissolved in LP30 electrolyte. Each metal cation was present at a concentration of 20 mM, collectively totalling 60 mM, referred to as “NMC salt” solution. This spiked electrolyte was used in a full-cell configuration of NMC811 vs graphite (Lifun), assembled into a coin cell (as described above) and cycled between 4.2 V and 3.0 V for two cycles at 0.05 C. For the lithiated graphite electrode, the full-cell was charged to an upper cutoff potential of 4.4 V at a 0.05 C rate and held at 4.4 V for 2 hours.

NEXAFS

NEXAFS measurements on thin film TM electrodes (employing the same fabrication method utilised for coin cells) were conducted on pristine electrodes (no cycling) as well as at specific potentials: 2.0 V, 0.05 V, and 1.5 V vs Li/Li^+ on the reverse scan. Separate scans for Mn were performed at 0.5 V vs Li/Li^+. Thin film metal electrodes used for NEXAFS measurements were disassembled from cells at designated potentials in the Ar-filled glovebox. Subsequently, the

electrodes were rinsed with DMC to remove surface lithium salt and EC residue and left to dry inside the glovebox.

The lithiated and delithiated graphite electrodes cycled in the NMC salt electrolyte were also disassembled in the same glovebox before being transported inside an inert transfer device to the B07 beamline at DLS. Measurements of the Ni, Mn and Co L-edge were performed on all the electrodes. All spectra were background subtracted by fitting a straight line to the pre-edge region, followed by an intensity normalisation to the post-edge region, and energy calibrated to initial resonance peak of the O K-edge of NiO at 532.0 eV.[32,33]

XAFS

Mn and Ni K–edge XAFS measurements of the Mn and Ni ion exchanged samples and the cycled graphite anodes were performed at beamline B18 at the DLS. A detailed description of the beamline can be found elsewhere.[34] The electron energy was 3 GeV and the ring current was 300 mA. The experiment was performed in fluorescence mode using an ion chamber detector (for I_0) and a 36 element Ge fluorescence detector with a fast scanning (QEXAFS) Si (111) double crystal monochromator. A reference foil is also placed behind the sample and the reference channel is acquired simultaneously to each measurement for energy calibration. Each spectrum took 4 minutes to acquire, and three scans were recorded per sample per edge, and the final spectra are an average of the three. XAFS data reduction and analysis was performed using the Demeter software package.[35] To analyse the speciation of Ni and Mn in the samples, linear combination analysis (LCA) was carried out for the Ni K-edge and Mn K-edge XANES data. Spectra in the energy range of –15 to 35 eV with respect to the absorption edge energy (E_0) were fitted with reference spectra of Ni(II)CO_3, Ni(II)$acac_2$, NiF_2, NiO and Ni

foil for Ni K-edge spectra. Similar analysis was performed for the Mn K-edge, fitting the spectra with Mn(II)acac2, MnF_2, MnO, Mn_3O_4 and Mn foil used as references.

Results

Ni Ion Exchange

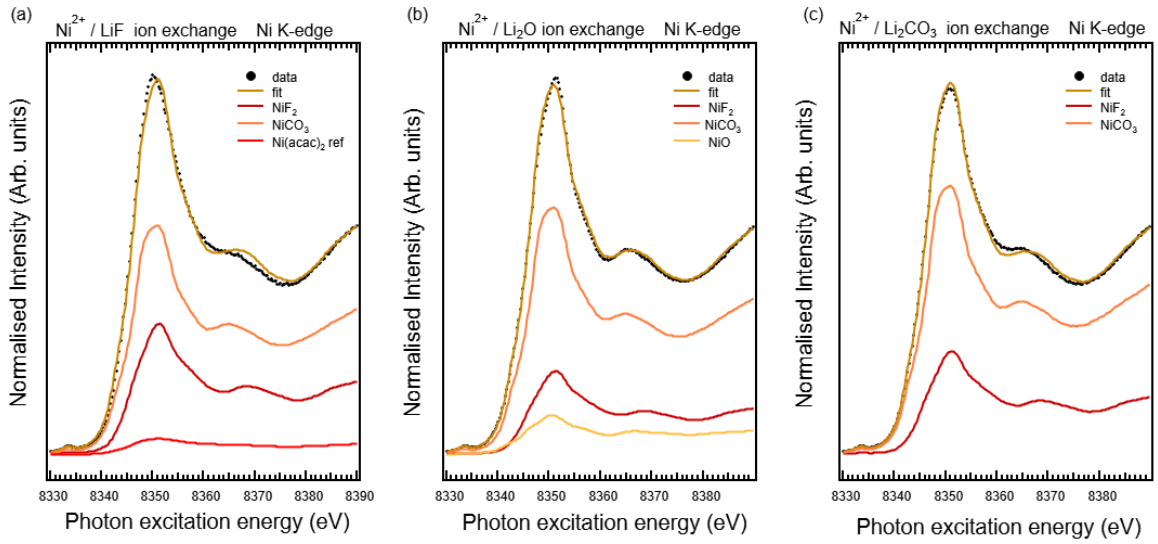

Figure 4.1. Ni cation exchange experiments (a) Ni^{2+} with LiF, (b) Ni^{2+} with Li_2O and (c) Ni^{2+} with Li_2CO_3. The normalised fluorescence Ni K-edge XANES spectra are shown as a scatter plot, while the fitted spectra from the LCA analysis are also plotted with individual weighted components (line plot).

Figure 4.1 shows XANES analysis coupled with LCA, revealing an ion exchange mechanism between Ni(II) ions and Li^+ ions in lithium fluoride (LiF), lithium oxide (Li_2O), and lithium carbonate (Li_2CO_3) salts. An additional component, $NiCO_3$, potentially formed through a side reaction between Ni(II) cations and the electrolyte, is observed in all Ni K-edge samples.

In Figure 4.1a, three components are evident in the LCA fit: $NiCO_3$, NiF_2, and Ni(II) $acac_2$, representing the exchange between Ni(II) $acac_2$ and Li^+ ions from LiF (Fit: 63.5% $NiCO_3$, 32.4% NiF_2, 4.1% $Ni(acac)_2$),. However, in Figure 4.1b, $NiCO_3$ and NiF_2 dominate the spectral features rather than the expected NiO, suggesting significant involvement of side reactions during the exchange process (Fit: 68.4% $NiCO_3$, 20.6% NiF_2, 10.9% NiO). Similarly, Figure 4.1c shows $NiCO_3$

as the largest component in the LCA fit with NiF_2 also present (Fit: 74.4% $NiCO_3$, 26.6% NiF_2), also indicating further side reactions.

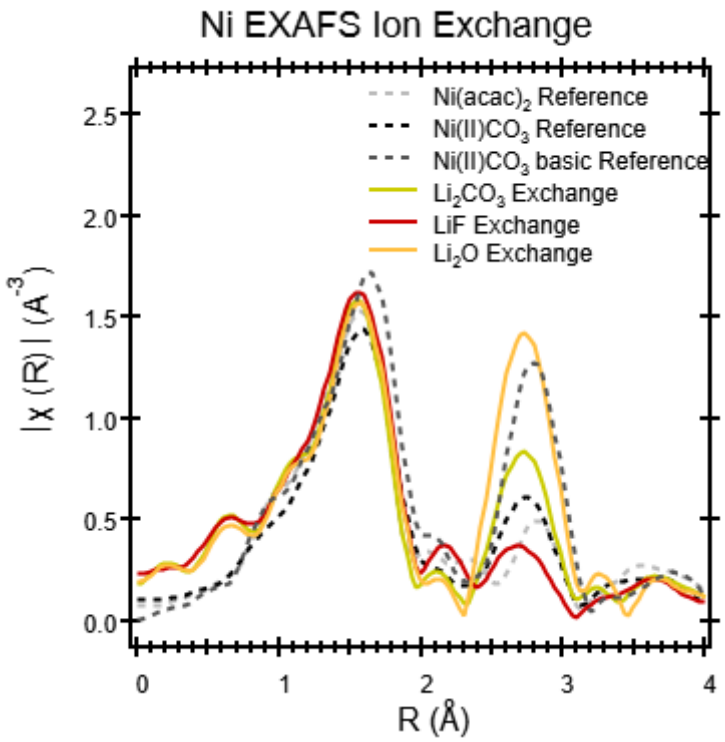

Figure 4.2. The phase uncorrected Fourier transform (FT)-EXAFS moduli of Ni^{2+} cation exchanged salts with $Ni(II)CO_3$ basic reference, $Ni(II)CO_3$ reference and $Ni(II)(acac)_2$ reference.

The accompanying FT-EXAFS moduli of both the ion-exchanged samples and references are plotted in Figure 4.2. All spectra display an intense first shell intensity around R=1.5 Å. A second shell feature around R= 2.75 Å, attributable to Ni-Ni scattering, is also shown in all ion-exchanged samples with varying intensities. Notably, that this second shell feature for the ion exchanged Li_2O shows the highest intensities and is more intense than any of the reference compounds plotted. This is likely due to the fact the ion exchange with the Li_2O forms NiO with a rock salt structure which has a significantly higher second shell Ni-Ni scattering intensity (not plotted here, see references) [36,37] than any other Ni reference. This result is also in agreement with the result from XANES LCA, where NiO is a component of the fit.

Mn Ion Exchange

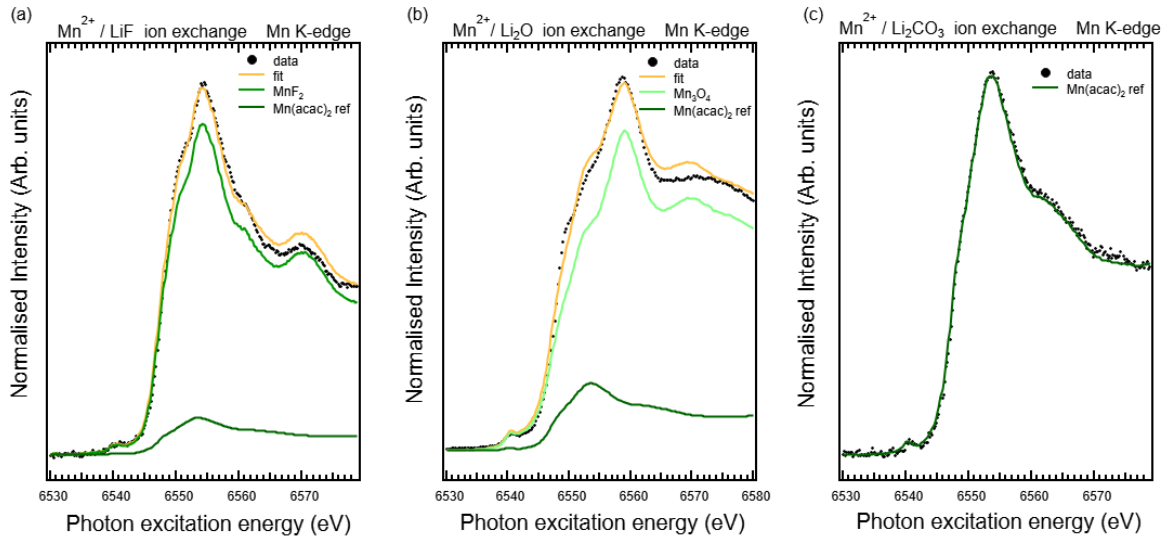

Figure 4.3. Mn cation exchange experiments (a) Mn^{2+} with LiF, (b) Mn^{2+} with Li_2O and (c) Mn^{2+} with Li_2CO_3 The normalised fluorescence Mn K-edge XANES spectra are shown as a scatter plot, while the fitted spectra from the LCA analysis are also plotted with individual weighted components (line plot).

XANES analysis coupled with LCA provides compelling evidence of an ion exchange mechanism between Mn(II) ions and Li^+ ion in lithium fluoride (LiF) and lithium oxide (Li_2O) salts as illustrated in Figure 4.3a (Fit: 90.3% MnF_2, 9.7% $Mn(acac)_2$) and Figure 4.3b, (Fit: 85.1% Mn_3O_4, 14.9% $Mn(acac)_2$) respectively. A Mn_3O_4 component fitted within the LCA on Figure 4.3b indicates the potential coexistence of manganese (Mn) in both +2/+3 oxidation states within the SEI. Figure 4.3c reveals no exchange between Mn(II) cations and Li^+ ions in lithium carbonate (Li_2CO_3). Vissers et al. used density functional theory to show that Mn(II) ions in the SEI layer preferentially form MnF_2 and MnO, with $MnCO_3$ being the least thermodynamically favourable which may partially explain the absence of $MnCO_3$.[38] These findings underscore a potential pathway for transition metals (TMs) to incorporate into the anode SEI driven by a

concentration gradient, eliminating the necessity for additional electrons to facilitate TM integration onto the SEI.

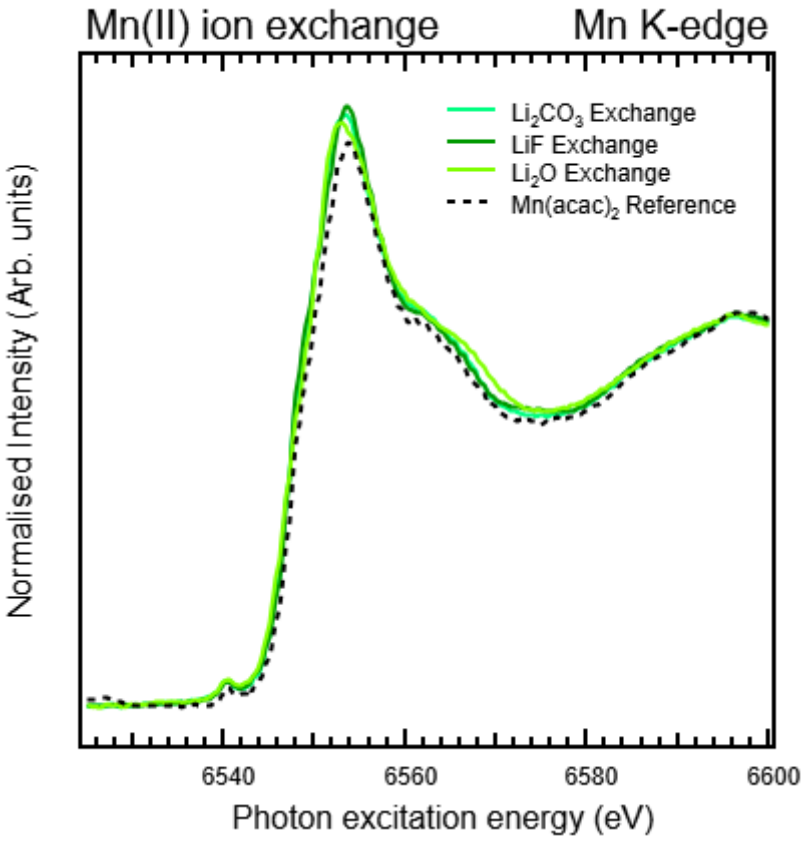

Figure 4.4. Mn cation exchange experiments without the presence of $LiPF_6$ in the electrolyte of Mn^{2+} with LiF, Mn^{2+} with Li_2O, Mn^{2+} with Li_2CO_3 and Mn (II) $acac_2$ reference plotted (dashed line plot).

Ion exchange experiments were also performed using a solution containing 60 mM Mn(II) $acac_2$ dissolved in a mixture of EC and DMC (1:1 ratio (v/v)). Subsequently, the same ion exchange procedures were repeated using three lithium salts. Figure 4.4 illustrates the absence of ion exchange between Mn^{2+} and Li^+ ions across all measured lithium salts, suggesting that Mn^{2+} ions in the electrolyte may solvate with anions of $LiPF_6$ and/or potentially HF.

Transition Metal Redox Behaviour at Anode Interfaces

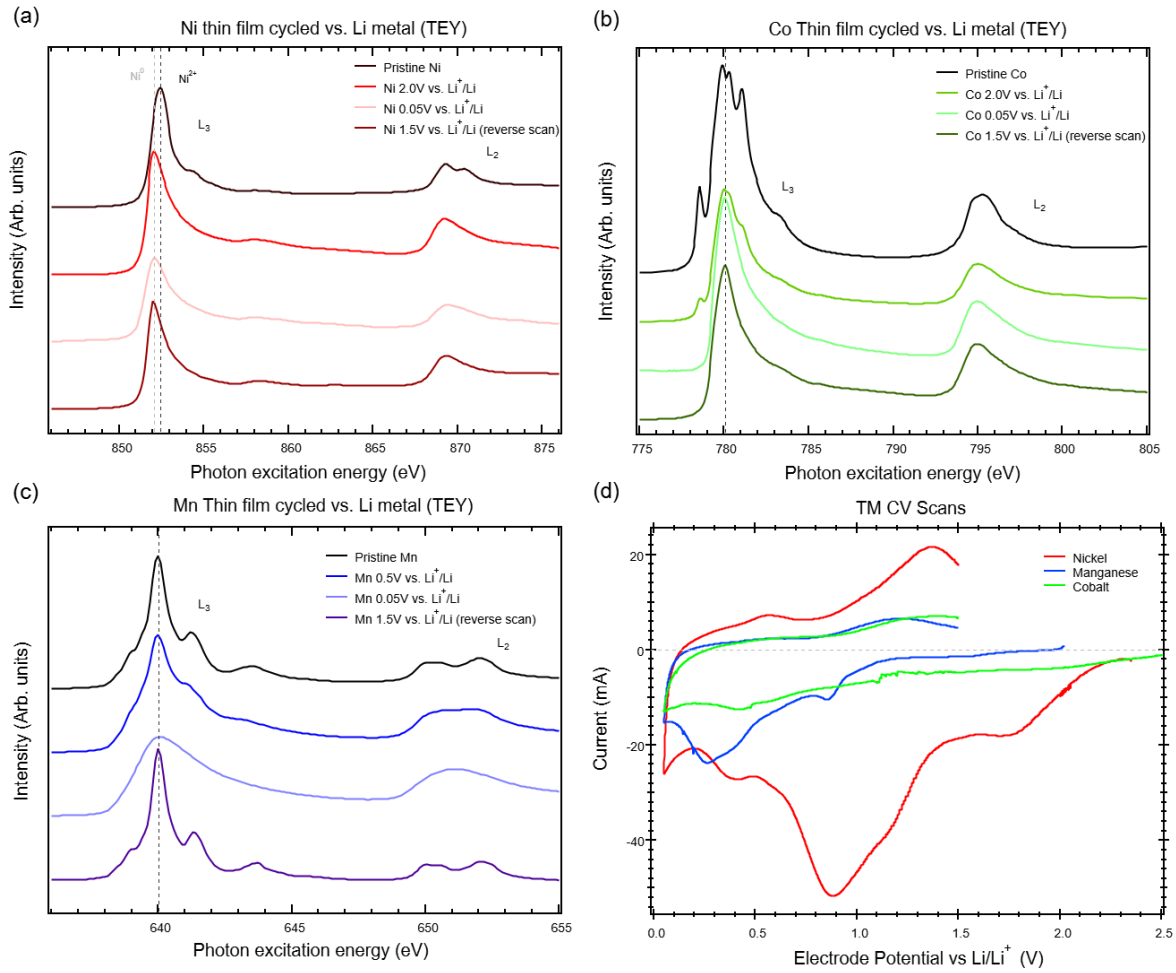

Figure 4.5. NEXAFS measurements of (a) Ni L-edge, (b) Mn L-edge, (c) Co L-edge and (d) CV seeps of the first cycle for Ni, Mn and Co vs Li/Li⁺.

After incorporation into the anode SEI, TMs can migrate towards the inner SEI and engage in ion exchange reactions with lithium salts. This proximity to the graphite electrode has the potential to facilitate the electrochemical reduction of TMs. To investigate the redox behaviour of TMs under reducing potentials, TMs (Ni, Mn, and Co) were deposited onto (16.0 mm diameter, 15 µm thick, 99.99%) Cu substrate. Subsequently, electrochemical cycling was performed to mimic the conditions encountered by TMs at the graphite electrode. NEXAFS measurements of the TM L edges were measured at B07-B beamline (DLS) to track the potential-dependent evolution of the TMs oxidation state with cells disassembled at fixed

potentials as displayed in Figure 4.5 in panels (a) -(c). A cyclic voltammetry (CV) sweep ranging from open circuit voltage (OCV) to 0.05 V to 2.0 V vs Li/Li^+ was employed to correlate the oxidation state with the electrochemistry of the TMs undergoing reduction and oxidation at the anode interface displayed in panel (d).

The initial CV sweep of nickel (Ni) versus Li/Li^+ exhibits four distinct reduction peaks at 1.5 V, 1.07 V, 0.6 V, and 0.39 V. However, none of these peaks correspond to Ni reduction, as NEXAFS measurements indicate that the Ni surface is already reduced by 2.0 V vs Li/Li^+ as seen by a shift to lower energy and increased asymmetry of the L_3 edge, as well as the disappearance of the split feature in the L_2 edge.[39] The peak at 1.5 V hints at the possible formation of lithium fluoride (LiF), likely arising from trace HF associated with hydrolysis of PF_6^- anions due to trace moisture within the electrolyte.[40] A further reduction peak at ~1.0 V is attributable to irreversible decomposition of the organic components in the electrolyte, associated particularly with LEDC/LEMC formation.[20] A redox couple at 0.9 V/1.4 V may be attributed to the partially reversible conversion reaction of lithium hydroxide (LiOH) into lithium oxide (Li_2O) and lithium hydride (LiH). This conversion process has been identified as a source of additional capacity generation in RuO_2 conversion electrodes.[41] At 0.39 V, another peak appears in the initial cathodic scan, indicating the formation of alkyl carbonate species and/or inorganic lithium compounds. The CV and NEXAFS measurements for Co electrodes exhibit similar trends to the Ni electrodes, with Co film reduction occurring around 2.0 V vs Li/Li^+. However, the Co electrode features a less prominent reduction peak at 1.07 V.

Measurements on the Mn show more significant variations from that seen for Ni. Four reduction peaks are observed in the initial CV sweep in the cathodic scan. The first peak at 1.3 V is linked to LiF formation due to trace HF in the electrolyte. At 0.85 V, another reduction

peak corresponds to electrolyte decomposition. By 0.5 V, NEXAFS measurements indicate the onset of electrochemical reduction on the Mn surface, confirmed by broadening features in the L_3 and L_2 edges, reaching full reduction at 50 mV. Upon sweeping the CV scan back up to 2.0 V, Mn undergoes reoxidation, indicating a reversible redox couple at 1.2 V/0.6 V associated with this process.

Electrochemical cycling of Spiked electrolyte

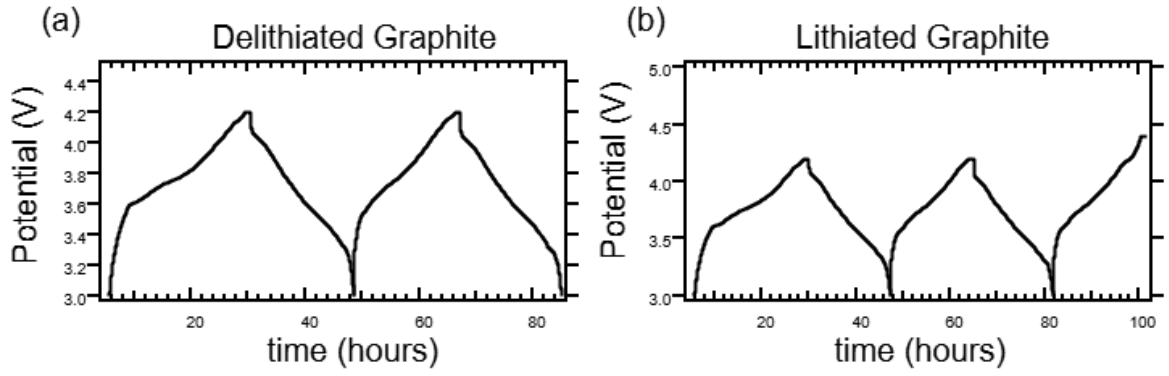

Figure 4.6. Galvanic cycling of NMC811 vs Graphite full cells containing spike NMC electrolyte (a) dilithiated graphite 3.0V (a) and (b) lithiated graphite 4.4V.

NMC-spiked electrolytes were employed to investigate the oxidation state of transition metals (Ni and Co) in a full-cell setup, aiming to understand the impact of TMs on the anode interface. Figure 4.6 presents two cells housing NMC811 and graphite electrodes immersed in the NMC-spiked electrolyte. Each cell underwent two formation cycles from 3.0 V to 4.2 V at a C-rate of 0.05 C. Panel (a) illustrates two formation cycles, while panel (b) depicts an additional half cycle up to 4.4 V to lithiate the graphite electrode. After galvanic cycling, graphite electrode in a lithiated and delithiated state were harvested from the cells in an Ar-filled glovebox (H_2O < 0.1 ppm, O_2 < 0.1 ppm, MBraun). The graphite electrodes were carefully removed without washing to prevent oxidation of metallic transition metals present on the electrodes. The electrodes were then immediately hermetically sealed in battery pouch material

(polypropylene inner layer, aluminium, and nylon outer layer) before transport to the beamline for XANES measurements. The samples were measured at the B18 beamline (DLS), focusing on measuring the Ni K- and Mn K-edges. Similar samples were also measured at the B07-B beamline (DLS) to investigate the oxidation state of the TMs near the surface (10-20 nm) of the SEI using TEY mode NEXAFS. [42] For the NEXAFS measurements the samples were washed with DMC prior to measurements to remove residual species (TM(II) $acac_2$, EC and $LiPF_6$) from the SEI surface.

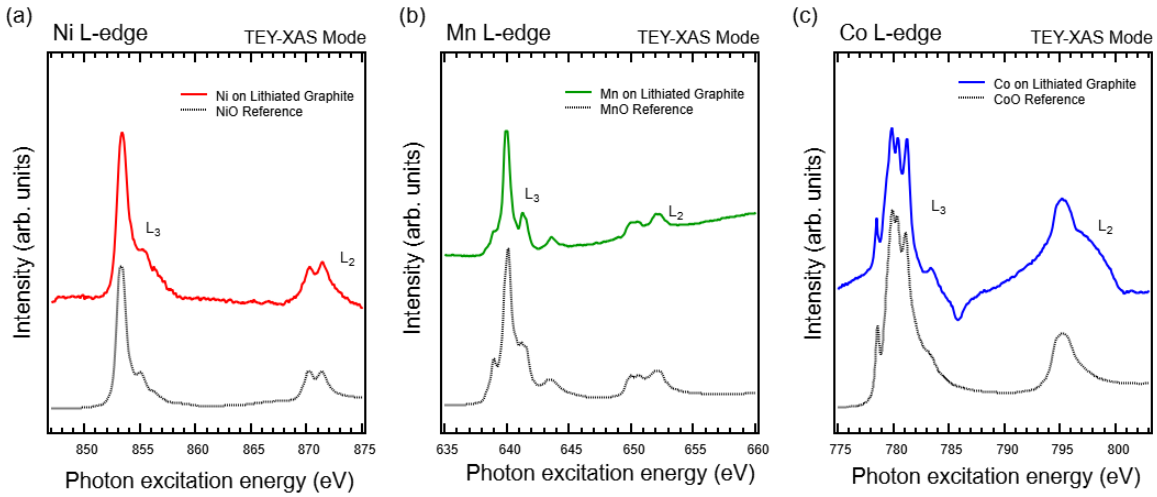

Figure 4.7 NEXAFS measurements of (a) Ni L-edge, (b) Mn L-edge and (c) Co L edge on the surface of lithiated graphite.

Figure 4.7 confirms that all TMs at the outer SEI predominantly exhibit a +2 oxidation state, reflecting their proximity to the electrolyte. While potentially controversial for oxidation state analysis, this washing step aimed to enhance the signal-to-noise ratio and eliminate TM(II) $acac_2$ precipitates on the SEI surface, ensuring only those trapped in the SEI are probed.[29,30]

Ni XANES on Graphite

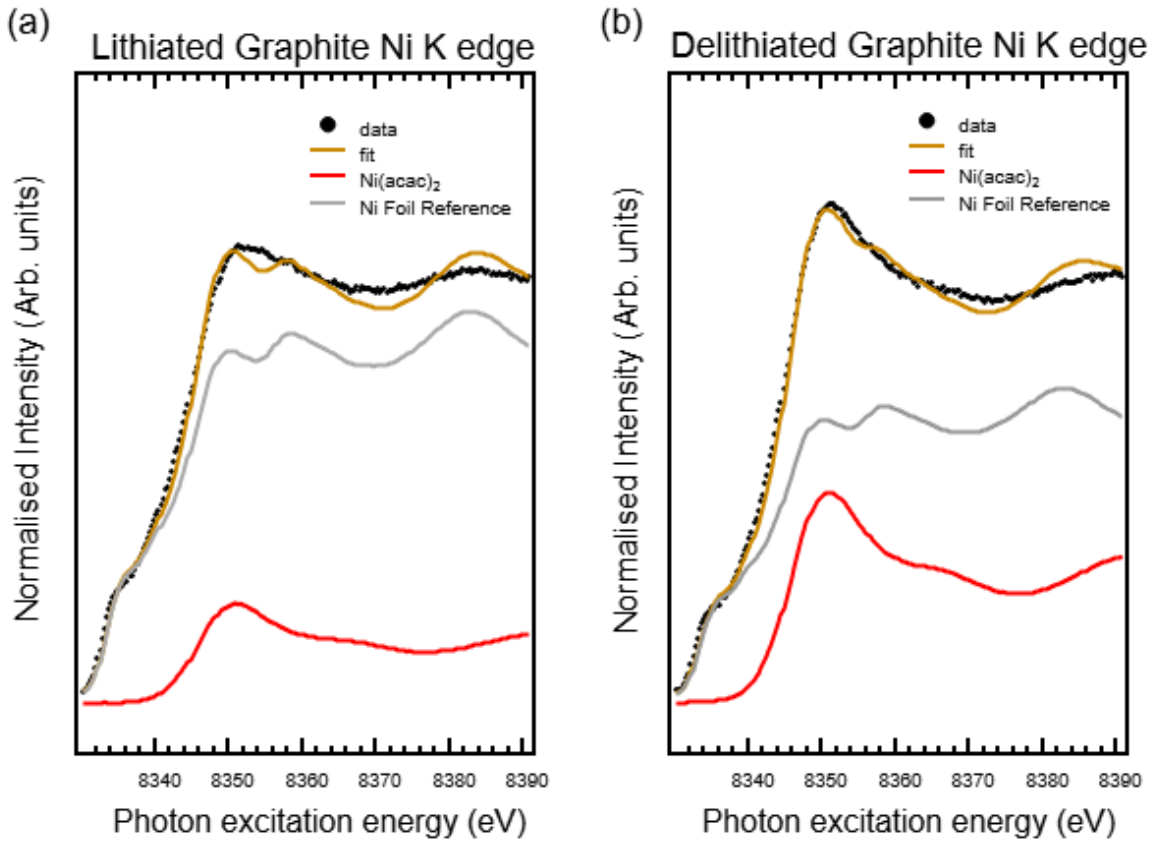

Figure 4.8. The normalised fluorescence Ni K-edge XANES spectra (a) Ni K edge of lithiated graphite and (b) delithiated graphite (shown as a scatter plot), while the fitted spectra from the LCA analysis are also plotted with individual weighted components (line plot).

The speciation of Ni at greater depths into in lithiated and delithiated graphite electrodes is discernible through XANES coupled with LCA. Analysis using reference spectra of Ni metal foil and Ni(II) $acac_2$ reveals metallic Ni as the predominant species on both electrodes, constituting 85.1% for lithiated graphite and 68.4% for delithiated graphite. Additionally, oxidized components in both electrodes correspond to Ni(II) $acac_2$, indicating the presence of Ni(II) species. It is noteworthy that other Ni(II) compounds within the SEI may also contribute to the observed spectra. The post-edge region of the spectra for graphite samples appears relatively flat and featureless, lacking the fine structures seen in the reference spectra,

particularly that of metallic Ni. This phenomenon is commonly observed in systems with particle sizes in the nanometer range (< 10 nm) or exhibiting severe structural disorder.[43]

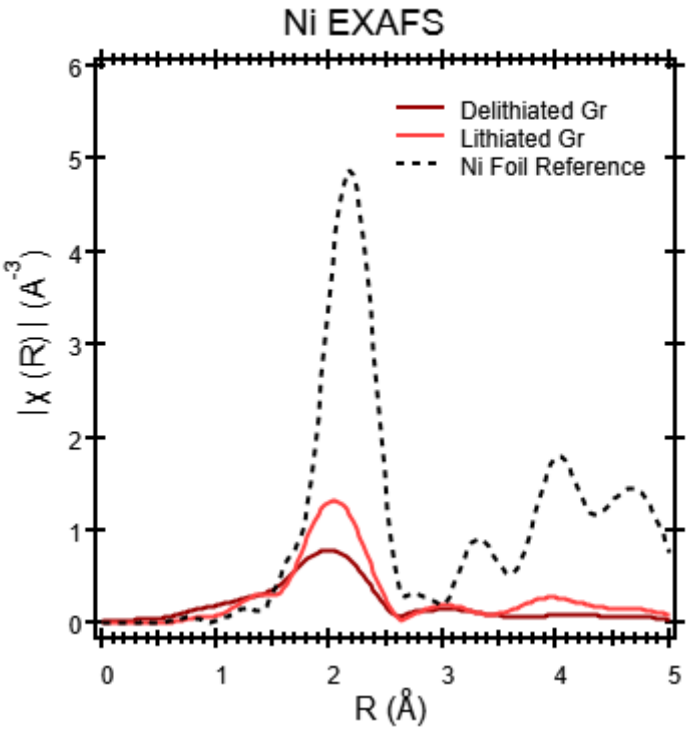

Figure 4.9. K^2 weighted phase uncorrected Ni K-edge FT-EXAFS moduli of lithiated graphite, delithiated graphite and Ni foil reference.

The Ni K-edge FT-EXAFS moduli of lithiated and delithiated graphite are shown alongside a Ni reference. Both lithiated and delithiated graphite electrodes reveal a weak intensity at 2.14 Å (phase uncorrected) most likely due to Ni-Ni scattering contribution from metallic species. A low R shoulder intensity is also observed in both samples that is likely due to Ni-O scattering from residual Ni(II)acac$_2$.

Mn XANES on Graphite

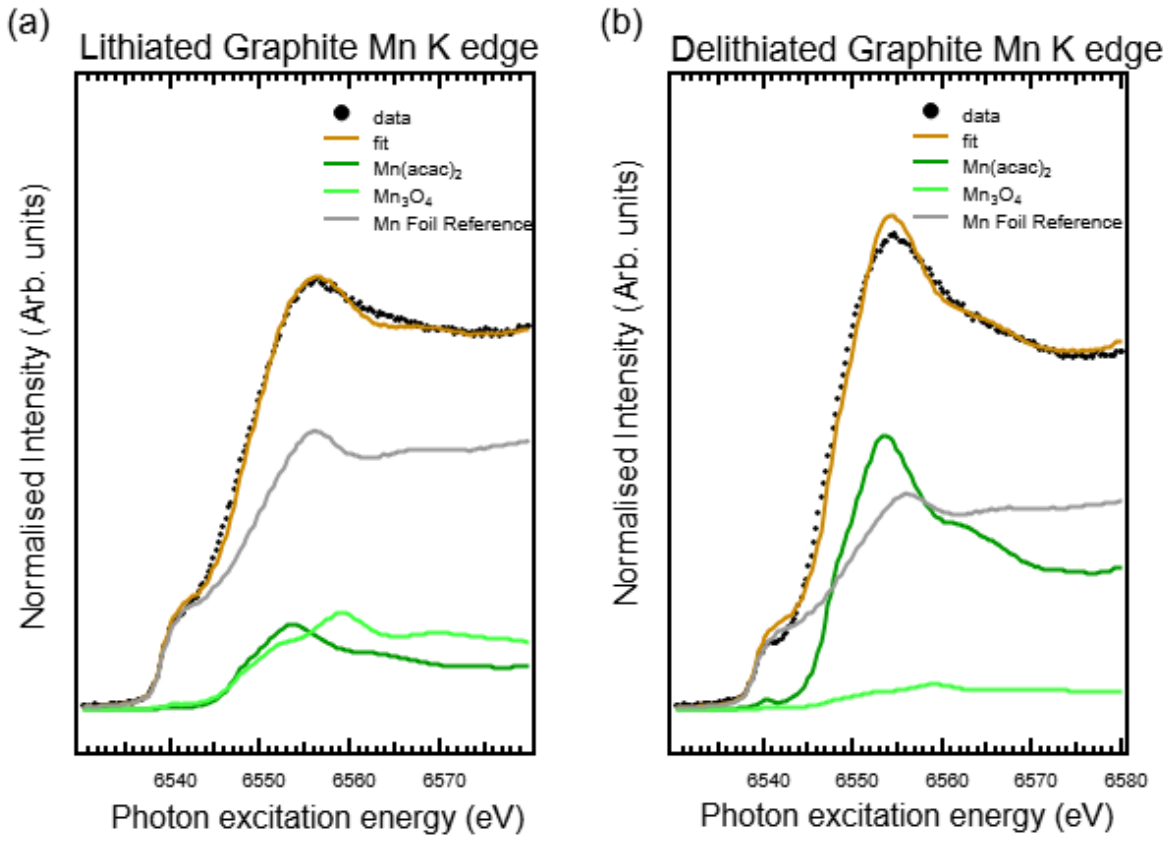

Figure 4.10. Normalised fluorescence Mn K-edge XANES spectra of (a) Ni K edge of lithiated graphite and (b) delithiated graphite (shown as scatter plot). The fitted spectra from the LCA analysis are plotted with individual weighted components (line plot).

The pronounced pre-edge feature observed in both lithiated and delithiated spectra, coupled with LCA fitting, signifies the presence of reduced Mn species (attributed to Mn^0 in the fit) on both electrodes. However, an additional oxidised component within the fitted data suggests that not all Mn species undergo reduction on the graphite. In the case of the other two reference standards, the pre-edge features arise from 1s–3d transitions that gain intensity through mixing with ligand orbitals with p-character.[44] Therefore, the intensity and position of this feature is sensitive to oxidation state, ligand type, and local symmetry. The oxidised components in both electrodes was fitted to Mn(II) $acac_2$ and Mn_3O_4. The obtained LCA values

for the lithiated and delithiated samples further elucidate the distribution and relative abundance of these Mn species, shedding light on the role Mn plays on the graphite electrode. On the lithiated graphite the metallic component is weighted as 69.5%, with Mn_3O_4 accounting for 17.7% and Mn (II)$acac_2$ for 12.8% respectively. On the delithiated graphite the metallic component is weighted as 53.9%, with Mn_3O_4 accounts for 4.6% and Mn (II)$acac_2$ accounting for 41.6% weighting respectively.

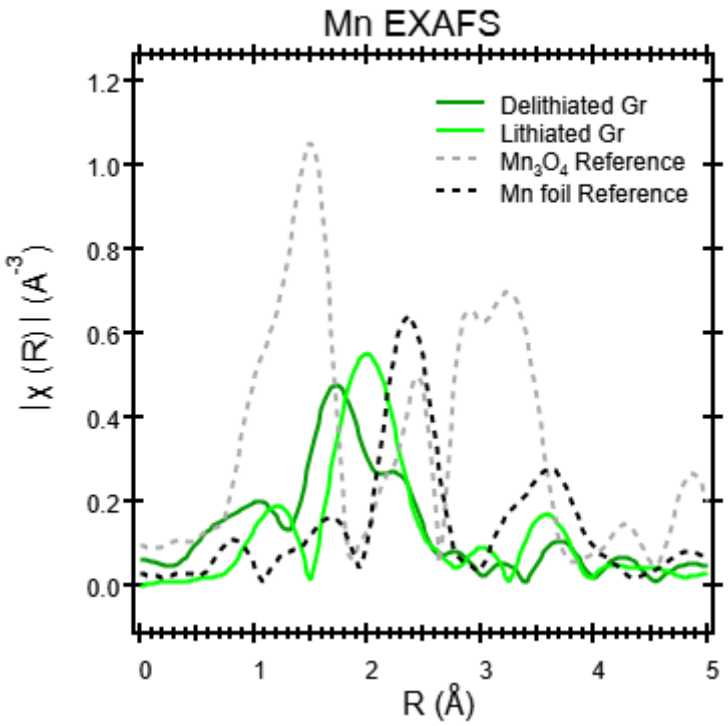

Figure 4.11. K^2 weighted phase uncorrected Ni K-edge FT-EXAFS moduli of lithiated graphite, delithiated graphite with accompanying Mn foil and Mn_3O_4 references.

The Mn K-edge FT-EXAFS moduli of lithiated and delithiated graphite are shown alongside metallic Mn and Mn_3O_4 mixed oxide reference. Both lithiated and delithiated graphite electrodes reveal a weak intensity around 2 Å (phase uncorrected) most likely due to multiple Mn-Mn scattering contributions from metallic species, although it is worth noting this intensity is shifted to lower R values compared to the Mn foil. Again a low R shoulder intensity

is also observed in both samples that is likely due to Mn-O scattering from residual Mn(II) $acac_2$.

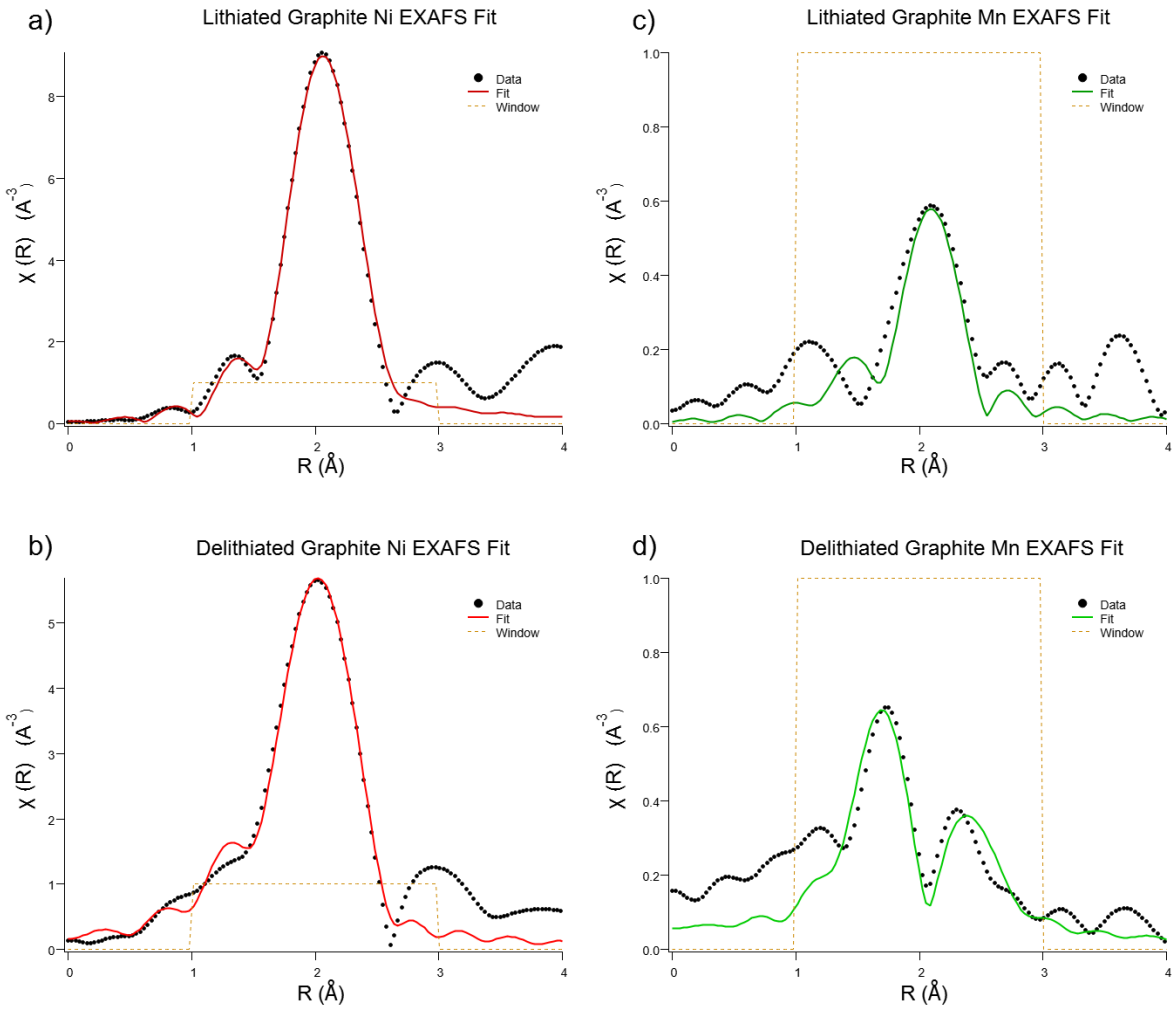

Figure 4.12. K^2 weighted phase uncorrected fitted FT-EXAFS moduli of a) Ni K-edge lithiated graphite, b)Ni K-edge delithiated graphite, c) Mn K-edge lithiated graphite, and d) Mn K-edge delithiated graphite.

Table 4.1. Results of Fitting the First Shell Fourier-Transformed Spectra at the Ni K-edge of lithiated and delithiated graphite with NiO and Ni foil references.

Sample/ Model	Scattering path	R (Å)	σ^2 (Å^2)	N	E_0 (eV)	R factor
Lithiated graphite (Ni)	Ni-O (Oxide)	1.890	0.0119	6 (fixed)	-9.5	0.0088
	Ni-Ni (Metallic)	2.472	0.0089	7.2		
Delithiated graphite (Ni)	Ni-O (Oxide)	1.966	0.0293	6 (fixed)	-12.9	0.172
	Ni-Ni (Metallic)	2.456	0.0092	6.1		

To confirm the identity of each scattering intensity and extract structural parameters, the EXAFS spectra of samples were fitted using the Artemis software of the Demeter package in R space. Scattering paths were calculated from crystal structure data of face-centred-cubic (FCC) metallic Ni (for metallic contribution) and rock salt NiO (for Ni-O contribution) using FEFF code v6L. A fitting range of 1.0-3.0 Å in R is used for all fits. The amplitude reduction factor was obtained from the refinement of simultaneously collected metallic Ni reference channel and fixed throughout the fitting procedure (0.689). Coordination number (*N*), changes in the absorber-backscattered distance (ΔR) and mean-square displacements, often referred to as the Debye-Waller factor (σ^2) were refined for each scattering path while the energy shift (ΔE_0) was refined globally. The fitted EXAFS spectra are shown in Figure 4.12a-b, and the values of refined parameters are tabulated in Table 4.1.

The average Ni-Ni coordination number of lithiated and delithiated graphite are 7.2 and 6.1, respectively (normalised to the metallic weight percentage using results from XANES LCA fit). Notably, these values do not converge to the expected bulk value of 12.[45] Reduction in average coordination number for metal nanoparticles is indicative of an increase in the surface to bulk atom ratio as the size of the particle decreases. These values suggest that the average metal particle size is in the <5 nm range.[46] The Ni-Ni bonding lengths are refined to 2.47 Å and 2.45

Å for lithiated and delithiated graphite, respectively. These values are consistent with the first shell Ni-Ni bond length for metallic species (2.530 Å for FCC Ni). They are significantly shorter than the second shell Ni-Ni distance seen in oxide (2.964 Å for NiO and 2.876 for $LiNiO_2$), confirming the metallic nature of the Ni species. In contrast, the bond length contraction relative to FCC Ni is a phenomenon often observed in metal nanoparticles.

Table 4.2. Results of Fitting the First Shell Fourier-Transformed Spectra at the Mn K-edge of lithiated and delithiated graphite with MnO and Mn foil references.

Sample/ Model	Scattering path	R (Å)	σ^2 (Å^2)	N or α	E_0 (eV)	R factor
Lithiated graphite (Mn)	Mn-O (Oxide)	1.882	0.0128	6 (fixed)	-5.2	0.16
	Mn-Mn (Metallic)	2.125	0.0038	0.63		
	Mn-Mn (Metallic)	2.211				
	Mn-Mn (Metallic)	2.281				
	Mn-Mn (Metallic)	2.375				
	Mn-Mn (Metallic)	2.421				
	Mn-Mn (Metallic)	2.467				
	Mn-Mn (Metallic)	2.514				
	Mn-Mn (Metallic)	2.548				
	Mn-Mn (Metallic)	2.592				
	Mn-Mn (Metallic)	2.724				
	Mn-Mn (Metallic)	2.758				
Delithiated graphite (Mn)	Mn-O (Oxide)	2.113	0.0046	6 (fixed)	9.7	0.09
	Mn-Mn (Metallic)	2.235	0.0089	0.76		
	Mn-Mn (Metallic)	2.326				
	Mn-Mn (Metallic)	2.399				
	Mn-Mn (Metallic)	2.498				
	Mn-Mn (Metallic)	2.546				
	Mn-Mn (Metallic)	2.594				
	Mn-Mn (Metallic)	2.643				
	Mn-Mn (Metallic)	2.680				
	Mn-Mn (Metallic)	2.726				
	Mn-Mn (Metallic)	2.865				
	Mn-Mn (Metallic)	2.901				

Again, to further confirm the identity of each scattering intensity and extract structural parameters, the Mn EXAFS spectra of both samples were fitted using the Artemis software of

the Demeter package in R space. Scattering paths were calculated from crystal structure data of FCC metallic (for metallic contribution) and Mn_3O_4 (for Mn-O contribution) using FEFF code v6L. Although metallic Mn is BCC, its unit cell is significantly more complex than other simple metals such as Co or Ni. Each unit cell contains four unique Mn sites and for the first shell Mn near neighbours, the FEFF generic pathfinder mechanism used in the Artemis software can generate up to 7 Mn-Mn single scattering paths for each site. To simplify the system whilst retaining the true complexity of the original structure as much as possible, the fuzzy degeneracy approximation is implemented in conjunction with aggregated FEFF calculation to the current EXAFS analysis. FEFF and the pathfinder are run for each inequivalent Mn site, and a path list is generated for each of them. All four path lists are then weighted by the fractional population of the site in the unit cell and merged together. Then the fuzzy degeneracy check is implemented over the merged path list, with paths grouped together according to their path length into bins of pre-set width (0.05 Å) and considered degenerate if their path lengths are within the same bin. Finally, using geometrical information from the fuzzily degenerate path list and photoelectron scattering factors computed from FEFF, backscattering contributions from each fuzzily degenerate path are generated by FEFF's normal mechanism. A fitting range of 1.0-3.0 Å in R is used for all fits. The amplitude reduction factor was obtained from the refinement of simultaneously collected metallic Mn reference channel using the aggregated FEFF and fixed throughout the fitting procedure (0.625). Instead of refining each N for eleven fuzzy Mn-Mn paths, a global pre-factor α is refined so N of each Mn-Mn path will vary proportionally. A similar approach is also used for ΔR (taking the isotropic contraction/expanding nature of the cubic lattice). The fitted EXAFS spectra are shown in Figure 4.12c-d and the value of refined parameters are tabulated in Table 4.2.

The α factors for the first shell Mn-Mn contribution of lithiated and delithiated graphite are 0.63 and 0.76, respectively. These values suggest that the average metal particle size is in the sub-5 nm range.[46] A significant bond-length/lattice contraction is also observed for the first shell Mn-Mn scattering (for reference, all second shell Mn-Mn scattering in Mn_3O_4 has a path length above 3 Å), which is consistent with the assignment of the Mn-Mn contribution been from metallic nanoparticles of less than 5 nm.

Discussion

TM Deposition Mechanism

Three lithium salts commonly encountered in the anode SEI (LiF, Li_2O, and Li_2CO_3) were employed to mimic SEI conditions, facilitating ion exchange with TM^{2+} species. Each of these salts was immersed in LP30 electrolytes spiked separately with $Ni(acac)_2$ and $Mn(acac)_2$. This ion exchange process involves a transition metal ion in the electrolyte replacing two lithium ions, requiring no additional electron charge compensation. Reaction mechanisms outlining this process are depicted in Figure 4.13:

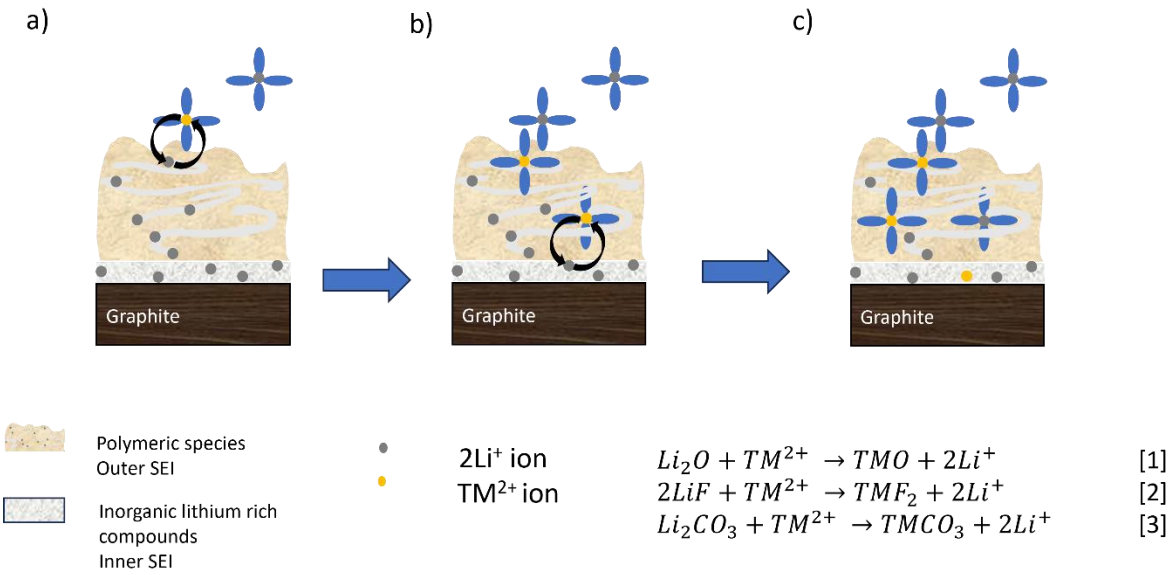

Figure 4.13. Schematic representation of ion exchange mechanism between TM^{2+} and $2Li^+$ ions.

In all instances, the exchange of TM^{2+} ions with lithium was observed using LCA to deconvolute the XANES spectra, except for the interaction between Li_2CO_3 and Mn^{2+}. During the ion exchange reaction with Ni^{2+}, LCA analysis unveiled the formation of a basic $Ni(CO_3)$ precipitate, indicating potential coordination between Ni^{2+} ions and carbonates in the electrolyte, or possibly side reactions. For ion exchange involving Mn^{2+} in the electrolyte, ion exchange occurred most preferably with LiF followed by Li_2O. Notably, in the absence of $LiPF_6$ in the

electrolyte, significant ion exchange reactions were not observed, as determined by XANES measurements in Figure 4.4. This suggests that Mn(II) ions in the electrolyte solvate with PF_6^- and/or F^- anions derived from $LiPF_6$ or HF (resulting from degraded $LiPF_6$ due to trace moisture in the electrolyte)[47] to facilitate the exchange reactions. Mn^{2+} did not interact significantly with Li_2CO_3 to form $MnCO_3$ salts, hinting at Li_2CO_3 as a possible suppressant of spontaneous ion exchange between Mn^{2+} and Li^+ ions. Nevertheless, carbonates, implicated in electrolyte degradation, may trigger an electrocatalytic reaction involving Mn^{2+} ions in the SEI. Leung et al.[48] proposed an electron transfer mechanism in which EC undergoes ring opening, forming a radical anion that binds to Li^+ ions in the SEI. This process initiates the anionic polymerisation of EC into an open-chain carbonate anion, trapping Mn^{2+} ions. Subsequently, Mn^{2+} ions create an active centre by complexing with these anions. Upon accepting electrons, these anions are reduced to alkoxide anions, generating $CO_2^{\cdot}$ Radicals which then diffuse through the outer SEI matrix, reducing the solvent and forming CO_2 while simultaneously trapping lithium. As carbonates replace oxides within the inner sphere of the electrocatalytic centre, the centre undergoes turnover.[48,49] This suggests a plausible degradation mechanism wherein Mn^{2+} ions on the outer SEI contribute to capacity fade. At the same time, the reduction of TMs on the graphite electrode induces reactions that further enhance SEI growth, which is discussed later in this chapter. However, these viewpoints are not mutually exclusive, as discussed below.

TM Redox Behaviour

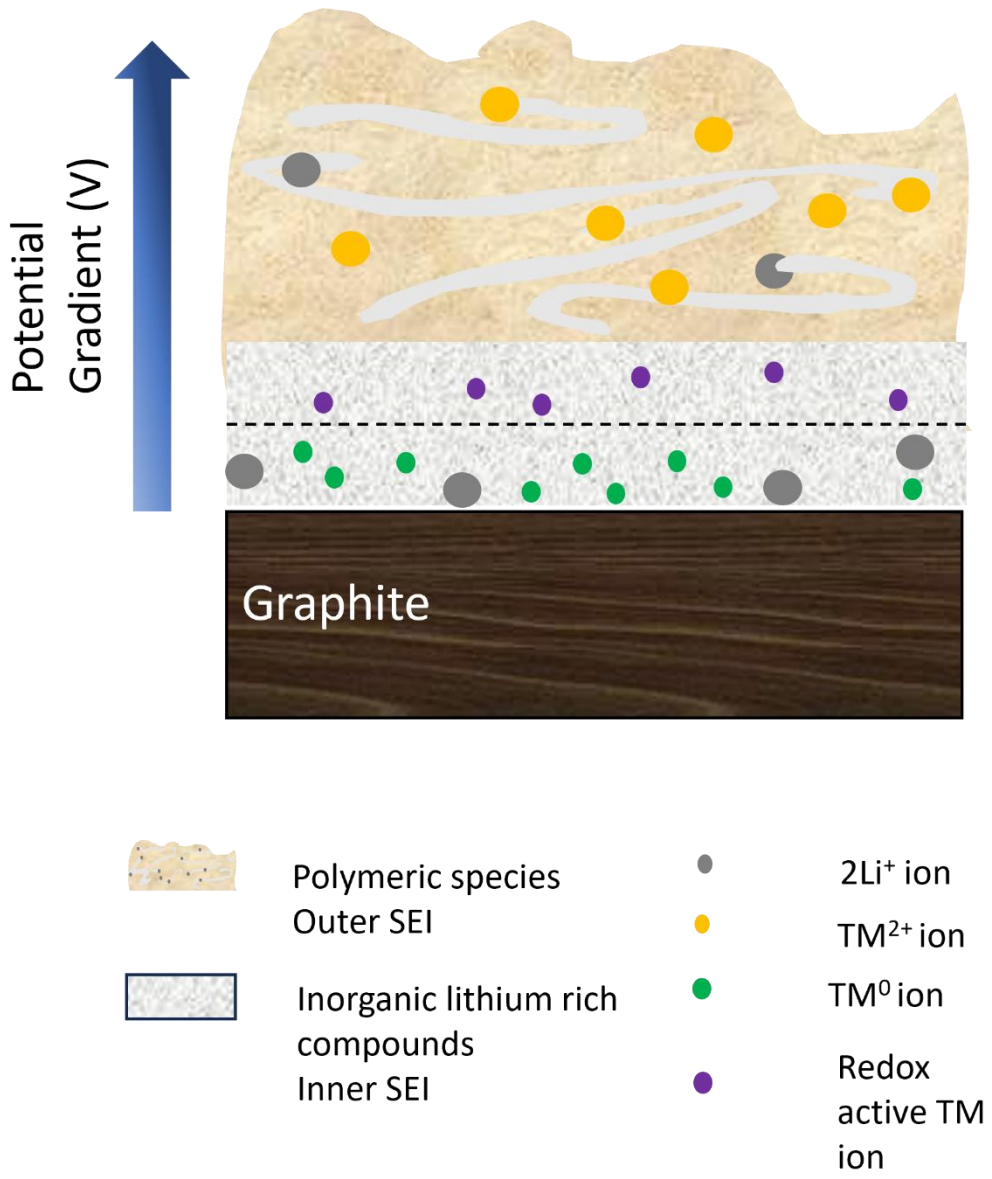

Figure 4.14. Schematic illustrating the potential gradient across the SEI layer.

Figure 4.14 illustrates how TMs are arranged on graphite electrodes. The x-ray spectroscopy measurements reveal a gradient of oxidation state across the SEI. Surface-sensitive NEXAFS measurements probing the top 10-20 nm of the SEI reveal the presence of trapped TM^{2+} in the primarily polymeric, organic component of the SEI. Based on the ion exchange mechanism previously discussed, these TM^{2+} ions will most likely migrate to the inner SEI driven by a

concentration gradient and undergo an exchange reaction with lithium salts. More bulk sensitive XANES measurements reveal more reduced TM species near the graphite surface. Based on the LCA XANES analysis, Mn undergoes noticeable redox reactions during graphite's lithiation and delithiation, whereas Ni species within the inner SEI exhibit less pronounced activity. Metallic Ni predominates on both lithiated and delithiated graphite electrodes, constituting 85.1% and 68.4% (atomic weight %), respectively. Conversely, Mn species on graphite appear more oxidised, with the metallic component comprising 69.5% on lithiated graphite and 53.9% on delithiated graphite (atomic weight %). Unfortunately, no data was collected on the Co due to mechanical errors at the beamline; however, based on the NEXAFS measurements on model thin film Co, it is reasonable to assume that the Co will behave more similarly to the Ni species rather than the Mn species on the graphite. The particle size was calculated using EXAFS refinement, showing that the Ni and Mn particles on both lithiated and delithiated electrodes were <5 nm. The Mn particles are slightly smaller than the Ni nanoparticles on both electrodes, which can cause surface strain and potentially destabilise the nanoparticles' surface making them highly reactive.

Both lithiated and delithiated graphite electrodes harvested from full cells containing the NMC salt electrolyte show reduced TM present on the electrode, which could result from the NMC salt being present in the electrolyte before the SEI has fully formed or that the graphite potential vs Li/Li^+ will not exceed ~0.3 V when the graphite electrode is delithiated.[50] According to the NEXAFS measurements depicted in Figure 4.5, one might expect all TMs to remain in their reduced state. However, the presence of oxidised TM species on the electrode suggests that the distribution of TMs throughout the SEI is influenced by the potential gradient across the SEI, as described in Figure 4.14.

After deposition into the SEI, TMs undergo a conversion electrode-type reaction (TM^{2}+ $2e^{-}$ →TM^{0}). Conversion reactions are notorious for high capacity losses, especially in initial cycles, due to irreversible side reactions. However, as discussed in the chapter's introduction, the observed capacity fade cannot be solely attributed to these two-electron conversion reactions.[51,52] TMs in close proximity to the graphite surface act as catalysts, initiating side reactions that modify the composition of the SEI. Metallic TM nanoparticles within the SEI can act as electron conductive pathways through an insulating SEI. This can cause further reduction of the electrolyte growing the SEI and forming products containing carboxylate groups, like ethylene dicarbonate, which have been reported to impede Li^{+} ion migration during anode delithiation. This altered SEI hinders the diffusion of Li^{+} ions during charging, resulting in the accumulation of impedance. The thickened SEI promotes lithium metal deposition, a process catalysed by previously deposited TM species. Initially, uniform lithium metal deposits form, driven by an electrostatic shielding mechanism influenced by the presence of TM species. Continued cycling prompts SEI growth and TM deposition, resulting in lithium dendrite formation. Further cycling exacerbates SEI fracture, promoting more dendritic lithium metal growth, contributing to capacity fade and, in severe cases, short-circuiting of the battery.[53,54] During high-rate or low-temperature charging, slow Li^{+} diffusion within the SEI causes significant voltage polarisation, worsening lithium plating. The presence of metallic nanoparticles like Mn, Ni, and Co during graphite lithiation around 0.1 V vs Li/Li^{+} could enable metallic lithium formation via underpotential deposition.[55] Additionally, trapped lithium within the SEI can induce electrode slippage due to capacity mismatches of the anode and cathode, leading to potential shifts and pushing the cathode to higher cutoff potentials.[27,56] This, in turn, exacerbates side reactions at the cathode-electrolyte interface, including further transitional metal dissolution.[57]

Conclusion

Combining hard and soft X-ray techniques offers depth-dependent information on the chemical state of TM species that are incorporated into the graphite SEI. NEXAFS measurements reveal Ni, Mn, and Co in a +2 oxidation state in the outer SEI, most likely trapped by polymeric organic species. The discussed ion exchange mechanism provides insight into TM migration towards the inner SEI. Compelling evidence from XANES measurements supports ion exchange experiments between Ni^{2+} and lithium oxide (Li_2O), lithium fluoride (LiF), and lithium carbonate (Li_2CO_3) within the SEI. Similarly, XANES analysis indicates ion exchange between Mn^{2+} and both LiF and Li_2O. Notably, the absence of ion exchange between Mn^{2+} and Li_2CO_3 suggests a potential lithium-based salt blocking Mn^{2+} permeation into the inner SEI.

NEXAFS measurements on thin film model electrodes demonstrate that Ni and Co undergo reduction at 50 mV vs Li/Li^+ and remain reduced at 1.5 V vs Li/Li^+ upon the reverse scan, indicating metallic behaviour based on the accompanying TM L-edge spectra. Similarly, evaporated Mn undergoes reduction at 50 mV vs Li/Li^+ but oxidises at 1.2 V vs Li/Li^+ upon reverse scan, as revealed by CV curves and the Mn L-edge spectra.

XANES measurements on lithiated and delithiated graphite electrodes cycled in full cells with NMC salt electrolyte unveil metallic TMs near the graphite surface and/or within the inner SEI in both states of charge, forming <5 nm-sized particles identified by EXAFS. Mn deposited in the inner SEI exhibits heightened redox activity (compared with Ni) acting as a catalyst within the SEI. This hampers Li^+ diffusion pathways by reacting with gas produced during the electrolyte's electrochemical reduction.

Furthermore, metallic nanoparticles formed through a conversion reaction on the SEI can induce underpotential deposition of lithium, leading to dendrite formation, which poses a significant risk of rapid capacity fade and critical battery failure through short-circuiting. A key finding is Mn exhibits heightened redox activity compared with Ni on the SEI.

References

1. Li, M., Lu, J., Chen, Z. & Amine, K. 30 Years of Lithium-Ion Batteries. *Advanced Materials* **30**, 1–24 (2018).

2. Manthiram, A. A reflection on lithium-ion battery cathode chemistry. *Nat Commun* **11**, 1–9 (2020).

3. Yi, T. F., Mei, J. & Zhu, Y. R. Key strategies for enhancing the cycling stability and rate capacity of LiNi0.5Mn1.5O4 as high-voltage cathode materials for high power lithium-ion batteries. *J Power Sources* **316**, 85–105 (2016).

4. Xiang, W. *et al.* Hydrothermal synthesis, evolution, and electrochemical performance of LiMn0.5Fe0.5PO4 nanostructures. *Physical Chemistry Chemical Physics* **17**, 18629–18637 (2015).

5. Lun, Z. *et al.* Design Principles for High-Capacity Mn-Based Cation-Disordered Rocksalt Cathodes. *Chem* **6**, 153–168 (2020).

6. Björklund, E. *et al.* Cycle-Induced Interfacial Degradation and Transition-Metal Cross-Over in LiNi0.8Mn0.1Co0.1O2-Graphite Cells. *Chemistry of Materials* **34**, 2034–2048 (2022).

7. Buchberger, I. *et al.* Aging Analysis of Graphite/LiNi 1/3 Mn 1/3 Co 1/3 O 2 Cells Using XRD, PGAA, and AC Impedance . *J Electrochem Soc* **162**, A2737–A2746 (2015).

8. Zheng, H., Sun, Q., Liu, G., Song, X. & Battaglia, V. S. Correlation between dissolution behavior and electrochemical cycling performance for LiNi 1/3Co 1/3Mn 1/3O 2-based cells. *J Power Sources* **207**, 134–140 (2012).

9. Gallus, D. R. *et al.* The influence of different conducting salts on the metal dissolution and capacity fading of NCM cathode material. *Electrochim Acta* **134**, 393–398 (2014).

10. Wandt, J. *et al.* Transition metal dissolution and deposition in Li-ion batteries investigated by operando X-ray absorption spectroscopy. *J Mater Chem A Mater* **4**, 18300–18305 (2016).

11. Zhan, C., Wu, T., Lu, J. & Amine, K. Dissolution, migration, and deposition of transition metal ions in Li-ion batteries exemplified by Mn-based cathodes-A critical review. *Energy and Environmental Science* vol. 11 243–257 Preprint at https://doi.org/10.1039/c7ee03122j (2018).

12. Peled, E. & Menkin, S. Review—SEI: Past, Present and Future. *J Electrochem Soc* **164**, A1703–A1719 (2017).

13. Urisu, T., Takahashi, J. & Utsumi, Y. *Synthesis Conditions and Oxygen Stoichiometry Effects on Li Insertion into the Spinel LiMn 2 O 4 You May Also like Synchrotron RadiationAssisted Si Epitaxial Growth Using Si 2 H 6 and SiH 2 Cl 2 Gases: Properties in the Low Temperature Region*. *J. Electrochem. Soc* vol. 141 (1994).

14. Shkrob, I. A. *et al.* Manganese in graphite anode and capacity fade in Li ion batteries. *Journal of Physical Chemistry C* **118**, 24335–24348 (2014).

15. Zhan, C., Qiu, X., Lu, J. & Amine, K. Tuning the Mn Deposition on the Anode to Improve the Cycle Performance of the Mn-Based Lithium Ion Battery. *Adv Mater Interfaces* **3**, (2016).

16. Zhan, C. *et al.* Mn(II) deposition on anodes and its effects on capacity fade in spinel lithium manganate-carbon systems. *Nat Commun* **4**, (2013).

17. Solchenbach, S., Hong, G., Freiberg, A. T. S., Jung, R. & Gasteiger, H. A. Electrolyte and SEI Decomposition Reactions of Transition Metal Ions Investigated by On-Line Electrochemical Mass Spectrometry. *J Electrochem Soc* **165**, A3304–A3312 (2018).

18. Joshi, T., Eom, K., Yushin, G. & Fuller, T. F. Effects of Dissolved Transition Metals on the Electrochemical Performance and SEI Growth in Lithium-Ion Batteries. *J Electrochem Soc* **161**, A1915–A1921 (2014).

19. Ruff, Z., Xu, C. & Grey, C. P. Transition Metal Dissolution and Degradation in NMC811-Graphite Electrochemical Cells. *J Electrochem Soc* **168**, 060518 (2021).

20. Zhuo, Z. *et al.* Breathing and oscillating growth of solid-electrolyte-interphase upon electrochemical cycling. *Chemical Communications* **54**, 814–817 (2018).

21. Peled, E. *et al.* Composition, depth profiles and lateral distribution of materials in the SEI built on HOPG-TOF SIMS and XPS studies. *J Power Sources* **97–98**, 52–57 (2001).

22. Schellenberger, M., Golnak, R., Quevedo Garzon, W. G., Risse, S. & Seidel, R. Accessing the solid electrolyte interphase on silicon anodes for lithium-ion batteries in-situ through transmission soft X-ray absorption spectroscopy. *Mater Today Adv* **14**, (2022).

23. Swallow, J. E. N. *et al.* Revealing solid electrolyte interphase formation through interface-sensitive Operando X-ray absorption spectroscopy. *Nat Commun* **13**, (2022).

24. Guo, R. & Gallant, B. M. Li2O Solid Electrolyte Interphase: Probing Transport Properties at the Chemical Potential of Lithium. *Chemistry of Materials* **32**, 5525–5533 (2020).

25. Shkrob, I. A., Zhu, Y., Marin, T. W. & Abraham, D. Reduction of carbonate electrolytes and the formation of solid-electrolyte interface (SEI) in lithium-ion batteries. 1. Spectroscopic observations of radical intermediates generated in one-electron reduction of carbonates. *Journal of Physical Chemistry C* **117**, 19255–19269 (2013).

26. Shkrob, I. A., Zhu, Y., Marin, T. W. & Abraham, D. Reduction of carbonate electrolytes and the formation of solid-electrolyte interface (SEI) in lithium-ion batteries. 2. Radiolytically induced polymerization of ethylene carbonate. *Journal of Physical Chemistry C* **117**, 19270–19279 (2013).

27. Björklund, E. *et al.* Cycle-Induced Interfacial Degradation and Transition-Metal Cross-Over in LiNi0.8Mn0.1Co0.1O2-Graphite Cells. *Chemistry of Materials* **34**, 2034–2048 (2022).

28. Xiao, X. *et al.* Unraveling manganese dissolution/deposition mechanisms on the negative electrode in lithium ion batteries. *Physical Chemistry Chemical Physics* **16**, 10398–10402 (2014).

29. Ochida, M. *et al.* Influence of Manganese Dissolution on the Degradation of Surface Films on Edge Plane Graphite Negative-Electrodes in Lithium-Ion Batteries. *J Electrochem Soc* **159**, A961–A966 (2012).

30. Gowda, S. R. *et al.* Oxidation state of cross-over manganese species on the graphite electrode of lithium-ion cells. *Physical Chemistry Chemical Physics* **16**, 6898–6902 (2014).

31. Delacourt, C. *et al.* Effect of Manganese Contamination on the Solid-Electrolyte-Interphase Properties in Li-Ion Batteries Effect of Manganese Contamination on the Solid-Electrolyte-Interphase Properties in Li-Ion Batteries. (2013) doi:10.1149/2.035308jes.

32. Kuiper, P., Kruizinga, G., Ghijsen, J., Sawatzky, G. A. & Verweij, H. Character of Holes in LixNi1−xO and Their Magnetic Behavior . *Phys Rev Lett* **62**, 1214–1214 (1989).

33. Frati, F., Hunault, M. O. J. Y. & De Groot, F. M. F. Oxygen K-edge X-ray Absorption Spectra. *Chemical Reviews* vol. 120 4056–4110 Preprint at https://doi.org/10.1021/acs.chemrev.9b00439 (2020).

34. Dent, A. J. *et al.* B18: A core XAS spectroscopy beamline for Diamond. in *Journal of Physics: Conference Series* vol. 190 (Institute of Physics Publishing, 2009).

35. Ravel, B. & Newville, M. ATHENA, ARTEMIS, HEPHAESTUS: Data analysis for X-ray absorption spectroscopy using IFEFFIT. in *Journal of Synchrotron Radiation* vol. 12 537–541 (2005).

36. Peck, M. A. & Langell, M. A. Comparison of nanoscaled and bulk NiO structural and environmental characteristics by XRD, XAFS, and XPS. *Chemistry of Materials* **24**, 4483–4490 (2012).

37. Anspoks, A., Kuzmin, A., Kalinko, A. & Timoshenko, J. Probing NiO nanocrystals by EXAFS spectroscopy. *Solid State Commun* **150**, 2270–2274 (2010).

38. Vissers, D. R. *et al.* Role of Manganese Deposition on Graphite in the Capacity Fading of Lithium Ion Batteries. *ACS Appl Mater Interfaces* **8**, 14244–14251 (2016).

39. Weatherup, R. S., Wu, C. H., Escudero, C., Pérez-Dieste, V. & Salmeron, M. B. Environment-Dependent Radiation Damage in Atmospheric Pressure X-ray Spectroscopy. *Journal of Physical Chemistry B* **122**, 737–744 (2018).

40. Strmcnik, D. *et al.* Electrocatalytic transformation of HF impurity to H2 and LiF in lithium-ion batteries. *Nat Catal* **1**, 255–262 (2018).

41. Hu, Y. Y. *et al.* Origin of additional capacities in metal oxide lithium-ion battery electrodes. *Nat Mater* **12**, 1130–1136 (2013).

42. Frazer, B. H., Gilbert, B., Sonderegger, B. R. & De Stasio, G. The probing depth of total electron yield in the sub-keV range: TEY-XAS and X-PEEM. *Surf Sci* **537**, 161–167 (2003).

43. Molenbroek, A. M., Nørskov, J. K. & Clausen, B. S. Structure and reactivity of Ni-Au nanoparticle catalysts. *Journal of Physical Chemistry B* **105**, 5450–5458 (2001).

44. Yamamoto, T. Assignment of pre-edge peaks in K-edge x-ray absorption spectra of 3d transition metal compounds: Electric dipole or quadrupole? *X-Ray Spectrometry* vol. 37 572–584 Preprint at https://doi.org/10.1002/xrs.1103 (2008).

45. Nayak, S. K., Khanna, S. N., Rao, B. K. & Jena, P. *Physics of Nickel Clusters: Energetics and Equilibrium Geometries*. https://pubs.acs.org/sharingguidelines (1996).

46. Beale Andrew M. & Weckhuysen, B. M. EXAFS as a tool to interrogate the size and shape of mono and bimetallic catalyst nanoparticles. *Physical Chemistry Chemical Physics* vol. 12 5502 Preprint at https://doi.org/10.1039/c0cp90010a (2010).

47. Phelan, C. M. E. *et al.* Role of Salt Concentration in Stabilizing Charged Ni-Rich Cathode Interfaces in Li-Ion Batteries. doi:10.1021/acs.chemmater.4c00004.

48. Leung, K. First-Principles Modeling of Mn(II) Migration above and Dissolution from LixMn2O4 (001) Surfaces. *Chemistry of Materials* **29**, 2550–2562 (2017).

49. Gilbert, J. A., Shkrob, I. A. & Abraham, D. P. Transition Metal Dissolution, Ion Migration, Electrocatalytic Reduction and Capacity Loss in Lithium-Ion Full Cells. *J Electrochem Soc* **164**, A389–A399 (2017).

50. Klett, M., Gilbert, J. A., Pupek, K. Z., Trask, S. E. & Abraham, D. P. Layered Oxide, Graphite and Silicon-Graphite Electrodes for Lithium-Ion Cells: Effect of Electrolyte Composition and Cycling Windows. *J Electrochem Soc* **164**, A6095–A6102 (2017).

51. Yu, S. H., Lee, S. H., Lee, D. J., Sung, Y. E. & Hyeon, T. Conversion Reaction-Based Oxide Nanomaterials for Lithium Ion Battery Anodes. *Small* **12**, 2146–2172 (2016).

52. Malini, R., Uma, U., Sheela, T., Ganesan, M. & Renganathan, N. G. Conversion reactions: A new pathway to realise energy in lithium-ion battery - Review. *Ionics* vol. 15 301–307 Preprint at https://doi.org/10.1007/s11581-008-0236-x (2009).

53. Klein, S. *et al.* Exploiting the Degradation Mechanism of NCM523‖ Graphite Lithium-Ion Full Cells Operated at High Voltage. *ChemSusChem* **14**, 595–613 (2021).

54. Klein, S. *et al.* Understanding the Outstanding High-Voltage Performance of NCM523||Graphite Lithium Ion Cells after Elimination of Ethylene Carbonate Solvent from Conventional Electrolyte. *Advanced Energy Materials* vol. 11 Preprint at https://doi.org/10.1002/aenm.202003738 (2021).

55. Li, W., Kim, U. H., Dolocan, A., Sun, Y. K. & Manthiram, A. Formation and Inhibition of Metallic Lithium Microstructures in Lithium Batteries Driven by Chemical Crossover. *ACS Nano* **11**, 5853–5863 (2017).

56. Dose, W. M. *et al.* Article Effect of Anode Slippage on Cathode Cutoff Potential and Degradation Mechanisms in Ni- Rich Li-Ion Batteries Effect of Anode Slippage on Cathode Cutoff Potential and Degradation Mechanisms in Ni-Rich Li-Ion Batteries. *Cell Rep Phys Sci* **1**, 100253.

57. Gilbert, J. A., Shkrob, I. A. & Abraham, D. P. Transition Metal Dissolution, Ion Migration, Electrocatalytic Reduction and Capacity Loss in Lithium-Ion Full Cells. *J Electrochem Soc* **164**, A389–A399 (2017).

Chapter 5 - Revealing the Potential-dependant Evolution of the SEI Using Operando NEXFAS

Abstract

The solid electrolyte interphase (SEI) is a complex layer formed on the surface of electrodes, which impacts the battery's performance, including longevity and operational efficiency. Understanding the behaviour of the SEI under operating conditions will be critical to enhancing its performance. Operando x-ray absorption spectroscopy (XAS) characterisation techniques developed as part of this thesis chapter can capture vital information about potential-dependent species formed, including the structural and chemical transformation of the SEI. Chapter 5 details the utilisation of operando near-edge X-ray absorption fine structure (NEXAFS) technique, probing surface-sensitive electrochemical dynamics on liquid-immersed interfaces. The chapter introduces the design of a novel ultra-high vacuum-compatible electrochemical cell featuring SiN_x membranes, enabling the investigation of the potential-dependent evolution of the SEI by tracking the changes in the electronic structure. This chapter serves as a crucial resource for battery researchers on the chemical makeup of the SEI.

Introduction

Ex-situ analysis has been pivotal for characterising lithium-ion batteries and elucidating on chemical transformations at electrode interfaces. This “post-mortem” analysis has been instrumental in unravelling mechanisms governing the formation of surface layers, notably the solid electrolyte interphase (SEI) and the cathode electrolyte interface (CEI), which impact battery performance.[1–5] However, the limitations of ex-situ techniques become evident in their inability to capture the transient nature of surface layer evolution during electrochemical cycling. Furthermore, post-mortem analysis fails to discern intermediate species formed during electrochemical cycling and washing and drying steps typically undertaken for ex-situ analysis can inflict irreversible damage[6], contaminate the sample and/or remove important artefacts from the electrode surface.[7]

Addressing these challenges, this chapter presents an innovative approach towards an enclosed operando cell design to achieve representative electrochemical performance whilst performing spectroscopy. O, F and TM L-edge absorption spectra are measured under applied bias; this methodology avoids the loss of critical information and potential ambiguity associated with conventional post-mortem measurement approaches. The operando soft X-ray absorption spectroscopy (XAS) in interface-sensitive total electron yield (TEY) mode and complementary bulk-sensitive fluorescent yield (FY) is demonstrated as a powerful technique for probing both organic and inorganic components during SEI formation. This method allows access to light elements forming at buried electrode-electrolyte interfaces, owing to the micrometre-scale penetration of incident x-rays and the nanometre-scale interface sensitivity of photo-generated auger and secondary electrons at the electrode-electrolyte interface.

The principle focus for the research in this chapter was to investigate the SEI formation on transition metal surfaces, with particular focus on Ni and MnO systems as these TMs have caused significant problems once incorporated into the SEI detailed in chapter 4. To probe the SEI evolution, an operando soft XAS approach was developed utilising a novel operando cell. This was compared with ex-situ analyses on the same samples to inform a holistic view on SEI formation on thin film Ni and MnO. Originally, the project aimed to build upon the research conducted in Chapter 4, employing Ni and Mn metals as model surfaces to investigate their behaviour under reducing conditions similar to those of TMs incorporated into the anode SEI in lithium-ion batteries. However, the Mn electrodes fabricated for this study were found to consist of MnO rather than Mn metal. While this deviation prevented a direct comparison of Mn metal behaviour on the anode SEI of graphite electrodes, it served as a valuable benchmark for developing operando NEXAFS measurements and gaining insights into the SEI growth on MnO electrodes.

Methods

Electrode deposition and characterisation

Ni thin films (50 nm for operando cells and 100 nm for the coin cells) were deposited as the active material on 15 um Cu foil using an RF Magnetron sputter coater (base pressure ≤1.0 × 10−6 mbar) using a Ni metal target (Testbourne, > 99.999%) pre-sputtered for ten minutes prior to deposition to remove any impurities from the target surface. MnO targets were prepared similarly to Ni using a Mn target (Testbourne, 99.95%) instead. The Mn target, composed of hot-pressed Mn pellets with heavily oxidised surfaces, resulted in the oxidation of the substrate film. Instead of producing a metallic Mn film, it synthesised a MnO film. This was only identified later when successfully fabricating Mn metal using an evaporation

technique, as detailed in Chapter 4. The as-deposited films were characterized by NEXAFS measurements at beamline B07 at Diamond Light source (Oxfordshire, United Kingdom). The film thicknesses were measured using a crystal quartz microbalance calibrated using a profilometer (DektakXT stylus profilometer, Bruker).

Coin cell assembly was carried out in an Ar-filled glovebox (H_2O < 0.1 ppm, O_2 < 0.1 ppm, MBraun) using 2032 coin cell components (Cambridge Energy Solutions ltd.), with Ni or MnO (100 nm) on Cu foil (Ø16 mm, 20 µm thick, >99.9%) and Li foil (Ø16.0 mm, 250 µm thick, >99.9%) electrodes. The counter and working electrodes are separated by Ø16 mm battery separator (glass fibre and Celgard 2325, dried at 80 °C in a vacuum oven), preventing electrical shorting. This separator is saturated with battery-grade liquid electrolyte (1 M $LiPF_6$ in EC/DMC 1:1 v/v, Sigma Aldrich, ≤15 ppm of H_2O) industrially referred as LP30. Coin cells were electrochemically cycled using cyclic voltammetry with a Biologic BSC battery cycler at a scan rate 0.1 mV/s from OCV to 0.05 V. After cycling was completed, cells were disassembled at specific potentials in the Ar-filled glovebox. The electrodes were rinsed with dimethyl carbonate (DMC) to remove surface lithium salt residue; each electrode was self-dried inside a glovebox before post-mortem analyses. x-ray photoelectron spectroscopy (Phi XPS) and x-ray absorption spectroscopy (B07, Diamond Light Source) were used to identify and analyse the surface components of the SEI layer.

X-ray Spectroscopy Methods

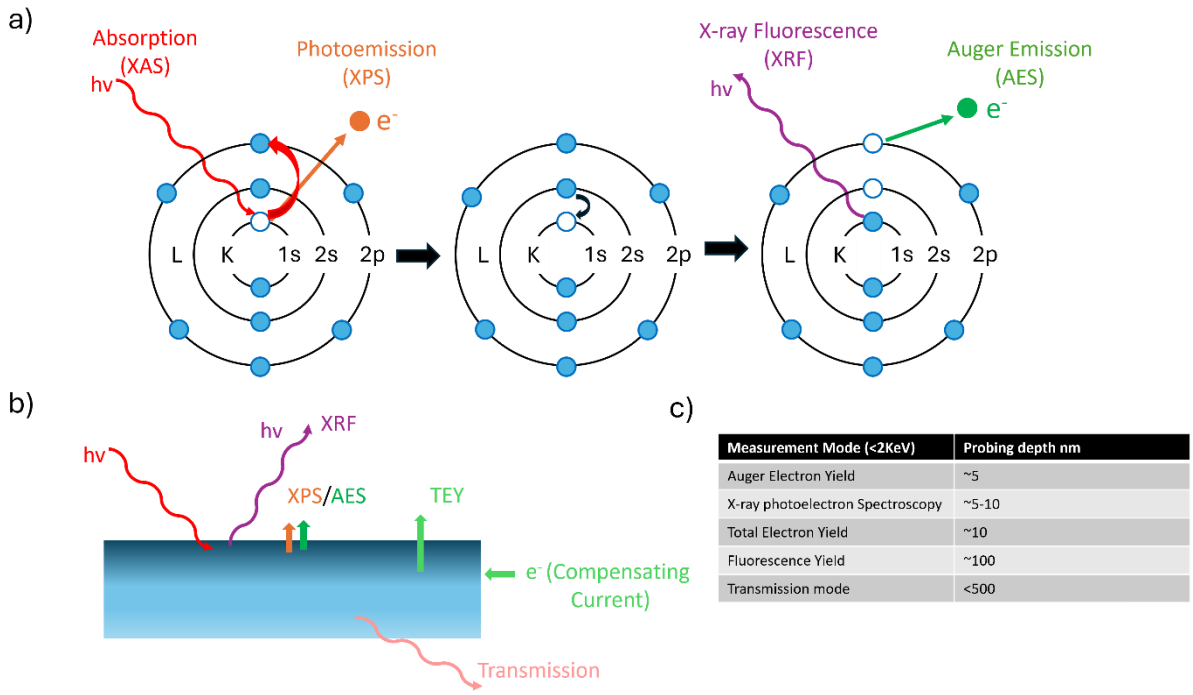

Measurement Mode (<2KeV)	Probing depth nm
Auger Electron Yield	~5
X-ray photoelectron Spectroscopy	~5-10
Total Electron Yield	~10
Fluorescence Yield	~100
Transmission mode	<500

Figure 5.1 shows a) an overview of electronic transitions and b) different modes of XAS measurement modes and c) the respective probing depths of each XAS measurement mode.

Soft NEXAFS measurements require a synchrotron radiation source to scan across a range of photon energies. An incident x-ray excites a core electron to an unoccupied state, leaving a core hole. Subsequently, nonradiative relaxation occurs with an electron from a higher energy level (L shell) decaying to a lower energy level (K-shell) and releasing an electron through the Auger process. Alternatively, radiative relaxation occurs through the emission of a fluorescent X-ray photon. When the photon energy changes, a distinct resonance occurs when electrons transition from their core level into energy states above the fermi level. Due to the precise symmetry of the orbitals undergoing excitation, only particular transitions are permitted from a given orbital, following the selection rules of quantum mechanics (dl=±1).[8–14] The most prominent spectral characteristics in XAS arise from the initial transitions permitted by dipole selection rules. These transitions have higher absorption probabilities compared to

quadrupole or higher-order transitions, thereby contributing significantly to the observed spectral features.[15] NEXAFS measurements concentrate on the energy range close to the transition edge, giving information on the chemical environment, oxidation state, and local charge distribution. When spectra recorded from samples of known oxidation state are available, these can be used for data interpretation for many materials. Ultra-high vacuum conditions are imperative due to the short inelastic mean free path (IMFP) of electrons and the constrained attenuation of soft X-rays in both gases and solids. Notably, K-edges of lightweight elements like C, N, O, and F, as well as the L edges of 3d transition metals, fall within the 0.1-2KeV energy range. In the energy range below 2KeV, the L-edge XAS of transition metals involves the excitation of 2p electrons into unoccupied valence orbitals. These specific excitations serve as a direct means to explore the covalent characteristics within coordination complexes of transition metals, delivering high resolution (less than 0.5 eV for 3d metals) compared to the analysis of metal K edges (>2KeV). [14]

Fluorescent Yield (FY) Mode

For experiments conducted in this chapter, I employed fluorescent yield (FY) and total electron yield (TEY) XAS. I will briefly address the challenges associated with both setups in this chapter. FY measurements collect information from a bulk solid or solution whereas, simultaneous collection of the TEY signal can provide more surface/interface-sensitive information. These techniques are complementary when measuring electrochemical cells with x-ray transparent membranes. Unfortunately, FY can suffer from self-absorption effects where the attenuation length of X-rays changes significantly close to an absorption edge, affecting the absorption of both incoming and fluorescent X-rays and distorting the measured spectrum. Furthermore, FY and TEY techniques can suffer from saturation effects, mainly when the incoming X-ray beam

is at a grazing angle. This arises from the X-ray penetration depth becoming comparable to the photon or electron escape depths so that nearly all X-rays are absorbed close enough to the surface that the generated photons/electrons are nearly all able to escape, meaning there is a slight variation in signal with X-ray energy.[16]

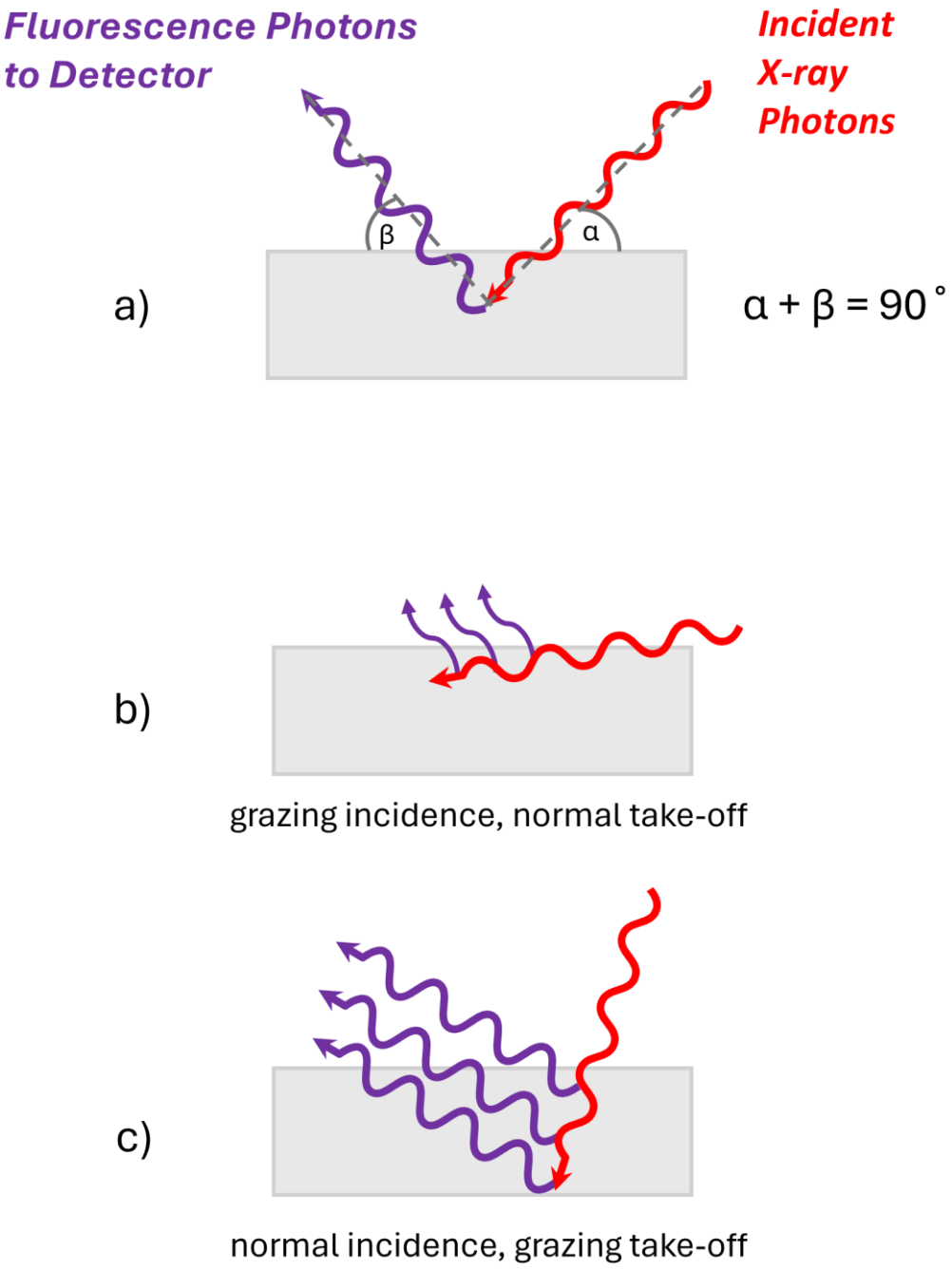

Figure 5.2 Influence of experimental geometry on saturation effects in FY mode measurements (a) general experimental geometry carried out for the measurements in this project, b) the

grazing-incidence normal-take-off limit and c) normal-incidence grazing-take-off limit. Recreated figure from reference.[17]

Figure 5.2 illustrates how the experimental setup affects saturation effects in fluorescence yield (FY). In panel (a), incident x-rays enter the sample at a glancing angle θ, causing fluorescence. The emitted fluorescence is detected at angle Φ. In our experiment setup, the sum of angles η and Φ is fixed at 90°. Panel (b) illustrates the grazing incidence of the X-ray hitting the sample and the normal take-off of fluorescence photons, where most absorbed fluorescence photons reside near the sample's surface. This proximity ensures a shorter path length in comparison to the penetration depth, facilitating the escape of most fluorescence photons to the detector. As a result, the signal exhibits independence from the absorption coefficient, presenting a saturated appearance, referred to as the "saturation effect". Panel c) illustrates normal incident x-rays hitting the sample, generating grazing take-off fluorescence photons. Here, the signal becomes more closely linked to the absorption coefficient. This is due to self-absorption experienced by the fluorescence photons. Essentially, fluorescence radiation from deeper within the sample struggles to reach the detector, causing the signal's dependency on the absorption coefficient to increase proportionally.[16–18]

The absorption of emitted fluorescent X-rays in the sample affects the observed fluorescence intensity. Self-absorption becomes more pronounced with longer X-ray paths or thicker, denser materials. This can reduce observed fluorescence signals, distorting measured spectra and impacting sample analysis accuracy. Researchers opt for thinner samples or materials with lower absorption coefficients to mitigate these effects. Correction methods are also employed to ensure more accurate fluorescence yield data.[19–21] Changes in spectral shape stemming from geometrical effects like self-absorption and saturation in FY mode measurements are complex in this system. The signal is derived from multiple layers in the SEI of varying

thicknesses and densities, including those that grow electrochemically during measurement. Implementing correction schemes is challenging due to the complex sample geometry, which often requires simplifying assumptions.

Total Electron Yield (TEY) Mode

When exploring surface-sensitive techniques like NEXAFS through electron yield measurements, the detection method involves assessing all electrons produced within a sample, encompassing Auger-Meitner electrons and those stemming from the inelastic scattering of photoelectrons. TEY mode measurements account for a broader range of energies, aligning the count of escaping electrons with the number of absorption events and enabling probing depths of sub 10 nanometres.[22,23]

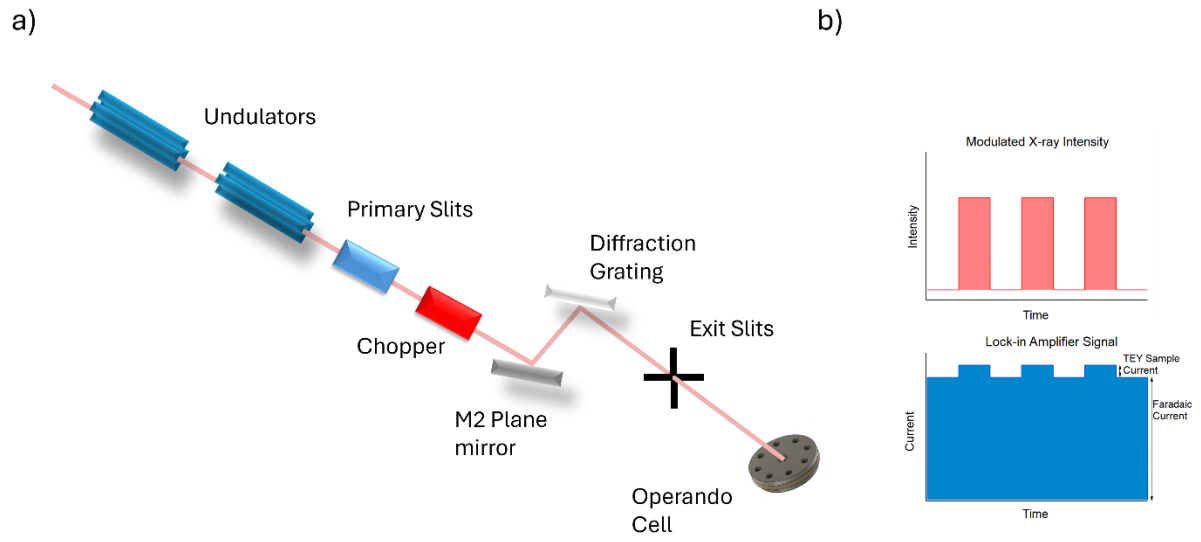

Figure 5.3 A schematic diagram of the I10 beamline using the TEY-XAS measurements enabled by measuring the current generated under X-ray illumination and b) the modulated x-ray intensity with the lock-in amplifier signal.

However, in the complex framework of an electrochemical cell, the large faradaic currents originating from electrode reduction or oxidation can pose significant challenges. Faradaic

currents often mask the sample drain current by several orders of magnitude, making it difficult to deconvolute the TEY signal. One proposed approach involves introducing a piezo-actuated chopper into the beamline as shown in figure 5.3a. This chopper modulates the incoming X-ray beam, subsequently modulating the TEY sample current as depicted in Figure 5.3b. The sample drain current is supplied into a lock-in amplifier, enabling the extraction of the segment modulated at the same frequency as the chopped X-ray beam. This approach has been used before by Velasco-Velez et al.[24] and Swallow et al.[25] used it to measure Si anodes in a similar electrochemical cell setup.

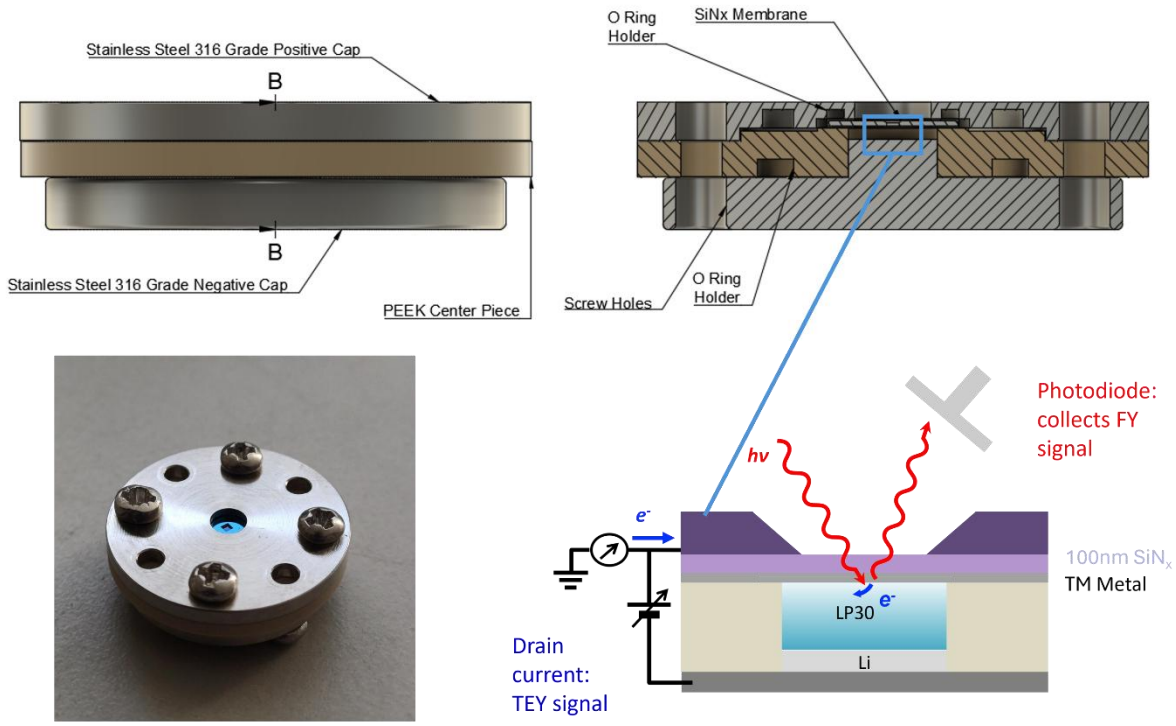

Figure 5.4 Schematic of the electrochemical cell used for operando *XAS measurements.*

Figure 5.4 shows the environmental cell setup for operando NEXAFS measurements, featuring a 50nm working electrode deposited onto a SiN_x(100 nm) membrane serving as the X-ray transparent window. The setup employs Li metal as both a reference and counter electrode, with LP30 as the electrolyte. The electrodes are connected to an external circuit, enabling

operando cycling during the spectroscopy measurements. For NEXAFS measurements, several types of membranes can be considered, depending on the specific requirements of the experiment. Silicon-based membranes (Si, SiC_x and SiN_x), polyimide-based membranes, aluminium membranes and beryllium membranes have all been used in XANES measurements for studying materials.[26] Membrane material choice for NEXAFS measurements in the soft X-ray region requires careful considerations like X-ray transparency, mechanical strength, chemical inertness and ease of handling. Optimisation of the membrane thickness and careful consideration of any interference due to absorption edges are crucial in ensuring accurate and reliable NEXAFS measurements.

The electrochemical cell design used for the measurements conducted at I10, displayed in Figure 5.4. uses suspended silicon nitride (SiN_x) membranes. SiN_x offers versatility, exhibiting a wide range of frame and window sizes and thicknesses, which offer a robust substrate and are chemically and thermally resistant. The main frame consists of a Si wafer frame (~200 µm thick, 5 × 5 mm frame) with a coating of 100nm SiN_x on either side. These membranes can withstand pressure differences exceeding 1 bar. The active material of interest is deposited prior to the assembly of the electrochemical cell via physical vapour deposition. A benefit of the membrane windows' chemical and thermal stability is the ability to perform any post-annealing step often required for thin film cathode materials. The commercial electrolytes are also typically carbonate-based, mitigating interference from the N absorption edge.[26,27]

Results

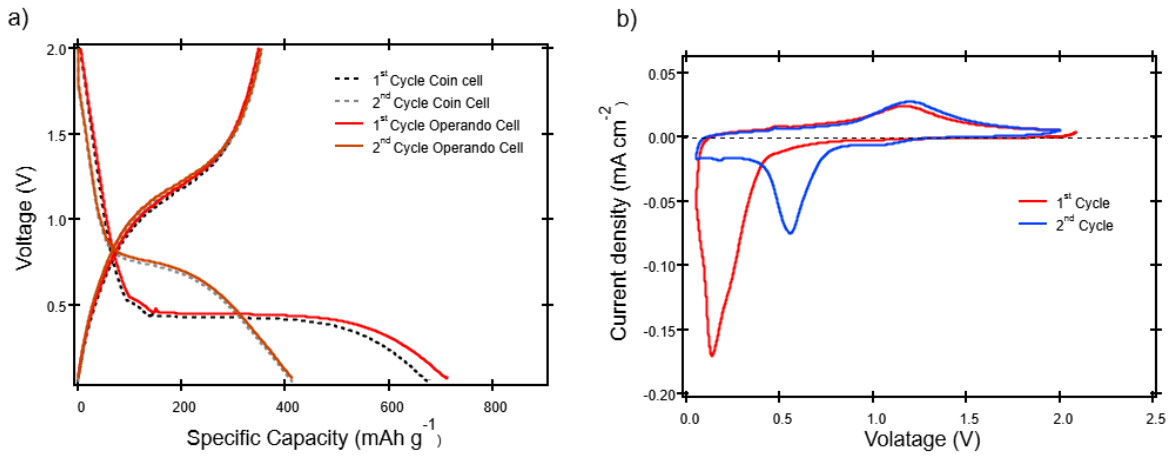

Figure 5.5 Showing the electrochemical performance of operando cells and performance in conventional coin cells with all cells cycled using an LP30 electrolyte and Lithium counter electrode. (a) voltage capacity profiles of MnO in a coin cell (b) Cyclic voltammetry of the MnO coin cell.

Figure 5.5a. shows the voltage profiles of amorphous MnO thin films cycled in coin cells and also using the operando cells set-up (described in figure 3). The cells used a lithium disc as a counter electrode and LP30 as the electrolyte. Potential cutoffs were set at 50 mV vs Li/Li^+ for both the MnO. Figure 5.5a displays the voltage capacity curves for the MnO thin film deposited onto Cu foil and onto the SiN_x window for the operando cell. For both films there is a significant voltage plateau exists at 0.44V and 0.72V for the first and second discharge respectively. The steep drop in voltage from 2.0 V to 0.44V in the first cycle can be attributed to partial intercalation of lithium as shown in equation 5.1:

$$MnO + 2Li^+ + 2e^- \rightarrow Mn^0 + Li_2O \quad [5.1]$$

The first cycle for the MnO thin film cycled in a half cell vs lithium shown in Figure 5.5 displays a large irreversible discharge capacity in the first cycle of 711 mAh g^{-1} with a cycle efficiency of ~52%. In the subsequent cycle this capacity fades to 413 mAh g^{-1} with the cycle efficiency increasing to ~95%. There is also a large shift in the discharge plateau in the first cycle

compared with the second cycle as displayed in the CV plot in figure 5.4b. This low discharge capacity may stem from amorphous regions of the electrode surface, which could be mitigated in future experiments by a post annealing step.[28]

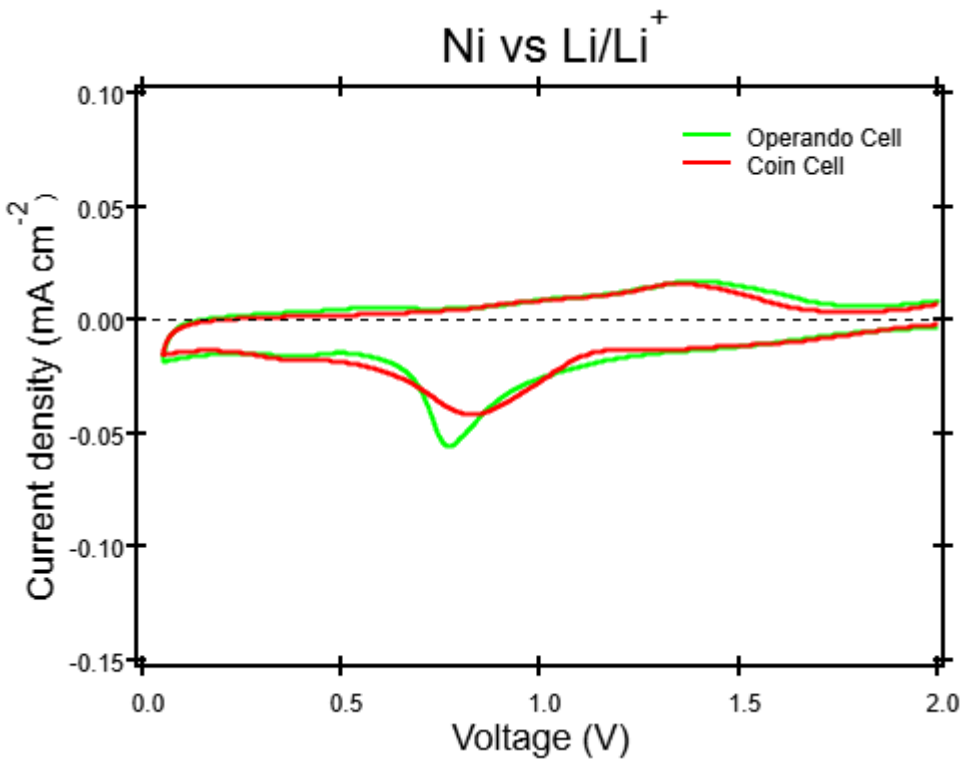

Figure 5.6 shows the electrochemical performance of Ni vs Li/Li+ in both operando and conventional coin cells using an LP30 electrolyte.

Operando cells, employing Ni thin film, underwent cyclic voltammetry (CV) cycling within a voltage range of 2.0 V to a lower cutoff potential of 50 mV. A comparative analysis was conducted with the CV curves of a coin cell, as depicted in Figure 5.6. Notably, the observed plots are similar, affirming that the operando cell's cycling behaviour is representative of a conventional coin cell during cycling. The CV profiles reveal peaks at various potentials during the initial cycle, implying the formation of a SEI and the reduction of Ni. Noteworthy peaks appear at ~2.0 V, ~1.4 V, ~0.8 V, and ~0.4 V, interestingly there is a redox couple at 0.8 V and 1.4 V some of which can be explained by the irreversible formation of SEI layer at ~0.8 V.[29–31]

Upon the reverse scan a redox peak cannot be assigned to the reoxidation of Ni metal to Ni (II) as shown in Figure 4.7 in Chapter 4. The origin of this reversible capacity possibly comes from the formation and reversible reaction of LiOH, derived from surface OH groups on MnO nanoparticles and the decomposition of the electrolyte. The LiOH then decomposes, forming Li_2O at low potentials and LiH at higher potentials, growing the SEI layer in the process, as reported by Hu et al. on the additional capacity for RuO_2 conversion electrode.[32]

Operando NEXAFS Measurements on MnO electrode

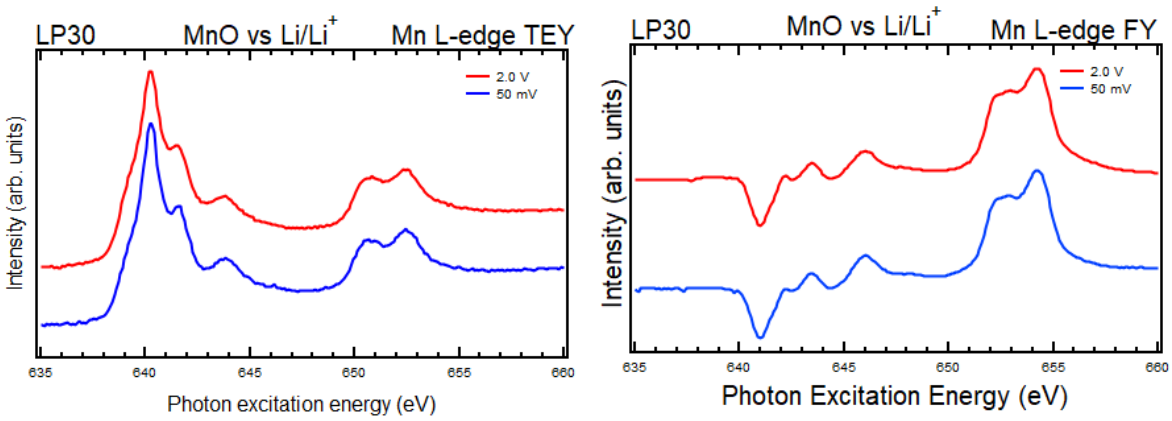

Figure 5.7. Operando Mn-L edge measurements (a) total electron yield mode and (b) fluorescence yield mode.

In Figure 5.7, operando TEY and FY mode measurements of the Mn L-edge are presented for the MnO electrode. Figure 5.7a illustrates the TEY data, where the initial measurement at 1.5 V reveals surface oxidation of the Mn. Notably, upon applying a potential bias at 50 mV, no detectable changes in the spectra are observed. The absence of spectral changes at the electrode-electrolyte interface indicates that the reduction of manganese is not observed at the surface due to the absence of anticipated broadening of the L_3- and L_2-edges associated with metallic manganese. The anticipated change in the formal oxidation state for conversion electrodes, from TM^{2+} to TM^0, is inherently dynamic and marked by several intermittent

stages, revealing a complex series of phase transformations during charge and discharge cycles. In the case of the MnO conversion reaction, the electrodes comprise the physical mix of MnO, Mn and Li_2O (and possibly other Li-containing compounds) during each cycle. Notably, the active material morphology exhibits nanosized Mn particles within the 1-10 nm range, embedded in a matrix of lithium compounds during charge cycles. At the delithiated state, nanosized MnO grains become prominent.[33–35] The TEY detection mode may not have been sensitive enough to discern these metallic Mn nanoparticles during the reaction as they are collecting an average area illuminated by a beam spot of ~200 × 300 μm^2.

There is significant distortion for the FY mode measurements due to contributions from self-absorption effects shown in Figure 5.7b. These self-absorption effects are caused when the photon energy equals or exceeds the binding energy of a core electron, generating a new absorption channel and causing an increase in the absorption coefficient, resulting in more self-absorption.

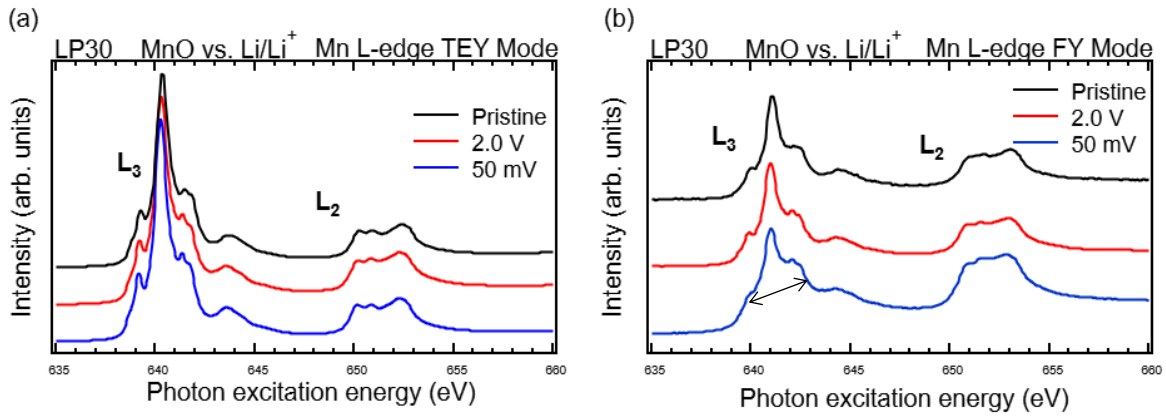

Figure 5.8. Ex-situ Mn-L edge measurements performed at B07 (a) total electron yield mode and (b) fluorescence yield mode.

Figure 5.8. shows the Mn L edge for both the surface TEY mode in Figures 5.8a and 5.8b. displaying bulk-sensitive FY mode measurements of the MnO electrode respectively. As the

electrode is cycled to 50 mV vs Li/Li^+, there is little change observed to the formal oxidation state of the MnO electrode apart from a subtle peak sift of ~0.1 eV, which may be an artefact related to the energy resolution of the instrument detector or the monochromator. The spectral shape indicates the formal oxidation state on the surface of the electrode is Mn^{2+}.[36] The XAS spectra in Figure 5.7b show the pristine electrode in a formal oxidation of +2. However, as the electrode is cycled to 50mV, there is a slight broadening of the spectra features on the L_3 edge, indicating the presence of some metallic Mn in the bulk of the electrode.

SEI Components O K- and F K-edge

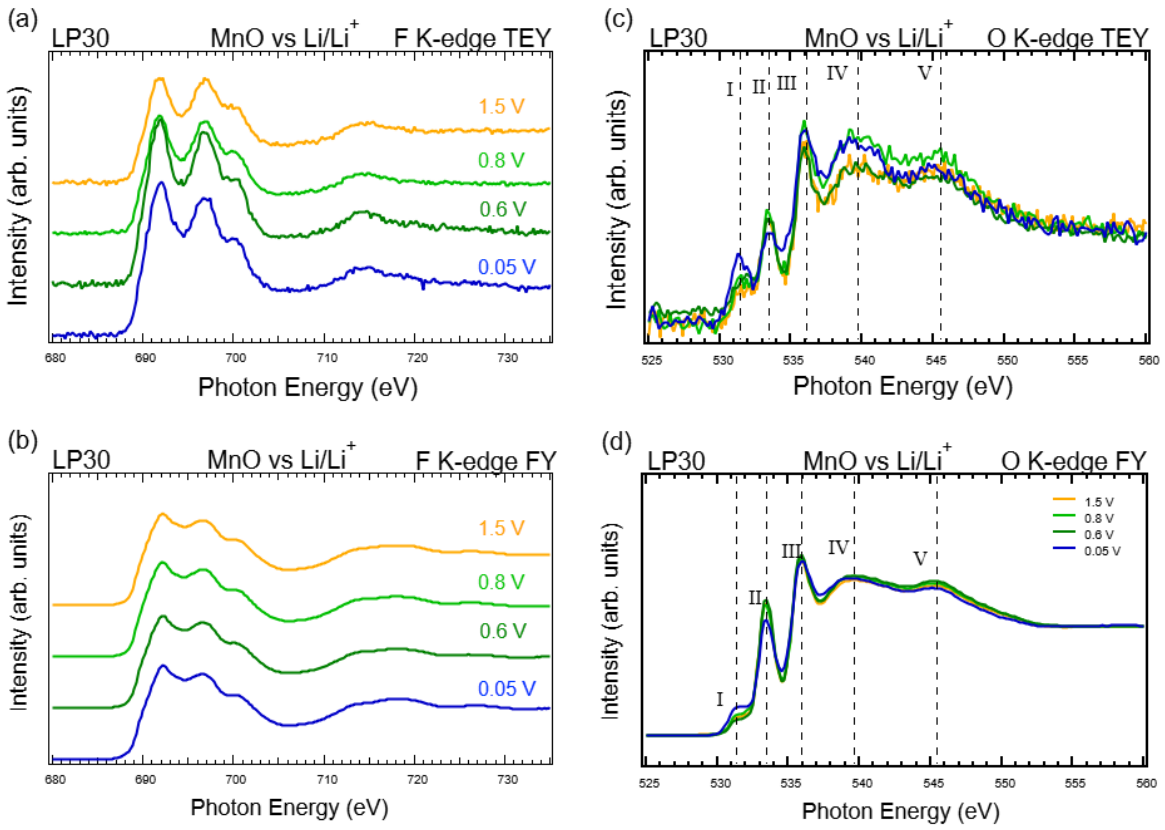

Figure 5.9. Operando XAS (a) TEY -mode (b) FY mode of the F K-edge and XAS (c) TEY mode and (d) FY mode of the O K-edge on SEI components grown on the MnO electrode.

Figure 5.9 displays the results of operando TEY-XAS and FY-XAS measurements performed using the operando cell assembly, as shown in Figure 5.4. with LP30 electrolyte and a lithium

counter electrode. Both F and O K-edge spectra were measured during several potential holds vs. Li/Li^+ (1.5 V, 0.8 V, 0.6 V, and 0.05 V), which were reached by potential step and holding for 15 minutes to allow the current response to reach equilibrium. The TEY F K-edge spectra are displayed in Figure 5.8a. shows three prominent peaks at ~692 eV, 697 eV, and ~700 eV; a fourth peak is also at ~714 eV. At 1.5V, the spectra resemble the line shape of the PF6- anions as reported in the literature.[37–39] The spectra remain unchanged until the cell is cycled to ~0.6 V, where the relative intensity of the peaks 692 eV and 697 eV starts to change. This peak represents the transitions into the $F_{(p)}$-$P_{(p)}$ hybridised orbitals (t_1u symmetry).[40,41] The slight decrease in intensity of the peak at 697 eV indicating that the bonds between the fluorine and phosphorous $PF6^-$ anions are changing, most likely decomposing (explained later for the Ni cell) into lithium fluoride. In the FY F-K edge measurements, there is virtually no spectral evolution; however, the spectra shape that would be expected should match the $PF6^-$ anion contribution, as shown in Figure 5.9a. However, it is possible this originates from other contributions, such as self-absorption effects.

The O K edge spectrum (Figure 5.9c-d) shows several features labelled I-IV) in surface-sensitive TEY mode (Figure 5.9c.) and bulk-sensitive FY mode (Figure 5.9d.). Resonance peaks are present at ~533 eV (II) and ~536 eV (III), with broader features also present at ~539 eV (IV) and ~545 eV (V). These features strongly resemble the main resonances for the O K-edge of EC/DMC as reported in the literature.[42–44] A peak at ~531 is also present, and as the cell is cycled to lower potentials, this peak begins to grow in intensity. At 0.8 V, there is a growth in peaks IV and V, which quickly diminishes at 0.6 V and reappears at lower potentials at 0.05 V (challenging to assign these peaks). This could be some intermediate species related to the decomposition of organic components in the electrolyte forming the SEI. At low potentials 50 mV, there is significant growth in the pre-edge feature I, which are attributed to the O 1s to

π* transition of carbonyl (C=O) groups. This increase in the O 1s to π* transition is accompanied by the decrease in peak II intensity, indicating the ring opening of EC forming the SEI layer at much lower potentials. The evolution of the SEI will be discussed in more detail, along with the results from the Ni cell, later in the chapter.

Operando NEXAFS Measurements on Ni Electrode

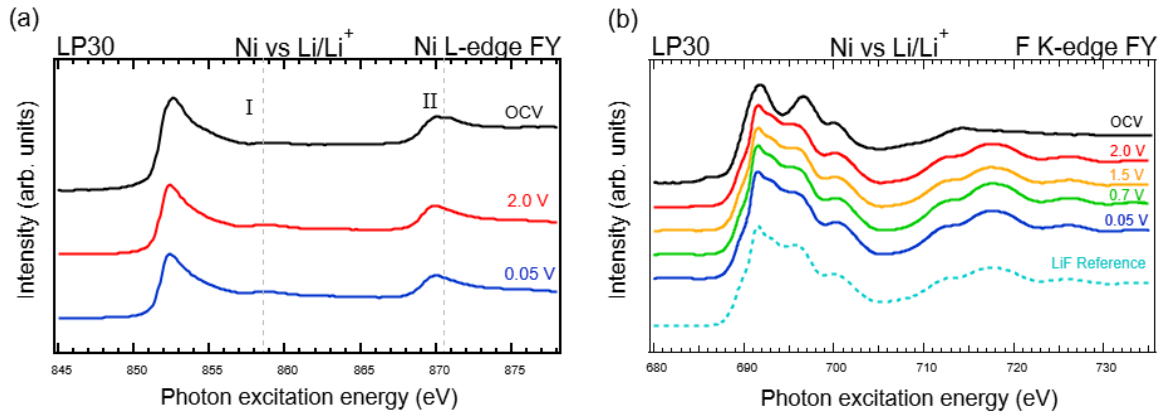

Figure 5.10. Operando FY-XAS measurements of Ni electrode (a) Ni L-edge and (b) F-Kedge.

In Figure 5.10, FY-XAS measurements on Ni electrodes are shown, with Figure 5.10a depicting the Ni L-edge and Figure 5.10b the F-K edge as a function of potential vs Li/Li^+. Under operando conditions and at OCV, three spectra were collected on the Ni electrode. Notably, the OCV spectra exhibit subtle differences in spectral features compared to those collected under applied potential bias. Two distinct features, labelled as peak (I) and peak (II), are observed. At OCV, there is a slight growth in the spectral feature around ~858.5 eV, possibly indicative of the ligand environment of the Ni electrode, potentially associated with hydroxyl groups. Furthermore, the L_2 edge in the OCV measurement displays a split peak feature with weak intensity, likely influenced by the presence of a slight oxide layer. The oxide layer disappears upon applying a potential bias to the cell, indicating a complete reduction of the Ni electrode surface to metallic Ni.

The F K-edge spectra in Figure 5.10b reveal the presence of PF_6^- anion during OCV measurements. However, upon applying a potential bias, LiF forms on the Ni electrode surface, most likely through catalytic reduction of HF to form LiF.[45]

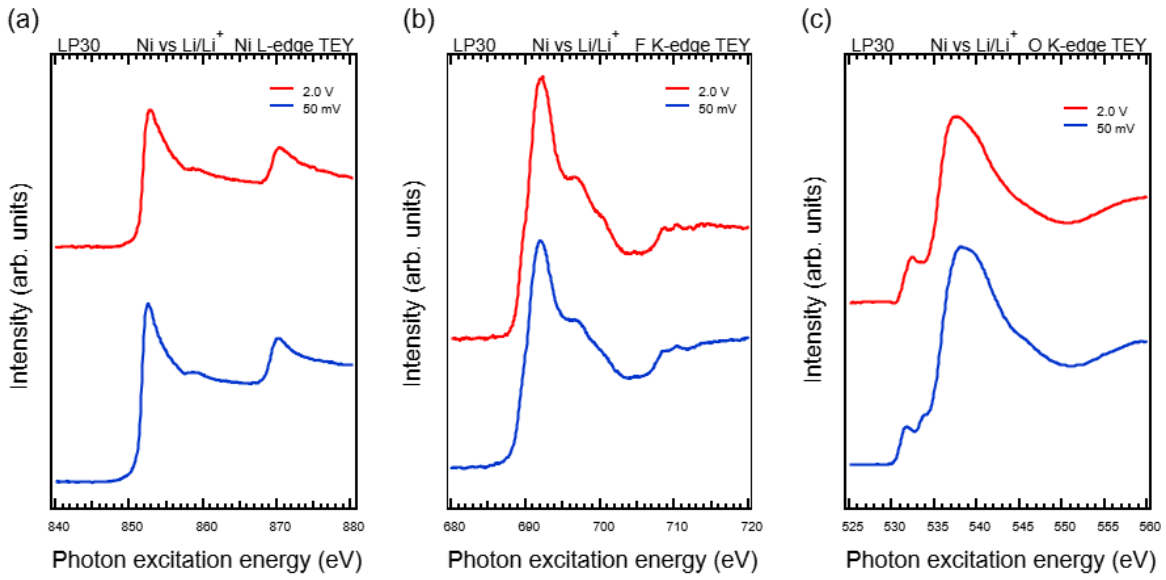

Figure 5.11. Operando TEY-XAS measurements on (a) Ni L-edge, (b) F K-edge and (c) O-K edge under applied bias.

Figure 5.11 presents TEY-XAS operando measurements conducted on the Ni electrode. Figure 5.11a showcases the Ni L edge, where metallic Ni features are discerned owing to the broad $L_{3,2}$-edges. The absence of a split feature on the L_2 edge strongly suggests that the Ni electrode surface undergoes reduction, ultimately achieving a metallic Nickel state at high potentials (2.0 V) vs Li/Li^+. The measurements depicted in Figure 5.11b, demonstrate the F K-edge spectra reveal the absence of features associated with PF_6^- anions. Instead, the spectra are dominated by the emergence of LiF features, signifying that SEI growth on the Ni electrode occurs at elevated potentials compared to the SEI on the MnO electrode. Figure 5.11c captures the O K-edge, where no discernible features that can be attributed to electrolyte components such as EC/DMC. However, the spectrum reveals distinctive features, notably a

low-energy peak at ~531.5 eV, providing a unique fingerprint of the electrochemical environment. Furthermore, an additional growth in intensity of a peak at 534 eV is potentially indicative of the formation of lithium carbonates.

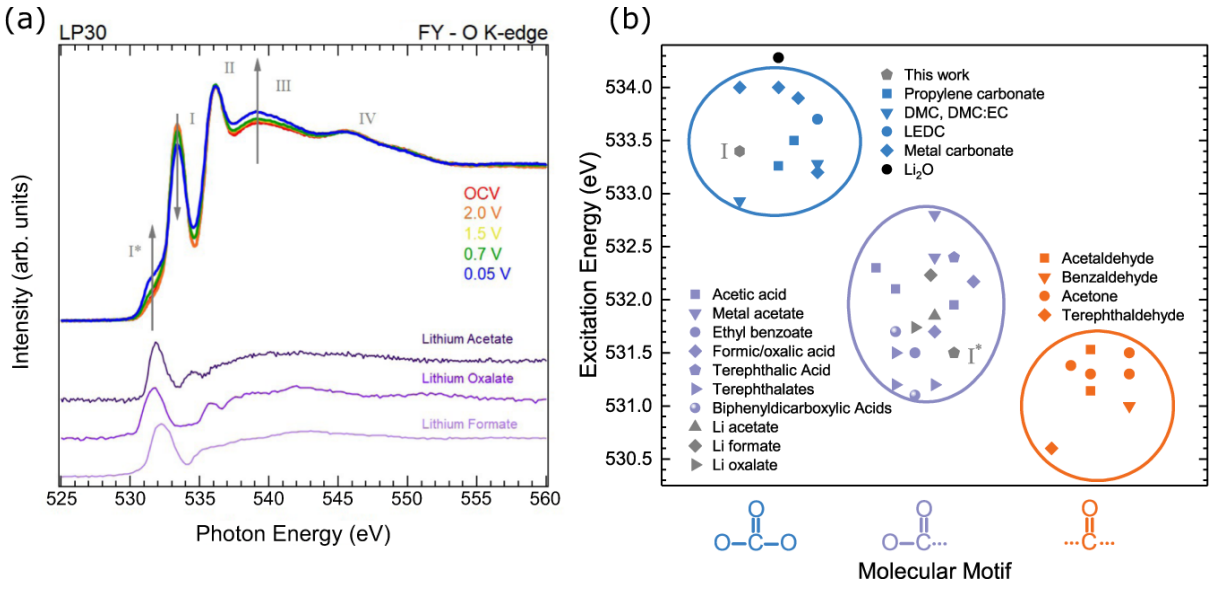

Figure 5.12. Operando FY-XAS measurements on (a) O K-edge of the Ni electrode and (b) possible motif groups associated with the low energy features on the O K-edge. Published in reference.[42]

Figure 5.12 shows the four main peaks (I-IV) are assigned to EC/DMC solvent apparent in the FY-XAS spectrum of the O K-edge at OCV.[43,44] Upon applying a potential bias, there is minimal variation in the spectral features until 0.7 V, where a low energy shoulder appears at 531.5 eV, corresponding to peak I*. This peak grows in intensity, becoming clearly visible at 50 mV. Alongside this peak (I*) growth, peak (I) decreases in intensity whilst peak (III) grows; however, peaks II and IV remain relatively similar during electrochemical measurements. A slight gain is also observed at 535 eV, corresponding to a decreased minimum at the trough. The growth of peak I* corresponds to the growth in the organic components of the SEI attributed to O 1s transitions of the C=O to π*- antibonding orbitals.[46,47]

Figure 5.12b plots a variety of organic components with corresponding transition energies. This allows each compound to be grouped based on distinct molecular motifs. Aldehyde (-C(=O)H), ketone (-C(=O)R), carboxyl (-C(=O) OH), and ester (-C(=O)OR) are possible sub-groups based on organic compounds related to the peak I* at ~531.5 eV.[48–55] The reduction of peak I corresponds to the attenuation of the C=O on the EC/DMC generating reaction products with -C(=O) or -C(=O)O containing motifs (peak I*). However, it is important to note that the formation of lithium carbonate species (LEC, LMC, LEDC, LEMC, LBDC) is not mutually exclusive at these low potentials.[56,57] However, it is difficult to deconvolute spectra features associated with these compounds as they overlap with spectral features relating to the EC/DMC. There is no significant attenuation of peaks II and IV. Peak III shows some attenuation, suggesting that peaks at 531.5 eV, 533 eV, 535 eV, and 539 eV can be attributed to the growth of the organic SEI components.

The additional C-O bond in carboxyl and ester groups contributes to additional features in this range. Indeed, recently reported simulations of O K-edge spectra for -C(=O)OH exhibit features at the appropriate energies, with peak I* arising from C=O to π* transitions, C-O to π* transitions contributing to peak II, whilst both C=O and C-O to σ* transitions contribute to peak III, and C=O to σ* to peak IV. Notably, experimental spectra acquired for polymers containing (-(C=O)OCH_x) motifs closely match the spectral features required, including a close alignment in energy for Peak I* and additional intensity at Peak III. This suggests that these spectral features at peak I* primarily arise for acyl oxygen cleavage via the reduction of EC or DMC as reported by gas evolution measurements.[58,59] -(C=O)O motifs are also expected to give similar lineshapes and can form by reduction of CO_2 generated from electrolyte decomposition forming lithium acetate, lithium oxalate and lithium formate as shown by TEY-XAS measurements of these lithium compound references in figure 5.12b. These reference

powders all possess -(C=O)O molecular motifs with the lowest energy features corresponding to a similar energy as peak I*.

Ex-situ Analysis

NEXAFS Measurements

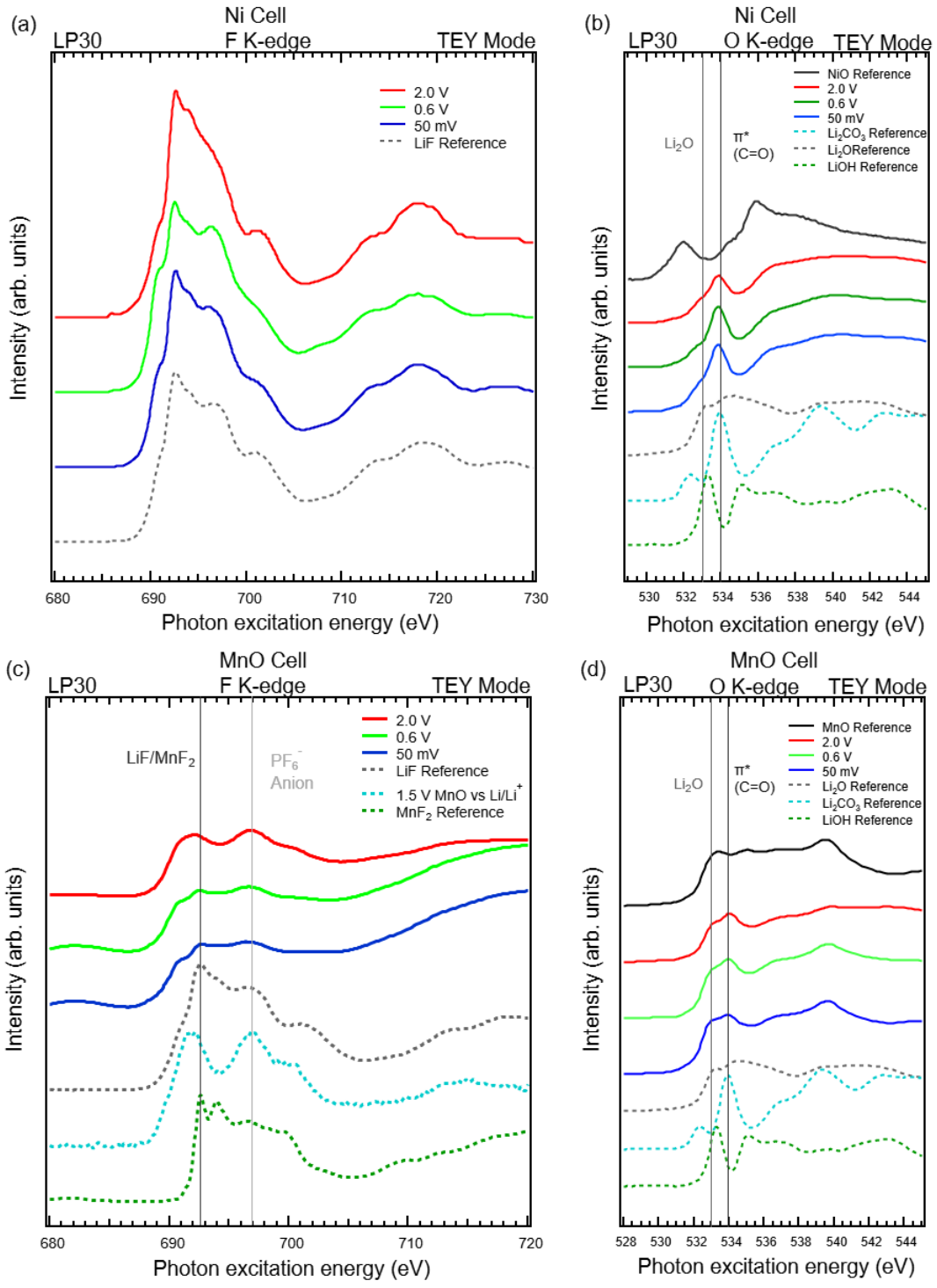

Figure 5.13. TEY-XAS measurements of SEI components on Ni electrodes at distinct potentials (a) F K-edge and (b) O K-edge and (d) F K-edge and (d) O K-edge spectra for SEI components on MnO electrodes with reference spectra plotted in dashed lines to aid fingerprint analysis.

To corroborate the operando XAS data measuring the evolution of the SEI, XAS TEY measurements were performed on Ni and MnO electrodes harvested from disassembled coin cells (using the same LP30 electrolyte and lithium counter electrodes). Figure 5.13a showcases F K-edge measurements conducted on Ni electrodes at 2.0 V, 0.6 V and 50 mV with a LiF F K-edge spectra plotted below for a reference. From 2.0 V the formation of LiF is evident and remains the dominant component of the F K -edge upon cycling to low potentials.[42] In the O K-edge shown in figure 5.13b, the pristine Ni surface shows NiO's presence due to the distinct pre-edge feature at 532 eV. As the Ni electrode is cycled, this pre-edge feature disappears, indicating that the oxide layer has been removed. New features at ~533 eV and 534 eV indicate the presence of Li_2O[60] and Li_2CO_3,[37,60] respectively. The peak at 534 eV continues to grow upon cycling to low potentials, most likely due to further formation of Li_2CO_3. However this peak may also be related to the formation of other carbonate containing species e.g. lithium ethyl carbonate (LEC), lithium methyl carbonate (LMC), lithium ethylene monocarbonate (LEMC), lithium ethylene dicarbonate (LEDC), lithium butylene dicarbonate(LBDC).[56]

MnO electrodes following cycling to distinct voltages: 2.0 V, 0.6 V, and 50 mV were also measured using TEY-XAS. Figure 5.13c. shows the F K-edge at 2.0 V, with the observed spectral features aligning with the PF_6^- anion characteristics[39–41] previously identified in operando MnO F K-edge measurements at 1.5 V. This alignment signifies the predominant presence of $LiPF_6$ salt on the electrode surface. However, as the electrode undergoes cycling to 0.6 V, notable changes in spectral features, with the emergence of a sharp peak around ~692 eV. This peak suggests the potential presence of MnF_2[36] or LiF.[37,42] Interestingly, minimal evolution in the spectra is observed upon cycling to 50 mV.

Figure 5.13d. presents O K-edge spectra, with the initial MnO surface exhibiting characteristics consistent with existing literature on MnO.[47,61] NEXAFS measurements observe the evolution of the SEI on the MnO surface with a distinct growth in the peak at 534 eV, which may be attributed to π*-antibonding orbitals from the O 1s of the C=O moiety indicating the presence of Li_2CO_3.[37] While LiOH is a likely species formed in the SEI. Furthermore, this peak may also incorporate contributions from Li2O.[60] Interestingly, the low energy feature at ~531 eV captured using the operando measurements is absent from the spectra, indicating that the DMC cleaning step either washed this away or related to an intermediate species present on the MnO surface. This highlights how powerful operando measurements can be to capture the dynamic formation of the SEI.

XPS Measurements

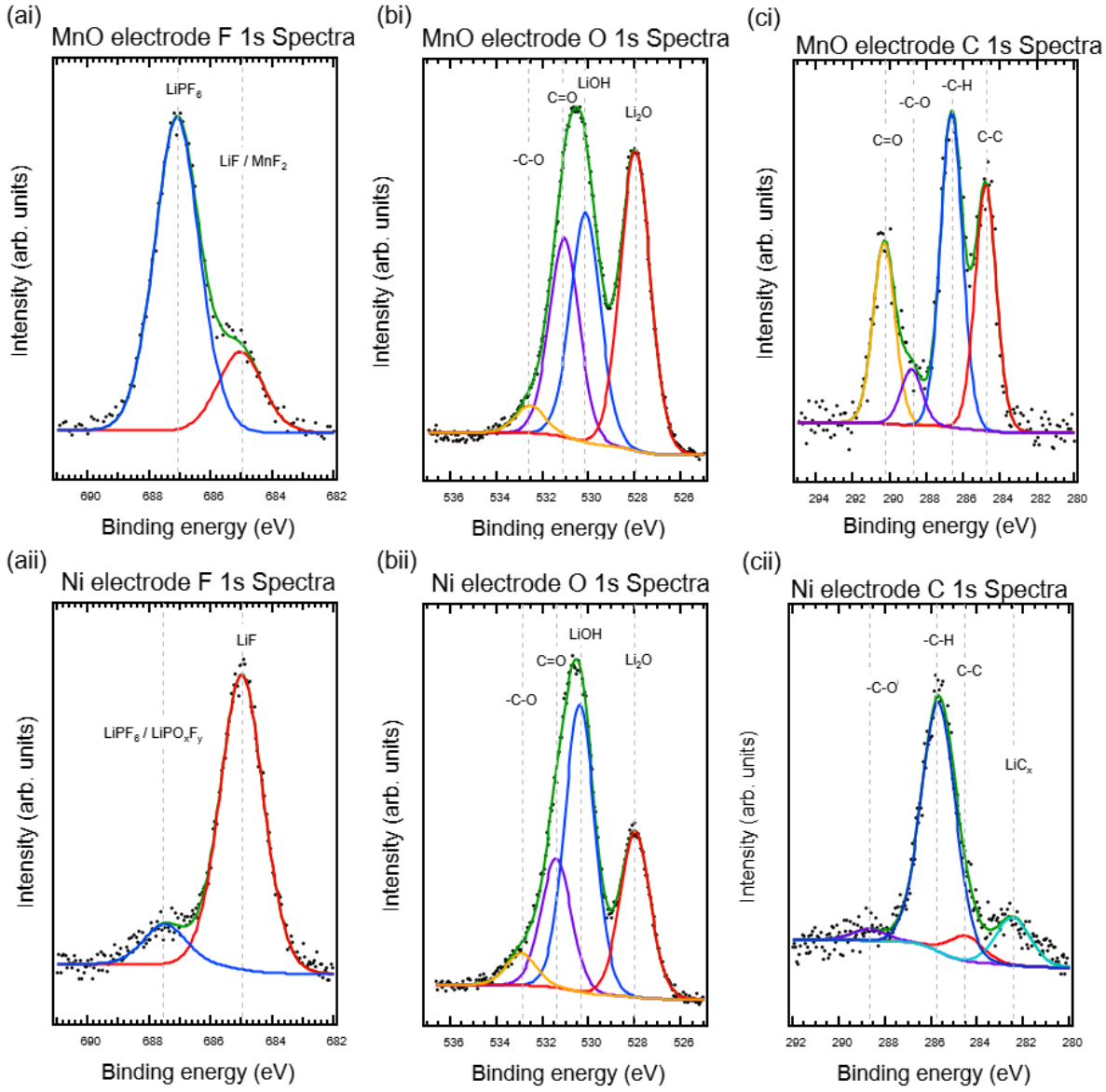

Figure 5.14. XPS measurements of (a) F 1s core level, (b) O 1s core level and (c) C 1s core level on MnO electrodes (i) and Ni (ii) electrodes at 50 mV vs Li/Li⁺.

XPS measurements were performed on Ni and MnO electrodes, which had been electrochemically cycled to 50mV vs. Li/Li⁺, to reveal the chemical composition of the SEI. Figure 9 shows the F 1s, O 1s and C 1s. The spectra were obtained using 1486.6 eV excitation energy corresponding to a 5-10nm probing depth.[62] In the F 1s region, in figure 5.14a peaks at 685 eV are assigned to LiF[63,64] and ~687 eV, which is assigned to other fluorine species

($Li_xPO_yF_z$ or $LiPF_6$ salt).[62,65] In the O 1s region displayed in figure 5.14b, peaks at ~528 eV and ~531 eV are related to the formation of Li_2O[66] and some species containing alkyl carbonate groups (-C=O).[67,68] The C 1s spectra shown by figure 5.14c. reveal a low energy feature at ~282 eV, which may be related to a carbidic species, most likely a lithium carbide species.[69] Intensities at ~285 eV correspond to the adventitious carbon ~286 eV correspond to hydrocarbons.[67,69,70] The C 1s spectra also have a feature at ~290 eV related to the -CO_3, corresponding to the presence of alkyl carbonates.[62,67]

In the F 1s spectra, the MnO electrode exhibits diminished LiF content compared to the prevalence of LiPF6 salts within the solid electrolyte interphase (SEI). The Ni electrode juxtaposed the MnO electrode with a higher concentration of LiF presence on the SEI relative to LiPF6 salts. In the O1s spectra of the MnO electrode, there is an elevated relative intensity of Li_2O, attributed potentially to the conversion reaction of $MnO + 2Li^+ \rightarrow Mn^0 + Li_2O$. Notably, both electrodes exhibit carbonates and LiOH in the SEI. The C 1s spectra highlight the difference between the MnO and the Ni electrode with lithium carbide on the later electrode.

Discussion

TEY-XAS detection relies on a three-step process:

1. The formation of a core hole through X-ray absorption
2. The release of Auger electrons and secondary electrons due to relaxation and inelastic scattering
3. The existence of an electron-conductive pathway to replenish the emitted electrons.

The X-ray attenuation length is a gauge for the distance from an interface where X-rays are absorbed by the material and core holes are generated, typically ranging from a few hundred nanometers to several micrometres for the relevant core levels mentioned in this chapter.[71] Auger emission occurs throughout this depth, but only the Auger and secondary electrons that escape across the electrode-electrolyte interface contribute to the TEY signal.

Two common configurations are utilised in conventional TEY-XAS measurements conducted in a vacuum. Firstly, the sample can be grounded, with emitted electrons collected by an isolated counter electrode (CE) connected through a current amplifier. Alternatively, the sample itself can be connected to the ground via the current amplifier while the CE is grounded through the chamber walls. In the operando TEY-XAS approach described here, the transition metal working electrode (WE) is linked to a current amplifier. The amplifier input is biased relative to the lithium counter electrode (CE) to maintain an equivalent voltage and prevent cell short circuits.[42,72]

Despite X-ray ionisation occurring within the bulk of the electrolyte, the limited range over which electrons scatter necessitates rapid recombination with ions in the electrolyte, maintaining local charge neutrality. Consequently, only electrons and ions illuminated at the

WE/electrolyte interface contribute to the collected TEY signal.[73] The corresponding charge transfer at the counter electrode ensures the charge neutrality of the electrolyte.

In TEY-XAS detection, the signal involving an insulating layer atop an electronic conductor requires electron tunnelling to fulfil a conductive pathway, which influences the surface sensitivity of the measurement. When dealing with an insulator thinner than the Auger electron escape depth, the limited range of electron tunnelling ensures that the TEY signal primarily reflects species close to the electronic conductor's concealed interface.[74]

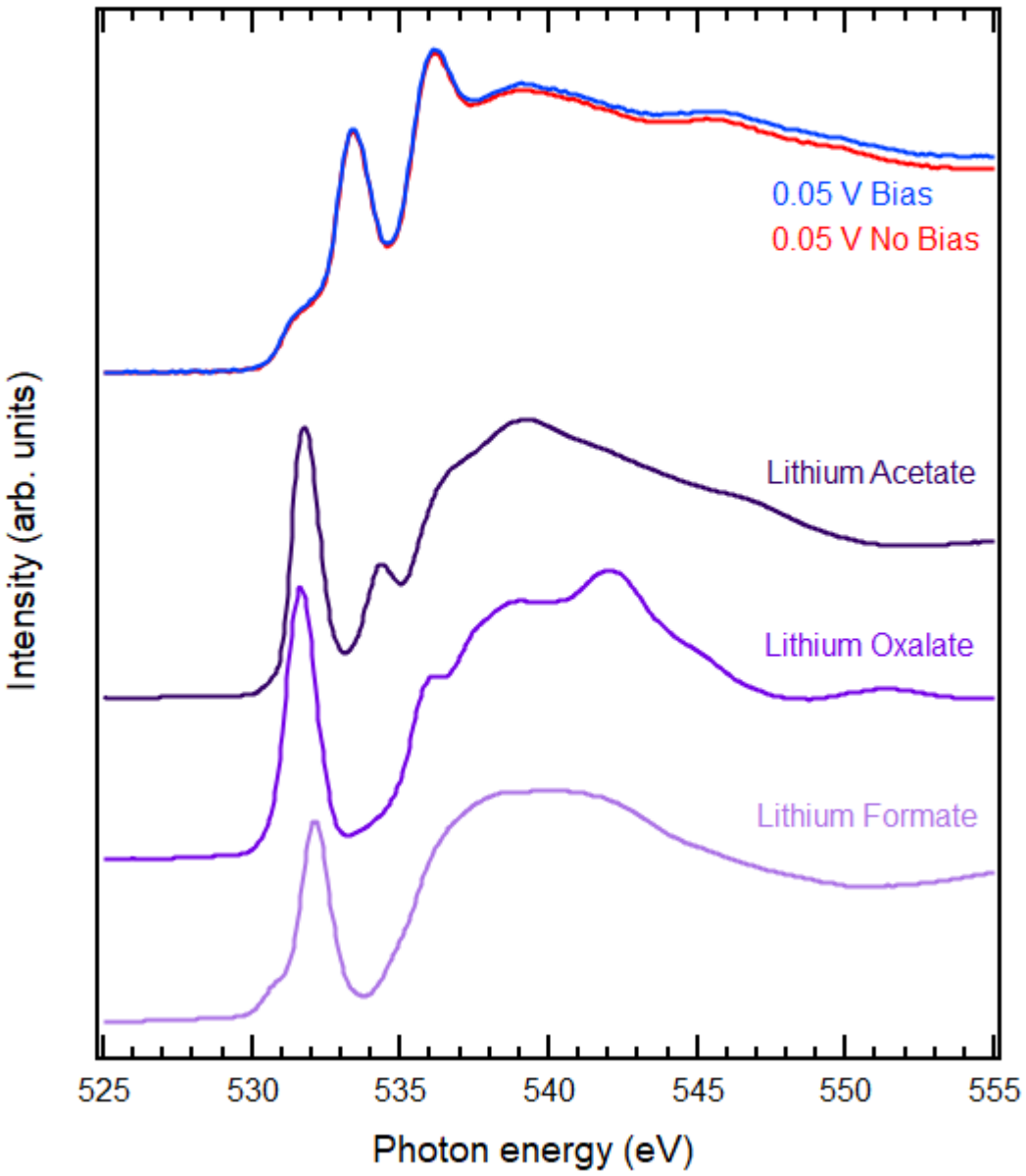

Figure 5.15. Bias vs non bias to assess the impacts of ion rearrangement.

Figure 5.15 displays the FY-XAS of the O K-edge during a 50 mV vs Li/Li+ bias applied and a further measurement after sample relaxation when the bias was removed for 30 mins. The spectral features remain unchanged, demonstrating that an applied bias does not influence the spectra. TEY measurements of reference powders: lithium acetate, lithium oxalate and lithium formate (measured in TEY-XAS mode) are also plotted showing a low energy feature

in their respective O K-edge spectra. The low energy features of the reference powders align with the energy of the low energy feature formed at low potentials in the operando cell.

The biased and non-biased measurements on the O K-edge demonstrate that the spectral features do not simply arise from self-absorption/saturation effects due to the ion arrangement under applied potential. Notably, the spectra features due to geometric effects of self-absorption/saturation related to the FY mode are complex in this system due to multiple layers of differing thicknesses and densities. This makes any correction models challenging to implement as they often simplify assumptions to correct for any geometric effects. It is difficult to claim that these measurements are free from self-absorption and saturation effects. To mitigate geometric effects, the environmental cell geometry was fixed during measurements, and it is assumed that the SEI is thinner than the x-ray attenuation length. The changes seen in the FY spectra are consistent with ex-situ measurements, indicating that the spectral changes are electrochemically driven and not purely self-absorption or saturation effects.

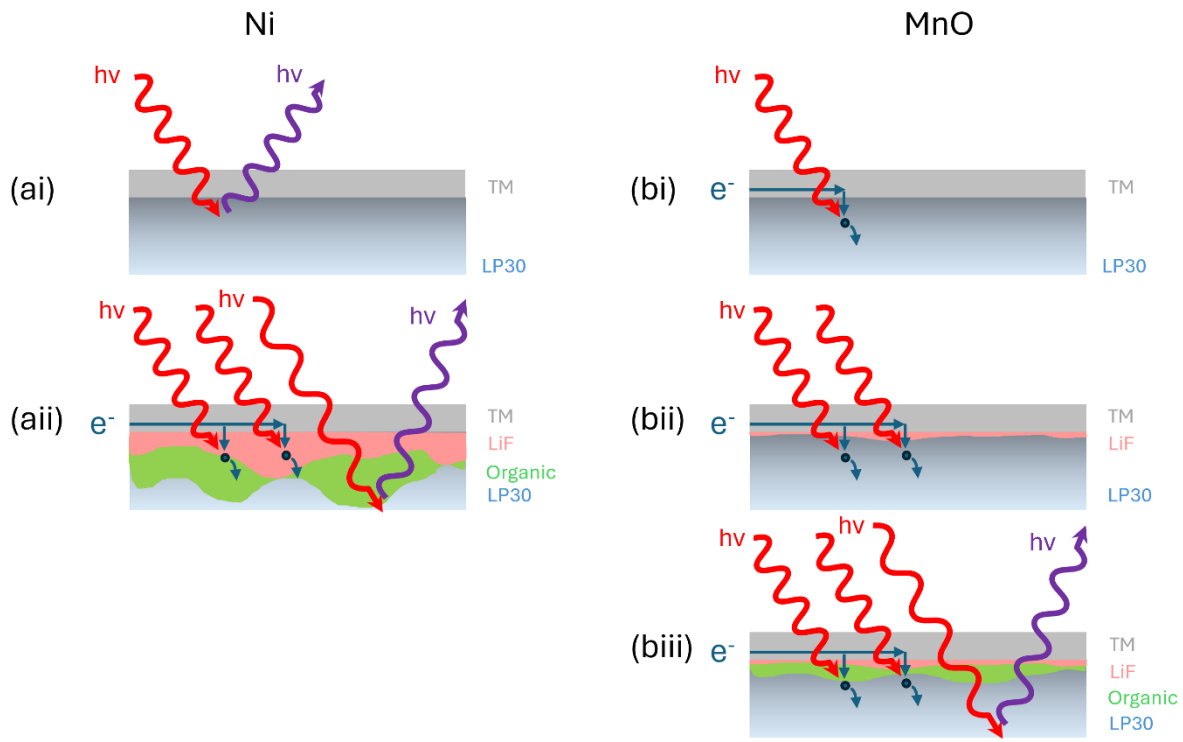

Figure 5.16. Schematic for SEI growth on (a) Ni electrode and (b) MnO electrode.

The schematic in Figure 5.16 describes the onset of SEI formation on the surfaces of Figure 5.16a Ni and Figure 5.16b MnO electrodes. For Figure 5.16ai, the Ni electrode was measured using FY mode at OCV; from this measurement, no bias is required, so spectral features in the F K-edge are dominated by features associated with the PF_6^- anions and in the O K-edge spectral features associated with EC/DMC features. As the 2.0 V bias is applied to the cell, the spectral features change dramatically, forming LiF and organic species. With the bias applied to the cell, measurements in the surface-sensitive TEY-XAS mode could be performed. However, there are no spectral features relating to the electrolyte in the TEY-XAS mode indicate that the SEI had already formed at higher potentials, possibly due to the catalytic reduction of HF forming LiF and/or by radiolysis. This indicated that the SEI formed at 2.0 V is

thick enough to prevent electron tunnelling to the electrolyte. In the FY-XAS, spectral features relating to the electrolyte are still present in the O K-edge.

A different spectral evolution is observed in the MnO electrode model for SEI growth, shown in Figure 5.16b. Here, no passivating layer is formed, which is thick enough to block electron tunnelling as we see spectral features associated with the electrolyte even at low potentials applied to the cell. In the TEY-XAS, this suggests that the SEI formed is sufficiently broken, indicating that it is not stable, possibly related to the surface reconstruction of the MnO at low potentials. Figure 5.16bii showcases the electrode at high potentials (1.5 V), whereas figure 5.16biii indicates the charge compensation mechanism for the TEY-XAS signal at low potential (50 mV).

Conclusions

In summary, we demonstrate operando XAS measurements during the electrochemical cycling of MnO and Ni electrodes prepared via physical vapour deposition in LP30 electrolytes, revealing how SEI formation proceeds as a function of potential. Using a modulated X-ray beam and lock-in technique, we can extract the TEY signal under applied bias and thus obtain an interface-sensitive account of the chemical evolution of the SEI.

The operando measurements highlight the distinctive nature of SEI growth on different electrode surfaces. The MnO electrode at 1.5V, features corresponding to the main electrolyte components (EC, DMC, $PF6^-$ ions) dominate the O K- and F K-edge spectra. We can see that LiF formation is absent mainly on the surface of MnO during the first cycle, even at low potentials.

Operando measurements on the Ni electrode revealed Ni's surface reduction and LiF formation at high potentials. A distinct spectral feature related to organic SEI components containing carbonyl groups emerges at lower potentials (<0.7 V). The spectral evolution observed is consistent with the layering of the SEI during formation, with LiF deposition occurring close to the electrode surface at higher potentials, followed by organic components forming on top as the potential is further reduced. The growth of the SEI is found to isolate the electrode from the electrolyte electronically, and thus, electrolyte components are no longer detectable in the TEY signal. More bulk-sensitive FY measurements are therefore used to assign the organic SEI feature to -C(=O)O-, most likely (-(C=O)OCH_x) arising from the reduction of EC/DMC by acyl oxygen cleavage. Our study of electrodes operating under reducing conditions in lithium-ion batteries herein shows the benefits of combining TEY and FY detection modes under operando conditions, with interface-sensitive TEY being well suited

to probing the early stages of SEI formation, whilst FY allows simultaneous probing of the SEI and electrolyte throughout formation. This same approach can be readily adapted to the study of a wide variety of thin-film anodes and cathodes, as well as different electrolyte formulations, where it can offer new insight into the formation mechanisms of electrode-electrolyte interphases and their chemical stability.

References

1. Liu, S. *et al.* Dynamic evolution of Cathode−Electrolyte interface of LiNi0.6Co0.2Mn0.2O2 during the initial Charge−Discharge process. *J Power Sources* **438**, 226979 (2019).

2. An, S. J. *et al.* The state of understanding of the lithium-ion-battery graphite solid electrolyte interphase (SEI) and its relationship to formation cycling. *Carbon N Y* **105**, 52–76 (2016).

3. Verma, P., Maire, P. & Novák, P. A review of the features and analyses of the solid electrolyte interphase in Li-ion batteries. *Electrochim Acta* **55**, 6332–6341 (2010).

4. Waldmann, T. *et al.* Review—Post-Mortem Analysis of Aged Lithium-Ion Batteries: Disassembly Methodology and Physico-Chemical Analysis Techniques. *J Electrochem Soc* **163**, A2149–A2164 (2016).

5. Lebens-Higgins, Z. W. *et al.* Evolution of the Electrode-Electrolyte Interface of LiNi0.8Co0.15Al0.05O2 Electrodes Due to Electrochemical and Thermal Stress. *Chemistry of Materials* **30**, 958–969 (2018).

6. Williard, N., Sood, B., Osterman, M. & Pecht, M. Disassembly methodology for conducting failure analysis on lithium-ion batteries. *Journal of Materials Science: Materials in Electronics* **22**, 1616–1630 (2011).

7. Somerville, L. *et al.* The Effect of Pre-Analysis Washing on the Surface Film of Graphite Electrodes. *Electrochim Acta* **206**, 70–76 (2016).

8. Penner-Hahn, J. E. *X-Ray Absorption Spectroscopy*.

9. Yano, J. & Yachandra, V. K. X-ray absorption spectroscopy. *Photosynthesis Research* vol. 102 241–254 Preprint at https://doi.org/10.1007/s11120-009-9473-8 (2009).

10. Gaur, A., Shrivastava, B. D. & Nigam, H. L. *X-Ray Absorption Fine Structure (XAFS) Spectroscopy-A Review*. *Proc Indian Natn Sci Acad* vol. 79 (2013).

11. Koningsberger, D. C. & Prins, R. *X-Ray Absorption: Principles, Applications, Techniques of EXAFS, SEXAFS and XANES*. vol. 92 (Wiley, New York , 1987).

12. Iglesias-Juez, A., Chiarello, G. L., Patience, G. S. & Guerrero-Pérez, M. O. Experimental methods in chemical engineering: X-ray absorption spectroscopy—XAS, XANES, EXAFS. *Canadian Journal of Chemical Engineering* vol. 100 3–22 Preprint at https://doi.org/10.1002/cjce.24291 (2022).

13. Castán-Guerrero, C. *et al.* A reaction cell for ambient pressure soft x-ray absorption spectroscopy. *Review of Scientific Instruments* **89**, (2018).

14. Baker, M. L. *et al.* K- and L-edge X-ray absorption spectroscopy (XAS) and resonant inelastic X-ray scattering (RIXS) determination of differential orbital covalency (DOC) of transition metal sites. *Coordination Chemistry Reviews* vol. 345 182–208 Preprint at https://doi.org/10.1016/j.ccr.2017.02.004 (2017).

15. De Groot, F. M. F. *et al. Oxygen 1s X-Ray-Absorption Edges of Transition-Metal Oxides*. *PHYSICAL REVIEW B* vol. 40.

16. Jaklevic, J. *et al. FLUORESCENCE DETECTION OF EXAFS: SENSITIVITY ENHANCEMENT FOR DILUTE SPECIES AND THIN FILMS*. *Solid State Communications* vol. 23 (1977).

17. Eisebitt, S., Boske, T., Rubensson, J.-E. & Eberhardt, W. *Determination of Absorption Coefficients for Concentrated Samples by Fluorescence Detection*. *PHYSICAL REVIEW B* vol. 47 (1993).

18. Wang, R. P. *et al.* Saturation and self-absorption effects in the angle-dependent 2 p3d resonant inelastic X-ray scattering spectra of Co3+. *J Synchrotron Radiat* **27**, 979–987 (2020).

19. Aziz, E. F. *et al.* Direct contact versus solvent-shared ion pairs in NiCl2 electrolytes monitored by multiplet effects at Ni(II) L edge X-ray absorption. *Journal of Physical Chemistry B* **111**, 4440–4445 (2007).

20. Troger, L. *et al. Full Correction of the Self-Absorption in Soft-Fluorescence Extended x-Ray-Absorption Fine Structure*. *PHYSICAL REVIEW B* vol. 46.

21. Inoue, D. & Komatsu, T. *Improved Self-Absorption Correction for Fluorescence Measurements of Extended x-Ray Absorption Fine-Structure You May Also like Local Structure of Fe 2+ and Fe 3+ in Organic Solvents*.

22. Frazer, B. H., Gilbert, B., Sonderegger, B. R. & De Stasio, G. The probing depth of total electron yield in the sub-keV range: TEY-XAS and X-PEEM. *Surf Sci* **537**, 161–167 (2003).

23. Abbate, M. *et al.* Probing depth of soft x-ray absorption spectroscopy measured in total-electron-yield mode. *Surface and Interface Analysis* **18**, 65–69 (1992).

24. Velasco-Velez, J. J. *et al.* Photoelectron Spectroscopy at the Graphene-Liquid Interface Reveals the Electronic Structure of an Electrodeposited Cobalt/Graphene Electrocatalyst. *Angewandte Chemie - International Edition* **54**, 14554–14558 (2015).

25. Swallow, J. E. N. *et al.* Operando X-ray Spectroscopy Reveals Solid Electrolyte Interphase Formation on Silicon Anodes for Li-ion Batteries. 1–41.

26. Jones, E. S., Swallow, J. E. N. & Weatherup, R. S. Enclosed Cells for Extending Soft X-ray Spectroscopies to Atmospheric Pressures and above. *ACS Symposium Series* **1396**, 175–218 (2021).

27. Dong, C. L. & Vayssieres, L. In Situ/Operando X-ray Spectroscopies for Advanced Investigation of Energy Materials. *Chemistry - A European Journal* vol. 24 18356–18373 Preprint at https://doi.org/10.1002/chem.201803936 (2018).

28. Cui, Z., Guo, X. & Li, H. Improved electrochemical properties of MnO thin film anodes by elevated deposition temperatures: Study of conversion reactions. *Electrochim Acta* **89**, 229–238 (2013).

29. Sångeland, C., Sun, B., Brandell, D., Berg, E. J. & Mindemark, J. Decomposition of Carbonate-Based Electrolytes: Differences and Peculiarities for Liquids vs. Polymers Observed Using Operando Gas Analysis. *Batter Supercaps* **4**, 785–790 (2021).

30. Bridel, J. S. *et al.* Decomposition of ethylene carbonate on electrodeposited metal thin film anode. *J Power Sources* **195**, 2036–2043 (2010).

31. Sun, B. *et al.* At the polymer electrolyte interfaces: the role of the polymer host in interphase layer formation in Li-batteries. *J Mater Chem A Mater* **3**, 13994–14000 (2015).

32. Hu, Y. Y. *et al.* Origin of additional capacities in metal oxide lithium-ion battery electrodes. *Nat Mater* **12**, 1130–1136 (2013).

33. Débart, A., Dupont, L., Poizot, P., Leriche, J.-B. & Tarascon, J. M. A Transmission Electron Microscopy Study of the Reactivity Mechanism of Tailor-Made CuO Particles toward Lithium. *J Electrochem Soc* **148**, A1266 (2001).

34. Lin, F. *et al.* Phase evolution for conversion reaction electrodes in lithium-ion batteries. *Nat Commun* **5**, (2014).

35. Kraytsberg, A. & Ein-Eli, Y. A critical review-promises and barriers of conversion electrodes for Li-ion batteries. *Journal of Solid State Electrochemistry* vol. 21 1907–1923 Preprint at https://doi.org/10.1007/s10008-017-3580-9 (2017).

36. Qiao, R., Chin, T., Harris, S. J., Yan, S. & Yang, W. Spectroscopic fingerprints of valence and spin states in manganese oxides and fluorides. *Current Applied Physics* **13**, 544–548 (2013).

37. Qiao, R. *et al.* Distinct Solid-Electrolyte-Interphases on Sn (100) and (001) Electrodes Studied by Soft X-Ray Spectroscopy. *Adv Mater Interfaces* **1**, (2014).

38. Vinogradov, A. S. *et al.* High Resolution F1 s Absorption Spectra of Solid Fluorides of 3 d Elements. *SOLID-STATE SPECTROSCOPY* **93**, 935–943 (2002).

39. Hudson, E. *et al. High-Resolution Measurements of near-Edge Resonances in the Core-Level Photoionization Spectra of SF6*. *PHYSICAL REVIEW A* vol. 47 (1993).

40. Hudson, E. *et al. High-Resolution Measurements of near-Edge Resonances in the Core-Level Photoionization Spectra of SF6*. *PHYSICAL REVIEW A* vol. 47 (1993).

41. Vinogradov, A. S. *et al.* Low-lying unoccupied electronic states in 3d transition-metal fluorides probed by NEXAFS at the F 1s threshold. *Phys Rev B Condens Matter Mater Phys* **71**, (2005).

42. Swallow, J. E. N. *et al.* Revealing solid electrolyte interphase formation through interface-sensitive Operando X-ray absorption spectroscopy. *Nat Commun* **13**, (2022).

43. Smith, J. W. *et al.* X-Ray absorption spectroscopy of LiBF4 in propylene carbonate: A model lithium ion battery electrolyte. *Physical Chemistry Chemical Physics* **16**, 23568–23575 (2014).

44. Schellenberger, M., Golnak, R., Quevedo Garzon, W. G., Risse, S. & Seidel, R. Accessing the solid electrolyte interphase on silicon anodes for lithium-ion batteries in-situ through transmission soft X-ray absorption spectroscopy. *Mater Today Adv* **14**, (2022).

45. Strmcnik, D. *et al.* Electrocatalytic transformation of HF impurity to H2 and LiF in lithium-ion batteries. *Nat Catal* **1**, 255–262 (2018).

46. Urquhart, S. G. & Ade, H. Trends in the carbonyl core (C 1S, O 1S) → π*c=o transition in the near-edge X-ray absorption fine structure spectra of organic molecules. *Journal of Physical Chemistry B* **106**, 8531–8538 (2002).

47. Frati, F., Hunault, M. O. J. Y. & De Groot, F. M. F. Oxygen K-edge X-ray Absorption Spectra. *Chemical Reviews* vol. 120 4056–4110 Preprint at https://doi.org/10.1021/acs.chemrev.9b00439 (2020).

48. Robin, M. B., Ishii, I., Mclaren, R. & Hitchcock, A. P. *FLUORINATION EFFECTS ON THE INNER-SHELL SPECTRA OF UNSATURATED MOLECULES***.

49. Yamamura, R., Suenaga, T., Oura, M., Tokushima, T. & Takahashi, O. pH dependence of aqueous oxalic acid observed by X-ray absorption and emission spectroscopy. *Chem Phys Lett* **738**, (2020).

50. Horikawa, Y. *et al.* Identification of valence electronic states of aqueous acetic acid in acid-base equilibrium using site-selective X-ray emission spectroscopy. *Physical Chemistry Chemical Physics* **11**, 8676–8679 (2009).

51. Tokushima, T. *et al.* Selective observation of the two oxygen atoms at different sites in the carboxyl group (-COOH) of liquid acetic acid. *Physical Chemistry Chemical Physics* **11**, 1679–1682 (2009).

52. Hitchcock, A. P., Urquhart, S. G. & Rightor, E. G. *Inner-Shell Spectroscopy of Benzaldehyde, Terephthalaldehyde, Ethyl Benzoate, Terephthaloyl Chloride, and Phosgene: Models for Core Excitation of Poly(Ethylene Terephthalate)*. *J. Phys. Chem* vol. 96 https://pubs.acs.org/sharingguidelines (1992).

53. Hitchcock, A. P. & Brion, C. E. *INNER-SHELL EXCITATION OF FORMALDEHYDE, ACETALDEHYDE AND ACETONE STUDIED BY ELECTRON IMPACT*. *Journal of Electron Spectroscopy and Related Phenomena* vol. 19 (1980).

54. Golnak, R. *et al.* Local electronic structure of aqueous zinc acetate: Oxygen K-edge X-ray absorption and emission spectroscopy on micro-jets. *Physical Chemistry Chemical Physics* **15**, 8046–8049 (2013).

55. Urquhart, S. G. & Ade, H. Trends in the carbonyl core (C 1S, O 1S) → π*c=o transition in the near-edge X-ray absorption fine structure spectra of organic molecules. *Journal of Physical Chemistry B* **106**, 8531–8538 (2002).

56. Zhuo, Z. *et al.* Breathing and oscillating growth of solid-electrolyte-interphase upon electrochemical cycling. *Chemical Communications* **54**, 814–817 (2018).

57. Michan, A. L., Leskes, M. & Grey, C. P. Voltage Dependent Solid Electrolyte Interphase Formation in Silicon Electrodes: Monitoring the Formation of Organic Decomposition Products. *Chemistry of Materials* **28**, 385–398 (2016).

58. Schwenke, K. U., Solchenbach, S., Demeaux, J., Lucht, B. L. & Gasteiger, H. A. The Impact of CO 2 Evolved from VC and FEC during Formation of Graphite Anodes in Lithium-Ion Batteries . *J Electrochem Soc* **166**, A2035–A2047 (2019).

59. Rinkel, B. L. D., Hall, D. S., Temprano, I. & Grey, C. P. Electrolyte Oxidation Pathways in Lithium-Ion Batteries. (2020) doi:10.1021/jacs.0c06363.

60. Qiao, R., Chuang, Y. De, Yan, S. & Yang, W. Soft X-Ray Irradiation Effects of Li2O2, Li2CO3 and Li2O Revealed by Absorption Spectroscopy. *PLoS One* **7**, (2012).

61. Kurata, H., Lefevre, E., Colliex, C. & Brydson, R. *Electron-Energy-Loss near-Edge Structures in the Oxygen E-Edge Spectra of Transition-Metal Oxides*. *PHYSICAL REVIEW B* vol. 47.

62. Björklund, E. *et al.* Cycle-Induced Interfacial Degradation and Transition-Metal Cross-Over in LiNi0.8Mn0.1Co0.1O2-Graphite Cells. *Chemistry of Materials* **34**, 2034–2048 (2022).

63. Malmgren, S. *et al.* Comparing anode and cathode electrode/electrolyte interface composition and morphology using soft and hard X-ray photoelectron spectroscopy. *Electrochim Acta* **97**, 23–32 (2013).

64. Bouayad, H. *et al.* Improvement of electrode/electrolyte interfaces in high-voltage spinel lithium-ion batteries by using glutaric anhydride as electrolyte additive. *Journal of Physical Chemistry C* **118**, 4634–4648 (2014).

65. Parimalam, B. S., MacIntosh, A. D., Kadam, R. & Lucht, B. L. Decomposition Reactions of Anode Solid Electrolyte Interphase (SEI) Components with LiPF6. *Journal of Physical Chemistry C* **121**, 22733–22738 (2017).

66. Guo, R. & Gallant, B. M. Li2O Solid Electrolyte Interphase: Probing Transport Properties at the Chemical Potential of Lithium. *Chemistry of Materials* **32**, 5525–5533 (2020).

67. Dedryvère, R. *et al.* Characterization of lithium alkyl carbonates by X-ray photoelectron spectroscopy: Experimental and theoretical study. *Journal of Physical Chemistry B* **109**, 15868–15875 (2005).

68. Madec, L. *et al.* The Effects of a Ternary Electrolyte Additive System on the Electrode/Electrolyte Interfaces in High Voltage Li-Ion Cells. *J Electrochem Soc* **163**, A1001–A1009 (2016).

69. Niehoff, P., Passerini, S. & Winter, M. Interface investigations of a commercial lithium ion battery graphite anode material by sputter depth profile X-ray photoelectron spectroscopy. *Langmuir* **29**, 5806–5816 (2013).

70. Zhu, Y., Li, Y., Bettge, M. & Abraham, D. P. Positive Electrode Passivation by LiDFOB Electrolyte Additive in High-Capacity Lithium-Ion Cells. *J Electrochem Soc* **159**, A2109–A2117 (2012).

71. Abbate, M. *et al.* Probing depth of soft x-ray absorption spectroscopy measured in total-electron-yield mode. *Surface and Interface Analysis* **18**, 65–69 (1992).

72. Weatherup, R. S., Wu, C. H., Escudero, C., Pérez-Dieste, V. & Salmeron, M. B. Environment-Dependent Radiation Damage in Atmospheric Pressure X-ray Spectroscopy. *Journal of Physical Chemistry B* **122**, 737–744 (2018).

73. Schön, D. *et al.* Introducing Ionic-Current Detection for X-ray Absorption Spectroscopy in Liquid Cells. *Journal of Physical Chemistry Letters* vol. 8 2087–2092 Preprint at https://doi.org/10.1021/acs.jpclett.7b00646 (2017).

74. Van Spronsen, M. A. *et al.* Interface Sensitivity in Electron/Ion Yield X-ray Absorption Spectroscopy: The TiO2-H2O Interface. *Journal of Physical Chemistry Letters* **12**, 10212–10217 (2021).

Chapter 6 - Conclusion

The aspiration of achieving Net Zero Emissions by 2050 presents a formidable challenge, with Li-ion batteries expected to play a pivotal role as energy storage systems. Over the past three decades, cell chemistry and design advancements have positioned Li-ion technology as a key solution for curbing carbon emissions, particularly in Battery Electric Vehicles (BEVs). As the industry shifts towards energy-dense batteries utilising Ni-rich materials, the imperative for effective stabilisation strategies at electrode interfaces becomes paramount. These strategies are essential for enabling efficient cycling of materials at elevated voltages and realising their full capacity potential.

The optimisation of battery materials and cells is crucial for extending battery life, enhancing EV range, and reducing overall battery costs, thereby facilitating wider adoption of this technology. Despite recent cost reductions driven by mass production, the widespread uptake of battery electric vehicles still faces barriers related to cost and durability. Battery lifetimes often fall short of consumer expectations for long-term applications such as transportation. Addressing these challenges necessitates ongoing efforts in research and development to enhance battery performance, durability, and affordability, ultimately accelerating the transition towards a sustainable energy future.

As part of the Faraday Institution's initiative to enhance the longevity of lithium-ion batteries, this DPhil project takes a comprehensive approach by refining characterisation techniques and data analysis pertinent to battery materials. Chapter 1 of this thesis introduces the foundational concepts of batteries and the key materials utilised for their operation. The latter half of the Introduction focuses on the degradation mechanisms affecting lithium-ion

batteries, particularly on cross-talk species, notably transition metal dissolution. Chapter 2 details the array of electrochemical, spectroscopic, and imaging techniques to investigate the degradation reactions associated with cross-talk species. This comprehensive approach, which encompasses both post-mortem and operando methodologies, is designed to provide a thorough understanding of battery degradation phenomena.

Chapter 3 of this thesis focused on developing XPEEM analysis for Nickel-rich cathode materials, specifically NMC811. The sample preparation was initially optimised to minimise mechanical degradation through the cold pressing method, which provided a flat surface for the XPEEM measurements. Spatiochemical measurements of 3d transition metal L-edges and O K-edges offered insights into degradation pathways on NMC811. Complementary C 1s, F 1s, and O 1s core-level maps revealed electrolyte decomposition at the particle surface. This integrated approach was successfully demonstrated on a particle with a reduced surface layer on electrode. Furthermore, spatial maps revealed the heterogeneity of charge distribution and degradation on the electrodes. Furthermore, it provided a correlation between a high Ni oxidation state and the low-energy pre-edge feature of the O K-edge, reflecting the covalency of the Ni-O bonds.

Combining XPEEM XAS and XPS microscopy modes enables high spatiochemical resolution imaging of surface alterations on cathode particles. This potentially offers valuable insight into the role of surface coatings, and electrolyte additives, which are essential for enhancing the cycle life and suitability for high-voltage applications of lithium-ion battery cathodes. XPEEM plays a key role in uncovering surface properties crucial to high-capacity cathode materials, with implications extending to other energy storage materials.

In Chapter 4, the focus was on addressing cross-talk issues, particularly the migration of TM dissolved from the cathode. TMs migrate and are incorporated into the anode SEI, which is known to cause capacity fade in lithium-ion batteries. Depth-dependent variations in TM behaviour on the anode SEI were revealed using a combination of soft and hard X-ray techniques.

XANES measurements on graphite electrodes cycled in full cells revealed metallic TMs within the inner SEI, forming <5 nm-sized particles. Mn in the inner SEI exhibited redox activity during lithiation and delithiation of the graphite electrode, whereas this activity was less pronounced for Ni species at the anode SEI. Notably, Mn^{2+} fails to ion exchange with Li_2CO_3, suggesting the potential for SEI engineering to incorporate more Li_2CO_3 on the anode SEI to mitigate Mn-related SEI issues.

Future work could expand upon XANES analysis on graphite electrodes to assess the impact of Co^{2+} ions on the SEI. Additionally, investigations into other TM effects in lithium-ion batteries, such as dissolved Fe species, and their impact on SEI growth and impedance could provide valuable insights. This research holds significant commercial and scientific relevance, particularly with the increasing adoption of cheaper cathode chemistries like LFP and LMFP, along with the underexplored role of Fe as a cross-talk species in the literature.

In chapter 5, the final results chapter a novel operando NEXAFS cell was developed to characterise the potential dependent evolution of the SEI. Using a combination of modulated TEY mode and FY mode, soft XAS techniques demonstrated the SEI growth on Ni and MnO thin film electrodes under realistic battery operating conditions. With its interface-sensitive nature, TEY proves particularly effective in elucidating the initial stages of SEI formation. At the same time, FY enables simultaneous monitoring of SEI evolution and electrolyte dynamics

throughout the process These operando measurements revealed the surface reduction of Ni electrodes, leading to the formation of LiF passivating the electrode. In contrast, the MnO electrode system did not form a thick layer, enabling measurements on the electrolyte even at low potentials. Through the use of O K-edge XAS spectra, the growth of a low photon energy peak was identified and associated with the formation of organic SEI components, previously linked to transitions from the oxygen 1s orbital of carbonyl (C=O) groups to π*-antibonding orbitals. Transition energies for various organic components, categorised by molecular motifs, reveal a trend, aiding in attributing to the low energy feature on both Ni and MnO electrodes at approximately 531.5 eV to aldehyde (-C(=O)H), ketone (-C(=O)R), carboxyl (-C(=O)OH), and/or ester (-C(=O)OR) groups. The decline in peak intensities at 533 eV associated with ethylene carbonate (EC) and dimethyl carbonate (DMC) corresponds to the ring opening of EC most likely through cleavage of the C-O bonds, indicating that SEI formation involves the breakdown of these carbonate species, yielding motifs containing -C(=O) or -C(=O)O functional groups.

The environmental cell provides broad applicability of the experimental setup detailed in this chapter, which can be readily extended to explore a diverse range of thin-film anodes, cathodes and the role of electrolyte salts and additives. By providing insights into the formation mechanisms and chemical stability of electrode-electrolyte interfaces, the method outlined in this chapter can catalyse advancements in energy storage and beyond.

Appendix

Igor Pro 8 procedure used for XPEEM analysis in Chapter 3:

```
#pragma TextEncoding = "UTF-8"
#pragma rtGlobals=3                    // Use modern global access method and strict wave access.


//Creates a drop down menu called Own XPS maccro, If you click on XPS plotting the maccro will start.
Menu "_XPS"
                                "XAS things", XYfixa()
End
Function XYfixa()
//creates a box where you can place buttons etc.
NewPanel /K=1 /W=(13,52.25,400,500) as "start Window"
//draws a box (in the first box) with pink color and a text
Button button0 title="Merge", size={130,20}, pos ={40,65}, proc=FixXYstuf
SetDrawEnv fillfgc= (1,32768,58981)
DrawRRect 23,12,176,85
DrawText 40,30,"make xy wave"
Button button1 title="fix merged", size={130,20}, pos ={230,65}, proc=FixXYstufds
SetDrawEnv fillfgc= (1,32768,58981)
DrawRRect 223,12,376,85
DrawText 230,30,"fix xy wave"
Button button2 title="combine waves", size={130,20}, pos ={40,120}, proc=backy
SetDrawEnv fillfgc= (1,32768,58981)
DrawRRect 23,95,376,150
DrawText 40,110,"add first wave to second wave"
PopupMenu popupmenuNu title="wave 1",pos={230,100},proc=startwave1;DelayUpdate
PopupMenu popupmenuNu value=WaveList("*",";","")
PopupMenu popupmenuNub title="wave 2",pos={230,120},proc=startwave2;DelayUpdate
PopupMenu popupmenuNub value=WaveList("*",";","")
Button button3 title="remove L. backG", size={130,20}, pos ={40,170}, proc=rlbkg
SetDrawEnv fillfgc= (1,32768,58981)
DrawRRect 23,155,376,195
DrawText 40,170,"remove a linear background by cursors"
Button button4 title="conv. to fitting", size={130,20}, pos ={40,200}, proc=fitwavestuf
Button button5 title="Merge2", size={130,20}, pos ={40,220}, proc=FixXYstufdfg
Button button6 title="Delete last point", size={130,20}, pos ={40,240}, proc=deletepointlegegse
Button button7 title="multiply wave", size={130,20}, pos ={40,260}, proc=multiplynekrg
```

```
SetVariable hejjjj title="multiplying value",value= K0, size={160,20}, pos ={200,260}
Button button8 title="Plot fitted XAS", size={130,20}, pos ={40,280}, proc=XASplotta
PopupMenu popupmenuNuKK title="raw y wave",pos={200,280},proc=startYwavexas;DelayUpdate
PopupMenu popupmenuNuKK value=WaveList("*",";","")
PopupMenu popupmenuNubLL title="raw x wave",pos={200,300},proc=startXwavexas;DelayUpdate
PopupMenu popupmenuNubLL value=WaveList("*",";","")
SetDrawEnv fillfgc= (1,32768,58981)
DrawRRect 23,320,376,420
Button button9 title="remove linear bkg", size={130,20}, pos ={40,360}, proc=bkgremove
PopupMenu popupmenuNubLLee title="raw x wave",pos={200,360},proc=startXwavexasee;DelayUpdate
PopupMenu popupmenuNubLLee value=WaveList("*",";","")
PopupMenu popupmenuNuKKdd title="raw y wave",pos={200,340},proc=startYwavexasdd;DelayUpdate
PopupMenu popupmenuNuKKdd value=WaveList("*",";","")
SetVariable hejjjjx1 title="x1",value= K1, size={140,20}, pos ={40,380}
SetVariable hejjjjy1 title="y1",value= K2, size={140,20}, pos ={200,380}
SetVariable hejjjjx2 title="x2",value= K3, size={140,20}, pos ={40,400}
SetVariable hejjjjy2 title="y2",value= K4, size={140,20}, pos ={200,400}
Button button10 title="nice xas graph", size={130,20}, pos ={200,200}, proc=nicexasgraph
Button button11 title="remove L. backG 1D wave", size={160,20}, pos ={40,300}, proc=linearBack1d
Button button12 title="divide XAS data by I0", size={160,20}, pos ={40,430}, proc=XASdivide
Button button13 title="transpose wave", size={160,20}, pos ={200,430}, proc=transposeAuto
end
//Button 0, Merges x and y wave to create one wave (one column)
// Button 0 starts the ChangeNY function
function FixXYstuf(button0) : ButtonControl
//Must write button0 as a string for Igor to recognice.
string button0
//I want the offset to be stored in a variable called XYdo, which has to be defined
variable XYdo
//Gives a value to XYdo from what is typed in
XYdo=K0
string xwave="energies"
string ywave="spectrum_data"
String savedDFee= GetDataFolder(0)//saves the path to the normal datafolder
savedDFee=ReplaceString("'", savedDFee, "")
string namn ="Int"+savedDFee
//print(namn)
duplicate/o $ywave,$namn
```

```
wavestats/Q $xwave
variable Value1=-(V_max-V_min)/V_endRow
//print(V_max)
//print(V_min)
//print(V_endRow)
//print(Value1)
SetScale/p x, V_max, Value1, "eV", $ywave
//the function must always have an end
end
function FixXYstufds(button1) : ButtonControl
//Must write button0 as a string for Igor to recognice.
string button1
//I want the offset to be stored in a variable called XYdo, which has to be defined
variable XYdoit
//Gives a value to XYdo from what is typed in
XYdoit=K1
string xwave
string ywave
String savedDFee= GetDataFolder(0)//saves the name of the normal datafolder
savedDFee=ReplaceString("'", savedDFee, "")
string namn ="Int"+savedDFee
String savedDFere= GetDataFolder(1)
string datafolders= DataFolderDir(1)
datafolders=ReplaceString("FOLDERS:", datafolders, "")
datafolders=ReplaceString(";", datafolders, "")
string sListItem
variable vlistitems
variable ic
vlistitems = ItemsInList(datafolders, ",")
string tempfolder
for (ic=0; ic<=vlistitems-2; ic+=1)
                sListItem = StringFromList(ic, datafolders, ",")
                //print(sListItem)
                sListItem="'"+sListItem+"'"+":"
                //print(sListItem)
                tempfolder=savedDFere+sListItem
                print(tempfolder)
                setdatafolder tempfolder
```

```
		print(GetDataFolder(0))
		ywave="spectrum_data"
		xwave="energies"
		duplicate/o $ywave,egrssg
		wavestats/Q $xwave
		variable Value1=-(V_max-V_min)/V_endRow
		SetScale/p x, V_max, Value1, "eV", $ywave
		setdatafolder savedDFere
Endfor
//print(GetDataFolder(1))
//duplicate/o $ywave,$namn
//wavestats/Q $xwave
//variable Value1=-(V_max-V_min)/V_endRow
//print(V_max)
//print(V_min)
//print(V_endRow)
//print(Value1)
//SetScale/p x, V_max, Value1, "eV", $ywave
end
function backy(button2) : ButtonControl
//combine datawaves
string button2
String savedDFolde= GetDataFolder(1)//saves the path to the normal datafolder
setdataFolder root:Areabox
string wave1
wave1="wave1tocombine"
string wave2
wave2="wave2tocombine"
Wave/t tempor1 = $wave1//creates a temporary wave named tempor. this wave name is used in the program
Wave/t tempor2 = $wave2//creates a temporary wave named tempor. this wave name is used in the program
variable wavelength
variable length1=str2num(tempor1[2])
variable length2=str2num(tempor2[2])
wavelength=str2num(tempor1[2])+str2num(tempor2[2])
wave1= tempor1[0]
wave2=tempor2[0]
SetDataFolder savedDFolde//restores the path to the normal data folder
string wave1data
```

```
wave1data="data1"
duplicate/o $wave1, $wave1data
Wave tempor3 = $wave1data//creates a temporary wave named tempor. this wave name is used in the program
string wave2data
wave2data="data2"
duplicate/o $wave2, $wave2data
Wave tempor4 = $wave2data//creates a temporary wave named tempor. this wave name is used in the program
//print(wavelength)
string combined_waves
combined_waves="combined"
make/o/n =(wavelength) $combined_waves
Wave temporCom = $combined_waves
temporCom[0,length1-1]=tempor3[x]//assign the new wave values in the index range 0 to a number. (x is the index variable igor automatically uses)
temporCom[length1,wavelength-1]=tempor4[x-length1]// assign the range starting from a higher index than 0
KillWaves $wave1data
KillWaves $wave2data
//the function must always have an end
end
Function startwave1 (ctrlName1a,popNuma,popStra) : PopupMenuControl
		String ctrlName1a
		Variable popNuma		// which item is currently selected (1-based)
		String popStra				// contents of current popup item as string
		//print popStr
		//print popNum
		String savedDFolde= GetDataFolder(1)//saves the path to the normal datafolder
		string option
		//print(savedDFolde)
		//print(popStra)
		WaveStats/Q $popStra
		//print (V_npnts)
		variable foldern
		foldern=DataFolderRefStatus(root:Areabox)//the variable folderstatus will become 1 if folder root:ErikWin exists, else it will become 0
		if(foldern==0)
			NewDataFolder/O/S root:Areabox
			else
		endif
```

```
		setdatafolder root:Areabox


		option="wave1tocombine"
		Make /O/t=(3) $option//creates a wave with only 1 number, wavename =Normalizationarea+samplenummer
		Wave/t temporO = $option//creates a temporary wave named tempor. this wave name is used in the program
		//temporO[0]=popStr //gives a name to the wave
		temporO[0]=popStra //gives a name to the wave
		temporO[1]=savedDFolde
		temporO[2]=num2str(V_npnts)
		SetDataFolder savedDFolde//restores the path to the normal data folder
End
Function startwave2 (ctrlName1b,popNumb,popStrb) : PopupMenuControl
		String ctrlName1b
		Variable popNumb		// which item is currently selected (1-based)
		String popStrb				// contents of current popup item as string
		//print popStr
		//print popNum
		String savedDFolded= GetDataFolder(1)//saves the path to the normal datafolder
		string option
		//print(savedDFolded)
		//print(popStrb)
		WaveStats/Q $popStrb
		//print (V_npnts)
		variable foldern
		foldern=DataFolderRefStatus(root:Areabox)//the variable folderstatus will become 1 if folder root:ErikWin exists, else it will
become 0
		if(foldern==0)
			NewDataFolder/O/S root:Areabox
			else
		endif
		setdatafolder root:Areabox
		option="wave2tocombine"
		Make /O/t=(3) $option//creates a wave with only 1 number, wavename =Normalizationarea+samplenummer
		Wave/t temporO = $option//creates a temporary wave named tempor. this wave name is used in the program
		//temporO[0]=popStr //gives a name to the wave
		temporO[0]=popStrb //gives a name to the wave
		temporO[1]=savedDFolded
		temporO[2]=num2str(V_npnts)
```

```
		SetDataFolder savedDFolded//restores the path to the normal data folder
End
//startYwavexas
Function startYwavexas (ctrlName1ac,popNumac,popStrac) : PopupMenuControl
		String ctrlName1ac
		Variable popNumac		// which item is currently selected (1-based)
		String popStrac				// contents of current popup item as string
		//print popStr
		//print popNum
		String savedDFoldeDD= GetDataFolder(1)//saves the path to the normal datafolder
		string optionc
		//print(savedDFoldeDD)
		//print(popStrac)
		WaveStats/Q $popStrac
		//print (V_npnts)
		variable foldernc
		foldernc=DataFolderRefStatus(root:Areabox)//the variable folderstatus will become 1 if folder root:ErikWin exists, else it will become 0
		if(foldernc==0)
			NewDataFolder/O/S root:Areabox
			else
		endif
		setdatafolder root:Areabox

		optionc="XASywave"
		Make /O/t=(3) $optionc//creates a wave with only 1 number, wavename =Normalizationarea+samplenummer
		Wave/t temporOc = $optionc//creates a temporary wave named tempor. this wave name is used in the program
		//temporOc[0]=popStr //gives a name to the wave
		temporOc[0]=popStrac //gives a name to the wave
		temporOc[1]=savedDFoldeDD
		//temporOc[2]=num2str(V_npnts)
		SetDataFolder savedDFoldeDD//restores the path to the normal data folder
End
Function startXwavexas (ctrlName1acd,popNumacd,popStracd) : PopupMenuControl
		String ctrlName1acd
		Variable popNumacd		// which item is currently selected (1-based)
		String popStracd				// contents of current popup item as string
		//print popStr
```

```
		//print popNum
		String savedDFoldeDDd= GetDataFolder(1)//saves the path to the normal datafolder
		string optioncd
		//print(savedDFoldeDDd)
		//print(popStrac)
		WaveStats/Q $popStracd
		//print (V_npnts)
		variable folderncd
		folderncd=DataFolderRefStatus(root:Areabox)//the variable folderstatus will become 1 if folder root:ErikWin exists, else it
will become 0
		if(folderncd==0)
			NewDataFolder/O/S root:Areabox
			else
		endif
		setdatafolder root:Areabox
		optioncd="XASxwave"
		Make /O/t=(3) $optioncd//creates a wave with only 1 number, wavename =Normalizationarea+samplenummer
		Wave/t temporOcd = $optioncd//creates a temporary wave named tempor. this wave name is used in the program
		//temporOc[0]=popStr //gives a name to the wave
		temporOcd[0]=popStracd //gives a name to the wave
		temporOcd[1]=savedDFoldeDDd
		//temporOc[2]=num2str(V_npnts)
		SetDataFolder savedDFoldeDDd//restores the path to the normal data folder
End
function rlbkg(button3) : ButtonControl
//Must write button0 as a string for Igor to recognice.
string button3
String savedDFoldsd= GetDataFolder(1)//saves the path to the normal datafolder
WAVE wA = CsrWaveRef(A)
String dfA = GetWavesDataFolder(wA, 1)//get folder cursor is on
String dfA2 = GetWavesDataFolder(wA, 2)//get folder and wave cursor is on
String waveCursorAIsOn = CsrWave(A)//get wave cursor is on
string xwave= CsrXWave(A)// get x wave
setdatafolder dfA
variable Ax, Ay, Bx, By, slope, konstant, Axp, Bxp
Ay=vcsr(A)
Axp=pcsr(A)
By=vcsr(B)
```

```
Bxp=pcsr(B)
string xenergywave=xwave+"en"
duplicate/o $xwave, $xenergywave
wave temmmenergy =$xenergywave
Ax=temmmenergy[Axp]
Bx=temmmenergy[Bxp]
slope=(By-Ay)/(Bx-Ax)
konstant=Ay-slope*Ax
//print(slope)
//print(konstant)
wavestats/q $waveCursorAIsOn
variable ic
string hej= waveCursorAIsOn +"B"
make /o/n=(V_npnts) $hej
wave inttempny=$hej
for (ic=0; ic<=V_npnts-1; ic+=1)
                inttempny[ic]=temmmenergy[ic]*slope+konstant
endfor
wave temmmpStartintensitet =$waveCursorAIsOn//intensitetswave at start
string NormIntensity=waveCursorAIsOn+"Norm"
duplicate/o $waveCursorAIsOn, $NormIntensity
wave temmmpNorm =$NormIntensity
temmmpNorm=temmmpStartintensitet-inttempny
killwaves temmmenergy
setdatafolder dfa
//String traceCursorAIsOn = CsrWave(A,"",1)              // trace name in top graph
//print(traceCursorAIsOn)
//Print CsrWaveRef(A)[50]//value at point 50 of wave
//print("lll")
//string cursora =CsrInfo(A,"")
//print(cursora)
//string list = tracenamelist("",";", 1)   //get list of normal traces on topmost graph
//print(list)
//string graph_name,spec_name
//variable specnummer
//string graph_name=WinName(0,1)
//print(graph_name)
//spec_name=Wavename(graph_name,specnummer,1)//get name of wave in graph
```

```
//position= GetWavesDataFolder(TraceNameToWaveRef(graph_name, spec_name ), 1)//get folder path of wave in graph
		//SetDataFolder position
		//string iw
		//iw="copy"
		//duplicate /O/R=(xcsr(A),xcsr(B)) $specname,$iw
		//wave temp =$iw
SetDataFolder savedDFoldsd
//the function must always have an end
end
function fitwavestuf(button4) : ButtonControl
//Must write button0 as a string for Igor to recognice.
string button4
string ywave=WaveList("*_A", "","")//WaveList("*_A", ";","") if multiple names ending with _A, ; will separate the names
string namn=ywave+"9000"
duplicate/o $ywave,$namn
wave grekrkn=$namn
grekrkn=grekrkn*9000
end
function FixXYstufdfg(button5) : ButtonControl
//Must write button0 as a string for Igor to recognice.
string button5
//I want the offset to be stored in a variable called XYdo, which has to be defined
String dummy, ActWaveList="", ActWaveNames="", ActWaveName0,ActWaveName1
		Variable pos, i, NumItems
		//creates a wave list from the browser selection
		do
			dummy=GetBrowserSelection(i)
			print dummy
			if (strlen(dummy)>0)
				ActWaveList+=dummy+";"
				pos=strsearch(dummy, ":",Inf,1)  //separates folders and wave
				ActWaveNames+=dummy[pos+1,strlen(dummy)-1]+";"
				i+=1
			else
				NumItems=i
				break
			endif
		while (1)
```

```
		ActWaveName0=StringFromList(0,ActWaveNames)
		ActWaveName1=StringFromList(1,ActWaveNames)
		//print(ActWaveName0)
		Wave ActWave0=$ActWaveName0  //gives IGOR the wave stored in ActWaveName0 (energies)
		String ActWave_op=ActWaveName0+"Subs2"//name of the new wave
		Duplicate/O ActWave0, $ActWave_op  //new wave with the name 'ActWaveName0+"Subs"'  is generated in the data folder
		Wave OpWave=$ActWave_op  //gives IGOR the wave
		wavestats/Q OpWave//energies
		variable pointsinuse=V_npnts
		variable maxvalue=V_max
		variable Value1=-(V_max-V_min)/(V_npnts-1)//Change to a new energy wave similar to the intensity wave
		wave ActWave1=$ActWaveName1  //gives IGOR the wave stored in ActWaveName1 (intensities)
		string wakjgnr=ActWaveName0+"int"
		Duplicate/o/R=[0, (pointsinuse-1)] ActWave1, $wakjgnr
		wave hej=$wakjgnr//intensitet wave utan extrapunkter
		SetScale/p x, maxvalue, Value1, "eV", hej
		killwaves OpWave
end
function deletepointlegegse(button6) : ButtonControl
//Must write button0 as a string for Igor to recognice.
string button6
String dummy, ActWaveList="", ActWaveNames="", ActWaveName0,ActWaveName1
		Variable pos, i, NumItems
		//creates a wave list from the browser selection
		do
			dummy=GetBrowserSelection(i)
			print dummy
			if (strlen(dummy)>0)
				ActWaveList+=dummy+";"
				pos=strsearch(dummy, ":",Inf,1)  //separates folders and wave
				ActWaveNames+=dummy[pos+1,strlen(dummy)-1]+";"
				i+=1
			else
				NumItems=i
				break
			endif
		while (1)
		ActWaveName0=StringFromList(0,ActWaveNames)
```

```
		Wave ActWave0=$ActWaveName0
		wavestats ActWave0
		DeletePoints V_npnts,1, ActWave0
end
function multiplynekrg(button7) : ButtonControl
//Must write button0 as a string for Igor to recognice.
string button7
variable hejjjj
hejjjj=K0
String dummy, ActWaveList="", ActWaveNames="", ActWaveName0,ActWaveName1
		Variable pos, i, NumItems
		//creates a wave list from the browser selection
		do
			dummy=GetBrowserSelection(i)
			print dummy
			if (strlen(dummy)>0)
				ActWaveList+=dummy+";"
				pos=strsearch(dummy, ":",Inf,1)  //separates folders and wave
				ActWaveNames+=dummy[pos+1,strlen(dummy)-1]+";"
				i+=1
			else
				NumItems=i
				break
			endif
		while (1)
		ActWaveName0=StringFromList(0,ActWaveNames)
		Wave ActWave0=$ActWaveName0
ActWave0=ActWave0*hejjjj
string newwavename=ActWaveName0+num2str(hejjjj)
Rename ActWave0, $newwavename
end
function XASplotta(button8) : ButtonControl
//this function plots xas data from ctm4xas together with the fit
//Must write button0 as a string for Igor to recognice.
string button8
String savedDFolde= GetDataFolder(1)//saves the path to the normal datafolder
//get the name of the raw x and y data
setdataFolder root:Areabox
```

```
string rawyXAS
rawyXAS="XASywave"
string rawxXAS
rawxXAS="XASxwave"
Wave/t tempor1 = $rawyXAS//creates a temporary wave named tempor. this wave name is used in the program
Wave/t tempor2 = $rawxXAS//creates a temporary wave named tempor. this wave name is used in the program
rawyXAS= tempor1[0]
rawxXAS=tempor2[0]
SetDataFolder savedDFolde//restores the path to the normal data folder
string rawy
//rawy="ratio39to8_582"
string rawx
//rawx="jenergy_582"
rawy=rawyXAS
rawx=rawxXAS
string fittedwave
fittedwave="fit_"+rawy
//input the reference waves from marking the waves in the data browser
String dummy, ActWaveList="", ActWaveNames="", ActWaveName
		Variable pos, i, NumItems
		//creates a wave list from the browser selection
		do
			dummy=GetBrowserSelection(i)
			print dummy
			if (strlen(dummy)>0)
				ActWaveList+=dummy+";"
				pos=strsearch(dummy, ":",Inf,1)  //separates folders and wave
				ActWaveNames+=dummy[pos+1,strlen(dummy)-1]+";"
				i+=1
			else
				NumItems=i
				break
			endif
		while (1)
//does the mathematical operation (i.e. add background to the reference waves and intensity normalization of them)
		//the folder that contains the wave(s) has to be activated
variable startx,endx,pointnumber,delta,ic,currentx,currenty
wave W_coef
```

```
display
make/o/N=(ItemsInList(ActWaveNames)*2) start_end//wave to store start and end values in (x values)
make/o/N=(ItemsInList(ActWaveNames)) area_save//wave to store the areas in
		for(i=0;i<NumItems;i+=1)
			ActWaveName=StringFromList(i,ActWaveNames)
			String info= TraceInfo("",NameOfWave($ActWaveName), 0)//get info about the wave
			//print info
			Wave ActWave=$ActWaveName  //gives IGOR each wave stored in WaveList
			String ActWave_op=ActWaveName+"_new"//name of the new wave
			Duplicate/O ActWave, $ActWave_op  //new wave with the name 'ActWaveName+"_new"'  is generated in the data folder
			Wave OpWave=$ActWave_op  //gives IGOR the wave
			startx=leftx(OpWave)+W_coef[2]
			endx=rightx(OpWave)+W_coef[2]
			start_end[2*i]=startx
			start_end[2*i+1]=endx
			wavestats/Q OpWave
			pointnumber=V_npnts
			delta=(endx-startx)/pointnumber
			for (ic=0; ic<=pointnumber-1; ic+=1)
				currentx=startx+ic*delta
				currenty=W_coef[0]*currentx+W_coef[1]//of the straight line
				OpWave[ic]=OpWave[ic]*W_coef[i+3]+currenty//fix background +adds the straight line
			endfor
			SetScale/i x  startx ,  endx  ,  OpWave//rescaling x axis
				appendtograph OpWave
				String tname= NameOfWave(OpWave)+"#0"//append to graph makes the wavename strange so this is the new name...(the trace name)
			if(i==0)
			ModifyGraph mode($tname)=7,hbFill($tname)=5,rgb($tname)=(3,52428,1)
				elseif(i==1)
				ModifyGraph mode($tname)=7,hbFill($tname)=5,rgb($tname)=(1,4,52428)
				elseif(i==2)
				ModifyGraph mode($tname)=7,hbFill($tname)=5,rgb($tname)=(65535,0,52428)
				else
				endif
			//save area of wave
			duplicate/o ActWave, wave__area//ActWave or (opwave?)
```

```
                wave__area= wave__area*W_coef[i+3]
                integrate wave__area
                wavestats/Q wave__area
                area_save[i]=wave__area[V_npnts-1]
                killwaves wave__area
                print(i)
        endfor
//"remove the filled background in the graph"
wavestats/Q start_end
make/o/n=2 ghrvy
ghrvy[0]=W_coef[0]*(V_min)+W_coef[1]//minimum y value
ghrvy[1]=W_coef[0]*(V_max)+W_coef[1]//maximum y value
make/o/n=2 ghrvx
ghrvx[0]=V_min//+W_coef[2]  //minimum x value
ghrvx[1]=V_max//+W_coef[2]
//calculate % of different references
        wavestats/Q area_save
        for(i=0;i<ItemsInList(ActWaveNames);i+=1)
                print(StringFromList(i,ActWaveNames))
                print(area_save[i]/V_sum*100)
        endfor
appendtograph ghrvy vs ghrvx
appendtograph $fittedwave
appendtograph $rawy vs $rawx
ModifyGraph mode($rawy)=2,lsize($rawy)=2,rgb($rawy)=(13107,0,5243)
ModifyGraph mirror=2,nticks(left)=0,fSize=12;DelayUpdate
ModifyGraph
mode(ghrvy)=7,usePlusRGB(ghrvy)=1,hbFill(ghrvy)=2,useNegPat(ghrvy)=1,hBarNegFill(ghrvy)=2,rgb(ghrvy)=(65535,65535,65535),plusRGB(
ghrvy)=(65535,65535,65535)
Label left "Intensity / a.u.";DelayUpdate
Label bottom "Photon excitation energy / eV"
 print("hej_EEe")
end
Function startYwavexasdd (ctrlName1acdd,popNumacdd,popStracdd) : PopupMenuControl
        String ctrlName1acdd
        Variable popNumacdd         // which item is currently selected (1-based)
        String popStracdd                       // contents of current popup item as string
        //print popStr
```

```
		//print popNum
		String savedDFoldeDDdd= GetDataFolder(1)//saves the path to the normal datafolder
		string optioncdd
		//print(savedDFoldeDD)
		//print(popStracdd)
		WaveStats/Q $popStracdd
		//print (V_npnts)
		variable folderncdd
		folderncdd=DataFolderRefStatus(root:Areabox)//the variable folderstatus will become 1 if folder root:ErikWin exists, else it will become 0
		if(folderncdd==0)
			NewDataFolder/O/S root:Areabox
			else
		endif
		setdatafolder root:Areabox
		optioncdd="ywavestart"
		Make /O/t=(3) $optioncdd//creates a wave with only 1 number,
		Wave/t temporOcdd = $optioncdd//creates a temporary wave named tempor. this wave name is used in the program
		//temporOcdd[0]=popStr //gives a name to the wave
		temporOcdd[0]=popStracdd //gives a name to the wave
		temporOcdd[1]=savedDFoldeDDdd
		//temporOcdd[2]=num2str(V_npnts)
		SetDataFolder savedDFoldeDDdd//restores the path to the normal data folder
End
Function startXwavexasee (ctrlName1acee,popNumacee,popStracee) : PopupMenuControl
		String ctrlName1acee
		Variable popNumacee	// which item is currently selected (1-based)
		String popStracee			// contents of current popup item as string
		//print popStr
		//print popNum
		String savedDFoldeDDee= GetDataFolder(1)//saves the path to the normal datafolder
		string optioncee
		//print(savedDFoldeDDee)
		//print(popStracee)
		WaveStats/Q $popStracee
		//print (V_npnts)
		variable folderncee
```

```
		folderncee=DataFolderRefStatus(root:Areabox)//the variable folderstatus will become 1 if folder root:ErikWin exists, else it will become 0
		if(folderncee==0)
			NewDataFolder/O/S root:Areabox
			else
		endif
		setdatafolder root:Areabox
		optioncee="xwavestart"
		Make /O/t=(3) $optioncee//creates a wave with only 1 number,
		Wave/t temporOcee = $optioncee//creates a temporary wave named tempor. this wave name is used in the program
		//temporOcee[0]=popStr //gives a name to the wave
		temporOcee[0]=popStracee //gives a name to the wave
		temporOcee[1]=savedDFoldeDDee
		//temporOcdd[2]=num2str(V_npnts)
		SetDataFolder savedDFoldeDDee//restores the path to the normal data folder
End
function bkgremove(button9) : ButtonControl
//Must write button0 as a string for Igor to recognice.
string button9
//I want the offset to be stored in a variable called XYdo, which has to be defined
variable Xdata1,ydata1,xdata2,ydata2
//Gives a value to XYdo from what is typed in
xdata1=K1
ydata1=K2
xdata2=K3
ydata2=K4
String savedDFoldeDDee= GetDataFolder(1)//saves the path to the normal datafolder
setdatafolder root:Areabox
string ywavenamme, xwavenamme, destxwave,destywave
ywavenamme="ywavestart"
xwavenamme="xwavestart"
Wave/t ydest= $ywavenamme
Wave/t xdest= $xwavenamme
destywave=ydest[0]
destxwave=xdest[0]
SetDataFolder savedDFoldeDDee
//make the future background subtracted wave and give it a temporary name for igor
string Newy
```

```
Newy=destywave+"Lbkg_startend"
duplicate/o $destywave, $Newy
wave temsenow = $Newy
//fix backgroundwave which is removed (start by getting the start x and end x of real wave)
wave xvalues = $destxwave
//slope of new backround
variable slope,mvalue
slope=(ydata1-ydata2)/(xdata1-xdata2)
// m value of background
mvalue=ydata1-slope*xdata1
variable lengthy,ic
lengthy=DimSize(temsenow, 0 )
//lengthy=numpnts(temsenow )
make/o/n=(lengthy) temporaryWave456
                for (ic=0; ic<=lengthy-1; ic+=1)
                                        temporaryWave456[ic]= slope*xvalues[ic]+mvalue
                endfor
//remove background
temsenow=temsenow-temporaryWave456
killwaves temporaryWave456
end
function nicexasgraph(button10) : ButtonControl
//Must write button0 as a string for Igor to recognice.
string button10
ModifyGraph margin(left)=28
ModifyGraph linTkLabel(left)=1
ModifyGraph nticks(left)=0
ModifyGraph mirror=2
Label left "Intensity / a.u.";DelayUpdate
Label bottom "Photon excitation energy / eV"
end
function linearBack1d(button11) : ButtonControl
//Must write button0 as a string for Igor to recognice.
string button11
// get area of all spectra after a linear background substraction between the start and the end points
String dummy, ActWaveList="", ActWaveNames="", ActWaveName
                Variable pos, i, NumItems
                //creates a wave list from the browser selection
```

```
		do
			dummy=GetBrowserSelection(i)
			print dummy
			if (strlen(dummy)>0)
				ActWaveList+=dummy+";"
				pos=strsearch(dummy, ":",Inf,1)  //separates folders and wave
				ActWaveNames+=dummy[pos+1,strlen(dummy)-1]+";"
				i+=1
			else
				NumItems=i
				break
			endif
		while (1)
//does the mathematical operation
		//the folder that contains the wave(s) has to be activated
		variable iii, NumItemsiii
		variable starty, endy, slope, startx, endx, mvalue, points,arean
		string wavearea
		for(i=0;i<NumItems;i+=1)
			ActWaveName=StringFromList(i,ActWaveNames)
			String info= TraceInfo("",NameOfWave($ActWaveName), 0)//get info about the wave
			//print info
			Wave ActWave=$ActWaveName  //gives IGOR each wave stored in WaveList
			String ActWave_op=ActWaveName+"area"//name of the new wave
			Duplicate/O ActWave, $ActWave_op  //new wave with the name 'ActWaveName+"area"'  is generated in the
data folder
			Wave OpWave=$ActWave_op  //gives IGOR the wave
			//OpWave[]=ActWave/SW
			wavestats/q OpWave
			starty=OpWave[0]
			endy=OpWave[V_npnts-1]
			startx=leftx(OpWave)
			endx=rightx(OpWave)
			slope=(endy-starty)/(endx-1-startx)
			mvalue=starty-startx*slope
			make/o/n=(V_npnts) bdnfklg
			NumItemsiii=V_npnts
			for(iii=0;iii<NumItemsiii;iii+=1)
```

```
                    bdnfklg[iii]=slope*(startx+iii)+mvalue
                    endfor
                    SetScale/i x, startx, endx-1, "eV", bdnfklg
                    OpWave=OpWave-bdnfklg
                    display OpWave
                    print area(OpWave, startx, endx)
                    if(4==3)
                    integrate OpWave
                    points = numpnts(OpWave)
                    points=points-1
                    arean=OpWave[points]
                    variable energimax=leftx(OpWave)
                    variable energimin=rightx(OpWave)
                    if (energimax>energimin)
                    arean=arean*-1
                    else
                    endif
                    sprintf wavearea, "%s%d", ActWave_op, arean
                    print wavearea
                    killwaves OpWave
                    else
                    endif
                    endfor
end
//Divide many XAS spectra by their I0 values. (I09 data)
//(mark the folder i09-123456 as active folder)
function XASdivide(button12) : ButtonControl
//Must write button0 as a string for Igor to recognice.
string button12
String savedDFolde= GetDataFolder(1)//saves the path to the normal datafolder
string subfolders, rawdatafolder, currentfolder
subfolders="entry1:instrument:sdc"
rawdatafolder=savedDFolde+subfolders
currentfolder=savedDFolde+"entry1:instrument:jl0"
setdataFolder rawdatafolder
wave data
duplicate/o data, rawdata
setdataFolder currentfolder
```

```
wave data
duplicate/o data, currentdata
setdataFolder rawdatafolder
string currentdata_path, energy_path
currentdata_path=currentfolder+":currentdata"
currentdata_path=ReplaceString("'", currentdata_path, "")
//Duplicate/O root:Areabox:YN YN
Duplicate/o $currentdata_path, currentdata2
Duplicate/o rawdata, normalised_data
normalised_data=normalised_data/currentdata2
//copy energy wave to the correct folder...
energy_path=savedDFolde+"entry1:instrument:jenergy:jenergy"
energy_path=ReplaceString("'", energy_path, "")
Duplicate/o $energy_path, energy
setdataFolder savedDFolde
end
function transposeAuto(button2) : ButtonControl
string button2
string startdatafolder
startdatafolder=getdataFolder(1)
//get the wave to append to graph
String dummy, ActWaveList="", ActWaveNames="", ActWaveName, foldername=""
        Variable pos, i, NumItems
        //creates a wave list from the browser selection
        Do
                dummy=GetBrowserSelection(i)
                //print dummy
                if (strlen(dummy)>0)
                        ActWaveList+=dummy+";"
                        pos=strsearch(dummy, ":",Inf,1)  //separates folders and wave
                        ActWaveNames+=dummy[pos+1,strlen(dummy)-1]+";"
                        //print(pos)
                        foldername+=dummy[0,pos-1]+";"
                        i+=1
                else
                        NumItems=i
                        break
                endif
```

```
		while (1)
string Actfoldername
//does the mathematical operation
		//the folder that contains the wave(s) is activated automatically
		for(i=0;i<NumItems;i+=1)
			Actfoldername=StringFromList(i,foldername)
			print(Actfoldername)
			if(stringmatch("root",Actfoldername)==1)
			setdataFolder root:
			else
			setdataFolder Actfoldername
			endif
			//print(getdataFolder(1))
				ActWaveName=StringFromList(i,ActWaveNames)
				//String info= TraceInfo("",NameOfWave($ActWaveName), 0)//get info about the wave
			//print info
			Wave ActWave=$ActWaveName  //gives IGOR each wave stored in WaveList
				MatrixTranspose ActWave
			endfor
setdatafolder startdatafolder
end
```